

OXIDATION AND OXIDATIVE DEHYDROGENATION OF *n*-OCTANE USING V₂O₅ SUPPORTED ON HYDROXYAPATITES

by

VENKATA D.B.C. DASIREDDY

This thesis has been prepared according to Format 3 as outlined in the guidelines from the Faculty of Science and Agriculture which states:

This is a thesis in which the chapters are written as a set of discrete research papers, with an overall Introduction and a Final Discussion. These research papers would not be published yet, but at least one paper would have already been submitted for publication. The references are reformatted to a uniform standard.

Submitted in fulfillment of the academic requirements for the degree of
Doctor of Philosophy in the School of Chemistry & Physics
University of KwaZulu-Natal
Durban,
South Africa

October 2012

As the candidate's supervisor I have/have not approved this thesis/dissertation for submission.

Signed: _____ Name: Prof. Holger B. Friedrich Date: _____

Signed: _____ Name: Dr. S. Singh Date: _____

DEDICATED TO
LATE SHRI DASIREDDY BAPAYYA
AND
LATE SHRI PENUMARTHI PATTABHI RAMANNA

ACKNOWLEDGEMENTS

My sincere thanks goes to my parents; I could not have done this without their love, patience, encouragement and understanding.

I would like to thank my supervisor Prof. Holger B Friedrich and my co-supervisor Dr. S. Singh for his guidance and valuable advice throughout the course of my PhD.

I also express my thanks and appreciation to:

- Mrs. Faiza Bibi Khan for her assistance, support and advice throughout my studies.
- Mrs. K. Madhuri Nadupalli and Dr. Srinivasu Nadupalli for their encouragement and support.
- The technical and support staff of the School of Chemistry, especially Mrs. Jayambal Govender, Mr. Kishore Singh, Mrs. Malini Padayachee and Mrs. Thiloshnee Naidoo for their help and assistance.
- Dr. James-Wesley Smith and technicians of the Electron Microscopic Unit, Westville Campus for their assistance with microscopic techniques.
- Previous and present members of the Catalysis Research Group (UKZN) with specific mention of Dr. Elwatig Elkhalifa, Mr. Ziyaad Mohammed, Mr. Leeven Chetty and Ms. Thashini Chetty.
- Mr. Ishaan Ramlakhan and technicians of the Central Academic Workshop for their assistance.
- School of Chemistry, University of KwaZulu-Natal for providing facilities.
- THRIP and the National Research Foundation (NRF) for financial assistance.

Most importantly I would like to thank God for this blessings and guidance.

ABSTRACT

Vanadium pentoxide with loadings varying from 2.5-15 wt% was supported on hydroxyapatite (HAp) by the wet impregnation technique. The materials were characterized by techniques such as X-ray powder diffraction (XRD), Inductively coupled plasma-optical emission spectroscopy (ICP-OES), Brunauer Emmett Teller (BET) surface area measurement, Fourier Transformation-Infrared Spectroscopy (FT-IR), Scanning Electron Microscopy (SEM), Transmission Electron Microscopy (TEM), Temperature Programmed Desorption (TPD) and Temperature Programmed Reduction (TPR). From XRD and IR analyses, vanadium is found in the vanadium pentoxide phase for the lower loadings, whereas for weight loadings in excess of 10%, an additional pyrovanadate phase exists. Electron microscopy provides evidence of a homogenous distribution of the vanadium species on the hydroxyapatite.

Oxidative dehydrogenation reactions carried out in a continuous flow fixed bed reactor showed that selectivity towards desired products was dependent on the vanadium concentration and the phase composition of the catalyst. Good selectivity towards octenes was achieved using the 2.5 wt% V_2O_5 on HAp loaded catalyst. There was a marked decrease in octene selectivity and a significant increase in the formation of C8 aromatics when higher loadings of vanadium were used. At a conversion of 24% at 450 °C, the 15 wt% V_2O_5 on HAp showed a selectivity of 72% towards octenes. A maximum selectivity of 10 % for C8 aromatics was obtained using the 15 wt% V_2O_5 on HAp catalyst at a conversion of 36 % at 550 °C.

Vanadium pentoxide with 2.5 wt% and 10 wt% loading supported on Ca-HAp, Sr-HAp, Mg-HAp, Ba-HAp was tested at different temperatures with varying *n*-octane to oxygen ratios. The

selectivity towards products depended on the hydroxyapatite support. Ca-HAp showed preference towards octenes, Sr-HAp towards aromatics, Mg-HAp towards oxygenates and Ba-HAp towards aromatics and oxygenates.

In the development of a more detailed mechanistic study for the oxidative dehydrogenation *n*-octane, the role of the intermediates such as 1-octene, 2-octene, 3-octene, 4-octene and 1, 7-octadiene was investigated. The influence of hydrocarbon to oxygen ratios was also considered. Ethyl benzene and styrene were produced with high selectivities using 1-octene and 1, 7-octadiene as feeds, whereas *o*-xylene was the main product when 2-octene, 3-octene and 4-octene were used as feedstocks.

PREFACE

The experimental work described in this thesis was carried out in the School of Chemistry & Physics, University of KwaZulu-Natal, Westville Campus from June 2009 to December 2011, under the supervision of Prof. Holger B. Friedrich and co-supervision of Dr. S. Singh.

These studies represent original work by the author and have not otherwise been submitted in any form or degree or diploma to any tertiary institution. Where use has been made of the work by the others authors it is duly acknowledged in the text.

DECLARATION 1 – PLAGIARISM

I, Venkata .D.B.C. Dasireddy, declare that

1. The research reported in this thesis, except where otherwise indicated, is my original research.
2. This thesis has not been submitted for any degree or examination at any other university.
3. This thesis does not contain other persons' data, pictures, graphs or other information, unless specifically acknowledged as being sourced from other persons.
4. This thesis does not contain other persons' writing, unless specifically acknowledged as being sourced from other researchers. Where other written sources have been quoted, then:
 - Their words have been re-written but the general information attributed to them has been referenced
 - Where their exact words have been used, then their writing has been placed in italics and inside quotation marks, and referenced.
5. This thesis does not contain text, graphics or tables copied and pasted from the Internet, unless specifically acknowledged, and the source being detailed in the thesis and in the References sections.

Signed:

DECLARATION 2 – PUBLICATIONS

Publication 1: Oxidative dehydrogenation of *n*-octane using vanadium pentoxide-supported hydroxyapatite catalysts. First author: Venkata .D.B.C. Dasireddy, Co-authors: Sooboo Singh and Holger B. Friedrich, Applied Catalysis A: General 421– 422 (2012) 58– 69.

Publication 2: Activation of *n*-octane using vanadium supported alkaline earth hydroxyapatites. First author: Venkata .D.B.C. Dasireddy, Co-authors: Sooboo Singh and Holger B. Friedrich (Submitted for publication in Applied Catalysis A: General)

Publication 3: Mechanistic studies for activation of *n*-octane using alkali earth metal supported hydroxyapatites. First author: Venkata .D.B.C. Dasireddy, Co-authors: Sooboo Singh and Holger B. Friedrich (In preparation)

Contributions by co authors:

Paper 1: co authors acted as supervisors

Paper 2: co authors acted as supervisors

Paper 3: co authors acted as supervisors

Apart from the contributions of people credited in the acknowledgements, I did all the experimental work.

Signed:

CONFERENCE CONTRIBUTIONS

1. Poster presentation, Catalysis Society of South Africa (CATSA) conference, Goudini Spa, Western Cape, RSA, November 2009, titled “Oxidative dehydrogenation of *n*-octane using vanadium supported on hydroxyapatites”.
2. Poster presentation, Microscopy Society of Southern Africa (MSSA) Conference, University of KwaZulu-Natal, Durban, RSA, December 2009, titled “Oxidation dehydrogenation of *n*-octane using vanadium supported on hydroxyapatites”.
3. Poster presentation, Catalysis Society of South Africa (CATSA) conference, Bloemfontien, RSA, November 2010, titled “Activation of *n*-octane using vanadium supported on hydroxyapatites”.
4. Poster presentation, Europacat X, University of Glasgow, Glasgow, Scotland, September 2011, titled “Activation of *n*-octane using V₂O₅ supported on alkali hydroxyapatites”.
5. Oral presentation, Catalysis Society of South Africa (CATSA) conference, Gauteng, RSA, November 2011, titled “Oxidation and Oxidative dehydrogenation of *n*-octane using V₂O₅ supported on alkali hydroxyapatites”.

CONTENTS

This dissertation is written as a series of three technical papers. Each paper has its own abstract, introduction, experimental section, results and discussion as well as figures, tables and schemes.

Chapter 1 gives an overall introduction to catalysis and contains the literature survey on oxidation and oxidative dehydrogenation of *n*-octane, the scope of hydroxyapatites as catalysts or supports and vanadium oxides as catalysts.

Chapter 2 contains the first paper, which discusses oxidative dehydrogenation of *n*-octane using V₂O₅ supported on hydroxyapatite catalysts (Published in Applied Catalysis A: General 421–422 (2012) 58–69)

Chapter 3 contains the second paper, which discusses the effect of different hydroxyapatites and the effect of *n*-octane to oxygen molar ratios on the oxidative dehydrogenation of *n*-octane.

Chapter 4 contains the third paper, which discusses the mechanistic route to the products in the oxidative dehydrogenation of *n*-octane.

Chapter 5 gives a summary and overall conclusion.

Appendix

TABLE OF CONTENTS

	Page No.
List of Abbreviations	xv
List of Figures	xvi
List of Tables	xxvii
Definitions and Calculations	xxviii
 Chapter 1 : Introduction and Literature review	
1.1 History of Catalysis	1
1.2 Heterogeneous Catalysis	6
1.2.1 Oxidation catalysis	7
1.3 Activation of <i>n</i> -octane	11
1.3.1. Dehydrogenation or dehydrocyclization (aromatization) of <i>n</i> -octane	11
1.3.2. Cracking of <i>n</i> -octane	14
1.3.3. Oxidation and Oxidative dehydrogenation of <i>n</i> -octane	15
1.4 Hydroxyapatites	18
1.4.1 Preparation methods	18
1.4.2 Structure of Hydroxyapatite	20
1.4.3 Catalytic properties of hydroxyapatites	21
1.4.4 Role as a support	22
1.5 Vanadium oxide catalysts	24
1.5.1 Structure of vanadium oxides	26
1.5.2 Vanadium oxide monolayers	27
1.5.3 Catalytic activity of vanadium	29
1.6 Catalytic testing of <i>n</i> -octane with vanadium	32
1.7 Aim of the study	34
References	35

Chapter 2: Oxidative dehydrogenation of *n*-octane using vanadium pentoxide supported on hydroxyapatites catalysts

2.1	Introduction	42
2.2	Experimental	44
2.2.1	Synthesis of catalysts	44
2.2.2	Characterization of catalysts	44
2.2.3	Catalytic Testing	46
2.3	Results and Discussion	48
2.3.1	Catalyst characterization	48
2.3.1.1	BET Surface Area and Elemental Analysis	48
2.3.1.2	Powder X-ray Diffraction	48
2.3.1.3	Infrared Spectroscopy	49
2.3.1.4	Temperature Programmed Reduction	49
2.3.1.5	Temperature Programmed Desorption	53
2.3.1.6	Scanning and Transmission Electron Microscopy	55
2.3.2	Catalytic Testing	55
2.3.2.1	Product Selectivity	58
2.3.2.2	Product selectivity at iso-conversion	62
2.3.2.3	Yields of 1-octene and <i>o</i> -xylene	67
2.4	Conclusion	69
	References	69

Chapter 3: Activation of *n*-octane using vanadium supported on alkaline earth metal hydroxyapatites

3.1	Introduction	73
3.2	Experimental	75
3.2.1	Catalyst synthesis	75
3.2.2	Catalyst characterization	75
3.2.3	Catalytic testing	76
3.3	Results and Discussion	77

	Page No.
3.3.1 Catalyst characterization	77
3.3.1.1 Infrared Spectroscopy	77
3.3.1.2 Raman Spectroscopy	77
3.3.1.3 BET Surface Area Analysis	79
3.3.1.4 Powder X-ray diffraction	85
3.3.1.5 Temperature Programmed Reduction	86
3.3.1.6 Temperature Programmed Desorption	90
3.3.1.7 Scanning and Transmission Electron Microscopy	92
3.3.2 Catalytic activity	96
3.3.2.1 Influence of <i>n</i> -octane to oxygen molar ratios	98
3.3.2.2 Unsupported Hydroxyapatites	98
3.3.2.3 2.5 wt% V ₂ O ₅ supported Hydroxyapatites	98
3.3.2.4 10 wt% V ₂ O ₅ Supported Hydroxyapatites	107
3.4 Conclusion	114
References	115

Chapter 4: Studies towards a mechanistic insight into the activation of *n*-octane using vanadium supported on alkaline earth metal hydroxyapatites

4.1 Introduction	120
4.2 Experimental	121
4.2.1 Catalyst synthesis and characterization	121
4.2.2 Catalytic testing	122
4.3 Results and Discussion	123
4.3.1 Characterization of fresh catalysts	123
4.3.1.1 Diffuse reflectance UV-Vis spectroscopy	123
4.3.1.2 Oxygen Chemisorption	124
4.3.1.3 Temperature programmed oxidation	125
4.3.1.4 Temperature programmed reduction after oxidation	131
4.3.1.5 X-ray photon spectroscopy	133

	Page No.
4.3.2 Catalytic Results	136
4.3.3 Modes of cyclization	154
4.3.4 Proposed mechanism for the reaction	157
4.4 Characterization of the used catalysts	160
4.4.1 Infrared spectroscopy	161
4.4.2 Raman spectroscopy	161
4.4.3 BET surface area analysis	161
4.4.4 X-ray Diffractograms	163
4.4.5 Temperature programmed desorption	164
4.4.6 Scanning and Transmission Electron Microscopy	166
4.5 Conclusion	167
References	168
Chapter 5: Summary and Conclusion	172
Appendix	
A1. Schematic representation of Reactor	176
A2. GC-Method used for analyzing organic (gaseous and liquid) samples	177
A3. GC-Method used for analyzing carbon oxides	179
A4. GC analysis	183
A5. FID sampling	183
A6. TCD sampling	187
A7. Karl Fischer calculation	187
A8. Calculation of Response Factors (RF)	187
A9. Determination of moles of trans-2-octene from a liquid organic sample	190
A10. Determination of moles of butane from a gaseous organic sample	190
A11. Determination of moles of CO from gaseous sample	191
A12. Analysis of Temperature programmed Reduction, Oxidation and Desorption	192

LIST OF ABBREVIATIONS

ATR	:	Attenuated Total Reflectance
BET	:	Brunauer-Emmett-Teller
EDX	:	Energy Dispersive X-ray Spectroscopy
EM	:	Electron Microscopy
FID	:	Flame Ionization Detector
FTIR	:	Fourier Transform Infrared
GC	:	Gas Chromatography
GC-MS	:	Gas Chromatography-Mass Spectrometry
GHSV	:	Gas Hourly Space Velocity
HAp	:	Hydroxyapatite
HPLC	:	High Performance Liquid Chromatography
ICP-OES	:	Inductively Coupled Plasma – Optical Emission Spectroscopy
JCPDS	:	Joint Committee on Powder Diffraction Standards
ODH	:	Oxidative dehydrogenation
SEM	:	Scanning Electron Microscopy
TCD	:	Thermal Conductivity Detector
TEM	:	Transmission Electron Microscopy
TPD	:	Temperature Programmed Desorption
TPO	:	Temperature Programmed Oxidation
TPR	:	Temperature Programmed Reduction
V-HAp	:	Vanadium supported on hydroxyapatite
VSr-HAp	:	Vanadium supported on strontium hydroxyapatite
VMg-HAp	:	Vanadium supported on magnesium hydroxyapatite
VBa-HAp	:	Vanadium supported on barium hydroxyapatite

LIST OF FIGURES

		Page No.
Figure 1.1	Schematic representation of a catalytic reaction.	7
Figure 1.2	Mechanism of catalytic oxidation	9
Figure 1.3	Oxidation-reduction cycles in selective catalytic oxidation	10
Figure 1.4	Reaction pathway diagram for <i>n</i> -octane oxidation at higher temperatures	16
Figure 1.5	Representation of the hydroxyapatite structure perpendicular to the crystallographic <i>c</i> and <i>a</i> axes, showing the OH ⁻ channels and the different types of Ca ions (Ca = green, O = red, P = purple, H = white)	20
Figure 1.6	Synthesis methods for the preparation of supported vanadium oxide catalysts: (a) impregnation with an aqueous solution of NH ₄ VO ₃ , followed by calcination in oxygen and (b) impregnation with VO(OC ₃ H ₇) ₃ in methanol, followed by calcination in oxygen or air and release of propanol	28
Figure 1.7	Reaction network in oxidative dehydrogenation of propane	32
Figure 2.1	XRD diffractograms of HAp (a), 2.5 wt% (b), 5 wt% (c), 7.5 wt% (d), 10 wt% (e) and 15 wt % (f) V ₂ O ₅ supported on HAp.	48
Figure 2.2	Infrared spectra of HAp (a), 2.5 wt% (b), 5 wt% (c), 7.5 wt% (d), 10 wt% (e) and 15 wt% (f) V ₂ O ₅ supported on HAp.	50
Figure 2.3	TPR profile of HAp (a), 2.5 wt% (b), 5 wt% (c), 7.5 wt% (d), 10 wt% (e) and 15 wt% (f) V ₂ O ₅ supported on HAp.	51
Figure 2.4	XRD diffractograms of the reduced catalysts after TPR experiments; 2.5 wt% (a), 5.0wt % (b), 7.5 wt% (c), 10 wt% (d) and 15 wt% (e) V ₂ O ₅ supported on HAp	53
Figure 2.5	TPD profile of (a), 2.5 wt% (b), 5 wt% (c), 7.5 wt% (d), 10 wt% (e) and 15 wt% V ₂ O ₅ supported on HAp (f).	54
Figure 2.6	SEM micrographs (scale = 50 nm) of HAp (a), 2.5 wt% (b), 5 wt% (c), 7.5 wt% (d), 10 wt% (e) and 15 wt% (f) V ₂ O ₅ supported on HAp.	56
Figure 2.7	TEM images (scale = 200 nm) of (a) HAp (b) 2.5 % V-HAp (c) 5 % V-HAp (d) 7.5 % V-HAp (e) 10 % V-HAp (f) 15 % V-HAp	57
Figure 2.8	Effect of temperature on the conversion of <i>n</i> -octane at a GHSV of 4000 h ⁻¹	58
Figure 2.9	Effect of temperature on the conversion of oxygen at a GHSV of 4000 h ⁻¹	59

	Page No.
Figure 2.10 Effect of temperature on the selectivity of octenes at a GHSV of 4000 h ⁻¹	59
Figure 2.11 Effect of temperature on the selectivity of aromatics at a GHSV of 4000 h ⁻¹	60
Figure 2.12 Effect of temperature on the selectivity of cracked products at a GHSV of 4000 h ⁻¹	60
Figure 2.13 Effect of temperature on the selectivity of oxygenates at a GHSV of 4000 h ⁻¹	61
Figure 2.14 Effect of temperature on the selectivity of CO _x at a GHSV of 4000 h ⁻¹	61
Figure 2.15 Selectivity of the product stream at iso-conversion (24%), Temperature = 450 °C	62
Figure 2.16 Selectivity of the product stream at iso-conversion (36%), Temperature = 550 °C	63
Figure 2.17 Selectivity of aromatics at iso-conversion (24%), Temperature = 450 °C	63
Figure 2.18 Selectivity of aromatics at iso- conversion (36%), Temperature = 550 °C	64
Figure 2.19 Selectivity of octenes at iso-conversion (24%), Temperature = 450 °C	64
Figure 2.20 Selectivity of octenes at iso-conversion (36%), Temperature = 550 °C	65
Figure 2.21 The percentage of the 1,6-cyclization at iso-conversion (24%), Temperature = 450 °C	66
Figure 2.22 The percentage of the 2,7- cyclization iso-conversion (36%), Temperature = 550 °C	67
Figure 2.23 Yield of 1-octene as a function of temperature	68
Figure 2.24 Yield of <i>o</i> -xylene as a function of temperature	68
Figure 3.1 Raman spectra of 2.5 wt% V ₂ O ₅ supported on hydroxyapatites (a), 10wt% V ₂ O ₅ supported on hydroxyapatites (b), and unloaded hydroxyapatites (c)	78
Figure 3.2 Nitrogen adsorption-desorption isotherms of 2.5VCa-HAp	79
Figure 3.3 Nitrogen adsorption-desorption isotherms of 2.5VSr-HAp	79
Figure 3.4 Nitrogen adsorption-desorption isotherms of 2.5VMg-HAp	80
Figure 3.5 Nitrogen adsorption-desorption isotherms of 2.5VBa-HAp	80
Figure 3.6 Nitrogen adsorption-desorption isotherms of 10VCa-HAp	82
Figure 3.7 Nitrogen adsorption-desorption isotherms of 10VSr-HAp	82
Figure 3.8 Nitrogen adsorption-desorption isotherms of 10VMg-HAp	83

	Page No.
Figure 3.9 Nitrogen adsorption-desorption isotherms of 10VMg-HAp	83
Figure 3.10 Pore width distributions of 2.5 wt% V ₂ O ₅ supported hydroxyapatites	84
Figure 3.11 Pore width distributions of 10 wt% V ₂ O ₅ supported hydroxyapatites	85
Figure 3.12 XRD diffractograms of 2.5 wt% V ₂ O ₅ supported strontium (a), magnesium (b) and barium (c) supported on hydroxyapatites	85
Figure 3.13 XRD diffractograms of 10 wt% V ₂ O ₅ supported strontium (a), magnesium (b) and barium (c) supported on hydroxyapatites	86
Figure 3.14 TPR profile of 2.5 wt% V ₂ O ₅ supported on hydroxyapatites	87
Figure 3.15 TPR profile of 10 wt% V ₂ O ₅ supported on hydroxyapatites	88
Figure 3.16 Acidic sites distribution on 2.5 wt%V ₂ O ₅ supported on hydroxyapatites	90
Figure 3.17 Acidic sites distribution on 10 wt%V ₂ O ₅ supported on hydroxyapatites	91
Figure 3.18 SEM images of 2.5 wt% V ₂ O ₅ supported strontium (a), magnesium (b) and barium (c) supported on hydroxyapatites	92
Figure 3.19 SEM images of 10 wt% V ₂ O ₅ supported strontium (a), magnesium (b) and barium (c) supported on hydroxyapatites	93
Figure 3.20 TEM images of 2.5 wt% V ₂ O ₅ supported strontium (a), magnesium (b) and barium (c) supported on hydroxyapatites	94
Figure 3.21 TEM images of 10 wt% V ₂ O ₅ supported strontium (a), magnesium (b) and barium (c) supported on hydroxyapatites	95
Figure 3.22 Effect of temperature on the conversion of <i>n</i> -octane over 2.5 V ₂ O ₅ wt% supported on hydroxyapatites at <i>n</i> -octane to oxygen molar ratio of 1:1 (GHSV = 4000 h ⁻¹)	96
Figure 3.23 Effect of temperature on the conversion of <i>n</i> -octane over 10 V ₂ O ₅ wt% supported on hydroxyapatites at <i>n</i> -octane to oxygen molar ratio of 1:1 (GHSV = 4000 h ⁻¹)	97
Figure 3.24 Product selectivity over 2.5 wt% V ₂ O ₅ supported on hydroxyapatites at iso-conversion (27 %), temperature = 450 °C and <i>n</i> -octane to oxygen molar ratio of 1:0.5	101

	Page No.
Figure 3.25 Product selectivity over 2.5wt% V ₂ O ₅ supported on hydroxyapatites at iso-conversion (27 %), temperature = 450 °C and <i>n</i> -octane to oxygen molar ratio of 1:1	101
Figure 3.26 Product selectivity over 2.5 wt% V ₂ O ₅ supported on hydroxyapatites at iso-conversion (27 %), temperature = 450 °C and <i>n</i> -octane to oxygen molar ratio of 1:2	102
Figure 3.27 Selectivity of octenes over 2.5 wt% V ₂ O ₅ supported on hydroxyapatites at iso-conversion (27 %), temperature = 450 °C and <i>n</i> -octane to oxygen molar ratio of 1:0.5	103
Figure 3.28 Selectivity of octenes over 2.5 wt% V ₂ O ₅ supported on hydroxyapatites at iso-conversion (27 %), temperature = 450 °C and <i>n</i> -octane to oxygen molar ratio of 1:1	103
Figure 3.29 Selectivity of octenes over 2.5 wt% V ₂ O ₅ supported on hydroxyapatites at iso-conversion (27 %), temperature = 450 °C and <i>n</i> -octane to oxygen molar ratio of 1:2	104
Figure 3.30 Selectivity of aromatics over 2.5 wt% V ₂ O ₅ supported on hydroxyapatites at iso-conversion (27%), temperature = 450 °C and <i>n</i> -octane to oxygen molar ratio of 1:0.5	105
Figure 3.31 Selectivity of aromatics over 2.5 wt% V ₂ O ₅ supported on hydroxyapatites at iso-conversion (27%), temperature = 450 °C and <i>n</i> -octane to oxygen molar ratio of 1:1	105
Figure 3.32 Selectivity of aromatics over 2.5 wt% V ₂ O ₅ supported on hydroxyapatites at iso-conversion (27%), temperature = 450 °C and an <i>n</i> -octane to oxygen molar ratio of 1:2	106
Figure 3.33 1,6-cyclisation of aromatics over 2.5 wt% V ₂ O ₅ supported on hydroxyapatites at iso- conversion (27%), temperature = 450 °C with varying <i>n</i> -octane to oxygen molar ratios	106
Figure 3.34 2,7-cyclisation of aromatics over 2.5 wt% V ₂ O ₅ supported on hydroxyapatites at iso- conversion (27%), temperature = 450 °C with varying <i>n</i> -octane to oxygen molar ratios	107

	Page No.
Figure 3.35 Product selectivity over 10 wt% V ₂ O ₅ supported on hydroxyapatites at iso-conversion (27%), temperature = 450 °C and <i>n</i> -octane to oxygen molar ratio of 1:0.5	108
Figure 3.36 Product selectivity over 10 wt% V ₂ O ₅ supported on hydroxyapatites at iso-conversion (27%), temperature = 450 °C and <i>n</i> -octane to oxygen molar ratio of 1:1	108
Figure 3.37 Product selectivity over 10 wt% V ₂ O ₅ supported on hydroxyapatites at iso-conversion (27%), temperature = 450 °C and <i>n</i> -octane to oxygen molar ratio of 1:2	109
Figure 3.38 Selectivity of octenes over 10 wt% V ₂ O ₅ supported on hydroxyapatites at iso-conversion (27%), temperature = 450 °C and <i>n</i> -octane to oxygen molar ratio of 1:0.5	110
Figure 3.39 Selectivity of octenes over 10 wt% V ₂ O ₅ supported on hydroxyapatites at iso-conversion (27%), temperature = 450 °C and <i>n</i> -octane to oxygen molar ratio of 1:1	110
Figure 3.40 Selectivity of octenes over 10 wt% V ₂ O ₅ supported on hydroxyapatites at iso-conversion (27%), temperature = 450 °C and <i>n</i> -octane to oxygen molar ratio of 1:2	111
Figure 3.41 Selectivity of aromatics over 10 wt% V ₂ O ₅ supported on hydroxyapatites at iso-conversion (27%), temperature = 450 °C and <i>n</i> -octane to oxygen molar ratio of 1:0.5	111
Figure 3.42 Selectivity of aromatics over 10 wt% V ₂ O ₅ supported on hydroxyapatites at iso-conversion (27%), temperature = 450 °C and <i>n</i> -octane to oxygen molar ratio of 1:1	112
Figure 3.43 Selectivity of aromatics over 10 wt% V ₂ O ₅ supported on hydroxyapatites at iso-conversion (27%), temperature = 450 °C and <i>n</i> -octane to oxygen molar ratio of 1:2	112

	Page No.
Figure 3.44 1,6- cyclisation of aromatics over 10 wt% V ₂ O ₅ supported on hydroxyapatites at iso- conversion (27%), temperature = 450 °C with varying <i>n</i> -octane to oxygen molar ratio	113
Figure 3.45 2,7- cyclisation of aromatics over 10 wt% V ₂ O ₅ supported on hydroxyapatites at iso- conversion (27%), temperature = 450 °C with varying <i>n</i> -octane to oxygen molar ratio	114
Figure 4.1 DR-UV-Vis spectrum of 2.5 wt% V ₂ O ₅ supported on hydroxyapatites	123
Figure 4.2 DR-UV-Vis spectrum of 10 wt% V ₂ O ₅ supported on hydroxyapatites	124
Figure 4.3 TPR-TPO-TPR profiles of 2.5VCa-HAp	125
Figure 4.4 TPR-TPO-TPR profiles of 2.5VSr-HAp	126
Figure 4.5 TPR-TPO-TPR profiles of 2.5VMg-HAp	126
Figure 4.6 TPR-TPO-TPR profiles of 2.5VBa-HAp	127
Figure 4.7 TPR-TPO-TPR profiles of 10VCa-HAp	128
Figure 4.8 TPR-TPO-TPR profiles of 10VSr-HAp	128
Figure 4.9 TPR-TPO-TPR profiles of 10VMg-HAp	129
Figure 4.10 TPR-TPO-TPR profiles of 10VBa-HAp	129
Figure 4.11 XPS spectra of 2.5 wt % V ₂ O ₅ supported on hydroxyapatites	134
Figure 4.12 XPS spectra of 10 wt % V ₂ O ₅ supported on hydroxyapatites	134
Figure 4.13 XPS spectra of 2.5 wt % V ₂ O ₅ supported on calcium hydroxyapatite catalyst samples under reduction and oxygen environments	135
Figure 4.14 Selectivity of products in the ODH of 1-octene with 2.5 V ₂ O ₅ wt% supported hydroxyapatites at iso- conversion (27%), temperature = 450 °C and an 1-octene to oxygen molar ratio of 1:0.5	136
Figure 4.15 Selectivity of products in the ODH of 1-octene with 2.5 V ₂ O ₅ wt% supported hydroxyapatites at iso- conversion (27%), temperature = 450 °C and an 1-octene to oxygen molar ratio of 1:1	137

	Page No.
Figure 4.16 Selectivity of products in the ODH of 1-octene with 2.5 V ₂ O ₅ wt % supported hydroxyapatites at iso- conversion (27%), temperature = 450 °C and an 1-octene to oxygen molar ratio of 1:2	137
Figure 4.17 Selectivity of products in the ODH of 1-octene with 10 wt% V ₂ O ₅ supported hydroxyapatites at iso- conversion (27%), temperature = 450 °C and an 1-octene to oxygen molar ratio of 1:0.5	138
Figure 4.18 Selectivity of products in the ODH of 1-octene with 10 wt% V ₂ O ₅ supported hydroxyapatites at iso- conversion (27%), temperature = 450 °C and an 1-octene to oxygen molar ratio of 1:1	139
Figure 4.19 Selectivity of products in the ODH of 1-octene with 10 wt% V ₂ O ₅ supported hydroxyapatites at iso- conversion (27%), temperature = 450 °C and an 1-octene to oxygen molar ratio of 1:2	139
Figure 4.20 Selectivity of products in the ODH of 2-octene with 2.5 wt% V ₂ O ₅ supported hydroxyapatites at iso- conversion (27%), temperature = 450 °C and an 2-octene to oxygen molar ratio of 1:0.5	140
Figure 4.21 Selectivity of products in the ODH of 2-octene with 2.5 wt% V ₂ O ₅ supported hydroxyapatites at iso- conversion (27%), temperature = 450 °C and an 2-octene to oxygen molar ratio of 1:1	141
Figure 4.22 Selectivity of products in the ODH of 2-octene with 2.5 wt% V ₂ O ₅ supported hydroxyapatites at iso- conversion (27%), temperature = 450 °C and an 2-octene to oxygen molar ratio of 1:2	141
Figure 4.23 Selectivity of products in the ODH of 2-octene with 10 wt% V ₂ O ₅ supported hydroxyapatites at iso- conversion (27%), temperature = 450 °C and an 2-octene to oxygen molar ratio of 1:0.5	142
Figure 4.24 Selectivity of products in the ODH of 2-octene with 10 wt% V ₂ O ₅ supported hydroxyapatites at iso- conversion (27%), temperature = 450 °C and an 2-octene to oxygen molar ratio of 1:1	142
Figure 4.25 Selectivity of products in the ODH of 2-octene with 10 wt% V ₂ O ₅ supported hydroxyapatites at iso- conversion (27%), temperature = 450 °C and an 2-octene to oxygen molar ratio of 1:2	143

	Page No.
Figure 4.26 Selectivity of products in the ODH of 3-octene with 2.5 wt% V ₂ O ₅ supported on hydroxyapatites at iso- conversion (27%), temperature = 450 °C and an 3-octene to oxygen molar ratio of 1:0.5	144
Figure 4.27 Selectivity of products in the ODH of 3-octene with 2.5 wt% V ₂ O ₅ supported on hydroxyapatites at iso- conversion (27%), temperature = 450 °C and an 3-octene to oxygen molar ratio of 1:1	144
Figure 4.28 Selectivity of products in the ODH of 3-octene with 2.5 wt% V ₂ O ₅ supported on hydroxyapatites at iso- conversion (27%), temperature = 450 °C and an 3-octene to oxygen molar ratio of 1:2	145
Figure 4.29 Selectivity of products in the ODH of 3-octene with 10 wt% V ₂ O ₅ supported on hydroxyapatites at iso- conversion (27%), temperature = 450 °C and an 3-octene to oxygen molar ratio of 1:0.5	146
Figure 4.30 Selectivity of products in the ODH of 3-octene with 10 wt% V ₂ O ₅ supported on hydroxyapatites at iso- conversion (27%), temperature = 450 °C and an 3-octene to oxygen molar ratio of 1:1	146
Figure 4.31 Selectivity of products in the ODH of 3-octene with 10 wt% V ₂ O ₅ supported on hydroxyapatites at iso- conversion (27%), temperature = 450 °C and an 3-octene to oxygen molar ratio of 1:2	147
Figure 4.32 Selectivity of products in the ODH of 4-octene with 2.5 wt% V ₂ O ₅ supported on hydroxyapatites at iso- conversion (27%), temperature = 450 °C and an 4-octene to oxygen molar ratio of 1:0.5	148
Figure 4.33 Selectivity of products in the ODH of 4-octene with 2.5 wt% V ₂ O ₅ supported on hydroxyapatites at iso- conversion (27%), temperature = 450 °C and an 4-octene to oxygen molar ratio of 1:1	148
Figure 4.34 Selectivity of products in the ODH of 4-octene with 2.5 wt% V ₂ O ₅ supported on hydroxyapatites at iso- conversion (27%), temperature = 450 °C and an 4-octene to oxygen molar ratio of 1:2	149
Figure 4.35 Selectivity of products in the ODH of 4-octene with 10 wt% V ₂ O ₅ supported on hydroxyapatites at iso- conversion (27%), temperature = 450 °C and an 4-octene to oxygen molar ratio of 1:0.5	149

	Page No.
Figure 4.36 Selectivity of products in the ODH of 4-octene with 10 wt% V ₂ O ₅ supported on hydroxyapatites at iso- conversion (27%), temperature = 450 °C and an 4-octene to oxygen molar ratio of 1:1	150
Figure 4.37 Selectivity of products in the ODH of 4-octene with 10 wt% V ₂ O ₅ supported on hydroxyapatites at iso- conversion (27%), temperature = 450 °C and an 4-octene to oxygen molar ratio of 1:2	150
Figure 4.38 Selectivity of products in the ODH of 1,7-octadiene with 2.5 wt% V ₂ O ₅ supported on hydroxyapatites at iso- conversion (27%), temperature = 450 °C and an 1,7-octadiene to oxygen molar ratio of 1:0.5	151
Figure 4.39 Selectivity of products in the ODH of 1,7-octadiene with 2.5 wt% V ₂ O ₅ supported hydroxyapatites at iso- conversion (27%), temperature = 450 °C and an 1,7-octadiene to oxygen molar ratio of 1:1	152
Figure 4.40 Selectivity of products in the ODH of 1,7-octadiene with 2.5 wt% V ₂ O ₅ supported hydroxyapatites at iso- conversion (27%), temperature = 450 °C and an 1,7-octadiene to oxygen molar ratio of 1:2	152
Figure 4.41 Selectivity of products in the ODH of 1,7-octadiene with 10 wt% V ₂ O ₅ supported hydroxyapatites at iso- conversion (27%), temperature = 450 °C and an 1,7-octadiene to oxygen molar ratio of 1:0.5	153
Figure 4.42 Selectivity of products in the ODH of 1,7-octadiene with 10 wt% V ₂ O ₅ supported hydroxyapatites at iso- conversion (27%), temperature = 450 °C and an 1,7- octadiene to oxygen molar ratio of 1:1	153
Figure 4.43 Selectivity of products in the ODH of 1,7-octadiene with 10 wt% V ₂ O ₅ supported hydroxyapatites at iso- conversion (27%), temperature = 450 °C and an 1,7- octadiene to oxygen molar ratio of 1:2	154
Figure 4.44 Percentage of 1,6 cyclization in the formation of aromatics at a hydrocarbon to oxygen ratio of 1:2 with 2.5 wt% V ₂ O ₅ supported hydroxyapatites at iso- conversion (27%), temperature = 450 °C	155
Figure 4.45 Percentage of 2,7 cyclization in the formation of aromatics at a hydrocarbon to oxygen ratio of 1:2 with 2.5 wt% V ₂ O ₅ supported hydroxyapatites at iso- conversion (27%), temperature = 450 °C	155

	Page No.
Figure 4.46 Percentage of 1,6 cyclization in the formation of aromatics at an hydrocarbon to oxygen ratio of 1:2 with 10 wt% V ₂ O ₅ supported hydroxyapatites at iso-conversion (27%), temperature = 450 °C	156
Figure 4.47 Percentage of 2,7 cyclization in the formation of aromatics at an hydrocarbon to oxygen ratio of 1:2 with 10 wt% V ₂ O ₅ supported hydroxyapatites at iso-conversion (27%), temperature = 450 °C	157
Figure 4.48 Transformation of V ₂ O ₅ phase in 2.5V-HAp during the catalytic testing reaction with <i>n</i> -octane (heating cycle)	158
Figure 4.49 Transformation of V ₂ O ₅ phase in 2.5V-HAp during the catalytic testing reaction with <i>n</i> -octane (cooling cycle)	159
Figure 4.50 Oxidation – Reduction pathway in vanadium supported hydroxyapatites	160
Figure 4.51 XRD diffractograms of used 2.5 wt% V ₂ O ₅ supported calcium (a) strontium (b), magnesium (c) and barium (d) hydroxyapatite catalysts used at a hydrocarbon to oxygen ratio of 1:2	163
Figure 4.52 XRD diffractograms of used 10 wt% V ₂ O ₅ supported calcium (a) strontium (b), magnesium (c) and barium (d) hydroxyapatite catalysts used at a hydrocarbon to oxygen ratio of 1:2	164
Figure 4.53 Distribution of acidic sites on 2.5 wt% V ₂ O ₅ hydroxyapatite catalysts used at a hydrocarbon of oxygen ratio of 1:2.	165
Figure 4.54 Distribution of acidic sites on 10 wt% V ₂ O ₅ supported hydroxyapatite catalysts used at a hydrocarbon of oxygen ratio of 1:2.	165
Figure 4.55 SEM images of 10wt % V ₂ O ₅ supported on calcium (a), strontium (b), magnesium (c)and barium (d) hydroxyapatite catalysts used at a hydrocarbon to oxygen ratio of 1:2	166
Figure 4.56 TEM images of 10 wt% V ₂ O ₅ supported on calcium (a), strontium (b), magnesium (c) and barium (d) hydroxyapatite catalysts used at a hydrocarbon to oxygen ratio of 1:2	167
Figure A1 Reactor design used for experimental work	176

	Page No.
Figure A2 GC-FID chromatogram for a gaseous sample	183
Figure A3 GC-FID chromatogram for a organic layer	184
Figure A4 GC-MS chromatogram for a organic layer	184
Figure A5 GC-MS NIST library search match for ethyl benzene (R. T = 18.46 min)	185
Figure A6 GC-FID chromatogram for a aqueous sample	185
Figure A7 GC-MS chromatogram for a aqueous layer	186
Figure A8 GC-MS NIST library search match for 1-octanol (R. T = 16.57 min)	186
Figure A9 Infrared spectra of 2.5 wt% V ₂ O ₅ supported on strontium (a), magnesium (b) and barium (c) hydroxyapatites	193
Figure A10 Infrared spectra of 10 wt% V ₂ O ₅ supported on strontium (a), magnesium (b) and barium (c) hydroxyapatites	193
Figure A11 Infrared spectra of 2.5 wt% V ₂ O ₅ supported on calcium (a), strontium (b), magnesium (c) and barium (d) hydroxyapatites used at a hydrocarbon to oxygen ratio of 1:2	194
Figure A12 Infrared spectra of 10 wt% V ₂ O ₅ supported on calcium (a), strontium (b), magnesium (c) and barium (d) hydroxyapatites used at a hydrocarbon to oxygen ratio of 1:2	195
Figure A13 Raman spectra of 2.5 wt% V ₂ O ₅ supported on hydroxyapatites used at a hydrocarbon to oxygen ratio of 1:2	196
Figure A14 Raman spectra of 10 wt% V ₂ O ₅ supported on hydroxyapatites used at a hydrocarbon to oxygen ratio of 1:2	196

LIST OF TABLES

	Page No.
Table 1.1 Examples of heterogeneous catalysis	6
Table 1.2 Catalytic oxidation process in industry	8
Table 2.1 BET surface area, pore volume and elemental analysis of fresh and used catalysts.	47
Table 2.2 Temperature programmed reduction and average oxidation state	52
Table 2.3 Distribution of acidic sites and specific acidity	54
Table 3.1 BET surface area, pore volume, pore size, pore width, crystallite size, crystallinity and elemental analysis of V ₂ O ₅ supported on hydroxyapatites	81
Table 3.2 TPR data of vanadium supported on hydroxyapatites	89
Table 3.3 TPD data of vanadium supported on hydroxyapatites	91
Table 3.4 Selectivity of octenes with 2.5 wt% V ₂ O ₅ supported hydroxyapatites at an iso- conversion 24% (Temperature = 450 °C)	99
Table 4.1 Oxygen chemisorption	124
Table 4.2 TPO data of vanadium supported hydroxyapatites	132
Table 4.3 TPR-TPO-TPR data of vanadium supported hydroxyapatites	133
Table 4.4 BET surface area, pore volume, pore size, pore width, crystallite size, crystallinity and elemental analysis of used V ₂ O ₅ supported hydroxyapatites	162
Table A1 Standards used for calibration	181
Table A2 Gaseous standards used for calibration	182
Table A3 Relative response factor of trans-2-octene	188
Table A4 Relative response factors and Gradients of the components used	188

DEFINITIONS AND CALCULATIONS

1. *Gas hourly space velocity, GHSV (h^{-1})* = $\frac{\text{total flow rate into the reactor}}{\text{volume of the catalyst used}}$

2. *Conversion (mol %)* = $\frac{\text{moles of } n\text{-octane in} - \text{moles of } n\text{-octane out}}{\text{moles of } n\text{-octane in}} \times 100$

3. *Selectivity (mol %)* = $\frac{\text{total moles carbon of product component}}{\text{total moles carbon of all product components}} \times 100$

4. *Yield (mol %)* = $\frac{\text{Selectivity of product component} \times \text{conversion}}{100}$

5. *Carbon balance* = $\frac{\text{moles of carbon in}}{\text{moles of carbon out}} \times 100$

CHAPTER 1

INTRODUCTION AND LITERATURE REVIEW

1.1 History of Catalysis

The development of catalysis as a concept is credited to Berzelius who in 1835 realised that a number of isolated observations made by various investigators in the early part of the nineteenth century could be rationalised in terms of what he described as “catalytic power”. This he defined as the ability of substances “to awaken affinities, which are asleep at a particular temperature, by their mere presence and not by their own affinity”. He further defined these substances as catalysts which increased the rate of a chemical reaction but which are not consumed by the reaction. This definition allows for the possibility that small amounts of the catalyst are lost in the reaction or that the catalytic activity eventually decreased. Berzelius did not carry out catalysis research himself but set out to systematize this field of chemistry, as he had done with the concept of isomerism, by observing work done by others. Liebig who had been in constant correspondence with Berzelius suggested that the function of a catalyst was to overcome a kind of “inertia” which prevented an unstable substance from undergoing chemical changes and to accelerate a process which takes place very slowly by itself. Other researchers whose experiments contributed to the crystallisation of catalysis as a concept included Priestley, Döbereiner, Dulong, Payen and Persoz, with Thénard showing as early as 1813 that ammonia decomposed when passed through a red-hot porcelain tube only if iron, copper, silver, gold or platinum were present. However, the first clear realisation that a chemical reaction between two gaseous reactants can occur at a metal surface without the latter being chemically changed is due to Humphry Davy and this was published by the Royal Society (London) in 1817 [1]. This paper described the discovery of a “new and curious series of phenomena”. The last significant contribution prior to Berzelius introducing the concept of catalysis was due to Mitscherlich, who in 1833 summarised the reactions which had occurred by “contact” substances. They included the formation of ether, the oxidation of alcohol to acetic acid, the fermentation of sugar and the formation of ethylene from alcohol by heating. The first report of an entrepreneurial role for catalysis is attributed to Peregrine Phillips who in 1831 filed a British Patent (No. 6069) for “Improvements in Manufacturing Sulphuric Acid” commonly called “Oil of Vitriol”. C.F. Kuhlmann, on the other hand, reported results to the Lille Scientific Society in France in 1838, describing how nitric acid could be produced through the catalytic oxidation of ammonia over platinum. Ostwald introduced the concept of reaction velocity as

a criterion of a catalytic process and asserted, in 1888, that a catalyst should be regarded as an accelerator (or inhibitor) of a reaction already taking place, i.e. in contrast with the view that a catalyst can initiate a reaction. He put forward the following definition of catalysis in 1895: “*Catalysts are substances which change the velocity of a reaction without modification of the energy factors of the reaction*”.

The contribution of many scientists in the development of the science of catalysis can be categorised into several periods.

First Period (1790-1834)

The principle features of catalysis were first presented by Fulhame in 1794 [1] when she suggested that the presence of small quantities of water was required for the oxidation of carbon monoxide and that water was unaffected by the chemical reaction. Similar observations were made by Kirchhoff (1812) who hydrolyzed starch to sugars by using dilute acids. Kirchhoff observed that the acids were not altered by the chemical reaction [2]. Sir Humphry Davy suggested in 1817 that combustible gases, when mixed with oxygen, could explode if they were exposed to heated platinum at temperatures below the ignition temperature. The work of Davy was continued by Ermanand in 1818 showed that it was possible to perform the combustion at 50 °C. In same year Thenard [3] suggested that it was possible to stabilize hydrogen peroxide in acidic solutions, since it decomposed in the presence of water. The deactivation of platinum-based catalysts was first studied by Henry [4] in 1825. Henry discovered that certain substances, for example hydrogen sulfide and carbon disulfide, inhibited the combustion of hydrogen. He also observed that platinum catalysts were less active for the combustion of methane and ethylene than for hydrogen and carbon monoxide. With this new discovery, he developed models for separating and analyzing combustible gases based upon their reactivity in the presence of platinum based catalysts.

Second Period (1835-1897)

Guldberg and Waage [5] proposed that there was a relationship between the tendency of a chemical reaction and the “active masses” of the reactants. The term “active mass” referred to the relationship between the number of molecules and the volume, which is synonymous with the concentration of the species. The degree of a chemical reaction was, according to them, dependent on the concentration of the reactants and a constant which could only be determined experimentally. The results of Guldberg and Waage were not accepted until Van’t Hoff pointed out in 1877 that the constant was in reality a rate constant, which could be used

to measure the chemical change. Van't Hoff's definition was much clearer than that of Guldberg and Waage's and as a result, the concept of affinity was immediately accepted. The dependence of a chemical reaction on the temperature and pressure was originally presented by Le Chatelier in 1884. Combining the results of Le Chatelier with that of Guldberg and Waage, it was possible to deduce a mathematical expression that quantitatively described the relationship between the rate of reaction and the temperature and pressure of the reaction. In 1877, Lemoine [6, 7] showed that by applying a catalyst to a chemical reaction the rate at which equilibrium was reached could be increased without altering its position and stated that *"A catalyst which contributes no energy to a chemical system cannot change the position of the equilibrium, it can only alter the rate at which it is reached"*

Third period (1898-1918)

The third period was marked by the discovery and implementation of new catalytic processes and was known as the birth of the industrial process. The ammonia process, which was without a doubt the most significant process of the period, was originally developed for the fertilizer industry. The first important advancement in the development of the ammonia process was in 1903 when Haber and Nernst discovered that in order to obtain significant activity, the process had to be operated at high pressure. During the course of their work, Haber and Nernst also realized that high activity and equilibrium concentration could be also achieved by operating the process at elevated temperatures. The first small scale catalytic production of ammonia began in 1905, when Haber used an iron-based catalyst. In 1915 Irving Langmuir presented his theories on the adsorption isotherm based upon early work done by Haber [8]. Langmuir also developed the temperature programmed desorption technique the following year [9].

Fourth Period (1918-1945)

The catalytic development of the fourth period was dominated by the petroleum industry. In 1922, Franz Fischer and Hans Tropsch synthesized hydrocarbons from carbon monoxide and hydrogen obtained from coal gasification at room temperature. This discovery was one of the most important chemical achievements during that period. Fischer and Tropsch continued the development of this process and in 1925 obtained high yields of hydrocarbons by operating the process at high pressures. The process was particularly important during WWII when the demands for hydrocarbons rapidly increased. The process is as relevant today as it was 80 years ago and is employed by several companies, including Shell and SASOL [10]. Catalytic cracking of petroleum was developed by Eugène Houdry in 1936 using fixed bed reactors.

The most important modification came in 1941 when fluid catalytic cracking (FCC) technology was introduced. The FCC technology was developed by Lewis and Gilliland at MIT for the Standard Oil Company. The modification made by Lewis and Gilliland solved most of the problems associated with the “Fixed-Bed Houdry Process” and played a very important part in providing the vast quantities of gasoline that was needed during WWII [11].

Fifth Period (1946-1970)

The petroleum industry that was prominent during the fourth period of catalysis played an equally important role in the fifth period with the only real difference being the commodities produced. A linear relationship between quinoline chemisorption and catalytic activity for gasoline cracking was developed by Oblad’s group [12]. In 1951, Ahlborn [13] discovered that diffusion had a significant impact on the activity and selectivity of a catalytic system and paved the way for the design of industrial catalytic systems. In 1954, the first method for characterization of catalysts was developed by Eischen and co-workers [14], where a method was developed for studying carbon monoxide adsorption on copper catalysts using IR-spectroscopy. They also developed methods for the characterization of active sites on metal and metal oxide surfaces by adsorption, as well as a method for distinguishing between Brønsted and Lewis acid sites. In 1964, an extraordinary number of new catalysts and processes were developed, with the most important one being Mobil’s development of the rare earth metal stabilized X-zeolite for catalytic cracking. The development of this zeolite revolutionized the petroleum industry and is today one of the most important catalytic materials available. Wilkinson developed a homogeneous catalyst for hydrogenation in 1965, introducing a new branch of catalysis [15]. At present, homogeneous catalysis plays an important role in the production of pharmaceuticals and fine chemicals.

Sixth Period (1970- present)

The role of the zeolite increased steadily during the sixth period as research groups all over the world attempted to find new areas of applications. The most notable processes involved the use of ZSM-5 as a catalyst for methanol to gasoline conversion [16] and Fe-ZSM-5 for the oxidation of benzene to phenol (1990). In 1980, Shell and Union Carbide developed a process for producing linear low-density polyethylene. The process was revolutionary as it gave the producers total control over the material properties of the product. The process was later extended to the production of polypropylene. Here, the advantages of using homogeneous catalysts in the production polymers were clearly demonstrated [17]. In 1982, Ertl’s group defined the energy profile for the synthesis of ammonia. In 1992, they presented

the first commercial use of a catalyst without iron for the synthesis of ammonia. Ertl won the Nobel Prize in 2007 due to his contribution towards the chemical process on solid surfaces. Other process developments during this period were the introduction of Reduced Crude Cracking (RCC) by Ashland Petroleum [18], the use of Fischer-Tropsch synthesis as a source for producing alpha-olefins [19] and the Cyclar Process for the production of aromatics from liquefied petroleum gas (LPG) [20, 21]. Also, this period was characterized by the integration of research with new technologies, such as super computers. The development of rapid, inexpensive computational systems has impacted significantly on the methods used today for developing new catalytic systems. The use of catalysis for the preparation of agrochemicals increased during this period. Bader and Blaser [22] used catalytic methods for the preparation of agrochemicals, which is illustrated by the case history of the herbicide, metolachlor (trade name DUAL) [22].

One of the most interesting developments in this period is the utilization of hydrogen as a renewable source of energy. The commercial relevance of the renewable chemical glycerol increased in this period because of its use in the production of bio-diesel. Santarelli et al. [23] developed a model of a stand-alone energy system equipped with an proton exchange membrane fuel cell (PEMFC) to generate electricity. The PEMFC is a efficient convertor of chemical energy to electric power using platinum as an anode and transition metal supported carbon cathode [24]. Behr and co-workers [25] developed a method to convert glycerol to synthesis gas or pure hydrogen, which is an alternative to the traditional synthesis routes based on raw fossil materials.

Deactivation studies of catalysts also increased during in this period. Câmara et al. [26] suggested that the deactivation of catalysts is due to poisoning and blockage of pores by coke formation. They developed a model for determining the kinetic constants for the deactivation process which correlated effectively with the experimental deactivation data. Of relevance is the study by Cavani and Trifiró [27] who investigated the active and selective properties of heterogeneous catalysts which they used for the oxidation of light paraffins. They developed vanadium supported catalysts for the selective oxidation and oxidative dehydrogenation of paraffins [28, 29]. The mechanistic studies of these oxidation reactions were studied by Nancy and Francisco [30] by using NiO as catalyst. Centi and Trifiró [31] developed a surface dynamic model for the kinetics of adsorbed intermediates in the selective oxidation of

C₄ and C₅ alkanes. Recently, the kinetic modeling for higher paraffins was studied by Jahangirian and co-workers for *n*-decane oxidation at elevated pressures [32].

In the all the periods catalysis is associated with the growth of nations, but it is also directly responsible for feeding that new growth through new products and processes to meet societal demands.

1.2 Heterogeneous Catalysis

In heterogeneous catalysis the reactant and the catalyst are in the different phases, i.e. solid-liquid, solid-vapour, vapour-liquid or solid-(liquid+gas). Heterogeneous catalysis is suitable for large-scale industrial applications and the catalysts employed are usually transition metals, transition metal oxides, zeolites, silica and alumina.

Table 1.1 Examples of heterogeneous catalysis [33, 34]

Phase of the Catalyst	Phase of the Reactant	Example of the reaction
liquid	gas	Polymerization of alkenes by phosphoric acid
solid	liquid	Decomposition of hydrogen peroxide catalysed by gold
solid	gas	Ammonia synthesis using iron catalyst
solid	liquid + gas	Hydrogenation of benzene to cyclohexane catalysed by nickel

Heterogeneous catalysis is complicated by the existence of a solid-gas or solid-liquid interface. The weak physical forces (van der Waals adsorption) or chemical bonding (chemisorption) between the reactant and catalyst are essential features in heterogenous catalysis. The amount of surface area, the nature of the crystal lattice, pore size, surface geometry, and electronic structure are all important factors affecting the activity of a solid catalyst. It is also necessary in heterogeneous reactions that reactants get to the surface and that products get away if the process is to work efficiently. A heterogeneous gas phase catalytic reaction begins with the adsorption of the reacting molecules on to the surface of the catalyst where intramolecular bonds are broken or weakened (Fig.1.1). The adsorbed species then react on the surface, often in several consecutive steps. Finally, the products desorb from

the surface into the gas phase, thereby regenerating the active sites on the surface for the following catalytic cycle.

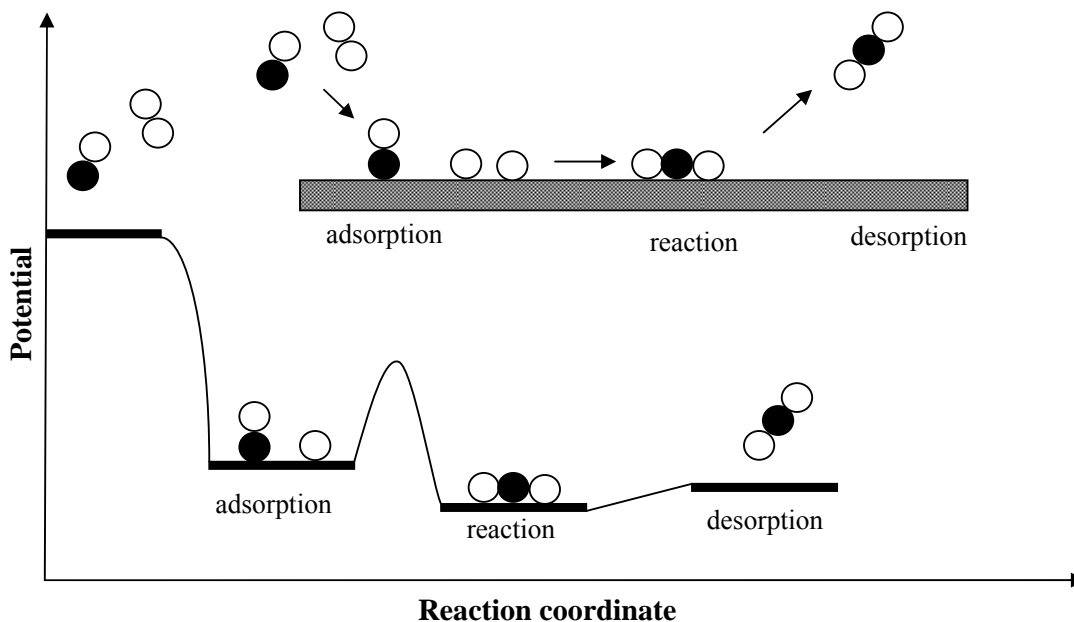


Figure 1.1 Schematic representation of a catalytic reaction.

Due to the flexibility of heterogeneous catalysis, many reactions are done by heterogeneous catalysis. The main type of reactions which follow heterogeneous catalytic processes are oxidation, oxidative dehydrogenation, cracking, preferential oxidation, dehydrogenation and hydrogenation. Among them, heterogeneous oxidation catalysis is of enormous importance, since it is one of the key reactions in chemistry, especially in industrial chemistry [35].

1.2.1 Oxidation catalysis

In view of the exhaustion of easily available sources and the increasing prices of olefins, there have been attempts to use cheaper and more abundant alkanes as feedstock for the production of oxygen containing products through oxidation, and olefins through oxidative dehydrogenation reactions (ODH) [36, 37]. More than 60 % of the chemicals and intermediates synthesized through catalytic processes are products of oxidation. Several monomers, which are essential precursors or additives in the polymer and plastic industries are derived from catalytic oxidation processes. In industry, heterogeneous oxidation catalysis is desirable because of the ease of separation of reactants and products from the catalyst. Many catalysts which show good catalytic performance in terms of both activity and selectivity towards desired products still remain to be developed to the level where such

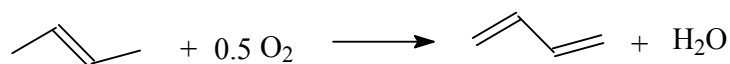
processes can become industrially *viabile*. Some of the heterogeneous oxidation reaction processes in the petrochemical industry are listed in Table 1.2.

Table 1.2 Catalytic oxidation processes in industry [27, 38]

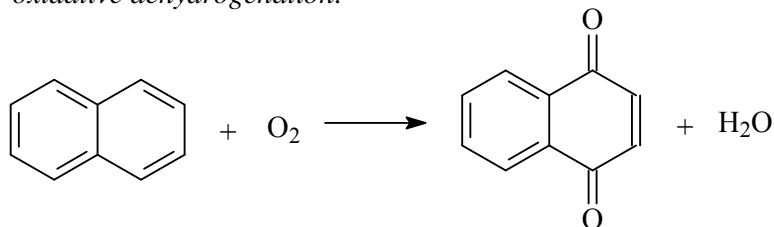
Reagents	Product/Co-product	Conversion (%)	Selectivity (%)
Methanol	formaldehyde	99	94
<i>n</i> -butane	maleic anhydride	75-80	67-72
Benzene	maleic anhydride	98	75
<i>o</i> -xylene	phthalic anhydride	100	79
Naphthalene	phthalic anhydride	100	84
propene (with NH ₃)	acrylonitrile	>99	73-77
Propene	acrolein	>90	80-85
Acrolein(Propenal)	acrylic acid	>95	90-95
Isobutene	methacrolein	>97	85-90
Methacrolein	methacrylic acid	70-75	80-90
Ethane	ethene epoxide	90	80
ethene (with HCl)	1,2-dichloroethane	>95	>95
cyclohexanone	cyclohexanoneoxime	>99	95-98

If an oxidative environment exists for the abstraction of a hydrogen atom, which is followed by the abstraction of a second hydrogen atom and the desorption of water, a new C-C bond may be formed. Such reactions are known as oxidative dehydrogenation. The two hydrogen atoms may originate from two different hydrocarbon molecules, which would facilitate dimerization resulting in the formation of a new C-C bond. Such a reaction is called an intermolecular reaction as opposed to intra molecular oxidative dehydrogenation, when both hydrogen atoms are abstracted from the same hydrocarbon molecule with the formation of a π C-C bond. These reactions are shown below:

Intramolecular oxidative dehydrogenation:



Intermolecular oxidative dehydrogenation:



When the first abstraction of a hydrogen atom is followed by addition of an oxygen atom, oxidation takes place and an oxygenated hydrocarbon derivative is formed.

Catalytic oxidation reactions can be categorized as electrophilic and nucleophilic oxidation reactions as shown in Fig.1.2. In electrophilic oxidation, the reaction proceeds through the activation of oxygen. It is the mildest form of oxidation, i.e. the addition of oxygen to the double bond resulting in the formation of epoxides or the oxyhydration of the double bond to form respective saturated ketones whereas in nucleophilic oxidation small structural changes occur due to the abstraction of hydrogen. Oxidative dehydrogenation of alkanes and alkenes to dienes are the best examples of nucleophilic oxidation.

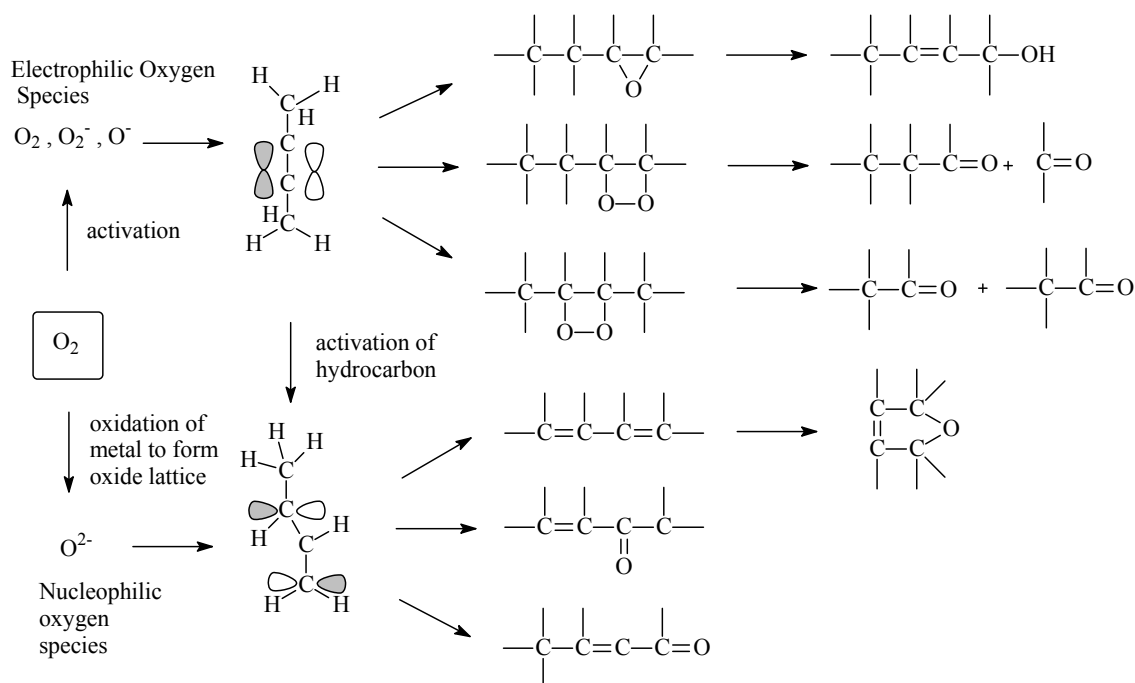


Figure 1.2 Mechanism of catalytic oxidation

Oxygen in catalysis is activated by interacting with the surface of the catalyst. The oxygen can be in the molecular or atomic and neutral or charged form. Oxygen adsorbed at metal surfaces can be present in the form of oxide, superoxide or peroxide ions. All three activated oxygen forms are strongly electrophilic reactants which attack the organic molecule in the region of high electron density. This reaction path commences with the activation of the organic molecule, which thus becomes prone to attack by the nucleophiles, and consists of consecutive steps of hydrogen abstraction and nucleophilic oxygen addition. Each of these steps requires different active centers to be present at the catalyst surface. In subsequent steps these undergo a nucleophilic attack by lattice oxygen ions and the oxygenated product is desorbed, leaving oxygen vacancies at the surface of the catalysts. In this kind of reaction, the reduction part and oxidation part are considered to be separate steps, and it is called the redox mechanism. This mechanism has become known as The Mars-van Krevelen mechanism [24, 39]. The abstraction of hydrogen from the hydrocarbon molecule in the first step and the subsequent nucleophilic addition of oxygen take place at different surface sites, the activated hydrocarbon species diffusing over the surface from one site to the other.

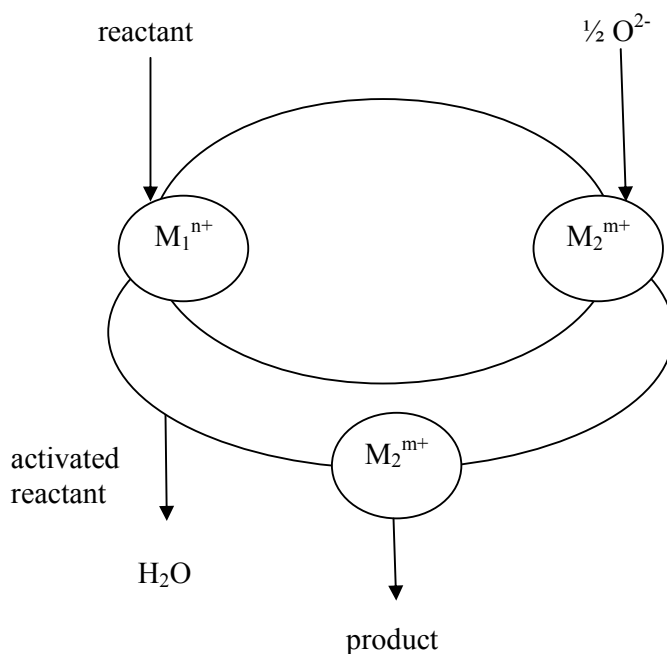


Figure 1.3 Oxidation-reduction cycles in selective catalytic oxidation ($n, m =$ oxidation states)

1.3 Activation of *n*-octane

Activation of *n*-octane using heterogeneous catalysts can be carried out by dehydrogenation or dehydrocyclization, cracking, oxidation and oxidative dehydrogenation.

1.3.1. Dehydrogenation or dehydrocyclization (aromatization) of *n*-octane

The dehydrogenation of *n*-octane is an important reaction with much industrial applications and can be carried out on both bi functional and mono functional catalysts [40]. During the WWII, butenes were synthesised from butanes using chromium-alumina catalysts. The butenes were then dimerized to octenes and hydrogenated to produce high octane fuel. The uses of metal catalysts on non acidic supports for this reaction have been investigated for many years. A different approach to catalytic dehydrogenation was first introduced in the mid 1960s to supply long chain linear olefins for the production of biodegradable detergents [41]. Long chain paraffins are highly prone to dehydrogenation. Therefore, in order to maintain high selectivity and yield towards value added products like aromatics and oxygenates, it is necessary to operate at relatively high temperatures typically 500 °C, and low per mass conversions. While this is economical for the production of heavy linear olefins, it is not for the production of light olefins. *n*-Octane can be dehydrogenated to *n*-octene, which can form *n*-octadiene by further dehydrogenation and aromatization of these products leads to the formation of aromatics and coke.

The key role of dehydrogenation catalysts is to accelerate the main reaction while controlling other reactions. The dehydrogenation of alkanes proceeds on the catalyst, which is followed by terminal ring closure on acidic sites of the support. Cracking and isomerization take place as side reactions, because the acid catalyzed steps are usually faster than the dehydrogenation process. This leads a large number of products, the distribution of which is very sensitive to the nature and to the ratio of active sites. Platinum is a highly active catalytic element which is used for dehydrogenation of *n*-octane and it is not required in large quantities to catalyze the reaction when it is dispersed on a high surface-area support. The high dispersion is also necessary to achieve high selectivity to dehydrogenation relative to undesirable side reactions, such as cracking [40].

The typical high surface area alumina supports employed have acidic sites that accelerate skeletal isomerization, cracking, oligomerization, and polymerization of olefinic materials, and enhance “coke” formation. Alkali or alkaline earth metals assist in the control of the acidity. Also, α -alumina supports that have essentially no acidity can be utilized; however,

the challenge is to obtain high dispersion of platinum on such very low surface area (>50) supports. Therefore, acidity must be eliminated by using suitable modifiers [40, 42].

The role of platinum modifiers is to weaken the platinum–olefin interaction without effecting platinum-paraffin interaction. Arsenic, tin, germanium, lead and bismuth are among metals reported as platinum activity modifiers. The consecutive dehydrogenation rate of mono-olefins and di-olefins is decreased by this modification without lowering the rate of paraffin dehydrogenation significantly. The modifier also improves the stability against fouling by heavy carbonaceous materials [41]. Modified catalysts possess high activity and high selectivity to mono-olefins. The major by-products are di-olefins, that can be controlled kinetically. Coke formation is also suppressed and, therefore, stability is greatly improved. Over modified catalysts, the major reaction pathways for both light and heavy paraffin dehydrogenation systems are simple [43, 44].

The mechanism of isomerization over these platinum supported catalysts has been rationalized in terms of a bifunctional mechanism. The metallic site dehydrogenates the alkanes into alkenes which are protonated at the Brønsted acidic site yielding alkyl carbenium ions. These ions, after rearrangements or scissions, desorb from the acidic sites and are hydrogenated on the metallic sites to produce saturated reaction products. However, the transfer of the molecules to sequential metal-acid sites in order to produce the branched species is not obvious, especially in the case of relatively long chain hydrocarbons such as *n*-heptane and *n*-octane [45].

According to Meriaudeau [46], the mechanism of isomerization and aromatization of *n*-octane can follow both mono and bi functional pathways. In the case of a mono functional pathway, two mechanisms leading to identical product distribution were considered. The first one involves the dehydrogenation of octane to yield octene, followed by 1,6 or 2,7 ring closure [45]. The next steps are the dehydrogenation of the cyclic compounds and the production of ethylbenzene and *o*-xylene. The second one consists of the stepwise dehydrogenation of octane into mono-, di- and triene, which is followed by terminal ring closure [46]. In the case of a bi-functional pathway, both the nature of the catalyst (metal or oxide) and the support have an important role in the octane transformation. From the comparison of the rates of the formation of aromatics from octene when compared to those measured in the reaction from octane, however, one could infer that ethylbenzene and *o*-xylene are produced with two times higher rates from octene compared to *n*-octane [45]. On

1.3.2. Cracking of *n*-octane

Catalytic cracking i.e Fluid Catalytic Cracking (FCC) is among the most important catalytic processes worldwide. Basically the active component in FCC catalysis is a Brønsted acid from the catalyst used as an additive for enhancing both the octane number of the gasoline produced by the yield of propane [51]. Further evidence for the involvement of Brønsted sites during cracking of *n*-octane to produce alkanes and alkenes can be seen from the effects of subjecting the catalyst to higher pretreatment temperatures. This activity decline can be associated with the conversion of Brønsted sites to Lewis sites as water is removed from the catalyst. It is now generally accepted that there are two fundamentally different mechanisms for acid catalyzed cracking of hydrocarbons, namely classical bimolecular cracking on the one hand and non-classical monomolecular cracking. Ratios of Brønsted to Lewis sites present on the catalyst have been discussed in terms of the ratio of alkanes to alkenes produced in cracking products. When comparisons are made at the same reaction temperature, the alkane to alkene ratio can be related to ratios of active Brønsted and Lewis sites present, but this does not describe the relative amounts of cracking to produce alkenes and alkanes *via* distinct mechanisms [52].

The bimolecular hydride transfer step in the classical cracking mechanism is sterically hindered in the pores of the catalyst. Cracking of *n*-octane can occur by different types of β -scission reactions [53]. When the bimolecular a hydrogen transfer reactions are hindered, more olefins than paraffins are formed. On bi-functional catalysts the hydrocarbons are dehydrogenated on the metal sites and C-C bond cleavage occurs over Brønsted acidic sites [54]. The more the *n*-octane is branched before the C-C bond cleavage, the higher will be the probability for a central β -scission, which will result in the generation of a higher amount of *n*-octane. In the cracking reactions, branched products cannot be formed by secondary isomerisation of linear fragments, since competitive adsorption at the acid sites becomes less favorable with decreasing chain length of a fragment [54]. In the case of thermal cracking of alkanes, the initiation step seems fairly well understood to be C-C bond fission to form two radicals, with the preferred C-C ruptures occurring between the most highly substituted carbons. In the case of acid-catalysed cracking of alkanes, the initiation steps have been the sources of a great deal of discussion for many years. Three possible activation mechanisms for the generation of the active carbenium ions have been discussed. The abstraction initiation idea features a Lewis acid catalyst stripping a hydride (H⁻) from an alkane to create a carbenium ion. The redox initiation idea features an oxidizing catalyst stripping an electron

from an alkane, with the alkane radical cation further decomposing to create a carbenium ion. The alkene initiation idea features the protonation by the catalyst of trace amounts of alkene in the feed, creating carbenium ions.

Solid acids are well known as catalysts that promote the cracking of alkanes.g.*n*-octane by accelerating the cleavage of C-C bonds. The first desired point of catalytic cracking is low temperature operation to save energy and to reduce the emission of carbon dioxide; the employed catalysts must have strong acid sites to produce a large amount of active carbonium ions even at low temperature. The second point is the selectivity for alkenes, especially ethene and propene. The high selectivity for propene increases the economic feasibility of the catalytic cracking of naphtha, because the production routes of propene are not varied compared with those for ethane. As a result, the pore structure and particle size of the catalysts, which determine the reaction path and the residence time of the catalytic cracking, are important factors in determining the product composition. Zeolites show very different conversion in the catalytic cracking of *n*-octane according to their acidities and pore shapes. The catalysts mostly employed for the cracking of *n*-octane are composed of metals like Pt, Pd, Ni, Re and Zr[40, 50, 51] in the combination with suitable supports [42, 45, 51].

1.3.3. Oxidation and Oxidative dehydrogenation of *n*-octane

Catalytic partial oxidation process (CPO) is a process by which valuable chemicals can be auto-thermally generated from hydrocarbon feed stocks [55]. Olefins will be made from refinery sources like naphtha and these chemical feed-stocks are complicated mixtures that typically contain linear and branched hydrocarbons as well as aromatic compounds. CPO of heavy alkanes, like octane shows that straight chain hydrocarbons produce the highest olefin selectivity to ethylene [56], while branched and cyclic hydrocarbons, like iso-octane and cyclo hexane, produce high selectivities to branched and cyclic olefins like *i*-butylene and cyclohexene [57].

In the oxidation of *n*-octane oxygen has been used as a oxidant and in some cases hydrogen peroxide was also used as oxidant [58]. The catalysts employed for these purposes were based on metals like Pt, Pd, Rh and Ni incorporated in a suitable support [42, 44, 54]. Partial oxidation of a variety of gaseous and liquid hydrocarbons to hydrogen and synthesis gas has been studied over rhodium based catalysts. It has been shown that most of the octane is converted to syngas over rhodium catalysts [59].

Catalytic partial oxidation of alkanes is used for the production of hydrogen. Hartmann et al. [59] studied the catalytic partial oxidation of iso-octane over a rhodium/alumina catalyst by varying both fuel-to-oxygen ratios and flow rates. They reported that under fuel rich conditions, the formation of by-products potentially serving as coke precursors. They observed that the quantity of by-products strongly depends on the flow rate. Both fuel conversion and hydrogen yield increase with increasing flow rate [59].

Due to the increase in the demand for the olefins, the oxidative dehydrogenation of lower alkanes e.g. *n*-butane has become an alternative route for the production of olefins [60]. The highest activity and selectivity towards olefins was reported when VO_x supported mesoporous silica was used as catalyst. The most abundant selective product in this reaction was 1,3-butadiene. The total sum of selectivity to all C₄ olefins reached up to 65 %, but the selectivity towards the products decrease with increasing vanadium content [60].

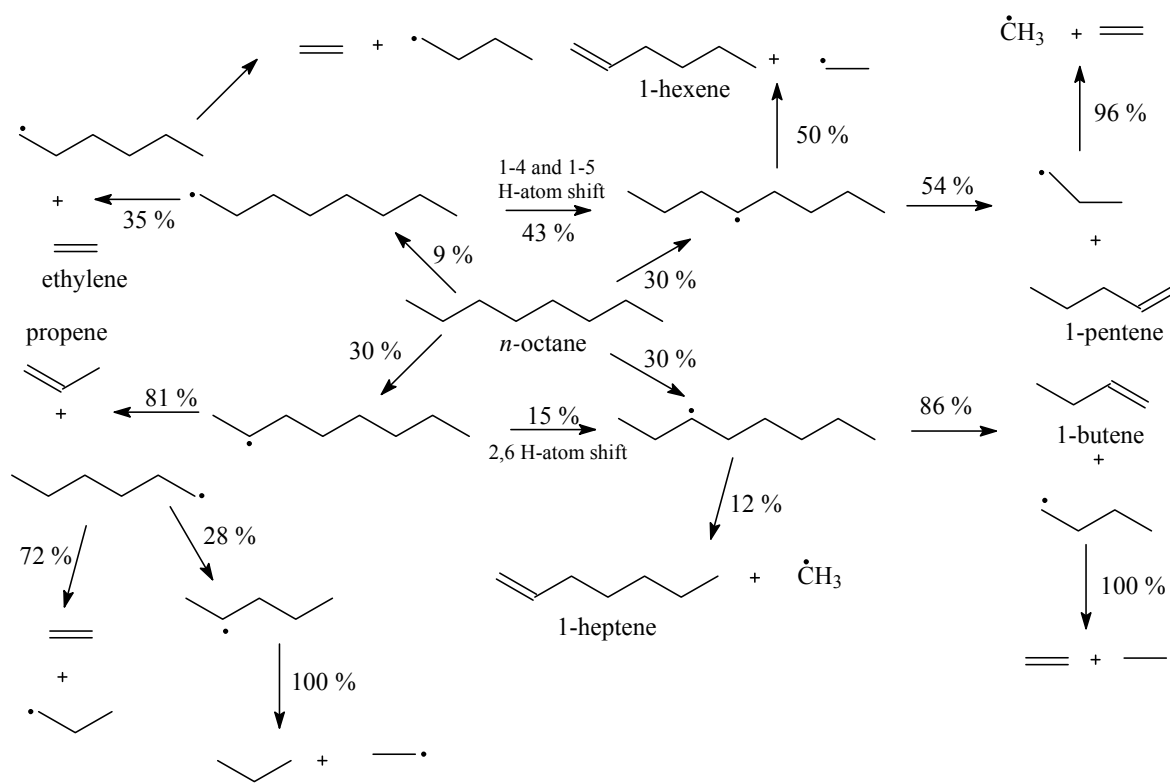


Figure 1.4 Reaction pathway diagram for *n*-octane oxidation at higher temperatures (Redrawn with permission from Elsevier Copyright © 2012) [61]

The oxidative dehydrogenation of alkanes is an exothermic reaction and able to proceed at much lower temperatures at which the formation of coke is insignificant, furthermore, the conversion is no longer limited by thermodynamic constraints (Fig. 1.4). The main limitation in ODH process is the formation of by-products [62]. The formation of carbon oxides in ODH of alkanes is thermodynamically more favoured than the formation of the corresponding olefin and a rapid decrease in the selectivity to the desired products with increasing alkane conversion is observed (Fig. 1.4). The main aim of ODH of lower alkanes is to improve olefin yields [36]. The development of catalysts for oxidative dehydrogenation of alkanes is important i.e. catalysts which are capable for activating the C-H bonds of the alkane molecule in a flow of oxygen and capable of desorbing alkene formed in the dehydrogenation step in order to avoid a further oxidation [36,63]. Acidic and basic properties, as well as the redox characteristics of the catalytic system, show an effect on the catalyst performance in the oxidative dehydrogenation of alkanes [64].

The use of zeolites as catalysts in the activation of *n*-octane was studied by Brillis and Manos [65] over a temperature range of 400-500 °C. They observed a product stream containing mainly iso-butene, propane, iso-pentane and *n*-butane as cracked products. No C₈ aromatics were found in this study. Similarly, Altwasser and co-workers [51] showed that with zeolites *n*-octane does not form any C₈ aromatics.

The catalytic performance in the oxidative dehydrogenation of alkanes depends on the type of catalyst and on the oxidized alkane [66]. The transition metal ions which are introduced to vanadia-based catalysts affected the selectivity towards the desired products. CO was the main product and it was formed in a consecutive oxidative dehydrogenation of lower alkanes. The activity and selectivity towards olefins was not dependent on the electronegativity of the transition metal ion present in the catalyst [66].

Friedrich and Mohammed [67] recently reported the oxidation and oxidative dehydrogenation of *n*-octane using catalysts derived from hydrotalcite-like precursors. These catalysts showed a good performance with regard to the formation of dehydrogenation products; especially of styrene.

And in other work, Elkhalfa and Friedrich [68] reported on the oxidative dehydrogenation of *n*-octane over VMgO catalysts with different vanadium loadings for the production of octenes and C₈ aromatics. *n*-Octane was also activated in the liquid phase by catalysts which are metal supported silica alumina [69], zeolites [70], polymolybdates [43] and titanium,

tantalum [71] and niobium [72] based catalysts. These catalytic systems produce predominantly alcohols, aldehydes, ketones, and carboxylic acids.

It can be concluded that the above research that the catalytic oxidation of *n*-octane was employed to produce hydrogen, syngas, octenes as well as aromatics and short chain alkanes. An interesting feature in the oxidative dehydrogenation of *n*-octane is *n*-octane will also give cracking products. For the production of linear olefins, oxidative dehydrogenation of *n*-octane can be employed. Oxidative dehydrogenation represents a potential alternative route to non oxidative dehydrogenation [68, 73]. The oxidative dehydrogenation becomes more important, though challenging, in the production of such long chain olefins like octenes, as *n*-octane [68] (like long chain alkanes) has a great tendency to crack when exposed to the high temperatures that are usually needed in the non-oxidative dehydrogenation.

1.4 Hydroxyapatites

In the last 30 years, the synthesized calcium phosphate compounds have generated a great deal of interest because of the wide variety of their medical applications, especially in orthopedics, plastic and dental surgery. The synthetic apatites were widely used initially as bio ceramic materials are also studied as potential adsorbents for heavy metals and have been applied as catalysts in various transformations [74]. The general chemical formula for the hydroxyapatite is $\text{Ca}_{10-x}(\text{HPO}_4)_x(\text{PO}_4)_{6-x}(\text{OH})_{2-x}$ where $0 \leq x \leq 2$. The molar ratio of calcium to phosphorus Ca/P varies from 1.2 to almost 2 in hydroxyapatites. The stoichiometric molar ratio of hydroxyapatites is 1.67. Although the chemical synthesis of hydroxyapatites was first achieved several decades ago, the synthetic methodology has been developing over the years in order to satisfy the requirements for various biomedical applications. Hydroxyapatite (HAp) is also available as a cation-exchange medium, because Ca^{2+} ions in HAp can be substituted by various other cations [75, 76], such as Sr^{2+} [77, 78], Mg^{2+} [79, 80], Ba^{2+} [81, 82], Pb^{2+} [83, 84] and Zn^{2+} [85, 86].

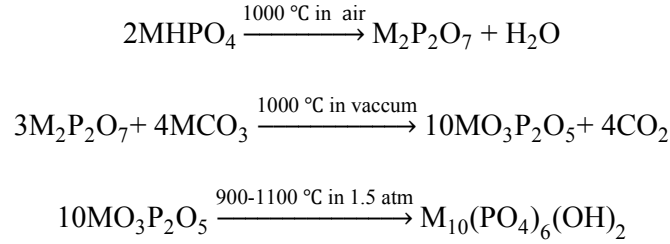
1.4.1 Preparation methods

Pure stoichiometric hydroxyapatite, $\text{M}_{10}(\text{PO}_4)_6(\text{OH})_2$, ($\text{M} = \text{Ca}^{2+}$, Sr^{2+} , Mg^{2+} and Ba^{2+}) is prepared by three types of procedures:

- Solid state reactions [87, 88]
- Wet process [89, 90]
- Sol- gel process [91, 92]

Solid State Reaction

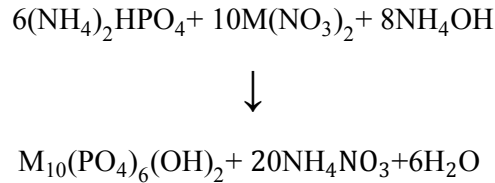
The hydroxyapatites are prepared in the solid state according to the following reactions.



The reactions were carried out in a controlled atmosphere in a tube inserted in a furnace.

Wet Process

In the wet procedure, the hydroxyapatite is prepared by the co-precipitation method. A solution of $\text{M}(\text{NO}_3)_2 \cdot 4\text{H}_2\text{O}$ ($\text{M} = \text{Mg}^{2+}, \text{Ca}^{2+}, \text{Sr}^{2+}, \text{Ba}^{2+}, \text{Co}^{2+}$) in 60 ml of H_2O was brought to pH 11-12 with aqueous NH_4OH and thereafter diluted to 120 ml. A solution of $(\text{NH}_4)_2\text{HPO}_4$ in 100 ml H_2O was brought to pH 11-12 with concentrated NH_4OH and thereafter diluted to 160 ml. The calcium solution was vigorously stirred at room temperature and the phosphate solution was added drop-wise over 30 min to produce a white gelatinous precipitate which was then stirred and boiled for 10min. The precipitate was filtered, washed and dried at 80 °C for overnight and calcined at 500 °C for 3 h.



Sol-gel Process

A conventional alkoxide processing methodology as described by Bogdaovivene et al. [93] is used to synthesize hydroxyapatite powders by the sol-gel technique. A calcium alkoxide solution is prepared by dispersing calcium diethoxide in ethanol and which is then dissolved using ethanediol with vigorous stirring. A phosphorus alkoxide solution, prepared by diluting triethyl phosphate in ethanol is added to the calcium alkoxide solution. Vigorous agitation is maintained throughout the addition process and for a further 10 min after the addition of reagents. The preparation is conducted in a glove box containing a nitrogen atmosphere and the vessels are closed to avoid any volatilization. The resultant solutions are then aged under inert atmosphere. After ageing, gels for thermal analysis are prepared by pouring the

appropriate solution into a petri dish and hydrolyzing at 70 °C in a convection oven. The resultant gels are then crushed using an agate mortar and pestle.

1.4.2 Structure of Hydroxyapatite

In biology, the structural synergy between HAP and organic substrates determines the unique and amazing elastic and mechanical properties of hard tissues. The form of HAP most frequently encountered is hexagonal, having the $P6_3/m$ space group symmetry, with the lattice parameters of $a=b= 9.342 \text{ \AA}$, $c = 6.881 \text{ \AA}$ and $\gamma = 120^\circ$ [94]. The structure consists of an array of PO_4 tetrahedra held together by Ca ions interspersed among them (Fig. 1.5). The Ca ions occur in two markedly different sites, in accurately aligned columns (Ca (I)) and in equilateral triangles (Ca (II)) centered on the screw axis. The OH's occur in columns on the screw axis, and the adjacent OH's point in opposite directions (Fig. 1.5). This configuration implies that there would be steric interferences between adjacent OH's. This can be accomplished by replacement of an OH⁻ with a vacancy [94, 95].

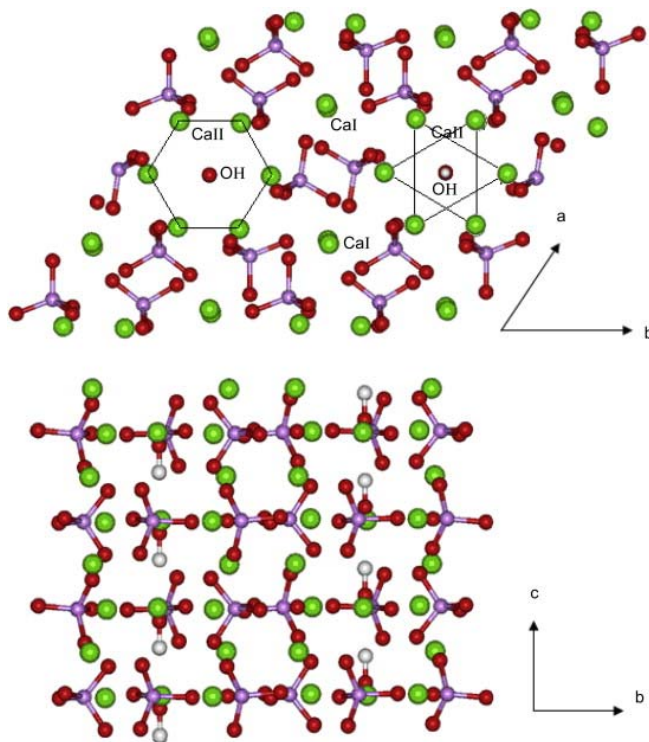


Figure 1.5 Representation of the hydroxyapatite structure perpendicular to the crystallographic c and a axes, showing the OH^- channels and the different types of Ca ions (Ca = green, O = red, P = purple, H = white) [96]. (Redrawn with permission from Elsevier Copyright © 2012)

1.4.3 Catalytic properties of hydroxyapatites

Zahouilyi et al. [97] used synthetic hydroxyapatite as a new basic catalyst for the Michael addition [97] of mercaptans to chalcone derivatives for producing high yields under mild reaction conditions. By-products of the usual undesirable reactions in the Michael Addition such as 1,2-addition, bis-addition and polymerisation are not observed. Zahouilyi et al. [97] reported a high catalytic activity and selectivity in Michael reaction of the HAp catalyst coupled with its ease of use and reduced environmental problems. In addition this catalyst can be regenerated and reused without loss of activity, making it an attractive alternative to homogeneous basic reagents.

Tsuchida et al. [98] studied the reaction of ethanol over HAp using catalysts of different Ca/P molar ratios. These were prepared by controlling the pH of the solution during precipitation. It was found that the distribution of acidic sites and basic sites on the catalyst surface varied with the Ca/P ratio of HAp. The yields of ethylene, 1-butanol and 1,3-butadiene correlates with the ratio of acidic sites and basic sites. They also proposed that yields of higher alcohols, such as 1-butanol, which are characteristic products of ethanol over HAp, are functions of the probability of ethanol activation on the catalyst surface [98].

Liptáková et al. [99] reported that the oxidation of benzene to phenol proceeds over hydroxyapatite catalysts in the presence of air and ammonia. Almost 97% selectivity of phenol formation was achieved at about 3–4% conversion of benzene. Trace amounts of aniline, biphenyl, diphenyl ether, benzofuran, dibenzofuran and benzo-1,4-dioxime were detected in the product stream. The reaction mechanism involved formation of N_2O from NH_3 in the first step of reaction. Benzene is oxidized by active oxygen species which are formed on the catalyst from the decomposition of N_2O .

In the study by Sugiyama et al. [100] partial oxidation of methane at 700 °C yields carbon oxides as the principal products, with a selectivity to CO of approximately 40%, while on calcium oxide and phosphate C_2 hydrocarbons predominate. However, on introduction of tetrachloromethane (TCM) into the feed stream, the selectivity to CO is increased to 71% on hydroxyapatites, while, in contrast, the conversion of methane and/or the selectivities to C_2 compounds, particularly to C_2H_4 , are enhanced [100].

1.4.4 Role as a support

Supported materials on hydroxyapatite have been employed as catalysts for many gas-phase acid/base reactions [101], gas-phase partial oxidation reactions [102, 103], liquid Knoevenagel Reactions [104] and Friedel-Crafts alkylation [105]. Complete hydrogenation of quinoline was carried out over Ru/HAp under the mild conditions and over short time. The good hydrogenation result is attributed to the existence of the surface hydroxyl group on HAp. The surface hydroxyl group on HAp forms a hydrogen bond with the nitrogen atom of quinoline or the hydrogenation products which weakens the interaction of the active centre and nitrogen atom, preventing poisoning and promoting the hydrogenation of quinoline. Alternatively, the surface hydroxyl group forms a hydrogen bond with the π electrons in the aromatic cycle of quinoline and this hydrogen bond promotes the adsorption of quinoline in aprotic solvent. Both factors cause the complete hydrogenation of quinoline [106]. Ru-HAp is an effective heterogeneous catalyst for the oxidation of various alcohols, which is dominated by the formation of a monomeric Ru species as the phosphate complex on the Ru-HAp surface [107]. No Ru leaching was observed during oxidations and the Ru catalyst was recyclable. It is believed that this design strategy for HAp-bound transition metal catalysts can be further applied to a wide range of functional transformations [107].

The catalytic activity of strontium hydroxyapatite (Sr-HAp) for the oxidation of methane was studied by Sugiyama et al. [108] with and without trichloro methane (TCM). They found that the catalytic activity of Sr-HAp exceeded that of HAp with and without TCM. The increase in activity was due to the conversion of Sr-HAp to $\text{Sr}_3(\text{PO}_4)_2$ at temperatures exceeding 500 °C. In the presence of TCM the hydroxyapatite is partially converted to chlorapatite resulting the increased selectivities towards C_2H_4 on Sr-HAp, particularly so with increase in time on stream. The presence of chlorapatite apparently suppresses the further oxidation of CO and C_2H_4 [108].

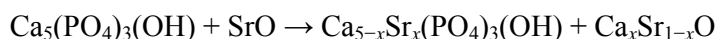
Iron/hydroxyapatite catalysts containing varying amounts of iron – $\text{Fe}(x)/\text{CaHAp}$ – were prepared by cation exchange and were tested in butan-2-ol conversion and the ODH of propane [109]. The increase in the iron content enhanced the acid properties of the catalysts, resulting in butan-2-ol dehydration with a yield of 55% to the presence of O_2 . In propane oxidative dehydrogenation (ODH), good propene selectivity (35–90%) was exhibited at low conversion. The maximum propene yield (6.2%) was obtained at low Fe content, whereas the dehydrogenation of butan-2-ol into methyl ethyl ketone (MEK) in the presence of di oxygen was much higher on pure CaHAp than on $\text{Fe}(x)/\text{CaHAp}$ [109]. Chromium-loaded

hydroxyapatite catalysts Cr(*x*)/CaHAp ($0.1 \leq x \leq 3.7$ wt.% Cr) [110] were prepared by ion-exchange and were also tested in propane oxidative dehydrogenation in the 300–550 °C temperature range. The Cr⁶⁺ centres present on the catalysts initiate the cracking of propane because of their acidity thus improves the conversion. However, the Cr is reduced by the reaction mixture and the propane conversion decreases with it [110].

Calcium-hydroxyapatite and calcium-fluoroapatite loaded with different amounts of nickel were synthesized by Boukha et al.[111]. These catalysts Ni(*x*)/CaHAp and Ni(*x*)/CaFAP were tested in methane dry reforming with CO₂. Methane conversion at 600 °C increased with the nickel loading up to $x = 4$, where the activity is around the thermodynamic equilibrium (78%) and the H₂/CO ratio close to 1. Carbon deposition on the catalysts was found to increase with nickel loading, but there was no significant decrease in activity after 4 h on stream. The encouraging results achieved were attributed to the synergy between the basic properties of the apatites, their ability to chemisorb CO₂ and the catalytic features of the supported nickel [111].

Nickel–calcium phosphate/hydroxyapatite catalysts [112] exhibited high activity and selectivity in the partial oxidation of methane (POM). As the Ca/PO₄ ratio increased, the calcium hydroxyapatite phase was more dominant than the calcium phosphate phase. For Ni supported catalysts, as the Ni/PO₄ ratio increased, the amount of NiO increased in the fresh samples, but decreased in the used samples, resulting in an increase in metallic Ni. The catalytically active component was found to be metallic nickel that is produced under a reduced environment during the reaction. However, its surface is totally reoxidized at 400 °C and activity is lost completely[112]. Therefore, most of the catalytic activity was attributed to the fine Ni metal particles. The amount of H₂ chemisorption was very small (the percentage exposed of Ni < 1%), while the amount of O₂ chemisorption was quite large ($O_{\text{sorb}}/Ni_{\text{total}} \sim 0.6$). The suppression of H₂ chemisorption might be attributed to the covering of the nickel particles with the phosphate and/or hydroxyl groups or to a strong interaction with those groups [112].

Chen et al.[113] proposed that for the preparation of Sr-HAp the reaction of solid phase ion-exchange occurred between Ca²⁺ from hydroxyapatite and Sr²⁺ which is obtained from the decomposition of Sr(NO₃)₂ at 600 °C.



The porous hydroxyapatite was able to support the $\text{Ca}_x\text{Sr}_{1-x}\text{O}$ phase and allow it to disperse spontaneously onto the surface as a monolayer or sub monolayer [113]. When the newly generated $\text{Ca}_x\text{Sr}_{1-x}\text{O}$ phase was dispersed spontaneously onto the surface of the porous hydroxyapatite as a monolayer or sub monolayer, it inhibited decomposition of the porous hydroxyapatite and also restrained recrystallization of the porous hydroxyapatite to retain porous morphology at 600 °C. The $\text{Ca}_x\text{Sr}_{1-x}\text{O}$ phase was, probably, the main reasons for the catalytic activity towards transesterification. The catalytic activity of porous HAp, and $\text{Sr}(\text{NO}_3)_2/\text{HAp}$ samples (without calcination) and the catalyst samples was evaluated in the

1.5 Vanadium oxide catalysts

Supported metal oxide catalysts have been successfully employed over the years in various industrial applications for the synthesis of bulk and fine chemicals along with chemical intermediates. In heterogeneous catalysis, metal oxides which are active components are supported on other materials. This improves the mechanical strength, increases the thermal stability and the dispersion of the active component on the surface. Catalyst supports were believed to be catalytically inert materials, however, it is now well established that the support properties, such as structure composition and acidity/basicity, can also have considerable influence on the catalytic activity of the active phase. Specific interaction between support and the active phase can lead to several consequences.

- the formation of monomolecular dispersion of the active component
- the formation of crystallites of the active component
- the formation of new compounds
- the diffusion of the active component into the lattice of the carrier to form a solid solution

The uses of supported catalysts have a number of advantages i.e. increase in the surface area, reducing the sintering of the catalysts and thermal stability. Often oxides are prepared by calcinations at relatively high temperatures that result in significant sintering or loss of surface area. Thus a suitable support can reduce the sintering of the catalyst. Generally, a support is used as a heat conduction medium. This may be particularly important in oxidation reactions which have large heats of reaction i.e. exothermic. A support of high thermal conductivity helps to remove the heat from the reaction site, and reduced hot spots, which usually degrade selectivity. The use of bulk oxides as catalysts leads to total combustion in oxidation reactions.

Among the transition metal oxide catalysts, supported vanadium oxides are useful, efficient catalysts in a number of heterogeneous catalytic oxidation reactions. In these oxidation reactions, the catalysts consist of the mainly active vanadium oxide phase, which is highly dispersed on the surface of the support. For example, V_2O_5 supported on TiO_2 is more active than the bulk or crystalline V_2O_5 . These observations have stimulated a detailed investigation on the vanadium oxide species regarding the nature of the surface and the catalytic properties. The information on the surface of vanadium oxide species can be obtained from a number of physical and chemical characterization methods. The physical characterization techniques provide insight into the reactivity of the surface vanadium oxide phase which is of paramount importance in gaining fundamental understanding of the origin of unique properties provided by supported vanadium oxide catalysts.

It is generally accepted that surface coordinative unsaturation (CUS) is an important aspect in surface chemistry and catalysis. The surface anions and cations have fewer numbers of nearest neighbors than the corresponding ions in the bulk and hence these surface anions and cations are coordinatively unsaturated. These unsaturated sites are principally responsible for the adsorptive and catalytic properties of the transition metal oxides, like vanadium oxides. Often the coordinatively unsaturated metal cation, e.g. V^{5+} , site behaves like a Lewis acid and the O^{2-} (CUS) ion is more basic than the bulk ions; there and acid-base pairs participate in heterolytic dissociative adsorption. More extensive surface coordinative unsaturation can be created either by dehydroxylating (addition of OH^- group) the surface further or by removing surface lattice oxygen by reduction. The oxygen vacancies created on reduced metal cations of vanadium are known as coordinatively unsaturated sites, to adsorb oxygen from the gas phase and activate it for participation in catalytic reactions.

For selective oxidation catalysis the lattice oxygen of a reducible metal oxide would serve as a versatile and useful selective oxidizing agent and is better than molecular gaseous oxygen, the metal oxygen bond must be in a range to allow rapid removal of lattice oxygen resulting in hydrocarbon oxidation and regeneration of the active site by molecular oxygen. It is also necessary to maintain a high oxidation state of the oxidant to achieve both high conversion and selectivity. The higher oxidation state of the metal oxide like vanadium is restored by contact with air at reaction temperature. The basic requirement of a selective oxidation catalyst is that the cation in the oxide must be able to interconvert between two oxidation states.

1.5.1 Structure of vanadium oxides

The valence shell electron configuration of vanadium is $4s^2 3d^3$. This configuration of valence electrons present in two different types of orbitals could make vanadium an interesting candidate in many different ways in terms of its chemical reactivity. Vanadium exhibits multiple valency of +2, +3, +4 and +5, with the +5 more commonly observed in many of its compounds. Vanadium pentoxide, V_2O_5 exists in a number of forms with different coordination geometries. One of the reasons for this behavior is that the ionic radius of the vanadium atom with respect to the oxygen atom is rather small to form four coordinated structures and may be too small for the formation of six coordinated structures. Perhaps for those reasons different vanadium oxides are four, five and six coordinated.

According to Baes and Mesmer [118] the different co-ordinations of vanadium oxide are demonstrated in its aqueous solutions with the variation in the concentration of vanadium species and this result in a change of pH. There are twelve different vanadium oxide species known to exist in aqueous solutions. At high pH values (basic region) with a low vanadium ion concentration, the vanadium oxide species is four coordinated and isolated (VO_4^{3-}). At low pH values with high vanadium ion concentrations, the vanadium oxide species is present as polymerized and exists as six coordinated decavanadates, $V_{10}O_{28-z}(OH)_z^{z-6}$. At the intermediate vanadium ionic concentrations (intermediate values of pH), vanadium give rise to various levels of polymerization as well as protonations resulting in four, five and six coordinated vanadium oxide species, e.g. $V_2O_6(OH)^{3-}$, $V_3O_9^{3-}$ and $V_{10}O_{27}(OH)^{5-}$.

Vanadium oxide in its crystalline form is usually more distorted. However, many examples of regular coordinated geometries of vanadium oxide structures exists and can be generally categorized as four coordinated vanadates, namely orthovanadates, pyrovanadates and meta vanadates, rarely occurring five coordinated vanadates and six coordinated vanadates. In the four co-ordinated system orthovanadates contain isolated VO_4 units and are the least distorted of the other two four coordinated vandates. Pyrovanadates contain V_2O_7 dimeric units, whereas metavanadate has polymeric chains of $-VO_2-O-$ units (VO_3 units). Six coordinated vanadates contain highly distorted octahedral VO_6 units [119].

On the basis of the results obtained from various spectroscopic techniques, many authors proposed two types of structural species of vanadia found on supported catalysts. These are (i) structures observed when the loading of the active phase does not exceed the monolayer capacity and (ii) structures seen at higher loadings. Up to one monolayer these structures are

classified surface vanadyl complexes, two to four mono layers as disordered vanadium oxide and above four monolayers as para crystalline V_2O_5 . The monolayer may have different single structures on the support and the vanadium is linked to the support surface OH groups through an oxygen bridge. The nature of bonding of metal oxide to the support surface can occur through one, two or three oxygen bridges.

1.5.2 Vanadium oxide mono layers

Generally the metal oxides exist as a monolayer or mono-molecular dispersion and are greatly influenced by the nature of the supported oxide [120]. The vanadium oxide mono layers in the fundamental studies of catalyzed reactions have several attractive features. Monolayer structures may change under vigorous reaction conditions through redox cycles [121] or during hydration and dehydrogenation processes. These changes are confined to the monolayer and migration of oxide ions to and from the subsurface region doesnot occur. Metal oxide mono layers are also thermally stable [120, 121]. The ease of formation and thermal stability of mono layers have been related to the ratio of the charge on the support cation to the sum of the cation and oxide ion radii [120]. The tendency of vanadium oxide species to form a surface compound with the support has also been related to the difference in its basicity, with acidic V_2O_5 a bi dimensional vanadate readily forms with the strongly basic MgO at high temperature, whereas a weak interaction with SiO_2 is all that is possible [122]. The amount of active component required for the total coverage of support as a monomolecular layer can be estimated. It is convenient to adopt some definition of monolayer capacity of a surface for VO_x , so that V_2O_5 contents of materials on supports of different surface areas can be compared on the basis of “number of equivalent mono layers”. A monolayer is thus defined as the fraction of V_2O_5 covered on unit area of support and where the isolated vanadium species completely cover the support surface [123].

The concentration of V_2O_5 needed for the monolayer coverage is determined on the basis of the vanadium compound is reaction with surface hydroxyl groups of the support in a stoichiometric reaction to form the monolayer species [124, 125]. It is generally believed that a maximum catalytic activity can be achieved if the active phase is deposited as a monomolecular layer, since the uncovered patches of the catalyst surface are probably responsible for non-selective oxidation [123].

The preparation of vanadia monolayer catalysts deposited on various oxide supports have been extensively studied and reported by several authors [119, 126, 127]. Some of the methods are:

Impregnation

Impregnation is the method of designing supported vanadium pentoxide catalysts with an aqueous oxalic acid (Fig.1.6). This method is useful to prepare any desired loading of vanadium pentoxide, either more or less than the equivalent [124, 128].

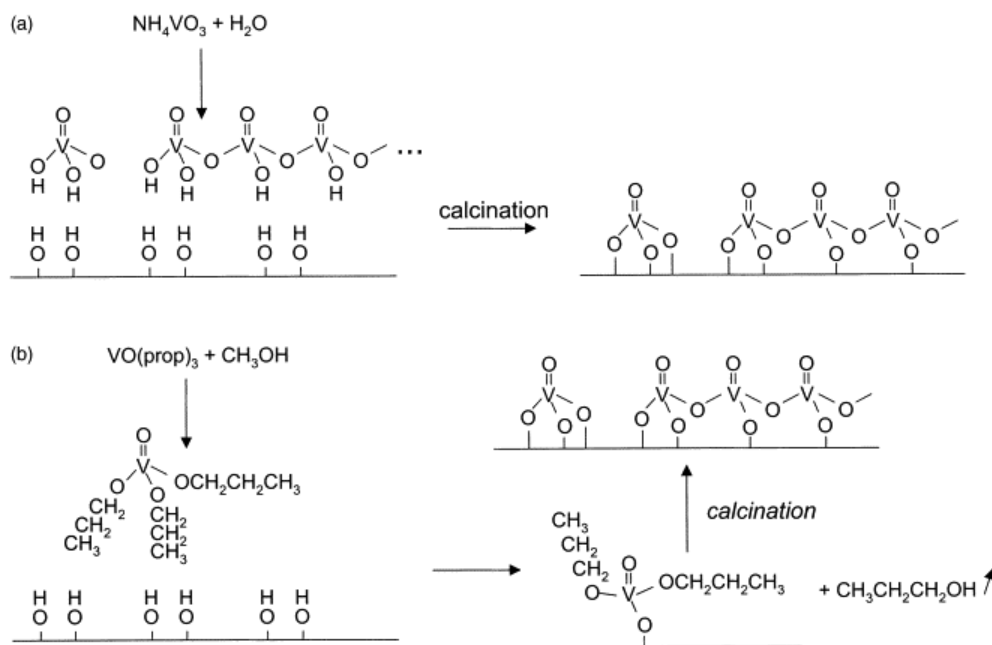


Figure 1.6 Synthesis methods for the preparation of supported vanadium oxide catalysts: (a) impregnation with an aqueous solution of NH_4VO_3 , followed by calcination in oxygen and (b) impregnation with $\text{VO}(\text{OC}_3\text{H}_7)_3$ in methanol, followed by calcination in oxygen or air and release of propanol [129]. (Redrawn with permission from Elsevier Copyright © 2012)

Grafting

The grafting technique is a more reliable method to achieve mono layers of V_2O_5 by the reaction of surface hydroxyl groups of the support with vanadium compounds such as VOCl_3 , $\text{VO}(\text{acac})_2$, $\text{VO}(\text{OR})_3$, either in gas phase or in solution[130, 131].

Solid-Solid wetting

The solid wetting method is based on mechanical mixing of two metal oxides, which on heating leads to the spreading of vanadium pentoxide on the supporting oxide. The spreading

of active component is due to decrease in surface free energy and the formation of surface bonds between the vanadia and support [132, 133].

Chemical vapour deposition

This method involves formation of an active component from a volatile inorganic or organometallic compound, like gaseous VOCl_4 , VOCl_3 and $\text{V}_2\text{O}_3(\text{OH})_4$ etc., onto the exterior surface of a support by the reaction with its hydroxyl groups [134, 135].

Co-precipitation

In this method the active component and the supporting oxides or their precursors may be precipitated simultaneously from a solution containing compounds of each element. This usually produces an intimate mixing of the catalyst and support, but the active component is dispersed throughout the bulk, as well as being at the surface [136, 137].

Supported vanadia catalysts have become an important class of catalytic material because of their numerous industrial applications and use as model systems for fundamental studies of monolayer catalysts. Vanadia catalysts exhibit high activity and selectivity for a variety of oxidation reactions. Vanadium pentoxide supported on TiO_2 (anatase) [138] exhibits better activity and selectivity for *o*-xylene oxidation compared with other catalysts. Deactivation, which is a major problem for $\text{V}_2\text{O}_5/\text{TiO}_2$ catalysts, has been mainly associated with the transformation of the anatase support into rutile. It is known that the presence of rutile in $\text{V}_2\text{O}_5/\text{TiO}_2$ catalyst used for *o*-xylene oxidation results in lower selectivities and activities [138].

1.5.3 Catalytic activity of vanadium

For partial oxidation of methane to formaldehyde, over a wide range of reaction temperatures studied, the incorporated V-MCM-41 [139] sample with the highest vanadium loading was shown to have the highest catalytic activity and formaldehyde yield. However, at temperatures exceeding 600 °C, the selectivity of formaldehyde decreased with an increase in vanadium loading. In this study, the high yields of formaldehyde by partial oxidation of methane at much lower temperature was associated with the large BET surface area of the V-MCM-41 [139]. For the V-MCM-41 catalyst, since a greater portion of the vanadium species are well inside the pore channels of the mesoporous support, they exist as inaccessible species for the reactant molecule, while the formation of higher but dispersed surface vanadia

species in the grafted catalyst may account for its enhanced activity behavior [140]. The high catalytic performance of the immobilized catalysts may arise from active metal site isolation and hence favor an easy approach for the reactants to the active extra framework metal sites. However, the observed activity of the V-MCM-41 (silica exchanged by vanadium) and V/MCM-41 (vanadium supported) catalyst is attributed to the presence of leached vanadia species and its interactions with H_2O_2 are highlighted with a series of experiments. Heterogeneity studies show that the immobilized catalysts are more stable than the incorporated/grafted catalysts; as for the former, the versatile coordination ability of the amino groups prevents the removal of vanadia species even during drastic reaction conditions and hence it proves the novelty of anchored complex species for various oxidation reactions [140].

Garcia et al. [141] studied the total oxidation of short-chain hydrocarbons using a titania-supported palladium catalyst modified with vanadium. A range of catalysts were prepared by co-impregnation of the titania support with palladium (II) chloride and ammonium meta vanadate. The addition of vanadium promoted the rates of oxidation at lower temperatures but decreased the palladium dispersion and the number of surface palladium sites [141]. Temperature-programmed reduction studies showed that the addition of palladium to V/TiO₂ significantly increased the ease of catalyst reduction. Characterisation using electron paramagnetic resonance spectroscopy showed that the presence of palladium significantly increased the concentration of V⁴⁺ species. It is proposed that the increased catalyst activity is related to the modified redox properties of the catalysts.

The oxidative dehydrogenation (ODH) of *n*-butane, 1-butene, and *trans*-2-butene on different vanadia catalysts has been compared by López Nieto et al. [142]. MgO, alumina, and Mg–Al mixed oxides with Mg/(Al+Mg) ratios of 0.25 and 0.75 were used as supports. The catalytic data indicate that the higher the acidic character of catalysts, the lower the selectivity to C₄-olefins from *n*-butane and the selectivity to butadiene from both 1-butene and *trans*-2-butene. Thus, ODH reactions were mainly observed for *n*-butane and butenes on basic catalysts. The different catalytic performance of acidic or basic catalysts is a consequence of the isomerisation of olefins on acidic sites, which appears to be a competitive reaction with the selective oxidative dehydrogenation process by a redox mechanism [142].

Selective photo oxidation of light alkanes, mainly methane and ethane, into the corresponding aldehydes was achieved using silica-supported vanadium oxide catalysts under UV irradiation at 250 °C [143]. The reaction with methane required UV irradiation of wavelength >310 nm, whereas the reaction with ethane or propane proceeded on irradiation at longer wavelength. According to the surface analysis of the catalysts, only isolated four-coordinated vanadium oxide surface species were considered to show catalytic activity towards the photo oxidation of methane, while accumulated vanadium surface species were shown to be active for the photo oxidation of other light alkanes [143].

Khodakov et al.[144] demonstrated that the structure and dispersion of VO_x species depend on their surface density and on their interaction with a given support. Support surfaces predominantly covered with poly vanadate structures or small V₂O₅ clusters containing V-O-V or V=O linkages lead to high oxidative dehydrogenation rates and selectivities [145, 146]. The composition of the support influences the speciation of VO_x species into monovanadates, polyvanadates and V₂O₅ clusters and thus the catalytic behavior of supported vanadia in oxidative dehydrogenation reactions. The concentration of polyvanadate structures increases with increasing VO_x surface density. Oxidative dehydrogenation rate coefficients increase initially with increasing VO_x surface density on all supports, concurrently with the densification of isolated monovanadates into polyvanadate domains, but ultimately decrease as the latter evolve into V₂O₅ crystallites with low specific surface area [145, 146]. Ratios of rate coefficients for oxidative dehydrogenation of propane to those for secondary propene combustion are relatively insensitive to structural modifications caused by changes in VO_x surface density or support composition. This suggests that sites required for oxidative dehydrogenation also catalyze the undesired combustion of propene [144].

Chen et al. [147] explained that oxidative dehydrogenation of propane on VO_x/ZrO₂ and on bulk V₂O₅ powders occurred through parallel and sequential reactions [147]. Propene is the most abundant primary product; CO and CO₂ form *via* secondary combustion of propene while CO₂ forms also by direct combustion of propane. The dependences of reaction rates on C₃H₈, O₂, and H₂O concentrations are identical on supported VO_x and on V₂O₅ powders, suggesting that similar active centers are present on both surfaces. The reaction kinetics are consistent with a Mars-van-Krevelen redox sequence in which lattice oxygen atoms participate in the irreversible activation of C–H bonds in propane [148]. The resulting alkyl species desorbs as propene and the remaining OH groups recombine to form water and

reduced vanadium centers. These reduced vanadium centers reoxidize by irreversible dissociative chemisorption of O_2 . The recombination of OH groups to form water is reversible. The assumption that surface oxygen and OH groups are the most abundant surface intermediates leads to a rate expression that describes accurately the measured kinetics of propane ODH reactions [147].

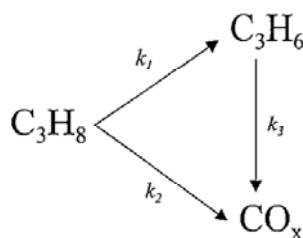


Figure 1.7 Reaction network in oxidative dehydrogenation of propane[147]. (Redrawn with permission from Elsevier Copyright © 2012)

Aboelfetoh et al. [130] prepared a series of VO_x/MgO catalysts *via* impregnation and grafting and investigated their structure and catalytic performance in the oxidative C–H activation of cyclohexane. According to their catalytic activity measurements, impregnated or grafted VO_x/MgO catalysts with low vanadium loading containing isolated VO_4 species do not show considerable activity for the oxidation of cyclohexane. In contrast, the catalysts containing ortho- $Mg_3V_2O_8$ and pyro- $Mg_2V_2O_7$ phases show conversions ranging from 40 to 67%. Bulk magnesium vanadates such as ortho- $Mg_3V_2O_8$, pyro- $Mg_2V_2O_7$ and meta- MgV_2O_6 show activities similar to the supported catalysts containing these phases. Ortho- $Mg_3V_2O_8$ exhibits a higher activity than pyro- $Mg_2V_2O_7$, which in turn has a higher activity than meta- MgV_2O_6 . By increasing the amount of VO_x on MgO catalysts the cyclohexane conversion is increased [130].

1.6 Catalytic testing of *n*-octane with vanadium

From the extensive literature reviewed, it becomes apparent that vanadium oxides, especially V_2O_5 are important materials employed in the catalytic oxidation of lower alkanes. The selectivity and yields of octenes and aromatics are significantly varied, when vanadium oxides are dispersed on different supports such as alumina, silica, zirconia, titania and mesoporous compounds. In the study of the oxidation of *n*-hexane [149], since the products obtained from the catalytic and non-catalytic oxidation of *n*-hexane are essentially identical, a free radical mechanism is suspected to apply. The same products were obtained in a glass

reactor, however, at lower conversions at similar operating temperatures. Since conversions at temperatures up to 400 °C were substantially higher for reactions in the presence of VMgO than without, Friedrich et al. [149] concluded that VMgO is a catalyst for these reactions.

Singh and Jonnalagadda [150] showed the catalytic efficiency of V₂O₅ supported on hydroxyapatite in the controlled oxidation of *n*-pentane to phthalic anhydride and maleic anhydride. The hydroxyapatite was prepared by co-precipitation and the loaded catalysts by wet impregnation using NH₄VO₃ solution. Selectivity towards the products was influenced by the total flow rate, reaction temperature and V₂O₅ loadings. Good selectivities towards the anhydrides (MA 40% and PA 25%) was obtained with 5.0 and 7.5 wt.% of V₂O₅ on HAp at 360 °C [150].

Friedrich and Mahomed [67] showed the partial oxidation of *n*-octane with various hydrotalcite-like compounds incorporating Mg and V in various ratios and synthesised at different temperatures gave mainly octenes and aromatics, of which the dominant product was styrene. Good results were obtained on the catalyst where the Mg/V ratio was 2.3. Catalysts where the precursors have more amorphous structures were found to be superior to those obtained from highly crystalline precursors because of their large surface areas. Increasing the temperature improved conversion, while increasing the fuel–air ratio and GHSV decreased the conversion. Styrene selectivity could be increased with increasing temperature, fuel–air ratio and GHSV, although linear relationships were not observed [67].

Elkhalifa and Friedrich [68] demonstrated that the partial oxidation of *n*-octane over VMgO catalysts produced mainly (in addition to carbon oxides) octenes, styrene, ethylbenzene and to a lesser extent xylene and some cracking products. 2-Octenes were found to be the dominant octene isomers, while 4-octenes were the minor compounds indicating that *n*-octane activation was favourable at C₂ and C₃, and unfavourable at C₄. 1-Octene was the dominant isomer over 15 wt% vanadium on MgO, while over 50 wt% vanadium on MgO 3-octene was the dominant isomer, with 1-octene being the minor product. 50 wt% vanadium on MgO showed the highest selectivity to the octenes and correspondingly the lowest to the aromatics. 15wt% vanadium on MgO was found to be superior to the other catalysts in activity as well as in the production of 1-octene and styrene [68].

The *n*-octane to oxygen molar ratio has an obvious impact on both the catalytic activity and selectivity; the strength of the oxidative environment was influential in determining the

catalytic performance. In this context enriching the reactant mixture with oxygen increased the conversion (up to 84%), but at the same time enhanced the formation of carbon oxides and lowered the selectivity to ODH products (octenes and C₈ aromatics) [73]. In contrast, enriching the reactant mixture with *n*-octane (mild oxidative environment) increased the selectivity to octenes. The best selectivities to C₈ aromatics were obtained at the *n*-octane to oxygen ratios of 0.4 and 0.8. For the combined selectivity to both octenes and C₈ aromatics, the tests at *n*-octane to oxygen ratios of 0.8 and 1.6 showed the highest values. The results of this study suggested that octenes are precursors to aromatics [73].

1.7 Aim of the study

Alkenes are the important raw materials in a wide range of applications in the petrochemical industry due to their low cost and ability to be functionalized easily. Potential precursors are the paraffins, which are easily obtained from natural gas and petroleum. Since gases to liquid (GTL) processes also produce considerable amounts of higher *n*-paraffins, and world production is expected to rise enormously as more of these plants are built, these easily available and cheap paraffins may be suitable substitutes for olefinic and aromatic feedstocks. Furthermore, the utilization of paraffins as feedstocks could facilitate processes with lower environmental impact and cost [27-29]. The conversion of alkanes into value added products such as olefins and aromatics is an important field of research with regard to both industrial and scientific values. In this context, the oxidation and oxidative dehydrogenation of *n*-octane may be seen a viable route to produce the corresponding octenes and C₈ aromatics.

The main objectives of the study are:

- To prepare the alkaline earth metal hydroxyapatites
- To impregnate the vanadium in the form of vanadium pentoxide on hydroxyapatites
- To investigate the effect of vanadium loading and conversion of *n*-octane to value added products like 1-octene and *o*-xylene
- To investigate the effect of temperature on the conversion and selectivity of the products
- To examine the effect of *n*-octane to oxygen molar ratio of the conversion and selectivities towards the products
- To investigate the mechanistic route to the formation of octenes and aromatics

References

- [1] S. Green, *Industrial Catalysis*, Macmillan Company, New York, 1928.
- [2] J.R. Partington, *A history of chemistry*, Macmillan Company, London, 1964.
- [3] L.B.G. Morveau, J.L. Gay-Lussac, F. Arago, M.E. Chevreul, M. Berthelot, É.É.N. Mascart, A. Haller, *Annales de chimie et de physique*, Masson., 1818.
- [4] W. Henry, *Phil. Mag.* 65 (1825) 269-283.
- [5] C.M. Guldberg, P. Waage, *Les Mondes.* 12 (1864) 107-113.
- [6] G. Lemoine, *Annales de chimie et de physique*, Masson.,(1877), 18-21.
- [7] L.B.G. Morveau, J.L. Gay-Lussac, F. Arago, M.E. Chevreul, M. Berthelot, É.É.N. Mascart, A. Haller, *Annales de chimie et de physique*, Masson.,(1877) 32-35.
- [8] I. Langmuir, *J. Am. Chem. Soc.* 37 (1915) 1139-1167.
- [9] I. Langmuir, *Phys. Rev.* 8 (1916) 149-176.
- [10] H. Heinemann, *Handbook of Heterogeneous Catalysis*, VCH, Weinheim, 1997.
- [11] H. Heinemann, *Catalysis Science and Technology*, Springer, New York, 1981.
- [12] A.G. Oblad, H. Shalit, H.T. Tadd, in: F. Adalbert (Ed.), *Advances in Catalysis*, Academic Press, New York ,1957, pp. 510-530.
- [13] W. Ahlborn, in: W.G. Frankenburg, V. I. Komarewsky, E. K. Rideal, P.H. Emmett, H.S. Taylor (Eds.), *Advances in Catalysis*, Academic Press, New York ,1951, pp. 249-327.
- [14] R.P. Eischens, W.A. Pliskin, S.A. Francis, *J. Chem. Phys.* 22 (1954) 1786-1787.
- [15] G. Wilkinson, *Platinum Metals Rev.* 12 (1968) 50-53.
- [16] S.L. Meisel, J.P. McCullough, C.H. Lechthaler, P.B. Weisz, *CHEMTECH.* 6 (1976) 86-89.
- [17] A. John, *Appl. Catal.* 78 (1991) 141-173.
- [18] P. Hettinger William, *Fluid Catalytic Cracking*, American Chemical Society, New York ,1988, pp. 308-340.
- [19] S. Soled, E. Iglesia, R.A. Fiato, *Catal. Lett.* 7 (1990) 271-280.
- [20] G. Ertl, *Solid State and Material Science*, CRC Press, New York, 1982.
- [21] G. Giannetto, R. Monque, R. Galiasso, *Catal. Rev. Sci. Eng..* 36 (1994) 271-304.
- [22] R.R. Bader, H.-U. Blaser, in: A.B. H.U. Blaser, R. Prins (Eds.), *Stud. Surf. Sci. Catal.*, Elsevier, New York ,1997, pp. 17-29.
- [23] M. Santarelli, M. Cali, S. Macagno, *Int. J. Hydrogen Energ.* 29 (2004) 1571-1586.
- [24] Y. Nabaie, I. Yamanaka, K. Otsuka, *Appl. Catal. A.* 280 (2005) 149-155.

- [25] A. Behr, J. Eilting, K. Irawadi, J. Leschinski, F. Lindner, *Green Chem.* 10 (2008) 13-30.
- [26] L.D.T. Câmara, K. Rajagopal, D.A.G. Aranda, in: G.W.R. J.J. Spivey, B.H. Davis (Eds.), *Stud. Surf. Sci. Catal.*, Elsevier, New York, 2001, pp. 61-68.
- [27] F. Cavani, F. Trifiró, *Catal. Today.* 34 (1997) 269-279.
- [28] F. Cavani, A. Colombo, F. Giuntoli, F. Trifiró, P. Vazquez, P. Venturoli, in: R.M. William (Ed.), *Advanced Catalysts and Nanostructured Materials*, Academic Press, San Diego, 1996, pp. 43-61.
- [29] G. Capannelli, E. Carosini, F. Cavani, O. Monticelli, F. Trifiró, *Chem. Eng. Sci.* 51 (1996) 1817-1826.
- [30] N.R. Gleason, F. Zaera, in: K. Grasselli, J.E. Lyons (Eds.), *Stud. Surf. Sci. Catal.*, Elsevier, New York, 1997, pp. 235-244.
- [31] G. Centi, F. Trifiró, *Chem. Eng. Sci.* 45 (1990) 2589-2596.
- [32] S. Jahangirian, S. Dooley, F.M. Haas, F.L. Dryer, *Combust. Flame.* 159 (2012) 30-43.
- [33] G.C. Bond, *Heterogeneous Catalysis: Principles and Applications*, 2nd Edition ed., Clarendon Press, Oxford, 1987.
- [34] G.C. Bond, *Principles of Catalysis*, W. Heffer & Sons Ltd., Cambridge, England, 1963.
- [35] N. Mizuno, *Modern heterogeneous oxidation catalysis: design, reactions and characterization*, Wiley-VCH, 2009.
- [36] K. Harold H, in: H.P. D.D. Eley, O.H. Werner (Eds.), *Advances in Catalysis*, Academic Press, New York, 1994, pp. 1-38.
- [37] M. Baerns, O. Buyevskaya, *Catal. Today.* 45 (1998) 13-22.
- [38] F. Cavani, F. Trifiró, *Appl. Catal.*, A. 88 (1992) 115-135.
- [39] P. Mars, D.W. van Krevelen, *Chem. Eng. Sci.* 3, Supplement 1 (1954) 41-59.
- [40] S. Jongpatiwut, P. Sackamduang, T. Rirksomboon, S. Osuwan, D.E. Resasco, *J. Catal.* 218 (2003) 1-11.
- [41] A. Trunschke, D.L. Hoang, J. Radnik, K.W. Brzezinka, A. Brückner, H. Lieske, *Appl. Catal.*, A. 208 (2001) 381-392.
- [42] P. Meriaudeau, A. Thangaraj, C. Naccache, S. Narayanan, *J. Catal.* 146 (1994) 579-582.
- [43] H. Al-Kandari, F. Al-Kharafi, A. Katrib, *Appl. Catal.*, A. 383 (2010) 141-148.
- [44] Á. Fürcht, A. Tungler, S. Szabó, Z. Schay, L. Vida, I. Gresits, *Appl. Catal.*, A. 231 (2002) 151-157.

- [45] R.C.R. Santos, A. Valentini, C.L. Lima, J.M. Filho, A.C. Oliveira, *Appl. Catal., A*, 403 (2011) 65-74.
- [46] P. Meriaudeau, C. Naccache, *Catal. Rev.* 39 (1997) 5-48.
- [47] A. Smiešková, E. Rojasová, P. Hudec, L. Šabo, *Appl. Catal., A*, 268 (2004) 235-240.
- [48] L. Chen, X. Wang, H. Guo, X. Guo, Y. Wang, H.o. Liu, G. Li, *Catal. Commun.* 8 (2007) 416-423.
- [49] J. Fling, I. Wang, *J. Catal.* 130 (1991) 577-587.
- [50] A.d. Lucas, J.L. Valverde, P. Sánchez, F. Dorado, M.J. Ramos, *Appl. Catal., A*, 282 (2005) 15-24.
- [51] S. Altwasser, C. Welker, Y. Traa, J. Weitkamp, *Micropor. Mesopor. Mat.* 83 (2005) 345-356.
- [52] J. Abbot, F.N. Guerzoni, *Appl. Catal., A*, 85 (1992) 173-188.
- [53] S. Kotrel, H. Knözinger, B.C. Gates, *Micropor. Mesopor. Mat.* 35-36 (2000) 11-20.
- [54] A. Lugstein, A. Jentys, H. Vinek, *Appl. Catal., A*, 176 (1999) 119-128.
- [55] G.J. Panuccio, K.A. Williams, L.D. Schmidt, *Chem. Eng. Sci.* 61 (2006) 4207-4219.
- [56] J.J. Krummenacher, K.N. West, L.D. Schmidt, *J. Catal.* 215 (2003) 332-343.
- [57] R.P. O'Connor, E.J. Klein, L.D. Schmidt, *Catal. Lett.* 70 (2000) 99-107.
- [58] G. Süß-Fink, L. Gonzalez, G.B. Shul'pin, *Appl. Catal., A*, 217 (2001) 111-117.
- [59] M. Hartmann, L. Maier, O. Deutschmann, *Appl. Catal., A*, 391 (2011) 144-152.
- [60] M. Setnička, R. Bulánek, L. Čapek, P. Čičmanec, *J. Mol. Catal. A: Chem.* 344 (2011) 1-10.
- [61] S.M. Sarathy, C. Yeung, C.K. Westbrook, W.J. Pitz, M. Mehl, M.J. Thomson, *Combust. Flame.* 158 (2011) 1277-1287.
- [62] G. Neri, A. Pistone, S. De Rossi, E. Rombi, C. Milone, S. Galvagno, *Appl. Catal., A*, 260 (2004) 75-86.
- [63] J.C. Vadrine, J.M.M. Millet, J.-C. Volta, *Catal. Today.* 32 (1996) 115-123.
- [64] B. Grzybowska-Świerkosz, *Top. Catal.* 21 (2002) 35-46.
- [65] A.A. Brillis, G. Manos, *Catal. Lett.* 91 (2003) 185-191.
- [66] A. Klisińska, K. Samson, I. Gressel, B. Grzybowska, *Appl. Catal., A*, 309 (2006) 10-16.
- [67] H.B. Friedrich, A.S. Mahomed, *Appl. Catal., A*, 347 (2008) 11-22.
- [68] E.A. Elkhalfifa, H.B. Friedrich, *Appl. Catal., A*, 373 (2010) 122-131.
- [69] M. Golombok, J. de Bruijn, *Appl. Catal., A*, 208 (2001) 47-53.

- [70] A. Fúnez, J.W. Thybaut, G.B. Marin, P. Sánchez, A. De Lucas, J.L. Valverde, *Appl. Catal., A*. 349 (2008) 29-39.
- [71] O. Krasnobaeva, I. Belomestnykh, T. Nosova, T. Elizarova, G. Isagulyants, S. Kolesnikov, V. Danilov, *Russ. J. Inorg. Chem.* 56 (2011) 1012-1016.
- [72] O. Krasnobaeva, I. Belomestnykh, T. Nosova, T. Elizarova, G. Isagulyants, S. Kolesnikov, V. Danilov, *Russ. J. Inorg. Chem.* 56 (2011) 168-172.
- [73] E. Elkhalfa, H. Friedrich, *Catal. Lett.* 141 (2011) 554-564.
- [74] A. Aklil, M. Mouflih, S. Sebti, *J. Hazard. Mater.* 112 (2004) 183-190.
- [75] J.C. Elliott, *Structure and chemistry of the apatites and other calcium orthophosphates*, Elsevier, New York, 1994.
- [76] P.W. Brown, B. Constantz, *Hydroxyapatite and related materials*, CRC Press, New York, 1994.
- [77] Y. Matsumura, S. Sugiyama, H. Hayashi, N. Shigemota, K. Saitoh, J.B. Moffat, *J. Mol. Catal.* 92 (1994) 81-94.
- [78] J.C. Trombe, G. Montel, *J. Inorg. Nucl. Chem.* 40 (1978) 15-21.
- [79] W.L. Suchanek, K. Byrappa, P. Shuk, R.E. Riman, V.F. Janas, K.S. TenHuisen, *Biomaterials*. 25 (2004) 4647-4657.
- [80] A. Yasukawa, T. Yokoyama, K. Kandori, T. Ishikawa, *Colloids Surf., A*. 238 (2004) 133-139.
- [81] A. Yasukawa, E. Ueda, K. Kandori, T. Ishikawa, *J. Colloid Interface Sci.* 288 (2005) 468-474.
- [82] Z. Xiu, M. Lü, S. Liu, G. Zhou, B. Su, H. Zhang, *Mater. Res. Bull.* 40 (2005) 1617-1622.
- [83] H. Xu, L. Yang, P. Wang, Y. Liu, M. Peng, *J. Environ. Manage.* 86 (2008) 319-328.
- [84] S. Brückner, G. Lusvardi, L. Menabue, M. Saladini, *Inorg. Chim. Acta.* 236 (1995) 209-212.
- [85] R. Tahir, K. Banert, A. Solhy, S. Sebti, *J. Mol. Catal. A: Chem.* 246 (2006) 39-42.
- [86] V. Stanić, S. Dimitrijević, J. Antić-Stanković, M. Mitrić, B. Jokić, I.B. Plečaš, S. Raičević, *Appl. Surf. Sci.* 256 (2010) 6083-6089.
- [87] T. A.Cüneyt, *J. Eur. Ceram. Soc.* 20 (2000) 2389-2394.
- [88] E.I. Dorozhkina, S.V. Dorozhkin, *Chem. Mater.* 14 (2002) 4267-4272.
- [89] S. Kannan, J.M.G. Ventura, J.M.F. Ferreira, *Ceram. Int.* 33 (2007) 1489-1494.
- [90] N.S. Resende, M. Nele, V.M.M. Salim, *Thermochim. Acta.* 451 (2006) 16-21.
- [91] C.S. Chai, K.A. Gross, B. Ben-Nissan, *Biomaterials*. 19 (1998) 2291-2296.

- [92] R.N. Panda, M.F. Hsieh, R.J. Chung, T.S. Chin, *J. Phys. Chem. Solids.* 64 (2003) 193-199.
- [93] I. Bogdanoviciene, A. Beganskiene, K. Tõnsuaadu, J. Glaser, H.J. Meyer, A. Kareiva, *Mater. Res. Bull.* 41 (2006) 1754-1762.
- [94] G. Ma, X.Y. Liu, *Crystal Growth & Design.* 9 (2009) 2991-2994.
- [95] M. Jevtić, M. Mitrić, S. Škapin, B. Jančar, N. Ignjatović, D. Uskoković, *Cryst. Growth Des.* 8 (2008) 2217-2222.
- [96] D. Laurencin, N. Almora-Barrios, N.H. de Leeuw, C. Gervais, C. Bonhomme, F. Mauri, W. Chrzanowski, J.C. Knowles, R.J. Newport, A. Wong, Z. Gan, M.E. Smith, *Biomaterials.* 32 (2011) 1826-1837.
- [97] M. Zahouily, Y. Abrouki, B. Bahlaouan, A. Rayadh, S. Sebti, *Catal. Commun.* 4 (2003) 521-524.
- [98] T. Tsuchida, J. Kubo, T. Yoshioka, S. Sakuma, T. Takeguchi, W. Ueda, *J. Catal.* 259 (2008) 183-189.
- [99] B. Liptáková, M. Hronec, Z. Cvenegrošová, *Catal. Today.* 61 (2000) 143-148.
- [100] S. Sugiyama, T. Minami, H. Hayashi, M. Tanaka, N. Shigemoto, J.B. Moffat, *Energy & Fuels.* 10 (1996) 828-830.
- [101] C.L. Kibby, W.K. Hall, *J. Catal.* 31 (1973) 65-73.
- [102] Y. Matsumura, J.B. Moffat, *J. Catal.* 148 (1994) 323-333.
- [103] Z. Opre, J.D. Grunwaldt, M. Maciejewski, D. Ferri, T. Mallat, A. Baiker, *J. Catal.* 230 (2005) 406-419.
- [104] S.d. Sebti, R. Tahir, R. Nazih, A. Saber, S.d. Boulaajaj, *Appl. Catal., A.* 228 (2002) 155-159.
- [105] F. Bazi, H. El Badaoui, S. Tamani, S. Sokori, A. Solhy, D.J. Macquarrie, S. Sebti, *Appl. Catal., A.* 301 (2006) 211-214.
- [106] Y.-P. Sun, H.-Y. Fu, D.-I. Zhang, R.-X. Li, H. Chen, X.-J. Li, *Catal. Commun.* 12 (2010) 188-192.
- [107] K. Yamaguchi, K. Mori, T. Mizugaki, K. Ebitani, K. Kaneda, *J. Am. Chem. Soc.* 122 (2000) 7144-7145.
- [108] S. Sugiyama, T. Minami, H. Hayashi, M. Tanaka, J.B. Moffat, *J. Solid State Chem.* 126 (1996) 242-252.
- [109] M. Khachani, M. Kacimi, A. Ensuque, J.-Y. Piquemal, C. Connan, F. Bozon-Verduraz, M. Ziyad, *Appl. Catal., A.* 388 (2010) 113-123.

- [110] C. Boucetta, M. Kacimi, A. Ensuque, J.-Y. Piquemal, F. Bozon-Verduraz, M. Ziyad, *Appl. Catal., A*. 356 (2009) 201-210.
- [111] Z. Boukha, M. Kacimi, M.F.R. Pereira, J.L. Faria, J.L. Figueiredo, M. Ziyad, *Appl. Catal., A*. 317 (2007) 299-309.
- [112] J.H. Jun, T.-J. Lee, T.H. Lim, S.-W. Nam, S.-A. Hong, K.J. Yoon, *J. Catal.* 221 (2004) 178-190.
- [113] W. Chen, Z. Huang, Y. Liu, Q. He, *Catal. Commun.* 9 (2008) 516-521.
- [114] F. Ma, M.A. Hanna, *Bioresour. Technol.* 70 (1999) 1-15.
- [115] G. Jon Van, *Fuel Process. Technol.* 86 (2005) 1097-1107.
- [116] H. Tounsi, S. Djemal, C. Petitto, G. Delahay, *Appl. Catal., B*. 107 (2011) 158-163.
- [117] J. Jemal, H. Tounsi, K. Chaari, C. Petitto, G. Delahay, S. Djemel, A. Ghorbel, *Appl. Catal., B*. 113–114 (2012) 255-260
- [118] C.F. Baes, R.E. Mesmer, *The hydrolysis of cations*, Wiley, 1976.
- [119] G.C. Bond, S.F. Tahir, *Appl. Catal.*, 71 (1991) 1-31.
- [120] J.B. Moffat, *Metal-oxygen clusters: the surface and catalytic properties of heteropoly oxometalates*, Kluwer Academic/Plenum Publishers, London, 2001.
- [121] G. Centi, D. Pinelli, F. Trifiro, *J. Mol. Catal.* 59 (1990) 221-231.
- [122] M. Del Arco, M.J. Holgado, C. Martin, V. Rives, *Langmuir*. 6 (1990) 801-806.
- [123] G. Centi, F. Trifiro, G. Busca, J. Ebner, J. Gleaves, *Faraday Discuss. Chem. Soc.* 87 (1989) 215-225.
- [124] G.C. Bond, J.P. Zurita, S. Flamerz, P.J. Gellings, H. Bosch, J.G. Van Ommen, B.J. Kip, *Appl. Catal.*, 22 (1986) 361-378.
- [125] M. Niwa, Y. Matsuoka, Y. Murakami, *J. Phys. Chem.* 91 (1987) 4519-4524.
- [126] G. Busca, L. Marchetti, G. Centi, F. Trifiro, *J. Chem. Soc., Faraday Trans. 1 F*. 81 (1985) 1003-1014.
- [127] F. Cavani, F. Trifirò, *Appl. Catal., A*. 157 (1997) 195-221.
- [128] N.V. Economidis, D.A. Peña, P.G. Smirniotis, *Appl. Catal., B*. 23 (1999) 123-134.
- [129] B.M. Weckhuysen, D.E. Keller, *Catal. Today*. 78 (2003) 25-46.
- [130] E.F. Aboelfetoh, M. Fechtelkord, R. Pietschnig, *J. Mol. Catal. A: Chem.* 318 (2010) 51-59.
- [131] D.-W. Kim, H. Kim, Y.-S. Jung, I. Kyu Song, S.-H. Baeck, *J. Phys. Chem. Solids*. 69 (2008) 1513-1517.
- [132] H. Jerzy, *Catal. Today*. 142 (2009) 100-113.
- [133] J. Leyrer, R. Margraf, E. Taglauer, H. Knözinger, *Surf. Sci.* 201 (1988) 603-623.

- [134] D. Vernardou, P. Paterakis, H. Drosos, E. Spanakis, I.M. Povey, M.E. Pemble, E. Koudoumas, N. Katsarakis, *Sol. Energy Mater. Sol. Cells.* 95 (2011) 2842-2847.
- [135] T.D. Manning, I.P. Parkin, *Polyhedron.* 23 (2004) 3087-3095.
- [136] N. Blangenois, M. Florea, P. Grange, R.P. Silvy, S.P. Chenakin, J.M. Bastin, N. Kruse, B.P. Barbero, L. Cadús, *Appl. Catal., A.* 263 (2004) 163-170.
- [137] C.-T. Wang, M.-T. Chen, *Mater. Lett.* 63 (2009) 389-390.
- [138] C.R. Dias, M.F. Portela, G.C. Bond, *J. Catal.* 157 (1995) 353-358.
- [139] G. Du, S. Lim, Y. Yang, C. Wang, L. Pfefferle, G.L. Haller, *Appl. Catal., A.* 302 (2006) 48-61.
- [140] S. Shylesh, A.P. Singh, *J. Catal.* 228 (2004) 333-346.
- [141] T. Garcia, B. Solsona, D.M. Murphy, K.L. Antcliff, S.H. Taylor, *J. Catal.* 229 (2005) 1-11.
- [142] J.M. López Nieto, P. Concepción, A. Dejoz, H. Knözinger, F. Melo, M.I. Vázquez, *J. Catal.* 189 (2000) 147-157.
- [143] K. Wada, H. Yamada, Y. Watanabe, T.-a. Mitsudo, *J. Chem. Soc., Faraday Trans.* 94 (1998) 1771-1778.
- [144] A. Khodakov, B. Olthof, A.T. Bell, E. Iglesia, *J. Catal.* 181 (1999) 205-216.
- [145] C. Gabriele, *Appl. Catal., A.* 147 (1996) 267-298.
- [146] I.E. Wachs, B.M. Weckhuysen, *Appl. Catal., A.* 157 (1997) 67-90.
- [147] K. Chen, A. Khodakov, J. Yang, A.T. Bell, E. Iglesia, *J. Catal.* 186 (1999) 325-333.
- [148] A. S. Lars T, *Appl. Catal., A.* 112 (1994) 209-218.
- [149] H.B. Friedrich, N. Govender, M.R. Mathebula, *Appl. Catal., A.* 297 (2006) 81-89.
- [150] S. Singh, S. Jonnalagadda, *Catal. Lett.* 126 (2008) 200-206.

CHAPTER 2

OXIDATIVE DEHYDROGENATION OF *n*-OCTANE USING VANADIUM PENTOXIDE SUPPORTED ON HYDROXYAPATITE CATALYSTS

Abstract

Vanadium pentoxide, with loadings varying from 2.5-15 wt%, was supported on hydroxyapatite by the wet impregnation technique. The materials were characterized by techniques such as XRD, ICP-OES, BET, FTIR, SEM, TEM, TPR and TPD. From XRD and IR analyses, vanadium is found in the vanadium pentoxide phase for the lower loadings, whereas for weight loadings in excess of 10%, an additional pyrovanadate phase exists. Electron microscopy provides evidence of a homogenous distribution of the vanadium species on the hydroxyapatite. Oxidative dehydrogenation reactions carried out in a continuous flow fixed bed reactor showed that selectivity towards desired products was dependent on the vanadium concentration and the phase composition of the catalyst. Good selectivity towards octenes was achieved using the 2.5 wt% V₂O₅ on HAp loaded catalyst. There was a marked decrease in octene selectivity and a significant increase in the formation of C₈ aromatics when higher loadings of vanadium were used. At a conversion of 24% at 450°C, the 15 wt% V₂O₅ on HAp showed a selectivity of 72% towards octenes. A maximum selectivity of 10 % for C₈ aromatics was obtained using the 15 wt% V₂O₅ on HAp catalyst at a conversion of 36 % at 550°C.

Keywords: hydroxyapatite, V₂O₅, *n*-octane, 1-octene, *o*-xylene, Oxidative dehydrogenation.

2.1 Introduction

Alkenes are important raw materials in a wide range of applications in the petrochemical industry due to their low cost and ability to be functionalized easily. However, it has been envisaged that the future of the petrochemical industry leans towards the direct use of alkanes as starting material, since they are a much more economical raw material and can be easily sourced from petroleum by-products [1]. For over sixty years and until recently, most of the commercial production of alkenes was through the dehydrogenation of alkanes in the absence of oxygen. These reactions are endothermic and operate at temperatures ranging from 450 to 550°C, but low conversions due to limitations associated with the thermodynamic equilibrium

are obtained [2]. Also, alkene selectivity is low and carbon deposition on the active sites of the catalyst is favoured. The introduction of oxygen renders the reaction exothermic, eliminates most limitations imposed by thermodynamics and reduces carbon deposits on the catalyst [3-5]. As a result, oxidative dehydrogenation (ODH) of alkanes is now preferred and plays a growing role in the petrochemical industry [6-8].

Catalytic performance relies on the acid-base properties of the material or the isolated cations capable of activating C-H bonds [9-12], therefore the use of supports with acid-base characteristics is advantageous. Hydroxyapatite (HAp) as support offers high stability and various substitutions are allowed by the apatite structure [13, 14]. Hydroxyapatite has the general formula, $[\text{Ca}_{10-x}(\text{HPO}_4)_x(\text{PO}_4)_{6-x}(\text{OH})_{2-x}]$, $0 \leq x \leq 1$. Stoichiometric HAp has $x = 0$ to give $\text{Ca}_{10}(\text{PO}_4)_6(\text{OH})_2$, whereas the calcium deficient non-stoichiometric hydroxyapatite has $0 \leq x \leq 1$ [15]. Various transition metal cations, which have potential as catalytic active centers, can be readily accommodated into the apatite framework based on the large cation exchange ability of HAp [16-19]. The OH group within the phosphate framework leads to the formation of active oxygen species which are essential for ODH reactions [20].

Among the transition metal oxide catalysts, the supported vanadium oxides find a variety of applications in heterogeneous catalytic oxidation reactions [21,22]. Indeed vanadium serves as an important component in oxidation catalysts for both chemical and biochemical systems [23-25]. The utility of vanadium stems from the facile inter-conversion of the vanadium ion among its higher oxidation states and the ability to activate molecular oxygen [26]. The abstraction of two hydrogens from the alkane is possible by the presence of an acid-base pair, the V^{5+} cation (Lewis acid centre) and the oxygen-associated O^{2-} anion (basic centre). Acidity is essential, however strong acidity favours the successive formation of oxygenated products. In most oxidation reactions, the catalysts consist of the vanadium oxide phase which is highly dispersed on the surface of the support, as shown by Mutralis et al. [27] who observed that V_2O_5 supported on TiO_2 was more active than the bulk or crystalline V_2O_5 . The analysis of structure activity relationships indicates that various species, characterized by different reactivities, exist on the surface of these catalysts. There is some evidence that catalysts with vanadium species having a tetrahedral geometry are efficient for alkane oxidative dehydrogenation [28]. They have been very few reports on oxidative dehydrogenation of *n*-octane. These are over V-Mg-Al hydrotalcites [28], tantalum and niobium substituted hydrotalcites [29, 30], and with VMgO

catalysts [31, 32]. The effectiveness of vanadium [33-35] and hydroxyapatite [2, 36] in the ODH of lower paraffins has stimulated our interest, leading to the study of the ODH of the higher paraffin, *n*-octane.

2.2 Experimental

2.2.1 Synthesis of catalysts

All the chemicals used in the preparation of the catalysts were purchased from Merck KGa (99%), Darmstadt, Germany. Hydroxyapatite (HAp) was prepared using the method of Yasukawa *et al.* [14]. In a typical method for the preparation of HAp, aqueous NH₃ was added to a 60 mL solution of Ca(NO₃)₂·4H₂O (6.67 x 10⁻² mol) to elevate the pH to 11. The solution was then diluted to 120 mL with distilled water. A 100 mL solution of (NH₄)₂HPO₄ (4.00 x 10⁻² mol) was also adjusted to pH 11 with the adding of aqueous NH₃ and diluted to 160 mL. The phosphate solution was added to the calcium solution drop wise over a period of 30 minutes at room temperature. A gelatinous precipitate formed which was stirred and boiled for 10 minutes. After filtration, the precipitate was washed thoroughly with distilled water and dried in an oven set at 100°C overnight, thereafter calcined at 550°C. Bulk V₂O₅ was prepared by the thermal decomposition of NH₄VO₃ at 450°C for 6 h in air. The loading of 2.5, 5.0, 7.5, 10.0 and 15.0 wt% vanadia on the hydroxyapatite support, which are noted as 2.5% V-HAp, 5% V-HAp, 7.5% V-HAp, 10% V-HAp and 15% V-HAp was performed by wet impregnation. The desired amounts of V₂O₅ were suspended in 20 mL of distilled water and added to the calcium hydroxyapatite support. The water was removed by evaporation with constant stirring. The solid was dried overnight at 110°C and later calcined at 550°C for 6 h.

2.2.2 Characterization of catalysts

The fresh and used catalysts were characterized by various physical and chemical methods.

BET surface area

BET surface areas were determined using a Micrometrics Gemini 2360 multi-point BET surface area analyzer. Prior to analysis, the powdered samples (~ 0.05 g) were degassed overnight at 200 °C using a Micromeritics FlowPrep 060 instrument.

Inductively coupled plasma-optical emission spectroscopy (ICP-OES)

Inductively coupled plasma (ICP) was performed using a Perkin Elmer Optical Emission Spectrometer Optima 5300 DV to determine the elemental composition of the materials.

Standards (500 ppm Ca, V and P) were purchased from Fluka.

X-ray diffraction (XRD)

The phases of the catalysts were observed using powder X-ray diffraction (XRD) conducted on a Bruker D8 Advance instrument, equipped with an Anton Paar XRK 900 reaction chamber, a TCU 750 temperature control unit and a Cu radiation source with a wavelength of 1.5406 λ . The crystallinity of the powder was estimated from the XRD data using the following equation:

$$X_c = 1 - (V_{112/300}/I_{300})$$

where X_c is the degree of crystallinity, $V_{112/300}$ is the intensity of the shoulder between the (112) and (300) diffraction peaks and I_{300} is the intensity of the (300) peak [37]. The crystallite size of the powder was evaluated from the peak broadening of XRD patterns based on Scherrer's formula given as follows:

$$X_s = 0.9 \lambda / \text{FWHM} \cos \theta$$

where X_s is the crystallite size (nm), λ is the wavelength of the monochromatic X-ray beam ($\lambda = 0.15406$ nm for $\text{CuK}\alpha$ radiation), FWHM is the full width at half-maximum for the diffraction peak under consideration (radians) and θ is the diffraction angle (degrees). Infra-red

Infrared spectroscopy (IR)

Infra-red spectra were obtained using a Perkin Elmer Precisely using a Universal ATR sampling accessory equipped with a diamond crystal.

Temperature programmed Techniques

Ammonia temperature programmed desorption (TPD) and temperature programmed reduction (TPR) were carried out using a Micromeritics 2920 Autochem II Chemisorption Analyser. Prior to the reduction of the sample in TPR, the catalyst was pretreated by heating under a stream of argon (30 mL/min) at 400 °C for 30 min and then cooled to 80 °C. Thereafter, 5% hydrogen in argon was used as a reducing agent at a flow rate of 30 mL/min. Samples were analyzed from room temperature to 950 °C using a ramp rate of 20 °C/min under static air. In the TPD experiments, the catalyst was pretreated at 350 °C under the stream of helium for 60 min. The temperature was then decreased to 80 °C. A mixture of 4.1 % ammonia in helium was passed over the catalyst at a flow rate of 30 mL/min for 60 min. The excess ammonia was removed by purging with helium for 30 min. The temperature was then raised gradually to 950 °C by ramping at 10 °C/min under the flow of helium and desorption data was recorded.

Scanning electron microscopy-Energy dispersive X-ray (SEM-EDX)

The surface morphology of the catalysts was observed using a Leo 1450 Scanning Electron Microscope. Prior to SEM analysis, the samples were mounted on aluminium stubs using double-sided carbon tape and subsequently gold spluttered using the Polaron E5100 coating unit.

Transmission electron microscopy (TEM)

Transmission electron microscopy (TEM) images were viewed using a Jeol JEM-1010 Electron Microscope and selected area electron diffraction (SAED) patterns for the catalyst samples were viewed in the adjusted diffraction mode of the JEM-1010 Electron Microscope. The images were captured and analyzed using iTEM software.

2.2.3 Catalytic Testing

Gas phase oxidation reactions were carried out in a continuous flow fixed bed reactor in down flow mode. A tubular stainless steel reactor tube with 10 mm internal diameter and 300 mm length was used to pack the catalyst. The catalyst bed (1mL) was located at the centre of the reactor with 24-grit carborundum packed in the spaces on either side of the bed. The catalyst pellets sizes were between 600-1000 μm . K-type thermocouples were used to monitor the temperature of the catalyst bed and the reactor furnace. The thermocouples were controlled by CB-100 RK Temperature Control Units. The *n*-octane (Merck, 99 %) was delivered into the system by a high precision isocratic pump (Lab Alliance Series II). The concentration of *n*-octane in the gaseous mixture was 11% (v/v) with a 1:0.5 *n*-octane to oxygen molar ratio. Air (N_2 , 21 % O_2) was used as an oxidant and nitrogen (Afrox, 98 %) was used as the make-up gas to achieve a total flow rate of 90 mL/min. To investigate the cyclization mode to the aromatics, isomers of octene, viz., 1-octene, 2-octene, 3-octene and 4-octene and 1,7 octadiene were fed through the reactor in separate experiments under the same reaction conditions as mentioned above to monitor the selectivity to aromatic compounds. The volume of the gaseous products was measured by a wet gas flow meter (Ritter Drum-Type Gas Meter). The gaseous and liquid products were analyzed offline using Perkin Elmer Clarus 400 FID and TCD gas chromatographs. The FID was used for analysis of organic products in both gaseous and liquid phases, whereas the TCD was used for carbon oxides. A Perkin Elmer Clarus 500 GC-MS was used to identify unknown products. Carbon balances ranged between 99-101% and all data points were obtained in duplicate with an error of $\pm 1\%$.

Table 2.1 BET surface area, pore volume and elemental analysis of fresh and used catalysts.

Catalyst	Surface area [†] (m ² /g)	Surface area [‡] (m ² /g)	Pore volume [†] (cm ³ /g)	Pore volume [‡] (cm ³ /g)	Ca/P ^{†1}	Ca/P ^{‡1}	Ca/V ^{†1}	Ca/V ^{‡1}	Ca/P ²	Ca/V ²	Crystallite size ³ (nm)	Crystallinity ⁴
HAp	72	-	0.2385	-	1.51	-	-	-	1.50	-	2.26	0.43
2.5V-HAp	51	51	0.1856	0.1795	1.49	1.50	0.030	0.030	1.50	0.033	2.32	0.45
5V-HAp	36	35	0.1589	0.1502	1.49	1.49	0.069	0.069	1.49	0.072	2.64	0.52
7.5V-HAp	17	16	0.1388	0.1311	1.48	1.49	0.098	0.098	1.49	0.098	2.91	0.52
10V-HAp	13	12	0.1185	0.1100	1.47	1.49	0.131	0.131	1.49	0.129	3.61	0.92
15V-HAp	9	9	0.1057	0.0922	1.49	1.49	0.174	0.174	1.49	0.165	5.48	0.87

[†]fresh catalyst, [‡] spent catalyst, ¹ICP-OES, ²EDX, ³Calculated by Scherer's equation and ⁴ $X_c = 1 - (V_{112/300} / I_{300})$, where X_c is degree of crystallinity $V_{112/300}$ is the intensity of the shoulder between (112) and (300) diffraction peaks and I_{300} is the intensity of the (300) peak [32].

2.3 Results and Discussion

2.3.1 Catalyst characterization

2.3.1.1 BET Surface Area and Elemental Analysis

The BET surface area for HAp was 72 m²/g. For the supported catalysts, an increase in vanadium pentoxide loading results in a decrease in the surface area probably due to pore blockage, since a similar pattern is observed for pore volume measurements. There appeared to be a minor decrease in the surface area and pore volume of the used catalyst in some cases. This could be attributed to the clogging of pores with the hydrocarbon molecules during the course of the reaction (Table 2.1).

2.3.1.2 Powder X-ray Diffraction

The powder XRD diffraction patterns (Fig. 2.1) of all the catalysts show the presence of the hydroxyapatite phase with d-spacing values of 2.79, 2.72 and 2.63 Å for 2θ angles between 30 to 35° correlating with JCPDS File No. 9-390 [38].

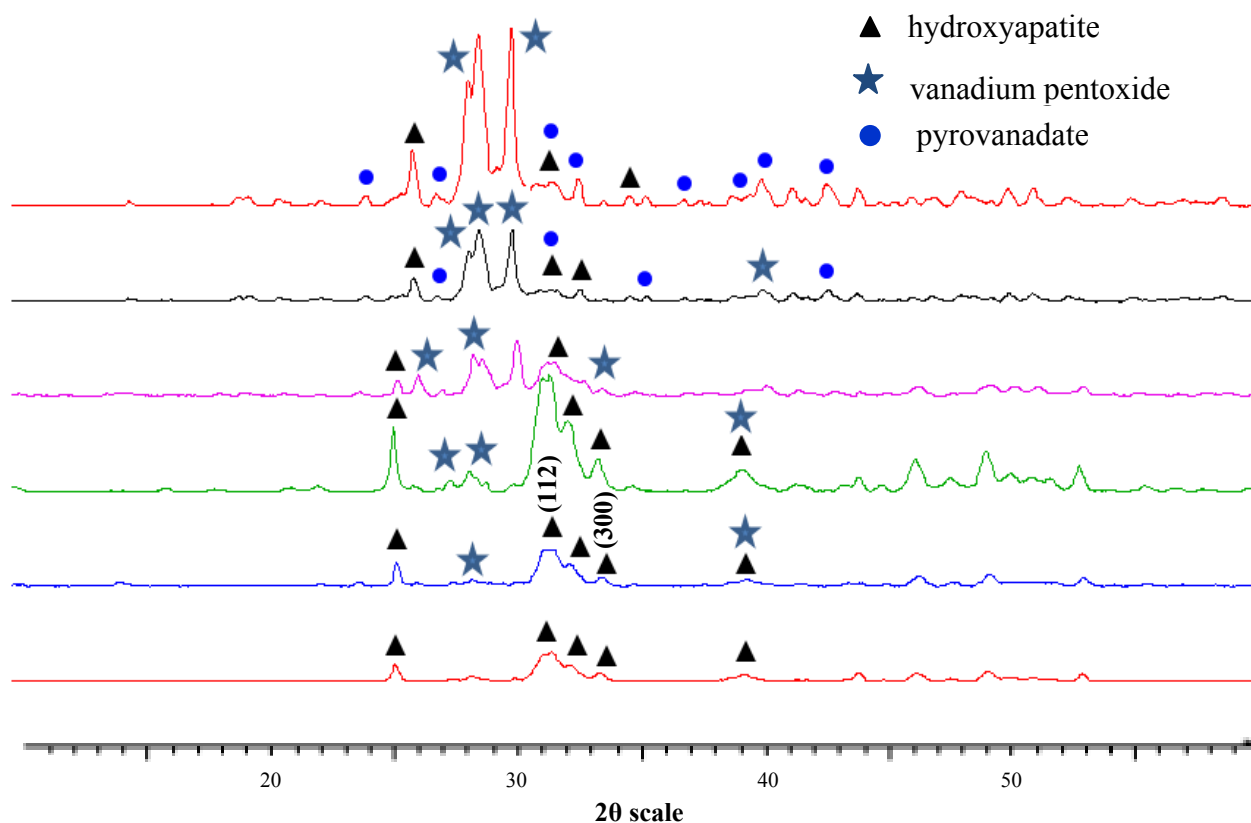


Figure 2.1 XRD diffractograms of HAp (a), 2.5 wt% (b), 5 wt% (c), 7.5 wt% (d), 10 wt% (e) and 15 wt % (f) V₂O₅ supported on HAp.

The presence of V_2O_5 is also evident in the diffractograms of the loaded catalysts with d-spacing values of 3.43, 2.88 and 2.76 Å corresponding to 2θ angles between 30 to 35° referenced in JCPDS File No. 9-387. For the higher vanadium loadings of 10 and 15 wt %, an additional phase, the pyrovanadate phase was observed with d-spacing values of 3.39, 2.64, 2.51 Å. This matches with the data found in JCPDS File No. 25-1103. There was a minimal increase of the crystallite size and crystallinity of the catalysts with an increase in the vanadium loadings up to 7.5 wt %. A significant increase in the crystallinity and the crystallite size values of the 10 and 15 wt % vanadia loadings is observed, probably due to the presence of the pyrovanadate phase (Table 2.1) [37]. For the used catalysts, XRD patterns showed no phase changes.

2.3.1.3 Infrared Spectroscopy

Hydroxide ion stretching was observed in the range of 3353-3059 cm^{-1} for all the catalysts [39]. Bands in the range 1612-1624 cm^{-1} were assigned to the bending modes of water. A peak in the range 630-665 cm^{-1} was assigned to the OH group of HAp. The symmetric ν_1 and asymmetric ν_3 phosphate bands in the region of 900-1200 cm^{-1} and ν_4 absorption bands in the region of 500-700 cm^{-1} were observed and are typical for the apatite structure (Fig. 2.2). Peaks seen at 630 and 3200 cm^{-1} are the characteristic peaks for stoichiometric HAp [36, 37]. In the supported hydroxyapatites, a band at 1020 cm^{-1} (V=O stretching) provides evidence that V_2O_5 exists as a single layer on hydroxyapatite [40]. Terminal V=O stretching was observed for the 10 and 15 wt% vanadia loaded materials between 1040-1080 cm^{-1} . Monomeric vanadyls, which exhibit peaks around 900-960 cm^{-1} and 700-850 cm^{-1} due to V-O-V stretching vibrations, are present in all samples, further indicating that the vanadium pentoxide is present as a monolayer on the hydroxyapatite [41].

2.3.1.4 Temperature Programmed Reduction (TPR)

From TPR analysis (Fig. 2.3), calcium is not reduced at the temperatures employed, whereas for the vanadium pentoxide supported catalysts, reduction occurs in the 600°C-850°C range. The reduction process of V_2O_5 is proposed to be as follows:



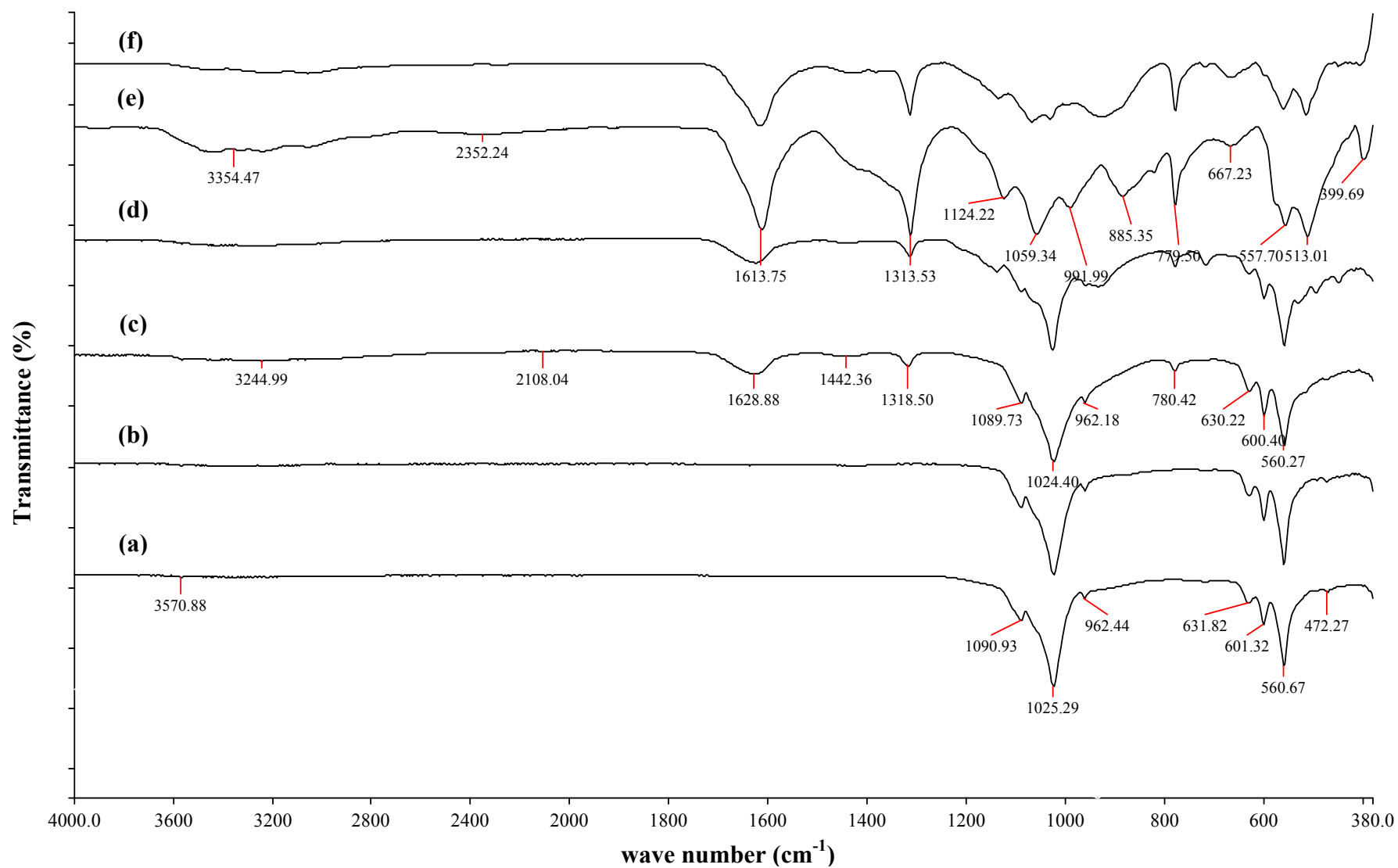


Figure 2.2 Infrared spectra of HAp (a), 2.5 wt% (b), 5 wt% (c), 7.5 wt% (d), 10 wt% (e) and 15 wt%(f)V₂O₅ supported on HAp.

According to Blasco et al.[42], the reduction peaks that appear at the higher temperatures correspond with the reduction of V^{5+} species belonging to the bulk structure of V_2O_5 . The TPR profile (Fig.3.3, Table 3.2) shows single peaks for the low vanadium loadings indicating that the vanadium exists in one phase, but this peak widened and shifted progressively to higher temperatures as the vanadium loading increased. This behavior is explained by the weakening of the vanadyl group due to interaction with the vanadium surface. Thus the variations observed in the reduction peak temperature and the line shape may be interpreted as follows: at low vanadium contents most of the vanadium atoms interact with the support surface but as the

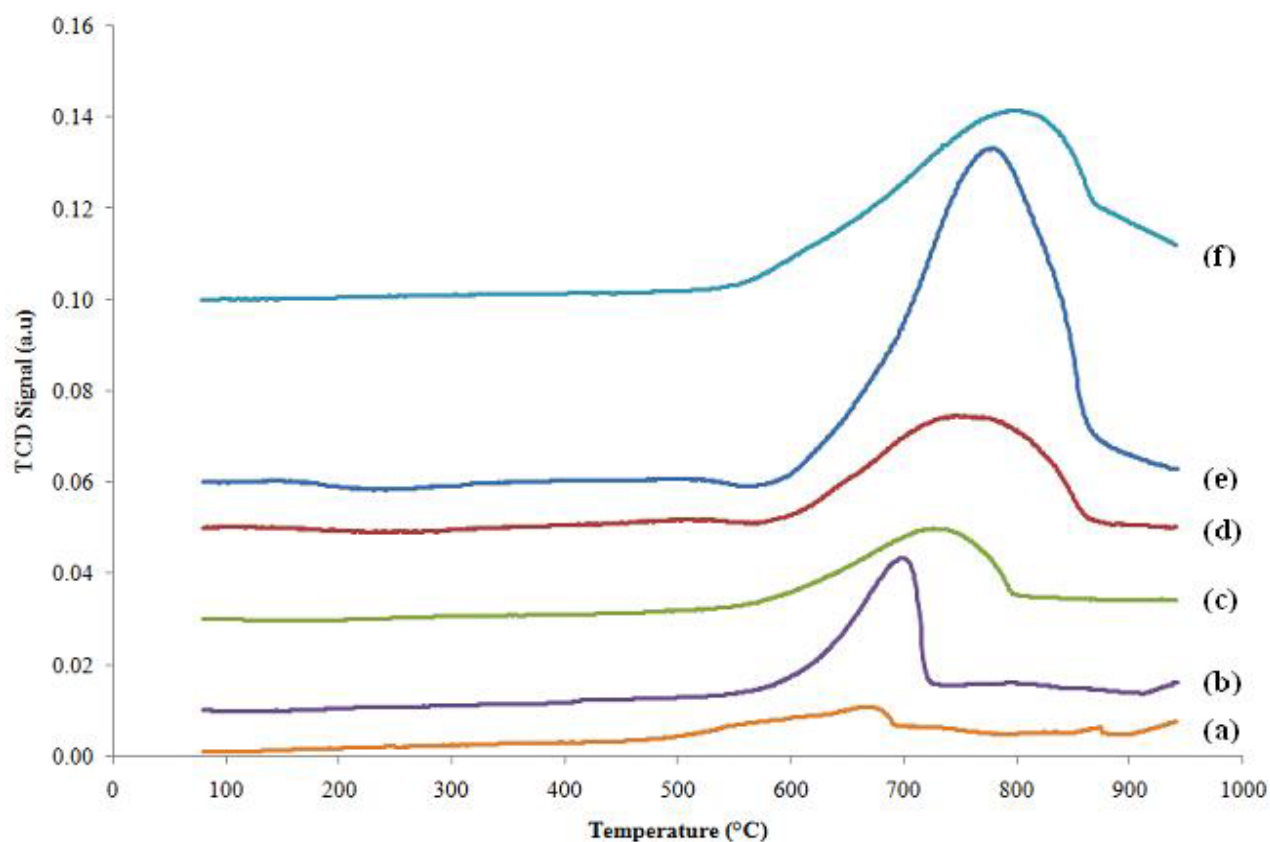


Figure 2.3 TPR profile of HAp(a), 2.5 wt% (b), 5 wt% (c), 7.5 wt% (d), 10 wt% (e) and 15 wt%(f) V_2O_5 supported on HAp.

vanadium increases a higher proportion of surface vanadium atoms interacts with internal vanadium layers, so increasing the bond strength of the vanadyl group, approaching it to that of pure V_2O_5 . This leads to the higher heterogeneity of the vanadium reduction centers which causes the widening of the reduction peak [27]. The peak shapes, along with the hydrogen

consumption and the corresponding oxidation states of the reduced vanadium, indicate that vanadium was predominantly reduced to V^{4+} and that some further reduction to V^{3+} occurred. The XRD investigations on the reduced catalysts show that vanadium is reduced to VO_4 (V^{4+}) and V_2O_3 (V^{3+}) phases (Fig. 2.4). The d-spacings correlate with the JCPDS File No. 25-1003 for VO_4 and JCPDS File No. 26-278 for V_2O_3 respectively. For the lower vanadium loadings the first peak between 630-660°C is probably due to reduction of the vanadium in slightly different environments, as indicated by the hydrogen consumption and average oxidation state (Table 2.2). The second peak, between 700-770°C, is presumably for a further reduction step of vanadium

Table 2.2 Temperature programmed reduction and average oxidation state

Catalyst	Peak Temp.(°C)	Moles of H ₂ consumed (cm ³ /g STP)	Average oxidation State
Hydroxyapatite	642	0.20	--
2.5% V-HAp	634	1.22	4.6
	693	1.85	3.9
5% V-HAp	647	1.44	4.5
	744	2.86	3.6
7.5% V-HAp	658	1.56	4.4
	777	3.13	3.6
10% V-HAp	754	4.13	4.0
	823	3.85	3.4
15% V-HAp	772	5.28	3.8
	840	3.25	3.0

(V^{5+} to V^{4+}). For the 10 and 15 wt % loadings, there are small shoulders present indicating that the vanadium exists in two phases, most likely including the pyrovanadate phase which is more reducible than V_2O_5 [31]. The reduction peak for pyrovanadate is found between 750-775°C. Compared to the V_2O_5 , the reduction of the oxygen species in distorted VO_4 units is relatively easy [39]. As the vanadium content increased, the peak at the lower temperature gradually grew in area; however, the peak at higher temperature progressively decreased. The shoulder at around 820-840°C shows the reduction to V^{3+} . The shifts of the peak temperatures from the lower vanadium loadings indicate that the reduction of the corresponding oxygen containing species becomes difficult in the samples with high vanadium content [41]. The TPR of HAp did not show any peaks, indicating that all the observed peaks are due to the reduction of vanadium.

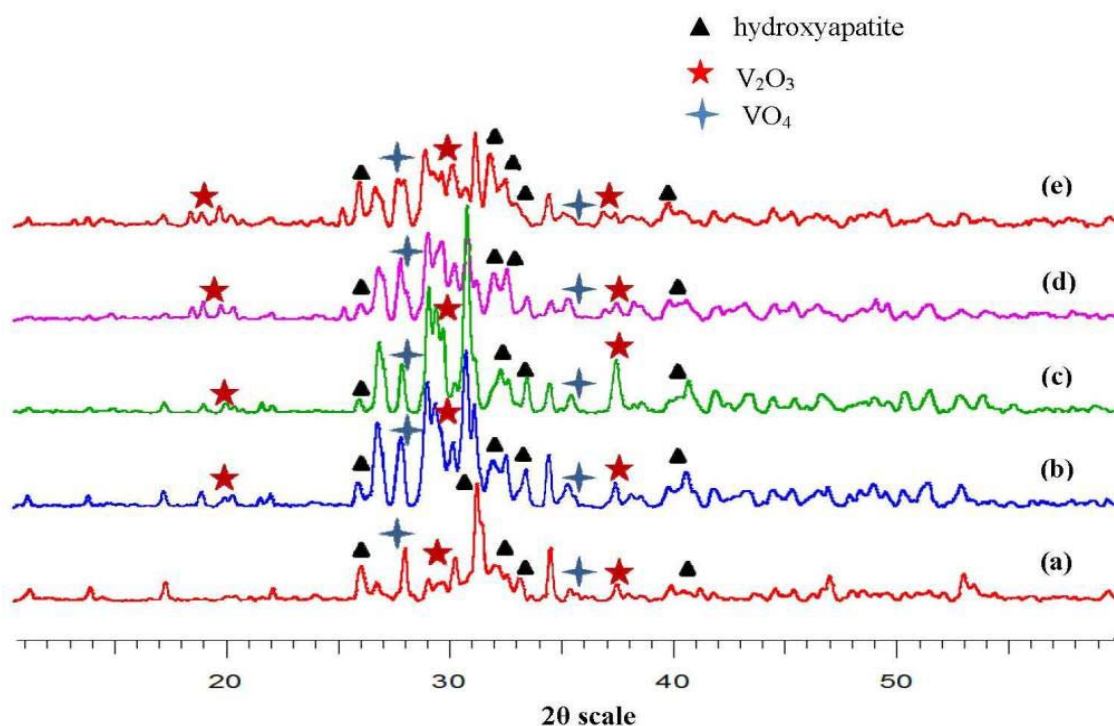


Figure 2.4 XRD diffractograms of the reduced catalysts after TPR experiments; 2.5 wt% (a), 5.0wt % (b), 7.5 wt% (c), 10wt% (d) and 15wt% (e) V_2O_5 supported on HAp

2.3.1.5 Temperature Programmed Desorption

From the TPD experiments (Table 2.3), each catalyst exhibits weak and strong acidic sites shown by the peaks at 480°C and 690°C respectively. There is a direct correlation in the

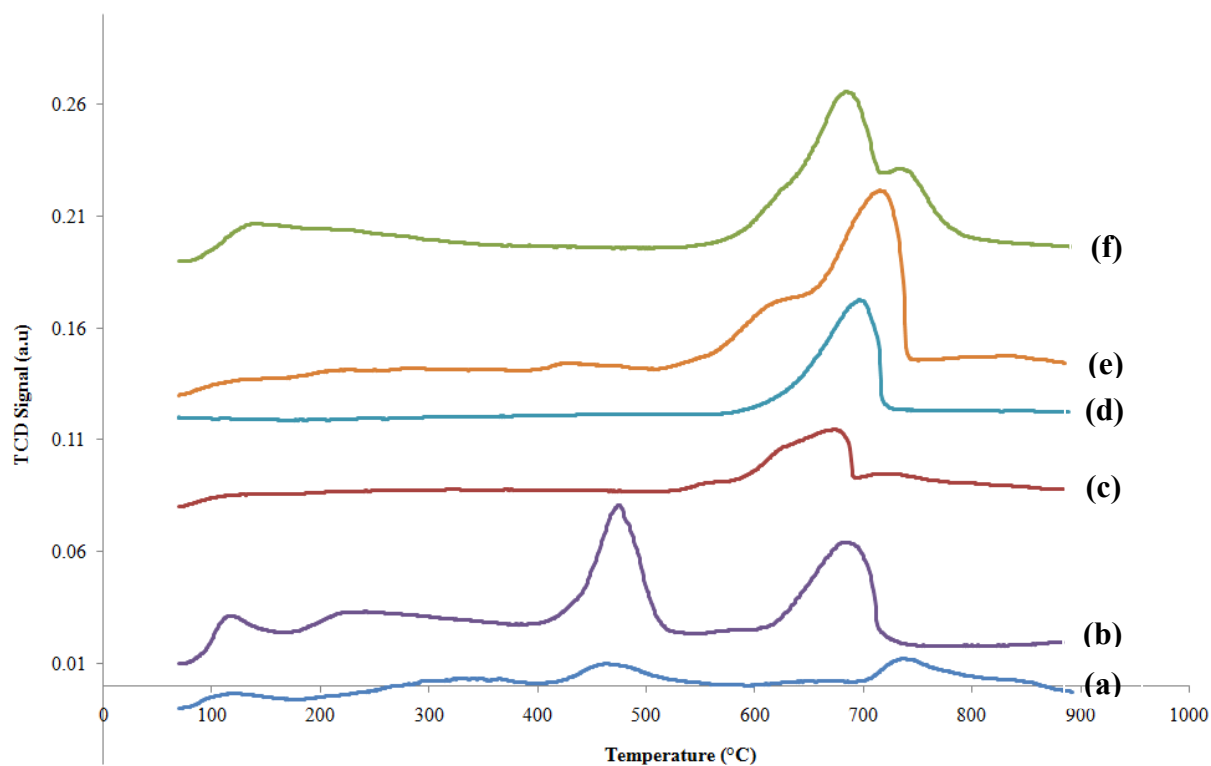


Figure 2.5 TPD profile of (a), 2.5 wt% (b), 5 wt% (c), 7.5 wt% (d), 10 wt% (e) and 15 wt% V_2O_5 supported on HAp (f).

Table 2.3 Distribution of acidic sites and specific acidity

Catalyst	Weak acidic sites (m mol NH_3/g)	Strong acidic sites (m mol NH_3/g)	Total acidic sites [†] (m mol NH_3/g)	Total acidic sites [‡] (m mol NH_3/g)	Specific acidity (m mol. m^{-2})
HAp	79.02	102.96	181.98	-	2.50
2.5% V-HAp	210.25	125.22	335.47	324.69	6.53
5% V-HAp	245.85	138.89	384.74	379.52	10.70
7.5% V-HAp	280.58	175.66	456.24	454.52	26.88
10% V-HAp	240.89	230.55	471.44	468.29	37.35
15% V-HAp	220.14	275.66	495.8	492.51	53.60

[†]fresh catalyst, [‡]used catalyst

magnitudes of the weak and strong acidic sites with respect to vanadium pentoxide loadings. The weak acidic sites increase gradually until a loading of 7.5 wt% V₂O₅ is reached and decrease for the higher loadings. On the other hand, the strong acidic nature of the catalysts increases for the higher loadings due to the presence of the strongly acidic pyrovanadate phase (Fig. 2.5). Acidic sites for the used catalyst are marginally decreased; this is probably due to the blocking of acidic sites by the hydrocarbon molecules (Table 2.3).

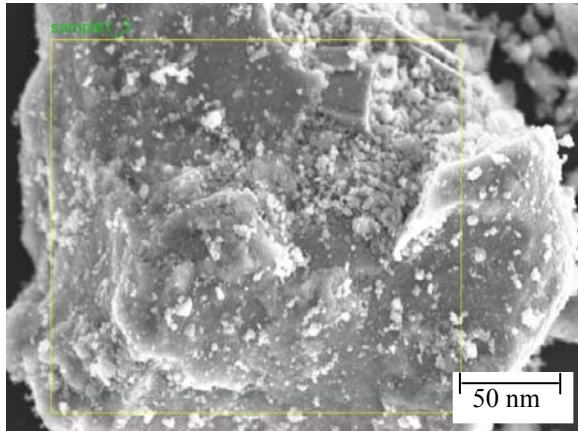
2.3.1.6 Scanning and Transmission Electron Microscopy

SEM micrographs (Fig. 2.6) show the surface morphologies of the hydroxyapatite crystals and from SEM-EDX data, the homogenous dispersion of vanadium pentoxide on the surface of the hydroxyapatite can be observed. From the SEM micrographs, the hydroxyapatite appears as a polycrystalline material. For the 2.5 wt % V₂O₅ supported hydroxyapatite, the loaded material seems to be uniformly distributed as small crystals on the surface. However, for the 5 and 7.5 wt % loadings, plate like structures are observed and these materials are more crystalline in nature. Micrographs of the 10 and 15 wt % supported catalysts show distorted plate like structures. EDX data also show a calcium to phosphorus ratio of 1.67 which correlates with the value from ICP (Table 2.1).

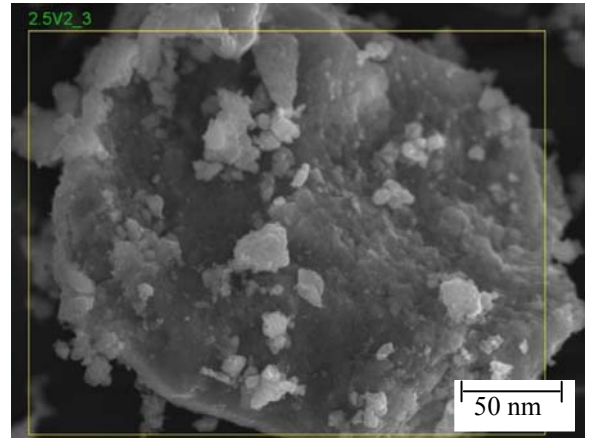
TEM micrographs (Fig. 2.7) show that the vanadium supported hydroxyapatite crystals are in the shape of rods of sizes varying from 180-220 nm. The SADP diffraction patterns for catalysts with lower loadings show that the crystals are polycrystalline, whereas for the 10 and 15 wt % loadings, diffractions spots along the concentric circles show the crystalline nature of the catalysts. The hydroxyapatite exists as clustered micro rod-like particles but as the vanadium loading increases, the micro rod-like particles become more defined. In general, the crystallinity of the catalysts increases with an increase in vanadium loading.

2.3.2 Catalytic Testing

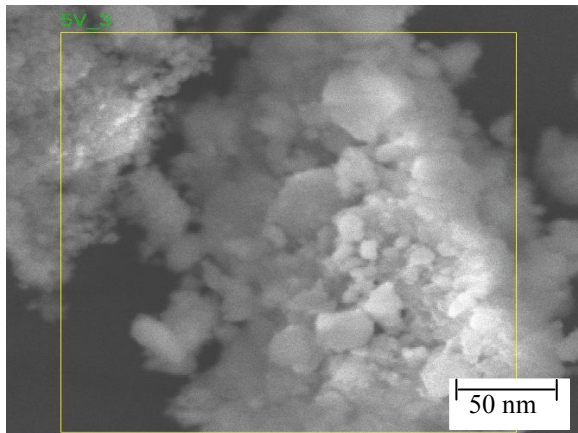
Catalytic testing was carried out in a fixed bed continuous flow reactor over a temperature range of 350 °C-550 °C with the gas hourly space velocity (GHSV) initially fixed at 4000 h⁻¹. Low conversion of *n*-octane was obtained over HAp compared to the supported vanadium pentoxide catalysts. All the supported catalysts showed an increase in conversion of *n*-



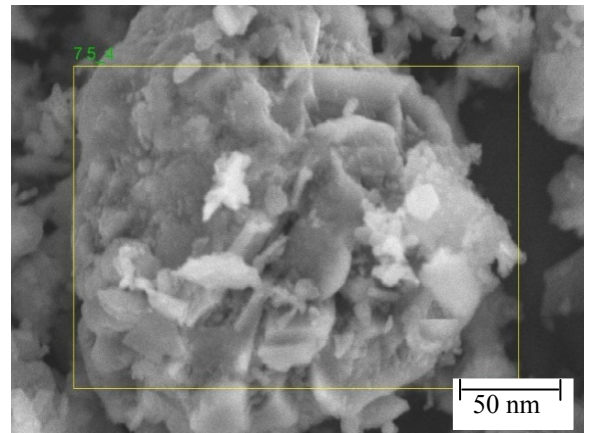
(a)



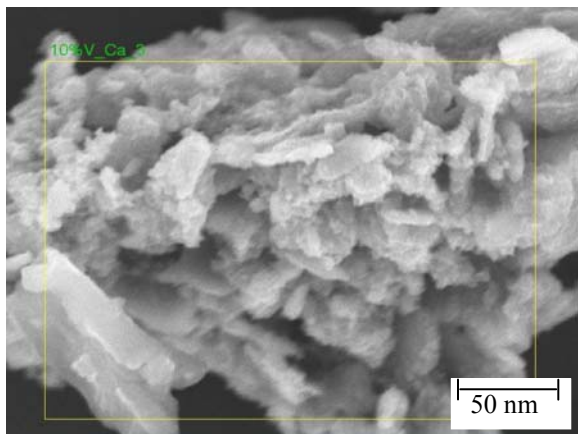
(b)



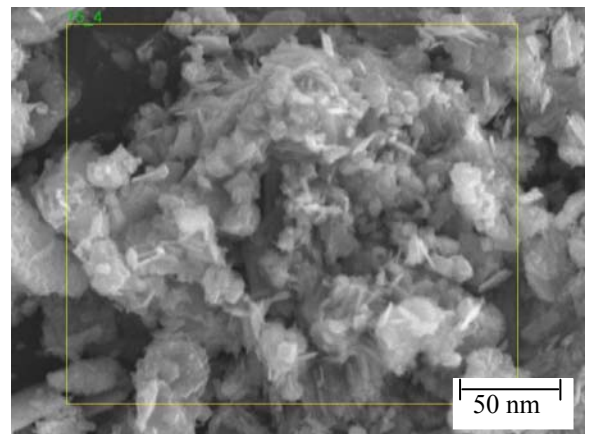
(c)



(d)

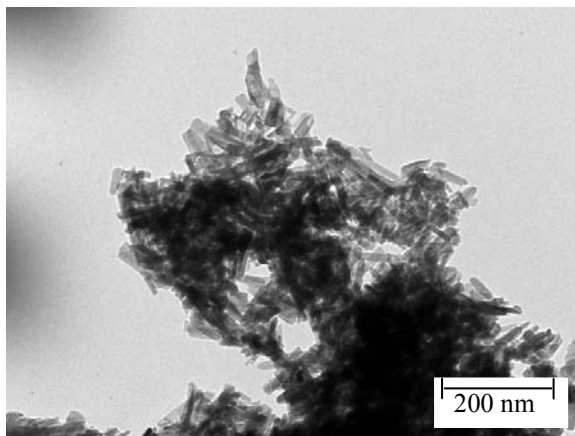


(e)

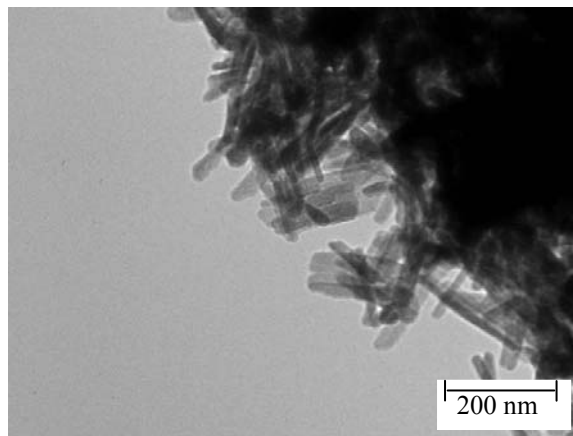


(f)

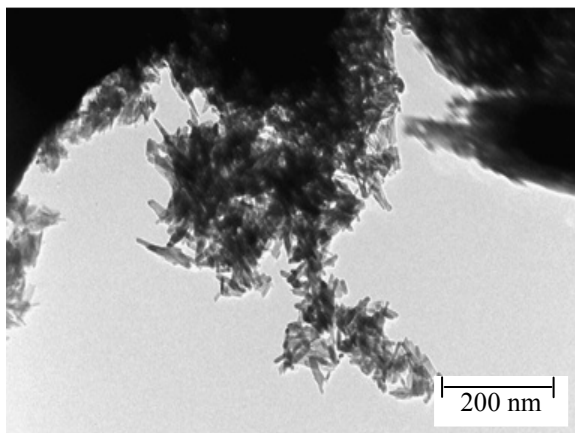
Figure 2.6 SEM micrographs (scale = 50 nm) of HAp(a), 2.5 wt% (b), 5 wt% (c), 7.5 wt% (d), 10 wt% (e) and 15 wt% (f) V_2O_5 supported on HAp.



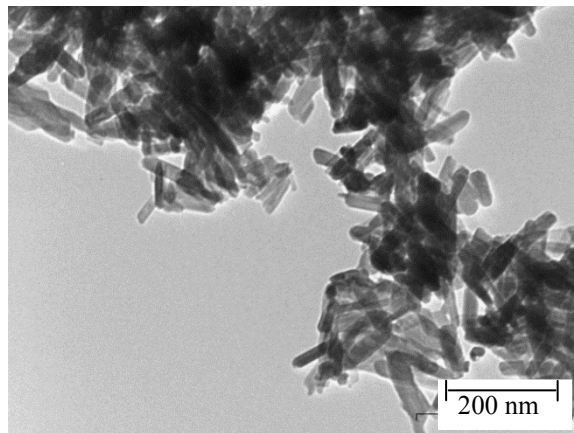
(a)



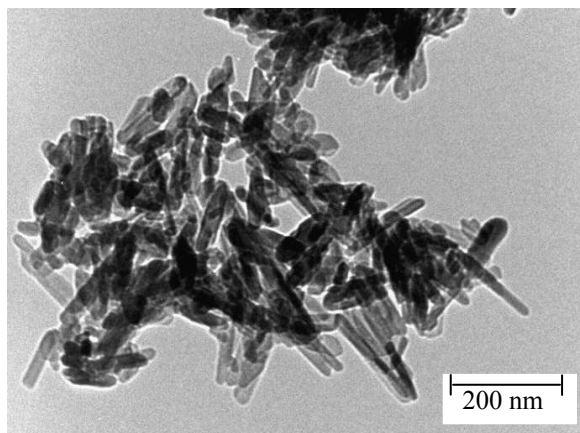
(b)



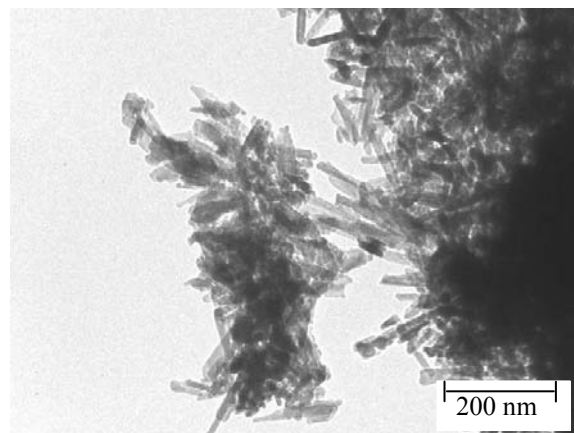
(c)



(d)



(e)



(f)

Figure 2.7 TEM images (scale = 200 nm) of (a) HAp (b) 2.5 % V-HAp (c) 5 % V-HAp (d) 7.5 % V-HAp (e) 10 % V-HAp (f) 15 % V-HAp

octane with an increase in temperature as expected (Fig. 2.8). All the catalysts showed activities parallel to their TPR profiles.

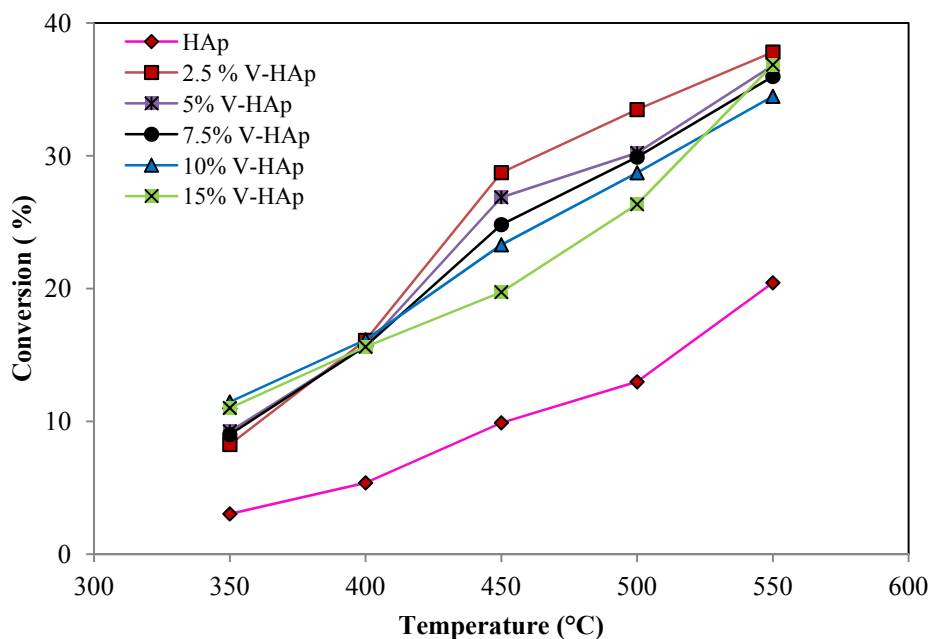


Figure 2.8 Effect of temperature on the conversion of *n*-octane at a GHSV of 4000 h⁻¹

At temperatures between 350°C and 400°C, low conversions were recorded due to the dominance of the vanadium pentoxide phase, where V⁵⁺ is found in an octahedral environment with terminal V=O bonds, resulting in incorporation of oxygen in the intermediate reaction products [43]. An increase in the oxygen conversion over the temperature range resulted in an increase in the formation of carbon oxides (Fig. 2.9).

2.3.2.1 Product Selectivity

A range of octenes and aromatics, cracked products and carbon oxides (CO_x) were present in the product stream. Cracked products included mainly butane, propane, and ethane. Oxygenates included C₈ oxygenates (octanal, octanol, 2-octanal and 2-octanol) and lower oxygenates (acetone, acetic acid, butanol and propanol). Octenes were the major products for all the catalysts. The selectivity towards octenes for low loadings (2.5-7.5 wt %) decreased as the catalyst loadings and temperature increased due to the increased formation of aromatics, cracked products and CO_x. Selectivity towards octenes increased with loading from 10 wt% to 15 wt %. (Fig. 2.10). This is explained by the presence of vanadium pyrophosphate which favours the

formation of alkenes from alkanes, since the octane adsorbed on the catalyst is activated by the highly reactive surface oxygen species in the isolated tetrahedral VO_4 which abstracts a hydrogen atom from the hydrocarbon molecule to form an adsorbed alkyl radical and a surface OH group.

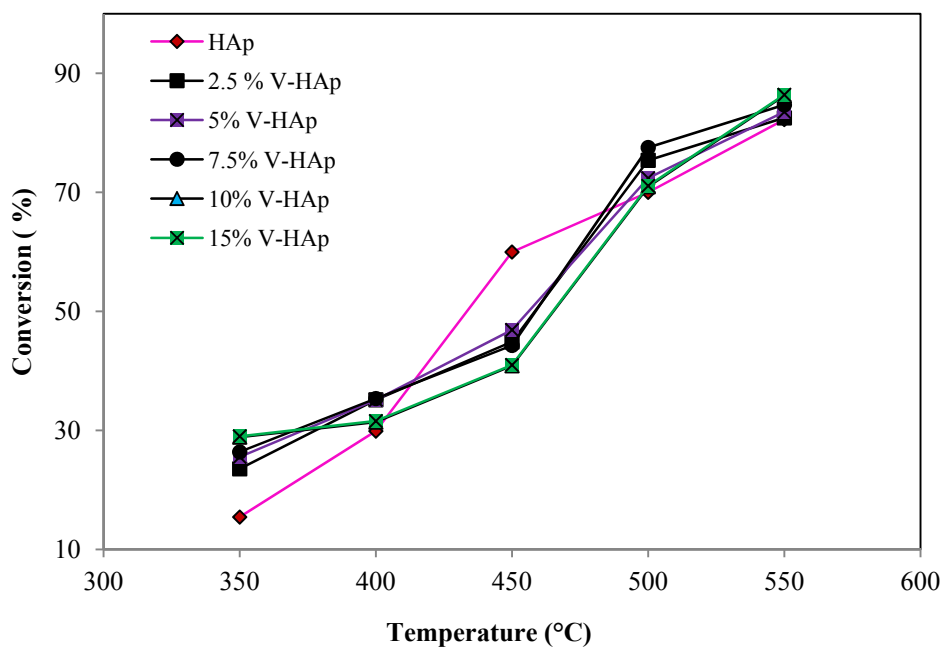


Figure 2.9 Effect of temperature on the conversion of oxygen at a GHSV of 4000 h^{-1}

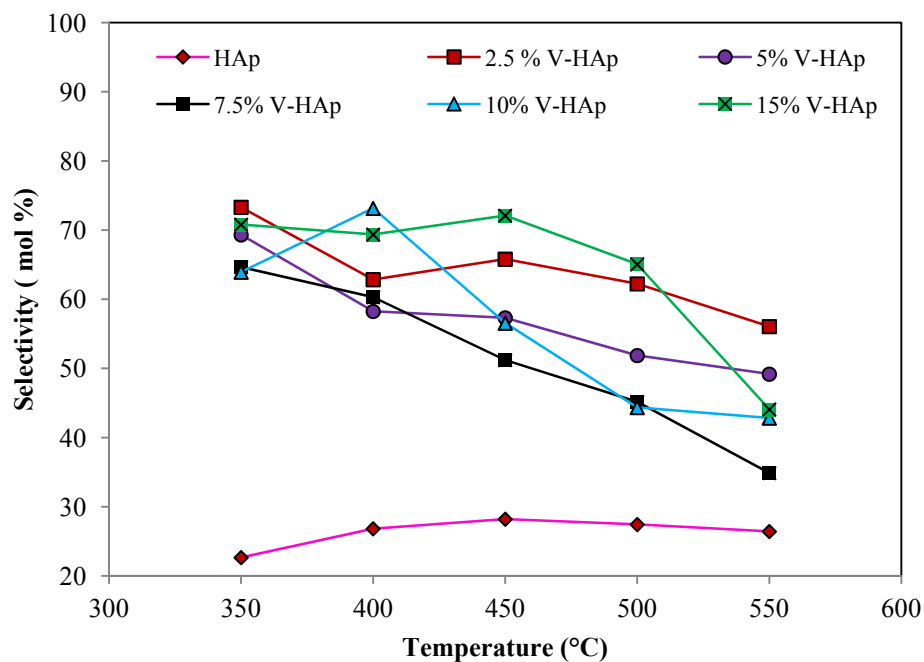


Figure 2.10 Effect of temperature on the selectivity of octenes at a GHSV of 4000 h^{-1}

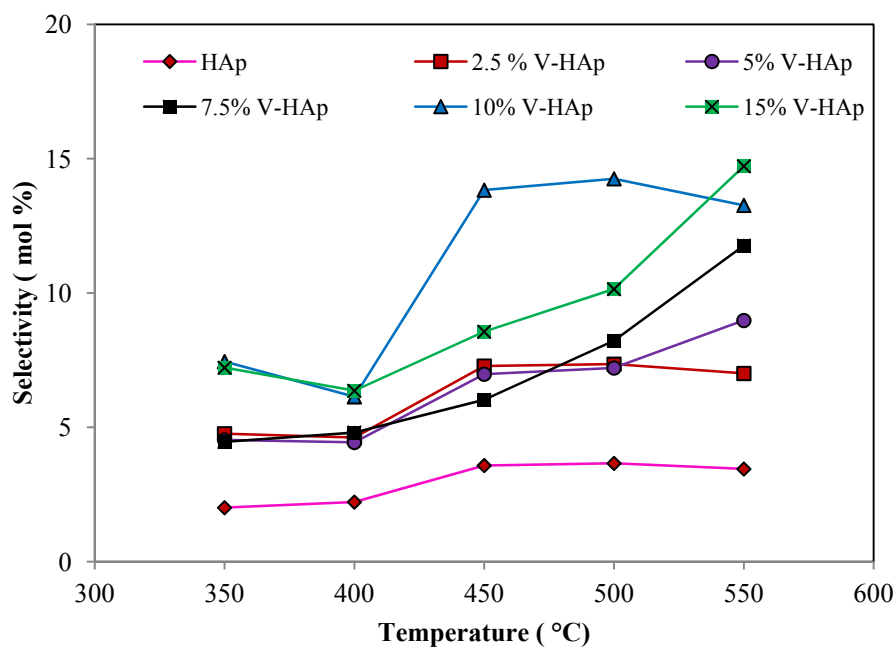


Figure 2.11 Effect of temperature on the selectivity of aromatics at a GHSV of 4000 h⁻¹

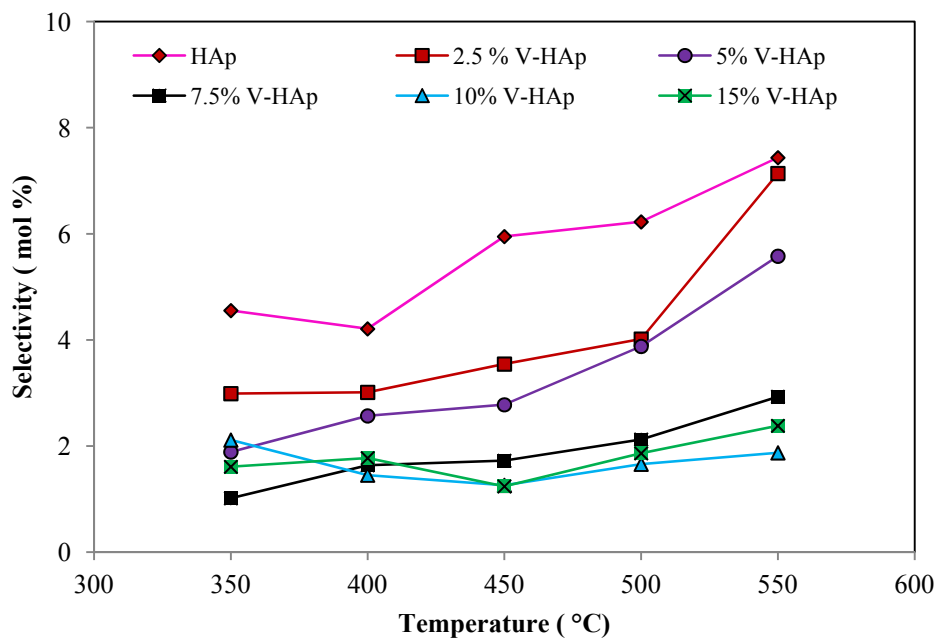


Figure 2.12 Effect of temperature on the selectivity of cracked products at a GHSV of 4000 h⁻¹

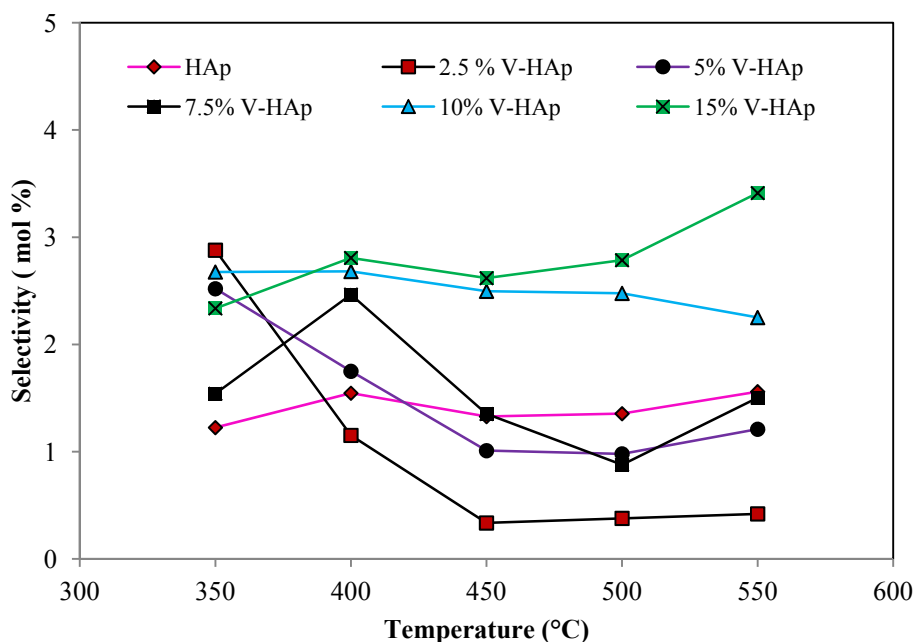


Figure 2.13 Effect of temperature on the selectivity of oxygenates at a GHSV of 4000 h⁻¹

The possible synergistic co-existence between the V₂O₅ and the pyrovanadate phases could also enhance the rapid desorption of the formed octenes from the catalyst surface and thereby increase their selectivity [41].

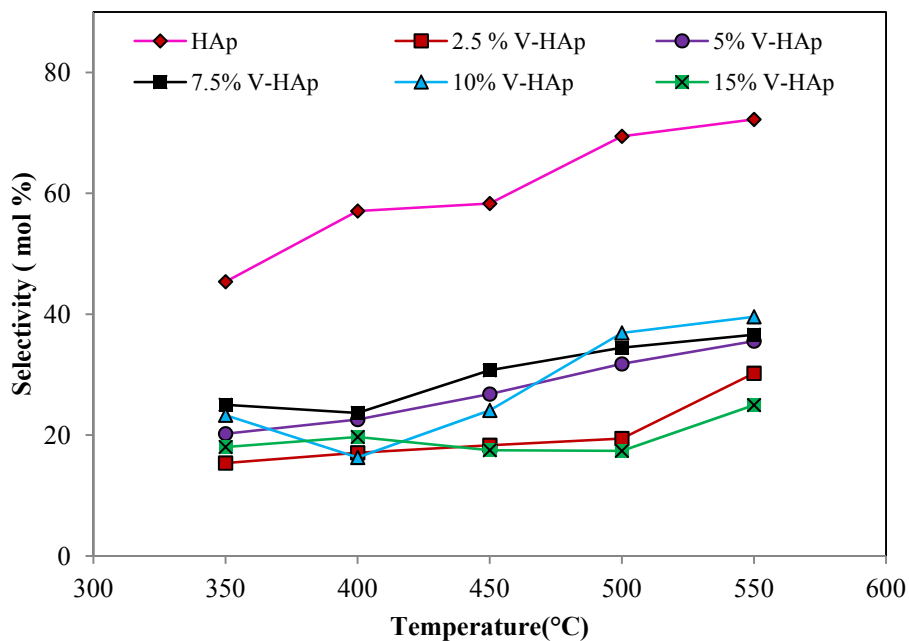


Figure 2.14 Effect of temperature on the selectivity of CO_x at a GHSV of 4000 h⁻¹

At 400 °C, the 10 wt % loaded catalyst shows highest selectivity to octenes (73%). In contrast, the high selectivity towards aromatics and low selectivity for CO_x shown by the 15 wt % loaded catalyst is attributed to the stable aromatic nucleus in *o*-xylene, representing a driving force for the formation of these compounds and thereby reducing the production of carbon oxides, especially the contribution from secondary combustion [44]. An opposite trend is shown for cracked products. As the vanadium content increases, cracked product selectivity decreases (Figs. 2.11-2.14).

2.3.2.2 Product selectivity at iso-conversion

Product selectivity at iso-conversion was monitored at 450°C (24% conversion of *n*-octane) and 550°C (36% conversion of *n*-octane) (Fig. 2.15 and Fig. 2.16). In both cases, octene selectivity decreases gradually with an increase in vanadium loading up to 7.5 wt %. Thereafter, an increase in octene selectivity is observed for the 10 and 15 wt% loadings. There was an increased appearance of aromatics as the vanadium concentration increased (2.5 to 7.5 wt %) and this shows an opposite trend to that exhibited by the octenes, suggesting that octenes are aromatics precursors.

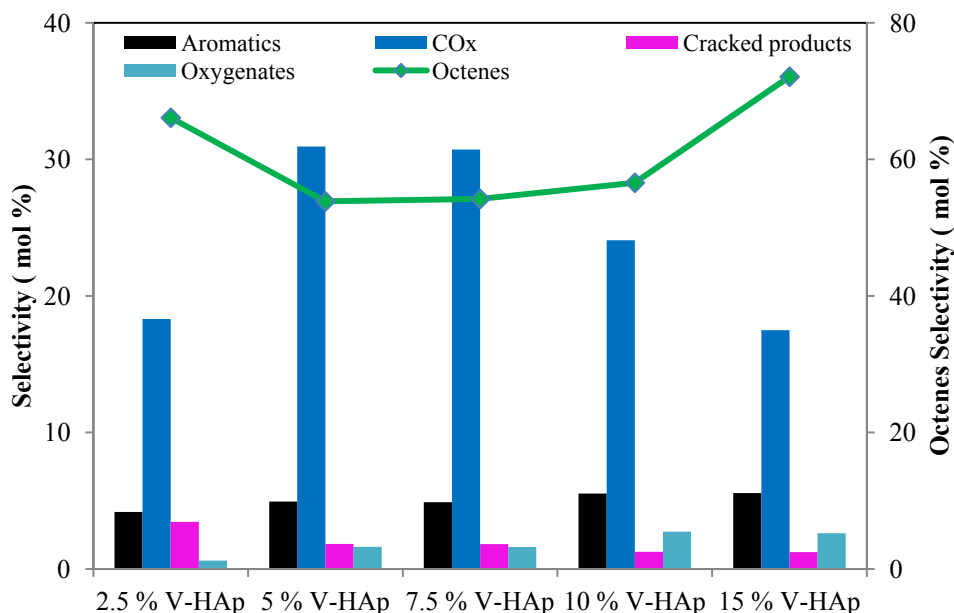


Figure 2.15 Selectivity of the product stream at iso-conversion (24%), Temperature = 450°C

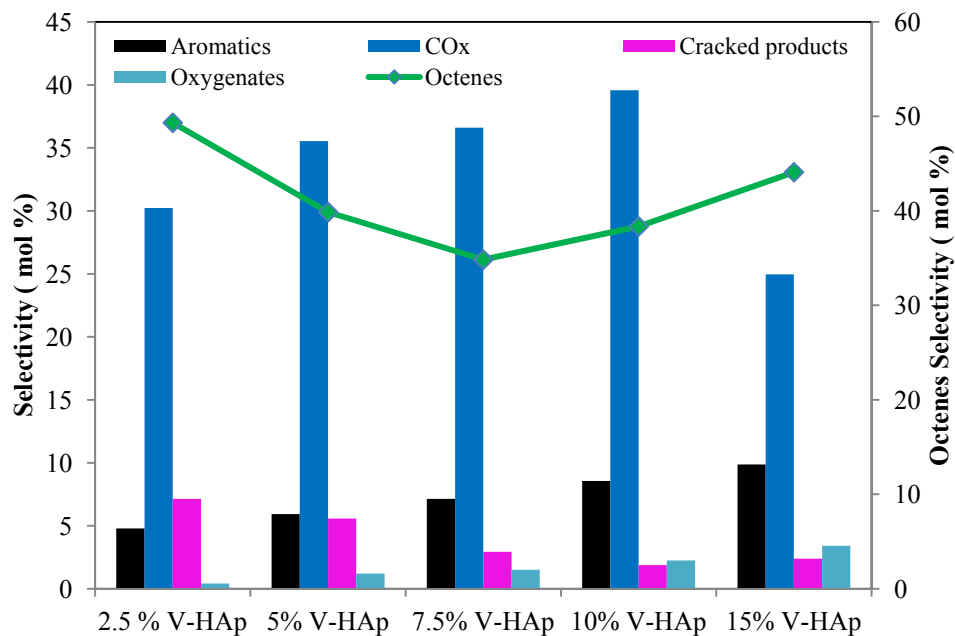


Figure 2.16 Selectivity of the product stream at iso-conversion (36%), Temperature = 550°C

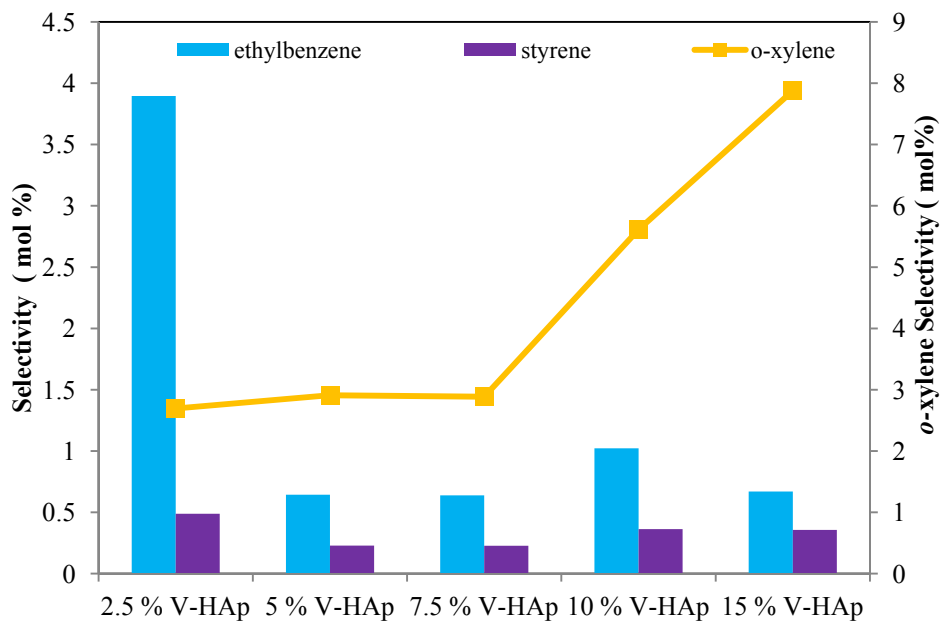


Figure 2.17 Selectivity of aromatics at iso-conversion (24%), Temperature = 450°C

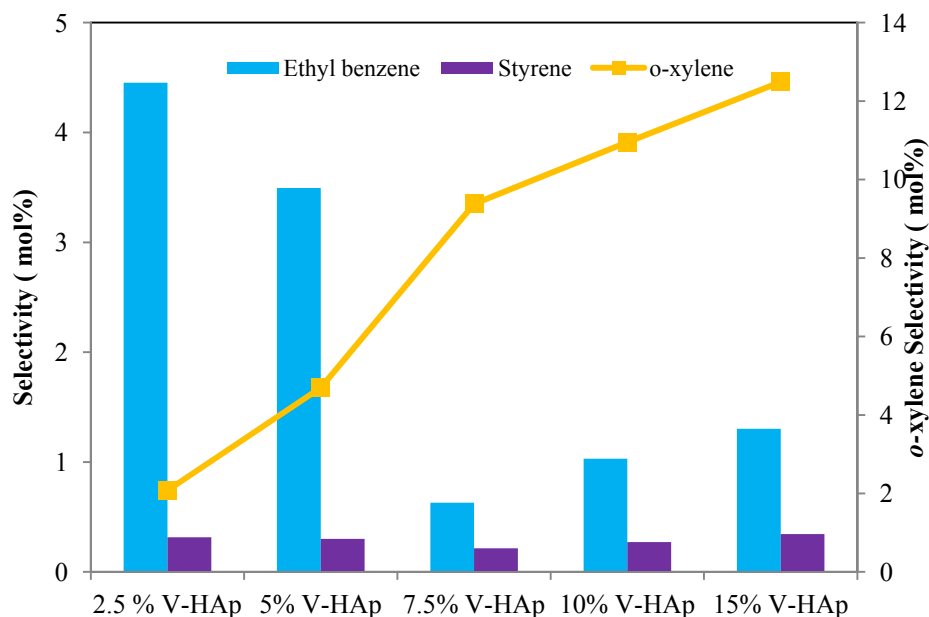


Figure 2.18 Selectivity of aromatics at iso- conversion (36%), Temperature = 550°C

For the 10 and 15 wt% loadings, a relatively slow desorption of the basic octenes from the catalyst surface lowers their selectivity slightly, but simultaneously causes aromatic selectivity to increase by allowing the formed octenes to be oxidized further to give the corresponding aromatics (Fig. 2.17 and Fig. 2.18).

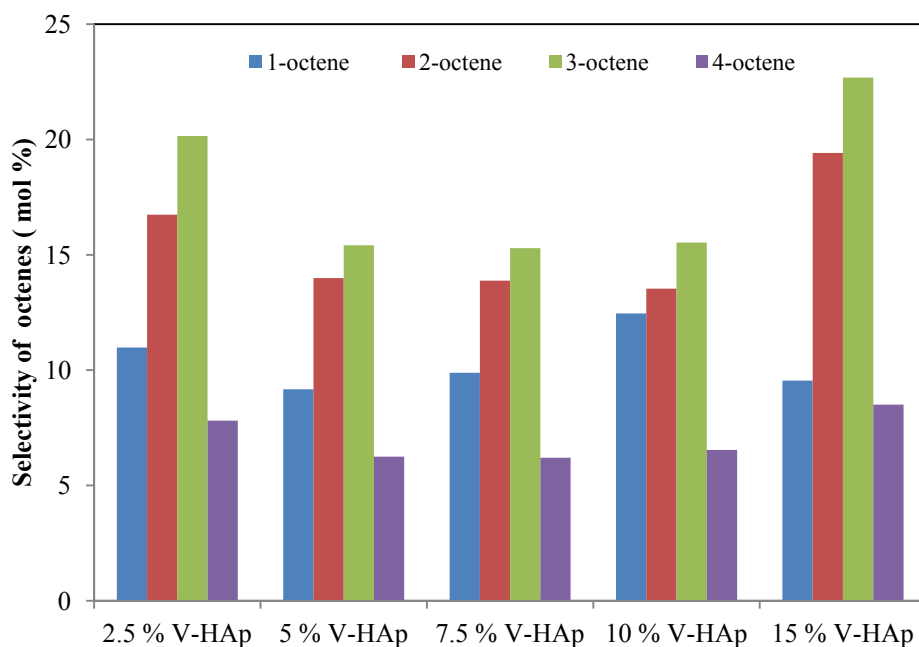


Figure 2.19 Selectivity of octenes at iso-conversion (24%), Temperature = 450°C

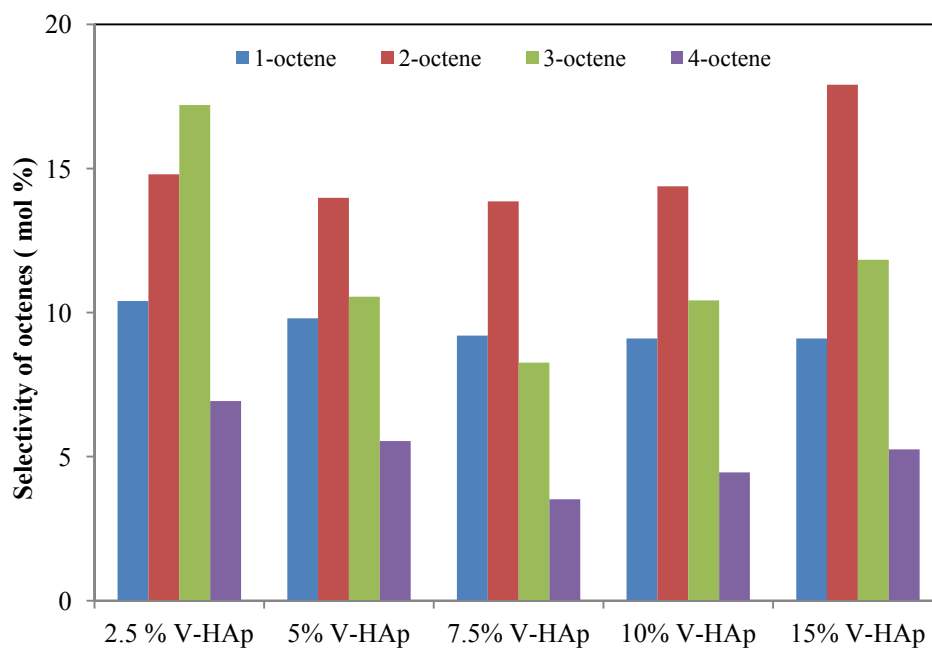


Figure 2.20 Selectivity of octenes at iso-conversion (36%), Temperature = 550°C

The desorption of products is dependent on the acid base character of the catalyst. The selectivities of octenes at iso-conversion correlates well with both acidic and basic character of the catalysts. The selectivity towards octenes is dependent on the vanadium concentration and the type of the secondary phase present on the catalyst.

The 2.5 wt% loading gives good selectivity towards 1-octene, but this decreases slightly with an increase in vanadium concentration (Fig. 2.19 and Fig. 2.20). The *cis*- and *trans*-2-octenes are the dominant products among all the octenes. The selectivity to *trans*-2-octene is found to be higher than *cis*-2-octene due to the relative thermodynamic stability of *trans*-isomers compared to the respective *cis*-isomers [45]. There is minimal selectivity towards 4-octene, although there is no difference in the energies of the C-H bond at C2, C3 and C4 in the alkane chain [45].

Hodnett *et al.* [46] proposed a mechanism for alkane activation where they suggested that the rate determining step is the homolytic breaking of C-H bonds from the surface alkyl species with the catalyst, followed by a fast elimination of second hydrogen from a neighbouring carbon to form the olefinic bond. A different study on the activation of *n*-octane, suggested that steric

effects are likely to play a vital role in the accessibility to active sites by large molecules and this is likely to become a limiting factor [31, 32].

The aromatics are formed by the cyclization via C1 to C6 and C2 to C7 bonding. Fig.2.20 shows the combined percentage of C1 to C6 cyclization mode products out of the selectivity of the total cyclization products. In a separate experiment, 1,7 octadiene was fed over the catalysts with low vanadium loadings (2.5 to 7.5 wt%), and the cyclization was found to have taken place predominantly through the C1 to C6 mode: over the 2.5 wt% loaded catalyst, more than 70 % of the cyclization follows this mode at lower temperatures. The modes of cyclization were further studied by feeding octenes i.e 1-octene, 2-octene, 3-octene and 4-octene at a GHSV 4000 h⁻¹, with a 1:0.5 *n*-octane to oxygen molar ratio. 1-Octene is preferentially consumed during the C1 to C6 cyclization and this eventually leads to the formation of ethyl benzene and styrene (Fig. 2.21). 1-Octene and 1,7 octadiene can provide 6 sequential sp³ carbon atoms for this type of cyclization. The sp³ carbons, unlike the sp² carbons, possess free rotation along the bond axis and hence the flexibility needed for the ring formation. The tendency towards the C2 to C7 cyclization of octane generally increases as the temperature increases, presumably because

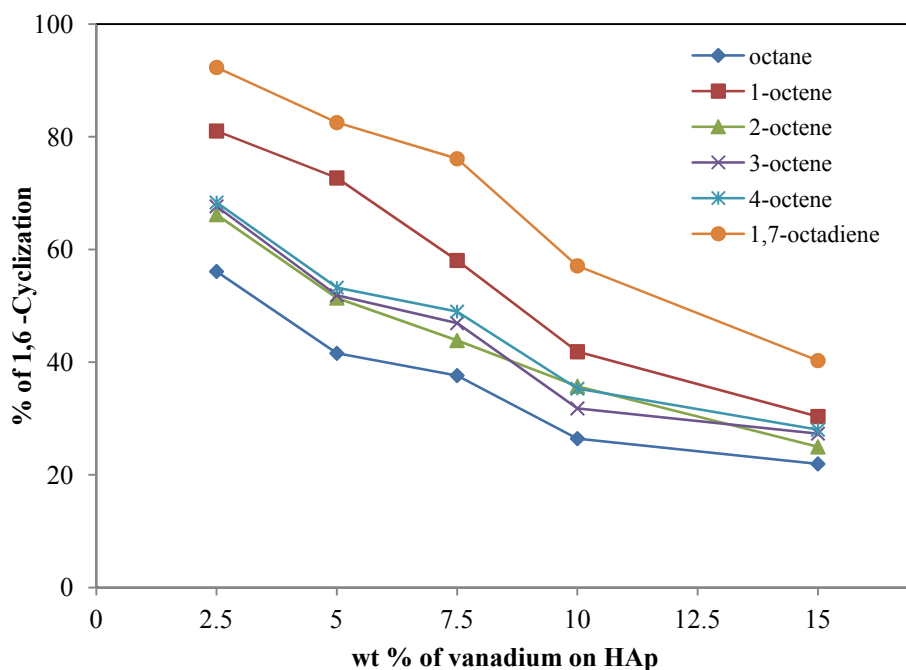


Figure 2.21 The percentage of the 1,6-cyclization at iso-conversion (24%), Temperature = 450°C

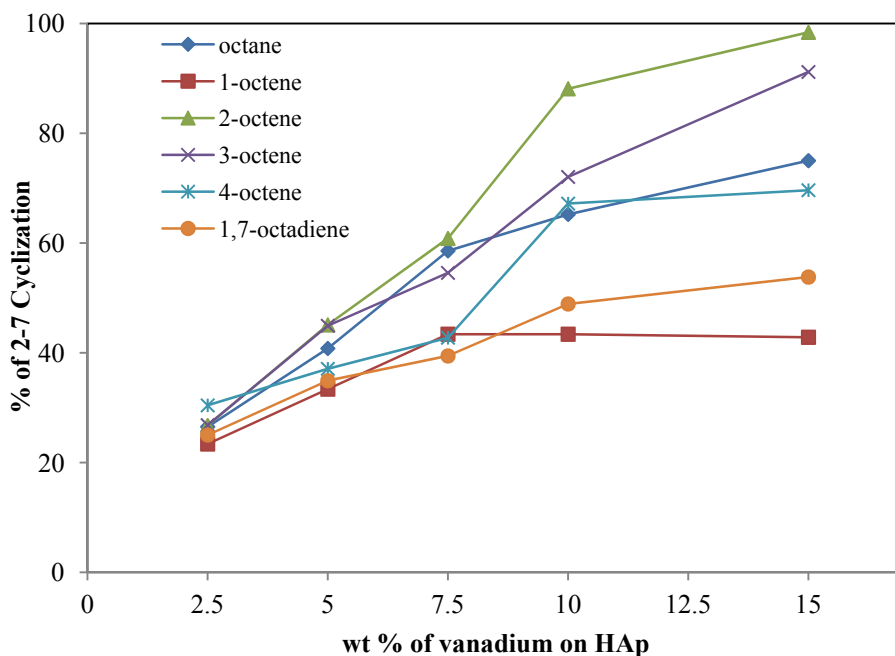


Figure 2.22 The percentage of the 2,7- cyclization iso-conversion (36%), Temperature = 550°C

raising the temperature will provide more energy to overcome any activation barrier. The higher vanadium loadings (10-15 wt%) showed the highest tendency (>90%) towards the C2 to C7 cyclization at 550 °C, while the 2.5 wt% loaded catalyst exhibited the lowest tendency to this mode especially at high temperatures (Fig. 2.22). Feeding the octenes showed that 2-octene is preferentially consumed during C2 to C7 cyclization and eventually leads to the formation of *o*-xylene. The C2 to C7 cyclization mechanism thus dominates over the C1 to C6 mechanism seen over VMgO catalysts [31, 32]. The 15 wt% loading showed a higher selectivity towards C₈ aromatics compared to carbon dioxides, indicating that aromatic formation provides an energetically favourable pathway, thus lowering CO_x formation. Here, *o*-xylene selectivity is far greater than that of styrene and ethyl benzene, in contrast to results over VMgO catalysts. Cracked products also decrease with increasing vanadium loading although the selectivity is low.

2.3.2.3 Yields of 1-octene and *o*-xylene

Among all the catalysts, 2.5 % V-HAp showed the highest selectivity and yield towards 1-octene (Fig. 2.23). This can be explained by the ease at which this catalyst is reduced at a lower temperature, compared to the other catalysts.

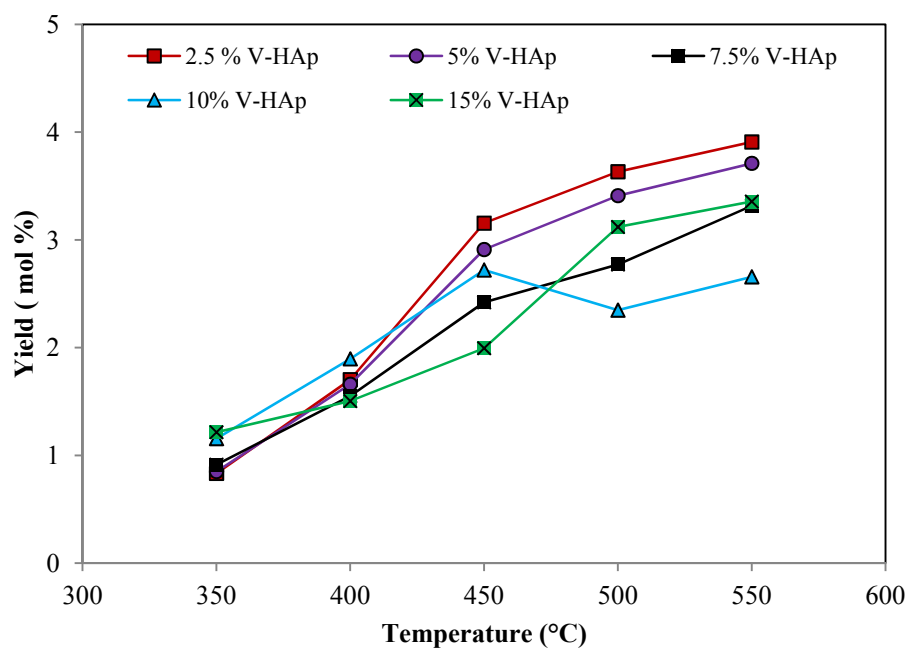


Figure 2.23 Yield of 1-octene as a function of temperature

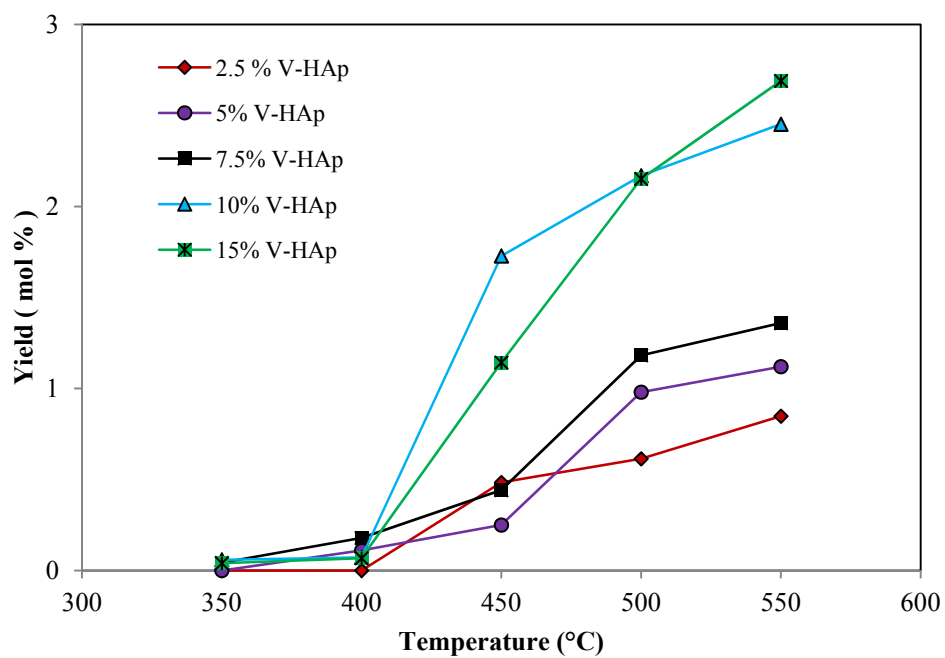


Figure 2.24 Yield of *o*-xylene as a function of temperature

At temperatures above 450°C, catalysts with low vanadium loadings showed high yields towards 1-octene but these decreased with an increase in vanadium concentration, since the formation of aromatics is favoured due to the presence of the pyrophosphate phase in those catalysts. For *o*-xylene formation, the 15 wt% loading showed good yields at 450°C and 550°C (Fig. 2.24). At low temperatures, all catalysts showed low selectivity towards aromatics and low yields of *o*-xylene were obtained because the dominant V₂O₅ phase favours the formation of oxygenates instead of alkenes and aromatics. This is confirmed by the presence of oxygenates as by-products and high selectivities towards CO_x [47, 48].

2.4 Conclusion

All the characterization techniques showed that vanadium pentoxide is supported on hydroxyapatite and is well dispersed. For the 10 and 15 wt% loadings, vanadium exhibits two types of phases, the vanadium pentoxide and pyrovanadate phase, confirmed by XRD diffractograms and supported by IR. TPR profiles showed that as the vanadium concentration increases, reduction occurs at higher temperatures. TPD showed that total acidity of the catalysts increases as the vanadium loading increases. There was minimal change in the structure and morphology of the used catalysts. Oxidative dehydrogenation experiments showed that vanadium pentoxide, which is the dominant phase in the lower loadings, gave high selectivity towards octenes and low selectivity towards aromatics. All the catalyst showed moderate to high selectivity towards carbon oxides, since vanadium pentoxide also favours the formation of oxygenates. The C₂ to C₇ is the favorable cyclization mode for formation of aromatics and aromatics selectivity increases with both vanadium content and temperature. At high wt% loadings (10 and 15 wt%), although octenes were the major products, a significant selectivity towards aromatics was obtained compared to the other catalysts due to the presence of the pyrovanadate phase.

Acknowledgements

We thank the NRF, THRIP and the EM Unit, UKZN for supporting this work.

References

- [1] F. Cavani, F. Trifiró, Appl. Catal. A88 (1992) 115-135.
- [2] A. Szechenyi, F. Solymosi, Appl. Catal. A306 (2006) 149-158.
- [3] A. de Lucas, P. Sanchez, F. Dorado, M.J. Ramos, J.L. Valverde, Appl. Catal. A 294

- (2005) 215-225.
- [4] K.A. Williams, L.D. Schmidt, *Appl. Catal. A* 299 (2006) 30-45.
- [5] G. Centi, F. Cavani, F. Trifiró, *Selective Oxidation by Heterogeneous Catalysis*, Kluwer Academic / Plenum Publishers, New York, 2001, pp. 334-338.
- [6] A.A. Lemonidou, *Appl. Catal. A* 216 (2001) 277-284.
- [7] C. Tellez, M. Abon, J.A. Dalmon, C. Miradatos, J. Santamaria, *J. Catal.* 195 (2000) 113-124.
- [8] M. Machli, E. Heracleous, A.A. Lemonidou, *Appl. Catal. A* 236 (2002) 23-34.
- [9] L. Lisi, P. Patrono, G. Ruoppolo, *Catal. Lett* 72(2001) 207-210.
- [10] M. Khachani, M. Kacimi, A. Ensuque, J.-Y. Piquemal, C. Connan, F. Bozon-Verduraz, M. Ziyad, *Appl. Catal. A* 388 (2010) 113-123.
- [11] K. Elkabouss, M. Kacimi, M. Ziyad, S. Ammar, F. Bozon-Verduraz, *J. Catal.* 226 (2004) 16-24.
- [12] J. Vedrine, *Top. Catal.* 21 (2002) 97-106.
- [13] J.C. Elliot, *Structure and Chemistry of the Apatites and Other Calcium Orthophosphates*, Elsevier, Amsterdam, 1994.
- [14] A. Yasukawa, T. Yokoyama, K. Kandori, T. Ishikawa, *Colloids Surf. A: Physico-Chem. Eng. Aspects* 238 (2004) 133-139.
- [15] S. Sugiyama, T. Miyamoto, H. Hayashi, J.B. Moffat, *J. Mol. Catal. A: Chem.* 135 (1998) 199-208.
- [16] C. Boucetta, M. Kacimi, A. Ensuque, J.-Y. Piquemal, F. Bozon-Verduraz, M. Ziyad, *Appl. Catal. A* 356 (2009) 201-210.
- [17] S. Sugiyama, T. Osaka, Y. Hirata, K. Sotowa, *Appl. Catal. A* 312 (2006) 52-58.
- [18] S. Sugiyama, E. Nitta, H. Hayashi, J.B. Moffat, *Appl. Catal. A* 198 (2000) 171-178.
- [19] K. Elkabouss, M. Kacimi, M. Ziyad, S. Ammar, F. Bozon-Verduraz, *J. Mater. Chem.* 16 (2006) 2453-2463.
- [20] H. Hayashi, H. Kanai, Y. Matsumura, S. Sugiyama, J.B. Moffat, *Stud. Surf. Sci. Catal.* 110 (1997) 673-681.
- [21] B. Kilos, A.T. Bell, E. Iglesia, *J. Phys. Chem. C* 113 (2009) 2830-2836.
- [22] R. Marx, H.-J. Wölk, G. Mestla, T. Turek, *Appl. Catal. A* 398 (2011) 37-43.

- [23] M. Nicolai G. Gonçalves , F. Natalio , M. Humanes, J. Inorg. Biochem. 105 (2011) 887-893.
- [24] Z. Janas, P. Sobota, Coord. Chem. Rev. 249 (2005) 2144-2155.
- [25] R. Wever, K. Kustin, Adv. Inorg. Chem. 35 (1990) 81-115.
- [26] Y. Maeda, M. Koyabu, T. Nishimura, S. Uemura J. Org. Chem. 69 (2004) 7688-7693.
- [27] H.K. Matralis, Ch. Papadopoulou, Ch. Kordulis, A. A. Elguezabal, V. C. Corberan, Appl. Catal. A 126 (1995) 365-380.
- [28] H.B. Friedrich, A.S. Mahomed, Appl. Catal. A347 (2008) 11-22.
- [29] O. Krasnobaeva, I. Belomestnykh, T. Nosova, T. Elizarova, G. Isagulyants, S. Kolesnikov, V. Danilov, Russ. J. Inorg. Chem. 56 (2011) 1012-1016.
- [30] O. Krasnobaeva, I. Belomestnykh, T. Nosova, T. Elizarova, G. Isagulyants, S. Kolesnikov, V. Danilov, Russ. J. Inorg. Chem. 56 (2011) 168-172.
- [31] E. A. Elkhalfa, H.B. Friedrich, Appl. Catal. A373 (2010) 122-131.
- [32] E. A. Elkhalfa, H.B. Friedrich, Catal. Lett. 141(2011)554-564.
- [33] E.A.Mamedov, C.V. Cortés, Appl. Catal. A127(1995) 1-40.
- [34] D.A Bulushev, L.K. Minster, A. Renken, Catal. Today61(2000) 271-277.
- [35] Y.M.Liu, Y. Cao, N.Yi, W.L.Feng, W.L.Dai, S.R. Yan, H.Y. He, K.N. Fan, J. Catal.224 (2004) 417-428.
- [36] S. Singh, S.B. Jonnalagadda, Catal. Lett. 126 (2008) 200-206.
- [37] H.-W. Kim, L.-H. Li, Y.-H. Koh, J.C. Knowels, H.-Ee Kim, J. Am. Ceram. Soc., 87 (2004) 1939-1944.
- [38] P. Parhi, A. Ramanan, A.R. Ray, Mater. Lett. 60 (2006)218-221.
- [39] R.A. Nyquist, R.O. Kagel, Infra Red Spectra of Inorganic Compounds, Academic Press, New York, 1991.
- [40] A. Rapacz-Kmita, A. Ślósarczyk, Z.C. Paszkiewicz, C. Paluszkiwickz, J. Mol. Struct., 704 (2004) 333-340.
- [41] L. Balderas-Tapia, I. Hernández-Pérez, P. Schacht, I.R. Córdova, G.G. Aguilar-Ríos, Catal. Today 107 (2005) 371-376.
- [42] T. Blasco, J.M. López Nieto, Appl. Catal. A 157 (1997) 117-142.
- [43] L. Balderas-Tapiaa,J.A. Wanga, I. Hernandez-Perez, G.G. Aguilar-Riosa, P. Schacht, Mater. Lett. 58 (2004) 3034-3039.

- [44] T. Blasco, J.M. López Nieto, A. Dejoz, M.I. Vázquez, *J. Catal.* 157 (1995) 271-282.
- [45] R.T. Morrison, R.N. Boyd, *Organic Chemistry, Sixth Ed.*, Prentice-Hall, New Jersey, 1992, 317–366.
- [46] B.K. Hodnett, *Heterogeneous Catalysis Oxidation: Fundamental and Technological Aspects of the Selective and Total Oxidation of Organic Compounds*, Wiley, 2000, pp. 65-101.
- [47] P. Meriaudeau, A. Thangaraj, C. Naccache, S. Narayanan, *J. Catal.* 146 (1994) 579-582.
- [48] B. Shi, B.H. Davis, *J. Catal.* 157 (1995) 626-630.

CHAPTER 3

ACTIVATION OF *n*-OCTANE USING VANADIUM SUPPORTED ON ALKALINE EARTH HYDROXYAPATITES

Abstract

Vanadium pentoxide was supported on calcium, strontium, magnesium and barium hydroxyapatite with loadings of 2.5 and 10 wt% by the wet impregnation technique. The materials were characterized by XRD, ICP-OES, BET, FTIR, SEM, TEM, TPR and TPD. From XRD and IR analyses, vanadium is found in the vanadium pentoxide phase for the 2.5 wt% loadings, whereas an additional pyrovanadate phase exists for the 10 wt% loadings. Electron microscopy provides evidence of a homogenous distribution of the vanadium species on the hydroxyapatite. Oxidative dehydrogenation reactions carried out in a continuous flow fixed bed reactor showed that selectivity towards desired products was dependent on the phase composition of the catalyst and the *n*-octane to oxygen molar ratios. For the *n*-octane to oxygen molar ratio of 1:0.5, selectivity towards aromatics and octenes was obtained, whereas the *n*-octane to oxygen molar ratio of 1:2 showed selectivity towards aromatics and oxygenates. Good selectivity towards octenes was achieved using the 2.5 wt% V₂O₅ loaded hydroxyapatite catalysts. There was a marked decrease in octene selectivity and a significant increase in the formation of C₈ aromatics when the 10 wt% loaded catalyst was used. In general, for the activation of *n*-octane, 3-octene in the octenes, *o*-xylene in the aromatics and 2-octanone in the oxygenates were the major products. At iso-conversion of 27% at 450 °C, V₂O₅ supported Ca-HAp showed highest selectivity towards octenes, V₂O₅ supported Sr-HAp showed highest selectivity towards aromatics, V₂O₅ supported Mg-HAp showed highest selectivity towards oxygenates and V₂O₅ supported Ba-HAp showed selectivity towards aromatics and oxygenates.

Keywords: hydroxyapatite, V₂O₅, *n*-octane, 1-octene and *o*-xylene, oxidative dehydrogenation.

3.1 Introduction

Olefins are important intermediates in a large number of industrial processes [1, 2]. Dehydrogenation (ODH) is a main manufacturing process of alkanes to alkenes and has been developed and commercialized for over 60 years [1]. The ODH of alkanes is highly desirable due

to its potentially low environmental impact and the relatively low cost of raw materials [3]. Also, the addition of O₂ to the reaction mixture allows for oxidative dehydrogenation and over appropriate catalysts can produce oxygenated compounds [4-6]. In addition, ODH of alkanes over redox catalysts has some advantages with respect to steam cracking or catalytic dehydrogenation, viz.: (i) the reaction is exothermic, (ii) a catalyst regeneration step is not required since catalyst regeneration occurs in situ by the oxygen feed and (iii) relatively low reaction temperatures (350–500 °C) are required [7]. Currently, considerable interest is devoted to studying the ODH of alkanes on supported vanadia catalysts and these catalysts show high activity in various partial oxidation and oxidative dehydrogenation reactions of hydrocarbons [8-12]. It has been suggested that V=O and/or V-O-V bonds participate in the activation of lower alkanes [13] assisted by the ease of abstraction of the lattice oxygen from vanadium, and the catalytic properties of vanadia catalysts can be related to the surface structure of vanadium species [14]. Generally, optimum surface vanadium dispersion is one of the contributing factors in obtaining very active and selective catalysts operating under mild temperature and pressure conditions, achieving high conversions and selectivities, preventing coke formation and at the same time improving the lifetime of the catalyst [15].

Phosphates with apatite-like structure are widely used in biomedical engineering and in many other fields, including heterogeneous catalysis. When loaded with nickel or palladium, hydroxyapatite (HAp), Ca₁₀(PO₄)₆(OH)₂, exhibits good activity in methane dry reforming for the direct synthesis of methyl isobutyl ketone [16]. In the ODH of ethane, cobalt exchanged (Co²⁺/Ca²⁺) hydroxyapatite showed an ethylene yield of 22% at 550 °C. This was attributed to isolated Co²⁺ sites on the apatite surface and to lattice oxygen mobility induced by cobalt incorporation in the phosphate network [17]. The ions in the apatite structure are tolerant to substitutions and can be replaced by various other cations and anions [18, 19]. It has been shown that favorable catalytic activities for the oxidation of short chain alkanes were found on hydroxyapatites containing calcium, strontium and barium [20-23]. The active site on the hydroxyapatite appears to be the OH⁻ group, which results in the enhancement of the formation of an active oxygen species contributing directly to hydrogen abstraction from alkanes [24].

These results indicate that the combination of OH and VO₄ groups, both of which are active catalytic sites in hydroxyapatites and vanadates, respectively, may enhance the activity of the

catalysts for the oxidative dehydrogenation of alkanes [25]. Recently, we reported on the oxidative dehydrogenation of *n*-octane over V₂O₅ supported on calcium hydroxyapatite with different V₂O₅ loadings [26]. The objective of this study is to investigate the effect of different hydroxyapatites on the oxidative dehydrogenation of *n*-octane with varying *n*-octane to oxygen molar ratios.

3.2 Experimental

3.2.1 Catalyst synthesis

All the chemicals used in the preparation of the catalysts were purchased from Merck KGa, Darmstadt, Germany. Various hydroxyapatites were prepared by the method of Ishikawa et al. [27] and Matsumura et al. [28]. Nitrate salts, M(NO₃)₂·*x*H₂O where M = Sr²⁺, Mg²⁺ and Ba²⁺ were dissolved in 300 mL distilled water. The solution was adjusted to pH 11 by the addition of 25 % ammonia solution and then diluted to 600 ml with water. This solution was added dropwise with vigorous stirring at room temperature to a 500 mL solution of (NH₄)₂HPO₄. The resulting precipitate was boiled for 10 min with stirring. The solid was filtered, washed to pH 7 with distilled water and dried in air at 110 °C for 12 hrs. The solid was calcined at 500 °C for 6 hrs in air. Loaded catalysts were prepared by adding the hydroxyapatites to a solution of ammonium metavanadate in oxalic acid at 50 °C to obtain weight percentages of 2.5 wt% and 10 wt% of V₂O₅. The materials were dried overnight at 110 °C and calcined at 550 °C for 6 hours. The 2.5 wt% V₂O₅ on Ca-HAp, Sr-HAp, Mg-HAp and Ba-HAp are noted as 2.5VCa-HAp, 2.5VSr-HAp, 2.5VMg-HAp and 2.5VBa-HAp respectively. The 10 wt% V₂O₅ on Ca-HAp, Sr-HAp, Mg-HAp and Ba-HAp are noted as 10VCa-HAp, 10VSr-HAp, 10VMg-HAp and 10VBa-HAp respectively.

3.2.2 Catalyst characterization

The BET surface area and pore volume studies were carried out by degassing the catalysts under N₂ flow overnight at 200 °C using a Micrometrics Flow Prep 060. The degassed samples were analyzed in a Micrometrics ASAP 2020 multi-point BET surface area analyzer. Inductively coupled plasma (ICP) was performed using a Perkin Elmer Optical Emission Spectrometer Optima 5300 DV. Standards (1000 ppm Sr, Mg, Ba, V and P) were purchased from Fluka. Powder X-ray diffraction (XRD) studies were conducted on a Bruker D8 Advance instrument, equipped with an XRK 900 reaction chamber and a Cu radiation source with a

wavelength of 1.5406λ . The crystallinity of the catalyst was calculated according to the method reported by H. E. Kim et.al [29]. Infra-red (IR) spectra were obtained using a Perkin Elmer Precisely equipped with a Universal ATR sampling accessory using a diamond crystal. The powdered sample was placed on the crystal and a force of 120 psi was applied to ensure proper contact between the sample and the crystal. The spectra were edited and analyzed using Spectrum 100 software. Raman spectroscopy was carried out using an Advantage 532 series spectrometer (NIR Spectrometer) utilizing Nuspec software. Ammonia temperature programmed desorption (TPD) and temperature programmed reduction (TPR) were carried out using a Micromeritics 2920 Autochem II Chemisorption Analyser using the method described in [26]. The surface morphology of the catalysts was obtained using scanning electron microscopy (SEM) utilizing a Leo 1450 Scanning Electron Microscope. Prior to SEM analysis, the samples were mounted on aluminium stubs using double-sided carbon tape and subsequently gold sputtered using the Polaron E5100 coating unit. Transmission electron microscopy (TEM) images were viewed on a Jeol JEM-1010 electron microscope. The images were captured and analyzed using iTEM software.

3.2.3 Catalytic testing

Gas phase oxidation reactions were carried out in a continuous flow fixed bed reactor in down flow mode. A tubular stainless steel reactor tube with a 10 mm diameter and 300 mm length was used. The catalyst bed (1mL) (pellet sizes between 600-1000 μm) was located at the centre of the reactor with 24-grit carborundum packed in the spaces on either side of the bed. An electrically heated block served as furnace with K-type thermocouples monitoring the temperatures of the furnace and catalyst bed. The thermocouples were controlled by CB-100 RK temperature control units. The concentration of *n*-octane in the gaseous mixture was 11 % (v/v) and its molar ratio to oxygen was varied from 1:0.5 – 1:2. Air was used as an oxidant and nitrogen as a make-up gas to produce a total flow of 90 ml/min. The feed was delivered by an HPLC pump and the total gas flow was measured by a Ritter drum-type wet gas flow meter. All gases and liquids were analyzed offline using Perkin Elmer Clarus 400 gas chromatographs equipped with FID and TCD detectors. For the identification of unknown products, a Perkin Elmer Clarus 500 GC-MS was used. Blank experiments were done under the same catalytic conditions and carbon balances ranged between 98-100 % and all data points were obtained in

duplicate with an error of ± 1 %. The diffusion limit per unit time was verified by measuring flow rates before and after the reactor.

3.3 Results and Discussion

3.3.1 Catalyst characterization

3.3.1.1 Infrared Spectroscopy

The symmetric ν_1 and asymmetric ν_3 P-O stretching modes of the phosphate groups from hydroxyapatite were observed at 900 and 1200 cm^{-1} . The multiple bands between 900-1200 cm^{-1} are due to the stretching of both ν_1 and ν_3 modes of the P-O group in the phosphate framework of hydroxyapatites. The multiple bands are due to the triple degeneration of ν_3 in the free ion and resolves into three separate modes when the degeneracy is lifted. Bands in the 500-700 cm^{-1} region, which were observed in all the hydroxyapatites, are due to the asymmetric P-O bending modes of the phosphate groups and peaks at 325 cm^{-1} and 260 cm^{-1} to the vibrations of the bond between the metal and the phosphate of the hydroxyapatite [30, 31]. The stretching bands around 920-1140 cm^{-1} in all vanadium supported on hydroxyapatites show the presence of the terminal V=O group in V_2O_5 and a band for the O=V=O mode of V_2O_5 is observed at 718 cm^{-1} [32]. The peaks which were observed around 900-960 cm^{-1} and 700-850 cm^{-1} suggest that the vanadium pentoxide is present as a monolayer on the vanadium supported on hydroxyapatites [33]. In addition to the V_2O_5 phase, a peak is seen at 666 cm^{-1} , which is characteristic of asymmetric stretching of the V-O-V group in the pyrovanadate phase for 10VCa-HAp, 10VSr-HAp, 10VMg-HAp and 10VBa-HAp. A slight shift of the bands to 20 cm^{-1} in 10VCa-HAp, 10VSr-HAp, 10VMg-HAp and 10VBa-HAp is due to the interaction between the vanadium pentoxide and the pyrovanadate form (Appendix, Fig. A2. Fig. A3).

3.3.1.2 Raman Spectroscopy

The Raman spectra of the compounds (200 cm^{-1} to 1400 cm^{-1}) are shown in Figure 3.1. For M-HAp, there are six peaks in the spectral region, three bands for stretching vibrations (in the range from 900 to 1125 cm^{-1}) and three bands for bending modes (in the range between 375 and 675 cm^{-1}) of PO_4^{3-} . Peaks at 284, 402, 476 and 521 cm^{-1} belong to the V_2O_5 phase present on the hydroxyapatites and bands between 200 - 300 cm^{-1} and 500 - 800 cm^{-1} are assigned to V-O-V vibrations. The phonon modes in the spectral range below 500 cm^{-1} originate from the bond-bending vibrations, whereas the higher frequency mode is the result of the stretching vibra-

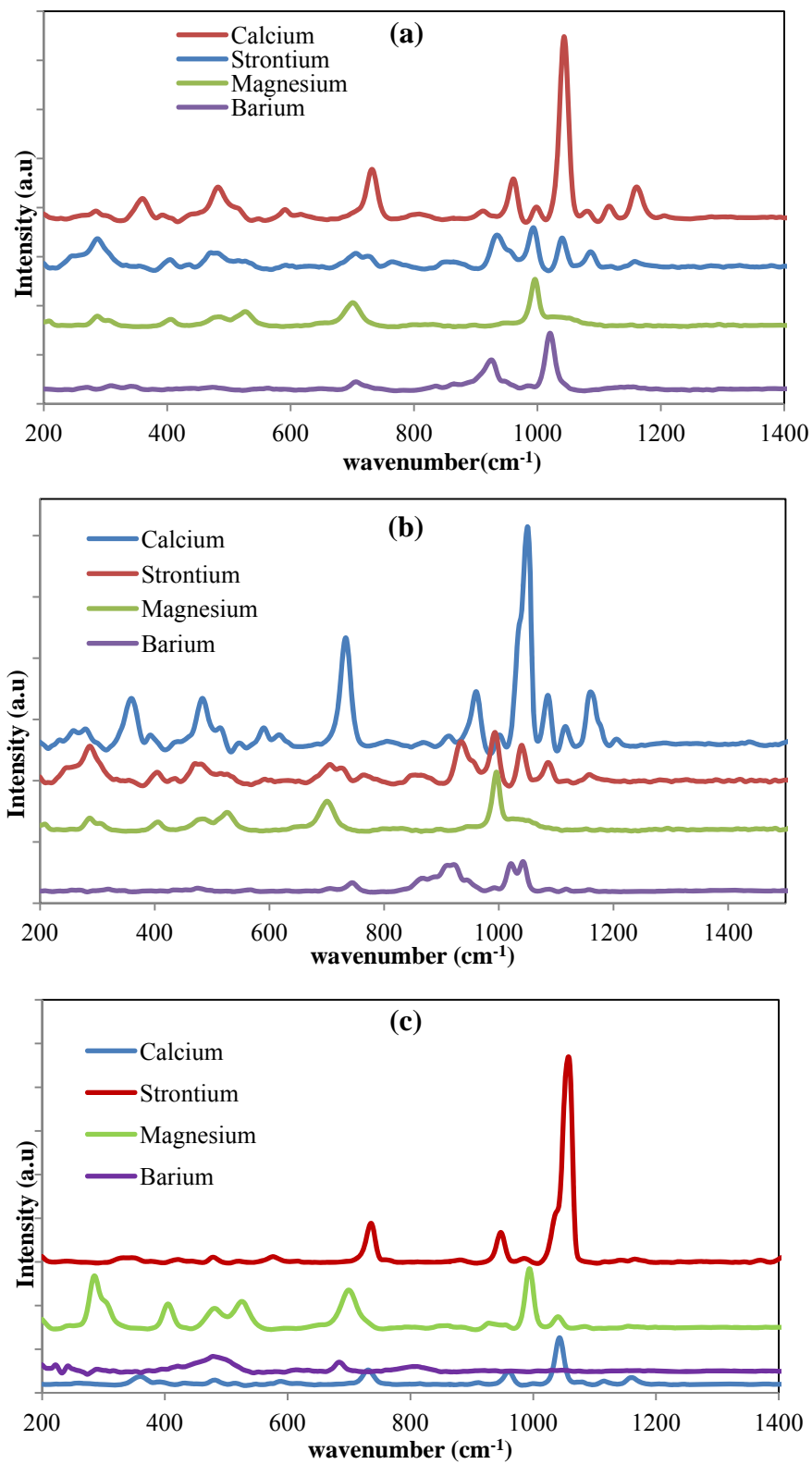


Figure 3.1 Raman spectra of 2.5 wt% V₂O₅ supported on hydroxyapatites (a), 10wt% V₂O₅ supported on hydroxyapatites (b), and unloaded hydroxyapatites (c).

-tions of the V–O ions. The highest frequency modes at 890, 911 and 986 cm^{-1} represent V–O bond stretching vibrations in V_2O_5 . These modes appear at the highest frequencies because they emanate from the shortest-distance V–O bonds (in the VO_5 pyramid and the VO_5 octahedron) [34, 35].

The Raman mode at 448 cm^{-1} is related to the V–O₃–V bending vibration, which appears at a frequency below its intrinsic value, between 470- 490 cm^{-1} in pure V_2O_5 , meaning that, although V_1 and V_3 are different site V ions, they are in the mixed valence state (+4.5). V_2 is in the +5 state at room temperature and the lines at 996, 703 and 530 cm^{-1} characterize crystalline V_2O_5 . The Raman band observed around 1050 cm^{-1} is assigned to the vibration mode of hydroxyl groups.

3.3.1.3 BET Surface Area Analysis

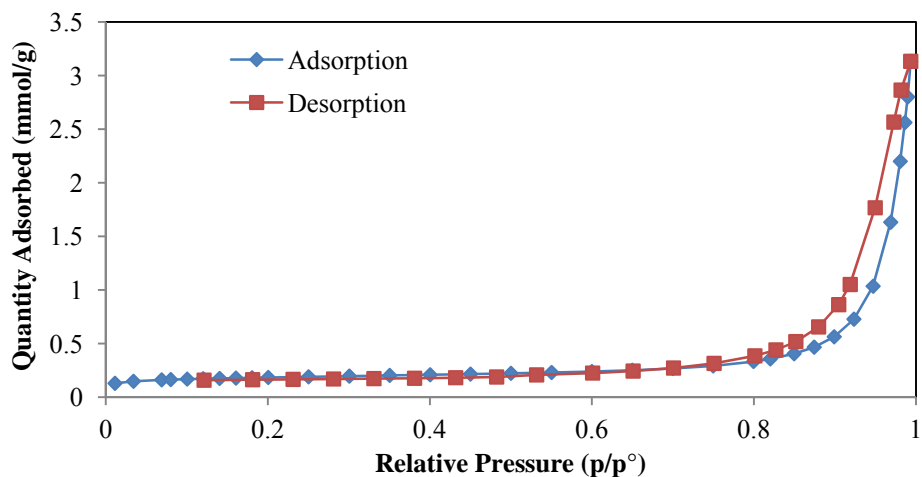


Figure 3.2 Nitrogen adsorption-desorption isotherms of 2.5VCa-HAp

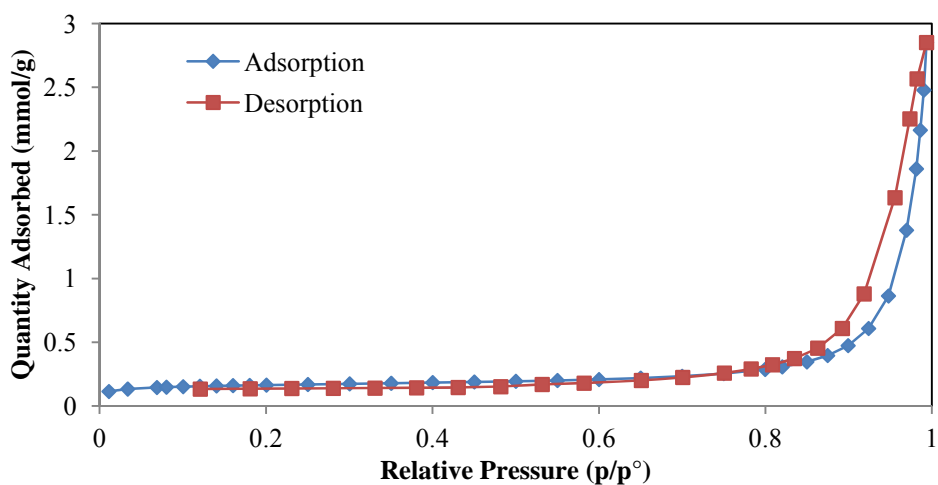


Figure 3.3 Nitrogen adsorption-desorption isotherms of 2.5VSr-HAp

The surface areas and the elemental composition for the catalysts are shown in Table 3.1. The texture of the catalysts was dependent on the V_2O_5 composition and the higher loading resulted in a drastic decrease in the surface area as well as the pore volume. This could be attributed to the blocking of the narrow pores of the support with the active component making it inaccessible to nitrogen molecules [36]. Figs. 3.2 - 3.9 show the nitrogen adsorption-desorption isotherms for the V_2O_5 -loaded hydroxyapatites.

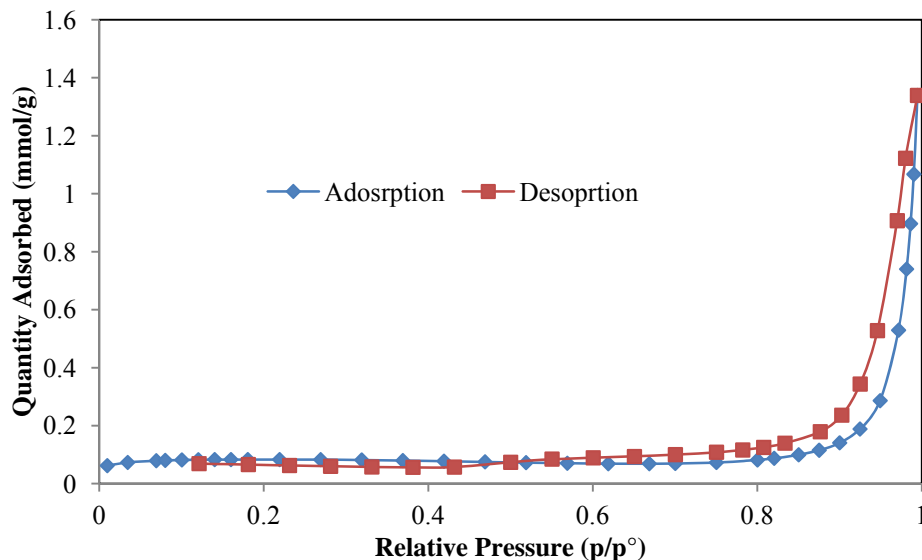


Figure 3.4 Nitrogen adsorption-desorption isotherms of 2.5VMg-HAp

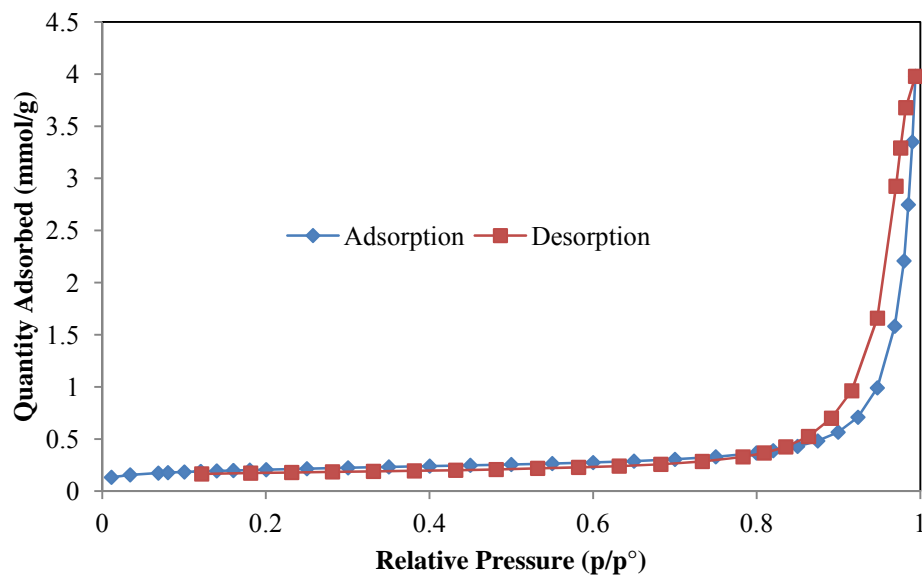


Figure 3.5 Nitrogen adsorption-desorption isotherms of 2.5VBa-HAp

Table 3.1 BET surface area, pore volume, pore size, pore width, crystallite size, crystallinity and elemental analysis of V₂O₅ supported on hydroxyapatites

Catalyst	M/P ¹	M/V ¹	M/P ²	M/V ²	Surface Area (m ² /g)	Pore Volume (cm ³ /g)	Average Pore Size(Å)	Average Pore	Crystallite Size ³	Crystallinity ⁴ (%)
2.5VSr- HAp	1.65	0.034	1.65	0.033	51.9	0.098	1046	469	3.13	0.18
2.5VMg- HAp	1.63	0.029	1.63	0.030	51.0	0.101	369	583	3.25	0.29
2.5VBa- HAp	1.63	0.031	1.63	0.030	36.3	0.031	202	619	3.16	0.34
10VSr- HAp	1.65	0.133	1.65	0.134	10.2	0.044	173	623	5.19	0.71
10VMg- HAp	1.63	0.131	1.63	0.130	11.8	0.063	344	881	5.98	0.81
10VBa -HAp	1.63	0.130	1.63	0.130	9.6	0.019	143	941	6.12	0.79

¹ICP-OES, ²EDX, ³Calculated by Scherer's equation and ⁴X_c = 1 - (V_{112/300} / I₃₀₀), where X_c is degree of crystallinity V_{112/300} is the intensity of the shoulder between (112) and (300) diffraction peaks and I₃₀₀ is the intensity of the (300) peak [29].

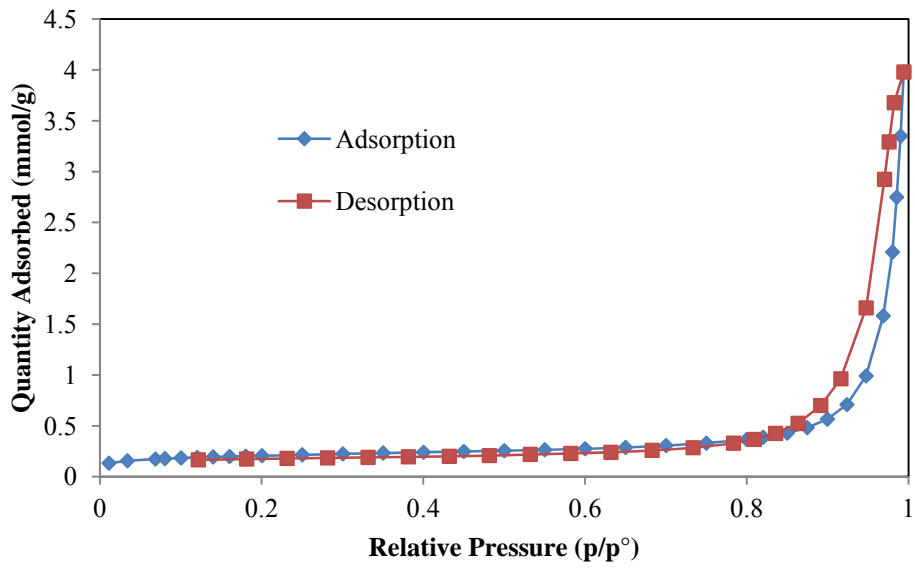


Figure 3.6 Nitrogen adsorption-desorption isotherms of 10VCa-HAp

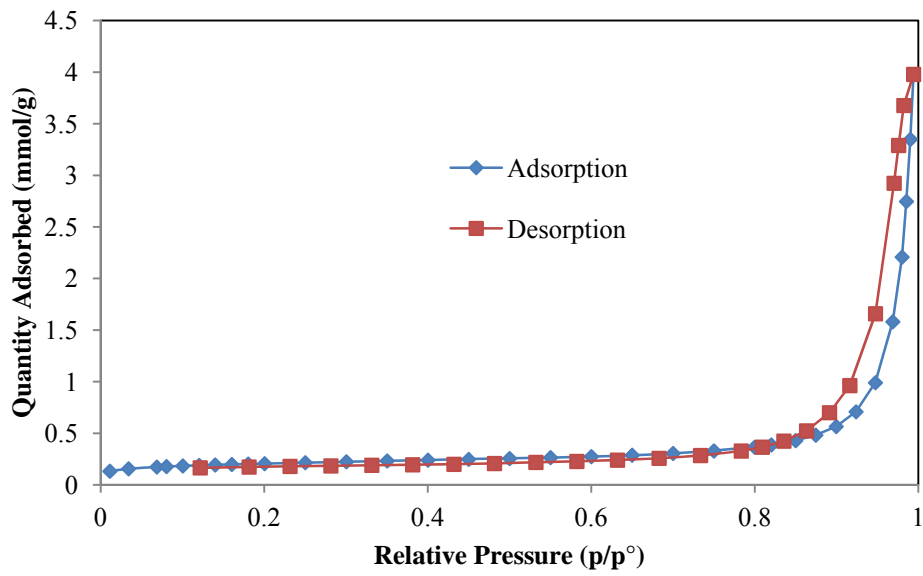


Figure 3.7 Nitrogen adsorption-desorption isotherms of 10VSr-HAp

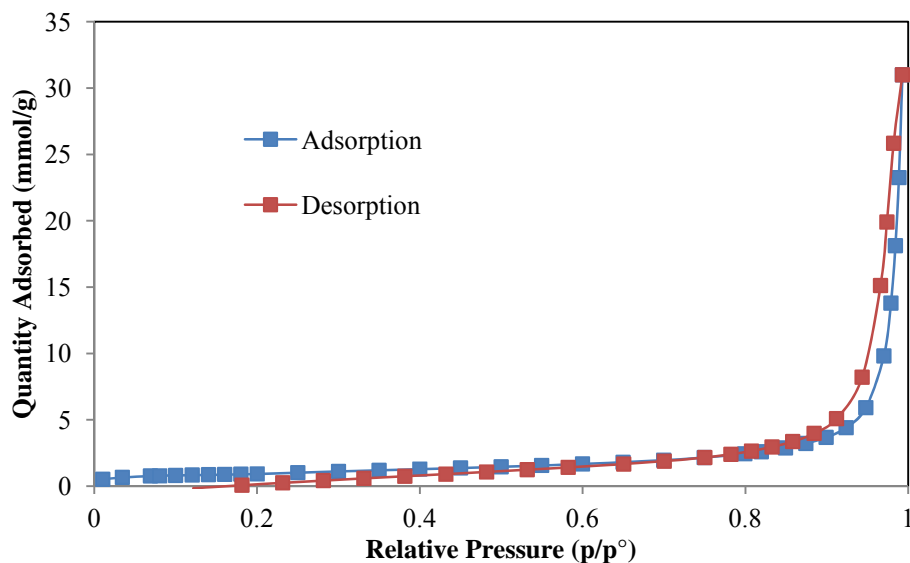


Figure 3.8 Nitrogen adsorption-desorption isotherms of 10VMg-HAp

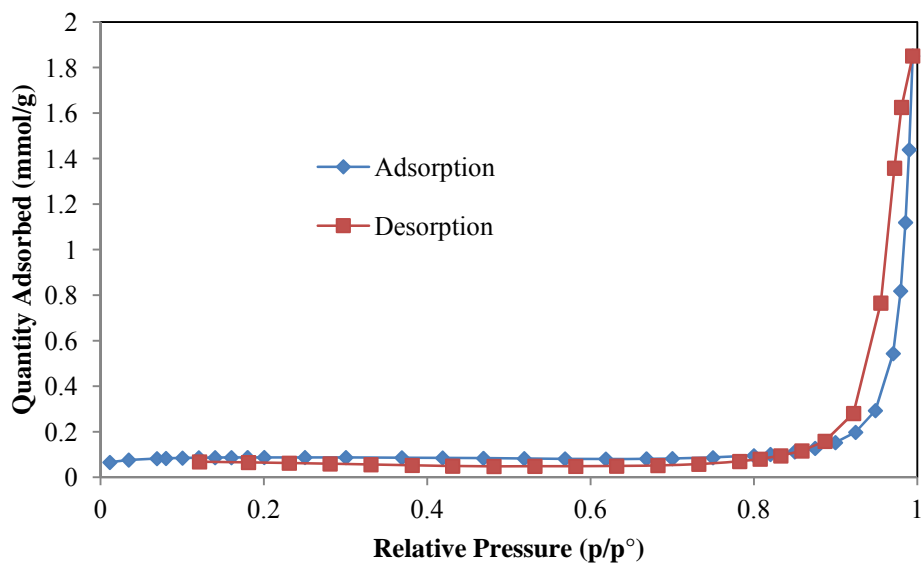


Figure 3.9 Nitrogen adsorption-desorption isotherms of 10VMg-HAp

All the catalysts display the characteristic hysteresis loop of a Type IV isotherm (IUPAC) lying in the p/p° range of 0.6-0.85, demonstrating mesoporous character [37]. All isotherms also show a step increase at a certain relative pressure to the specific pore size in the sample (Table 3.1). An inflection observed between the p/p° range of 0.85-0.95 may be attributed to the macropores

caused by particle-particle porosity, demonstrating that all catalysts have highly ordered regular pore structures. The catalysts also exhibit a step increase at this relative pressure range due to the filling of interparticle macropores of the catalyst with the nitrogen [38]. The desorption isotherms support data obtained from nitrogen physisorption that the samples have uniform pore size distribution (Fig. 3.10 and Fig. 3.11). The isotherms and pore size distributions remained substantially the same over the range of vanadium concentration which means that the vanadium-containing species did not clog the pore structure but was incorporated into the framework of hydroxyapatites [39]. Also, the incorporation of vanadium enlarges the pore width of the catalyst because the V–O bond length is greater than that of M–O (M= Ca²⁺, Sr²⁺, Mg²⁺, Ba²⁺). The sharp step observed for the isotherms becomes smaller when the source vanadium concentration increases in the original synthesis mixture and the pore width distribution peak becomes broader.

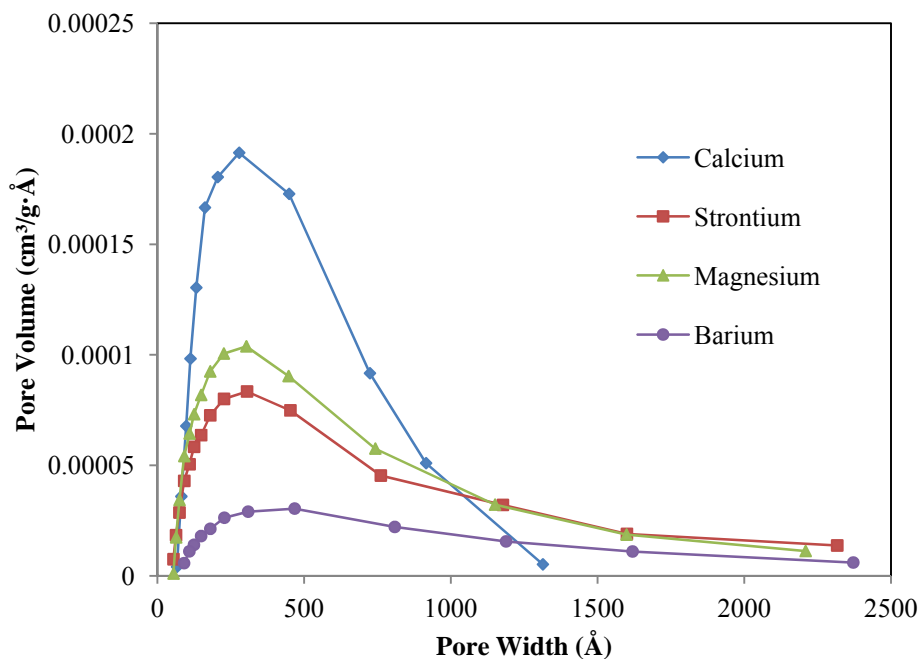


Figure 3.10 Pore width distributions of 2.5 wt% V₂O₅ supported on hydroxyapatites

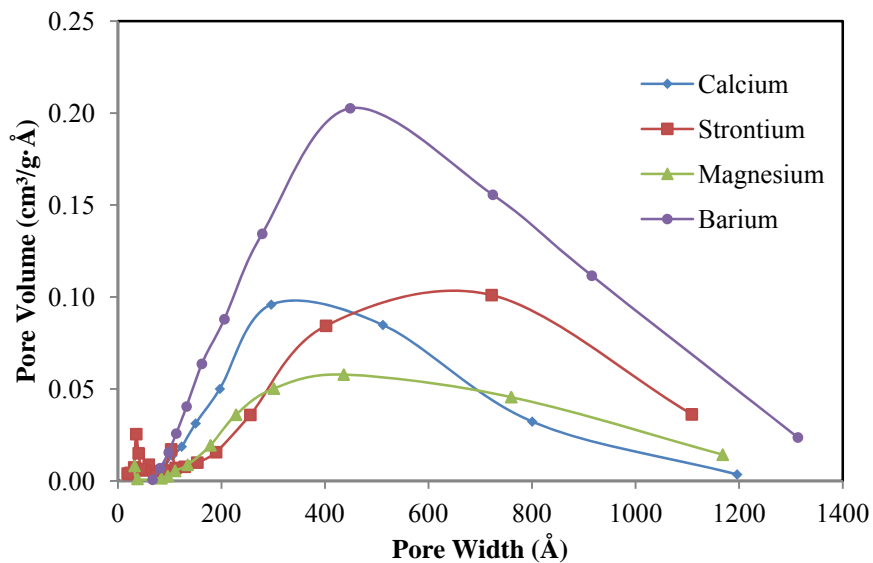


Figure 3.11 Pore width distributions of 10 wt% V_2O_5 supported on hydroxyapatites

3.3.1.4 Powder X-ray diffraction

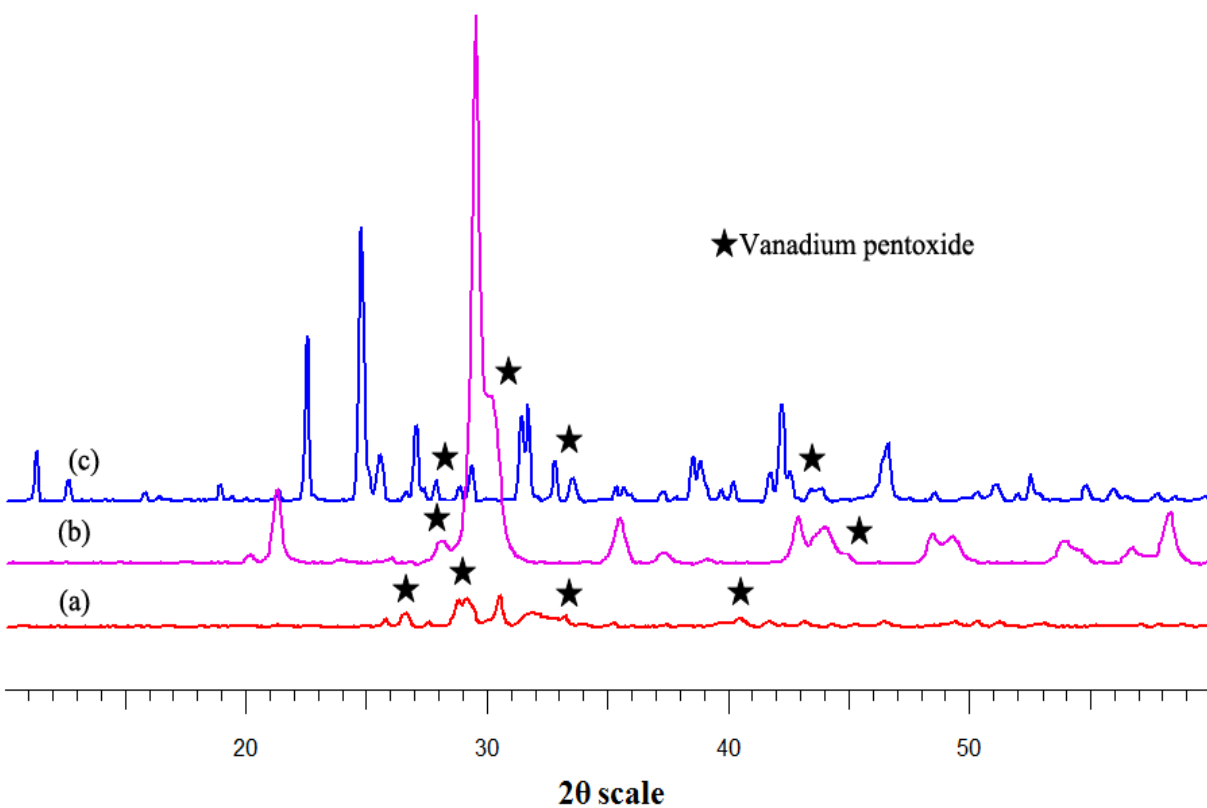


Figure 3.12 XRD diffractograms of 2.5 wt% V_2O_5 supported on strontium (a), magnesium (b) and barium (c) hydroxyapatites

From the powder diffraction pattern for the catalysts taken at room temperature, the d spacing values correlate with the JCPDS File Nos 33-138, 36-0272, 13-0404 and 9-387 for the strontium, barium and magnesium hydroxyapatites and vanadium pentoxide structures respectively (Fig. 3.12). As the vanadium pentoxide loading increases, the crystallite size decreases (Table 1), but the crystallinity [29] of the catalysts increases. For the 10 wt% V_2O_5 loaded hydroxyapatites, the additional phase of pyrovanadate (VO_4) is evident (Fig. 3.13) and correlates with the JCPDS File No. 25-1103.

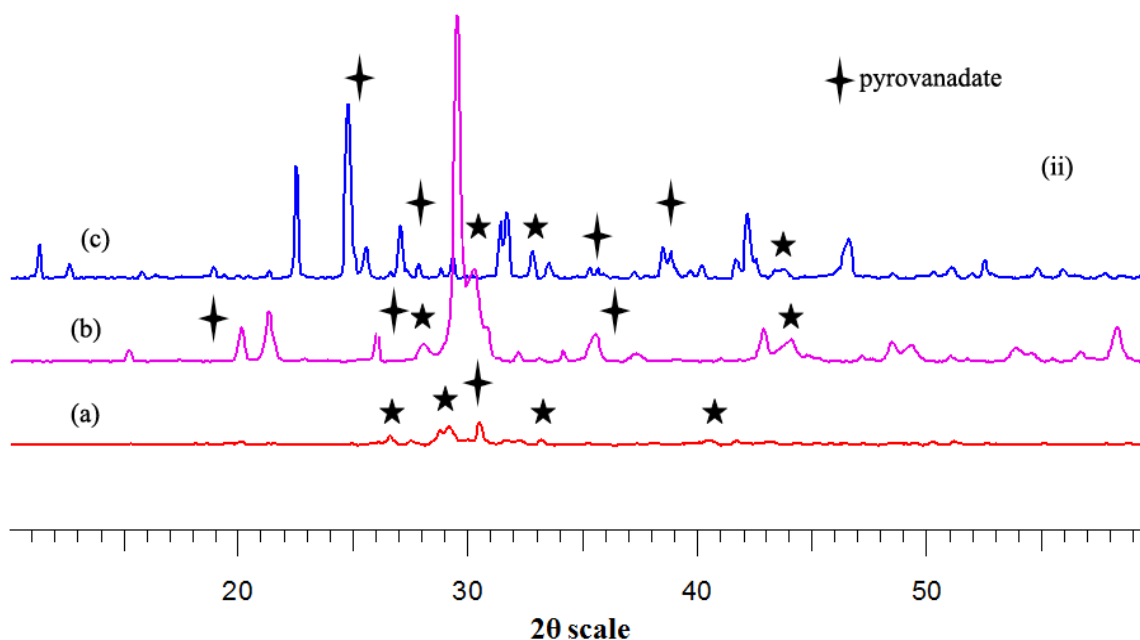


Figure 3.13 XRD diffractograms of 10 wt% V_2O_5 supported on strontium (a), magnesium (b) and barium (c) hydroxyapatites

3.3.1.5 Temperature Programmed Reduction

From the TPR profiles for V_2O_5 supported on hydroxyapatite catalysts, a shoulder and a peak appear between 600 and 700 °C (Fig. 3.14 and Fig. 3.15). The TPR of the un loaded hydroxyapatites did not show any peaks, indicating that all observed peaks are due to the reduction of vanadium [26]. According to Bond and co-workers [40, 41] the first peak can be attributed to the VO_x monolayer species which are more reducible than pure V_2O_5 . The shoulder detected is probably associated with small crystallites of V_2O_5 . This is probably due to the samples being prepared by the wet impregnation technique. It is generally accepted that monomeric vanadates and polyvanadates chains are formed at low vanadia loading [42, 43]. When the concentration increases, polyvanadate chains condense to form surface vanadia

monolayers and finally crystalline V_2O_5 appears for concentrations above the monolayer capacity. From TPR analysis, hydroxyapatite is not reduced at the temperatures employed, whereas for the vanadium pentoxide supported catalysts, reduction occurs in the 600 - 850 °C range (Fig. 3.14 and Fig. 3.15). According to the Blasco and López Nieto [10], the reduction peaks that appear at the higher temperatures correspond with the reduction of V^{5+} species belonging to the bulk structure of V_2O_5 . The TPR profile shows single peaks for the low vanadium loadings indicating that the vanadium exists in a single phase, but these peaks become wider and shift progressively to higher temperatures as the vanadium loading increases (Table 3.2). Thus, the variations are due to the low vanadium content, where most of the vanadium atoms interact with the support surface, but as the vanadium increases, a higher proportion of surface vanadium atoms interact with internal vanadium layers, increasing the bond strength of the vanadyl group, eventually approaching that of pure V_2O_5 . Thus this variation leads to the higher heterogeneity of the vanadium centers, which causes the widening of the reduction peak [44].

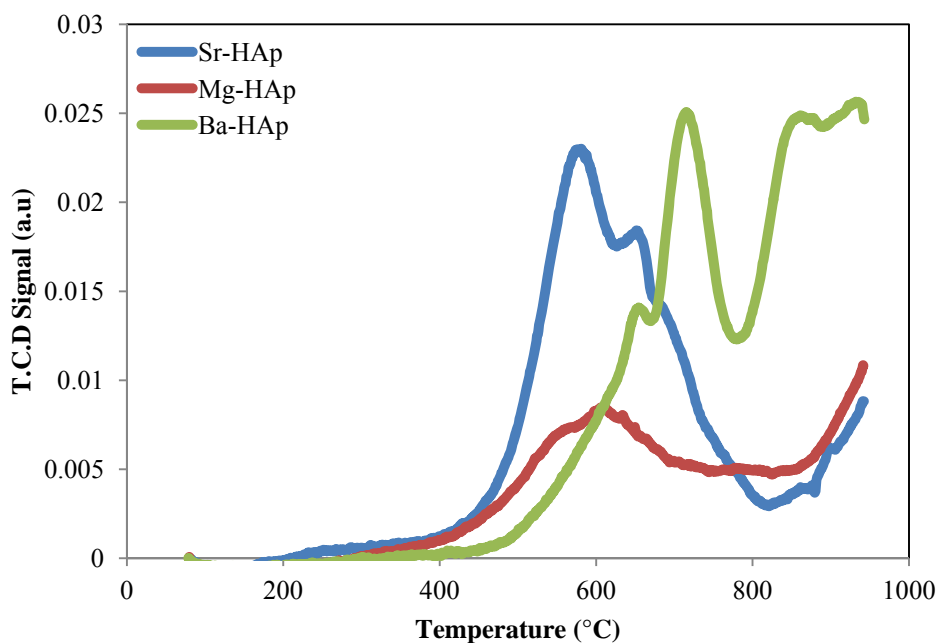


Figure 3.14 TPR profile of 2.5 wt% V_2O_5 supported on hydroxyapatites

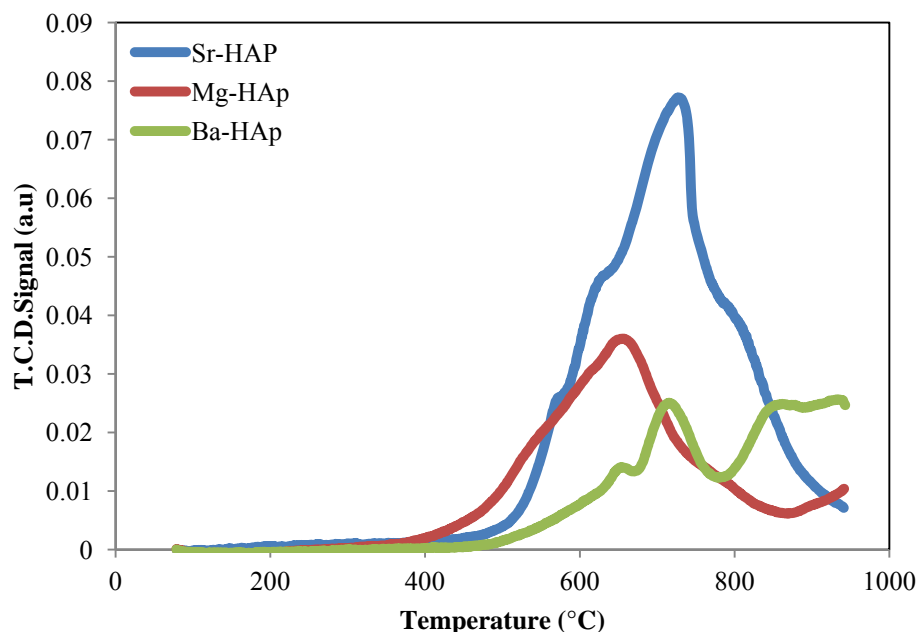


Figure 3.15 TPR profile of 10 wt% V_2O_5 supported on hydroxyapatites

The hydrogen consumption and the corresponding oxidation states of the vanadium indicate that vanadium was predominantly reduced to V^{4+} and further reduction to V^{3+} also occurred (Table 2). XRD investigations on these catalysts after the reduction showed that vanadium is reduced to the V_2O_4 (V^{4+}) and V_2O_3 (V^{3+}) phases. The d spacings correlate with data found in JCPDS File No. 25-1003 for V_2O_4 and JCPDS File No. 26-278 for V_2O_3 respectively. For the lower vanadium loadings, the first peak between 500-600 °C is probably due to reduction of the vanadium in slightly different environments as indicated by the hydrogen consumption and average oxidation state. The second peak, between 600-750 °C, is presumably for a further reduction step of vanadium (V^{5+} to V^{4+}) (Table 3.2). For the 10 wt% loaded hydroxyapatite catalysts, there are small shoulders present indicating that the vanadium exists in two phases (i.e vanadium pentoxide and pyrovanadate), most likely including the pyrovanadate phase which is more reducible than V_2O_5 . The reduction peak for pyrovanadate appears between 750-775 °C and the reduction of the oxygen species in these distorted VO_4 units, compared to the V_2O_5 , is relatively easy [45]. The shoulder at around 800-850 °C shows reduction to V^{3+} (Table 3.2). The shifts of the peak temperatures for the lower vanadium loadings indicate that the reduction of the corresponding oxygen species is more difficult in 10VCa-HAp, 10VSr-HAp, 10VMg-HAp and 10VBa-HAp [33].

Table 3.2 TPR data of vanadium supported on hydroxyapatites

Catalyst	Peak Temperature (°C)	Mol. of Hydrogen consumed (cm³/g)	Average Oxidation state of vanadium	Degree of Reducibility (%)
2.5VSr-HAp	584	2.4	4.1	49.8
	657	1.9	3.2	41.9
2.5VMg-HAp	531	1.5	4.2	36.2
	640	2.1	3.4	40.2
2.5VBa-HAp	661	0.9	4.7	14.3
	720	3.1	3.2	68.9
10VSr-HAp	634	1.9	4.6	7.7
	716	2.2	3.5	63.9
	742	0.2	3.4	8.1
	791	0.2	3.3	4.5
10VMg-HAp	664	3.9	3.9	62.5
	761	1.2	3.4	16.3
10VBa-HAp	659	0.9	4.1	19.2
	725	2.9	3.2	58.2
	849	0.5	3.0	9.8

3.3.1.6 Temperature Programmed Desorption

Weak, strong and some moderate acidic sites are attributed to the three peaks present in the TPD profile of the loaded HAp catalysts (Table 3.3), at 350 to 450 °C weak acidic sites, at 450 to 550 °C moderate acidic sites and above 650 °C strong acidic sites [46, 47]. The TPD studies reveal the existence of both Lewis and Brønsted acidic sites. Below the monolayer coverage for the lower loadings, Lewis acidity is due to the main group metal ions not covered with vanadia, whereas at high loadings, the acidity is attributed to the unsaturated vanadyl groups. With regards to Brønsted acidity, the V-OH species of the adsorbed V-oxide and the V-OH species of precipitated V₂O₅ were responsible for this acidity. TPD results showed that NH₃ desorbed from Lewis acid sites when heated at 440 °C and from Brønsted acid sites of adsorbed V-oxide at 670 °C (Table 3.3). At higher loadings of vanadium, Lewis acidity of the catalyst diminishes due to coverage with precipitated V₂O₅, whereas Brønsted acidity of these precipitates was not affected. The acidic sites on the catalysts increase as the loading of vanadium pentoxide increases. At high loading mainly strong acidic sites result because of the covering of the acidic pores on the surface of HAp with the vanadium pentoxide (Table 3.3). Strong acidic sites are seen to dominate in all catalysts. Fig. 3.16 and Fig. 3.17 show the acidic site distribution on the catalysts. Strong acidic sites are seen to dominate in all catalysts.

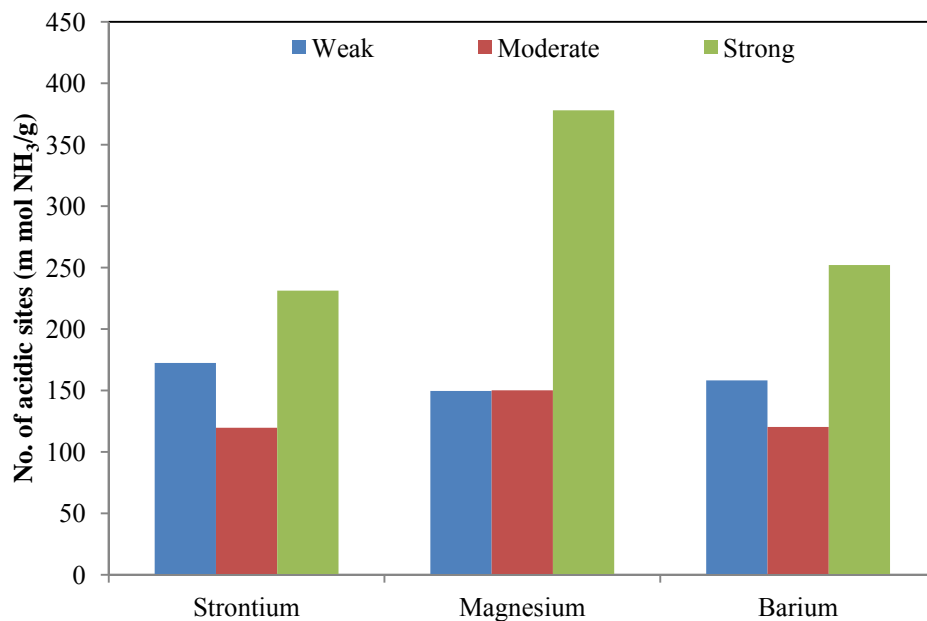


Figure 3.16 Acidic sites distribution on 2.5 wt%V₂O₅ loaded hydroxyapatites

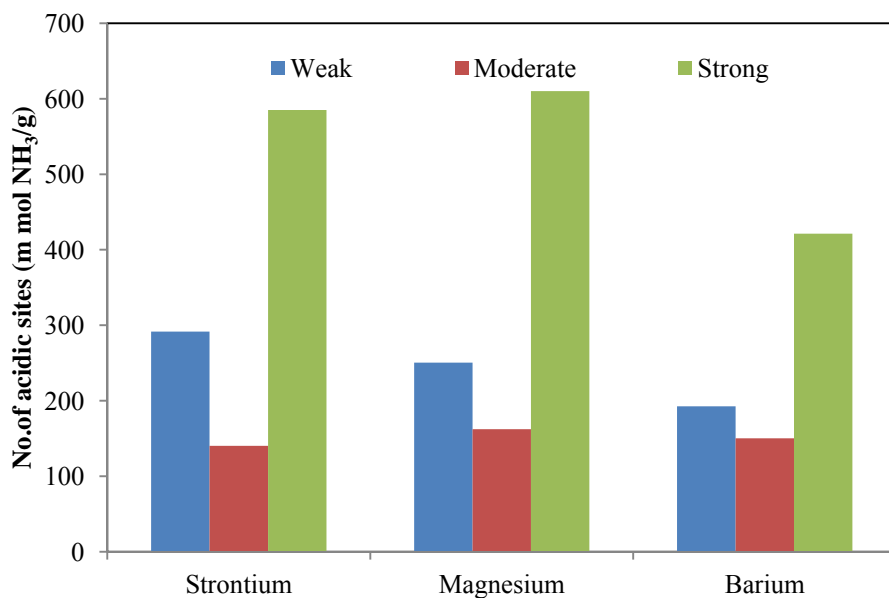


Figure 3.17 Acidic sites distribution on 10 wt%V₂O₅ loaded hydroxyapatites

Table 3.3 TPD data of vanadium supported on hydroxyapatites

Catalyst	No. of Acidic Sites (mmol. NH ₃ /g)			Total Acidic Sites (mmol. NH ₃ /g)	Specific Acidity (mmol.m ⁻²)
	Weak	Moderate	Strong		
2.5VSr-HAp	172	119	231	522	10.1
2.5VMg-HAp	149	150	378	677	13.3
2.5VBa-HAp	158	120	252	530	14.6
10VSr-HAp	291	140	585	1017	100.2
10VMg-HAp	250	162	610	1022	87.0
10VBa-HAp	182	150	421	754	79.9

3.3.1.7 Scanning and Transmission Electron Microscopy

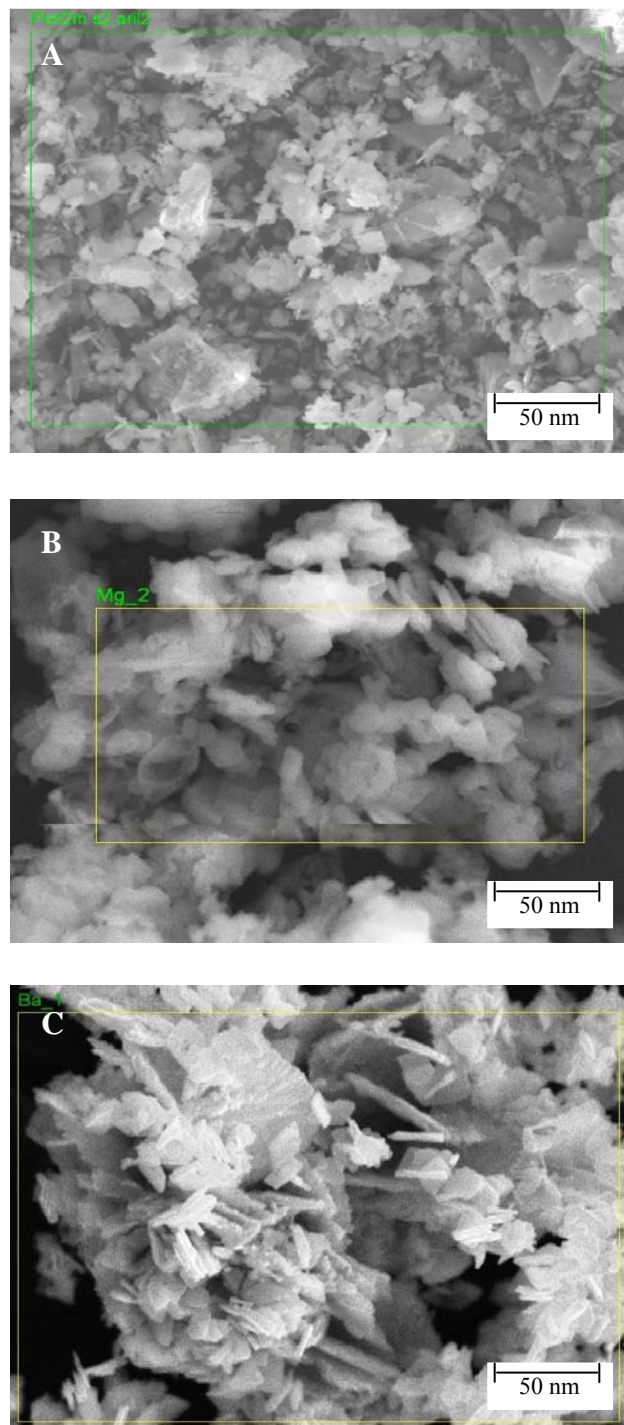


Figure 3.18 SEM images of 2.5 wt% V_2O_5 supported on strontium (a), magnesium (b) and barium (c) hydroxyapatites

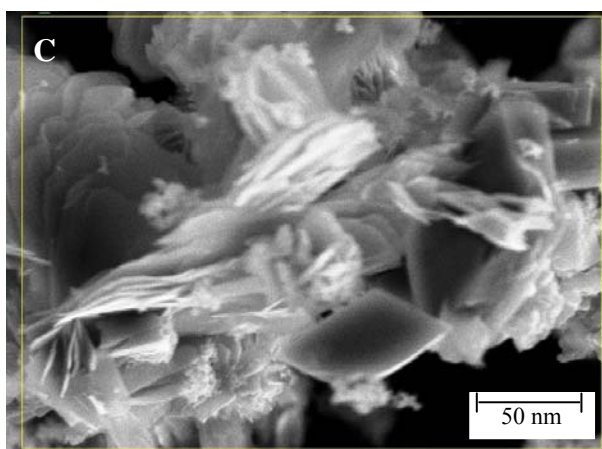
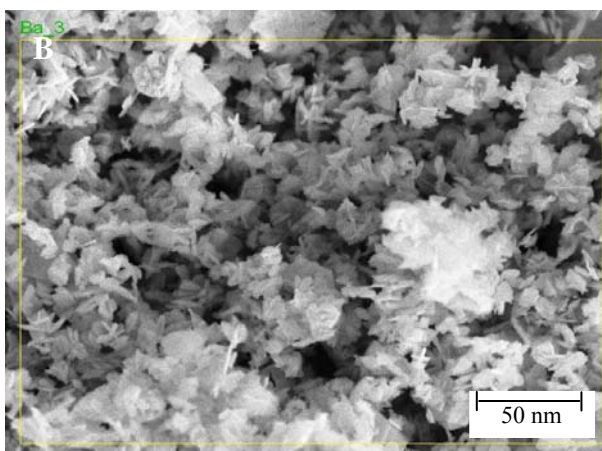
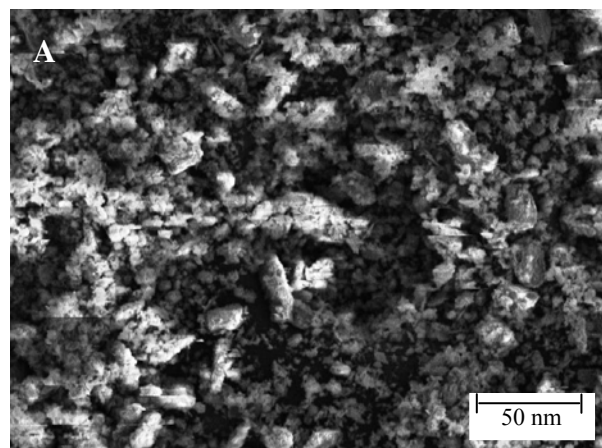


Figure 3.19 SEM images of 10 wt% V₂O₅ supported on strontium (a), magnesium (b) and barium (c) hydroxyapatites

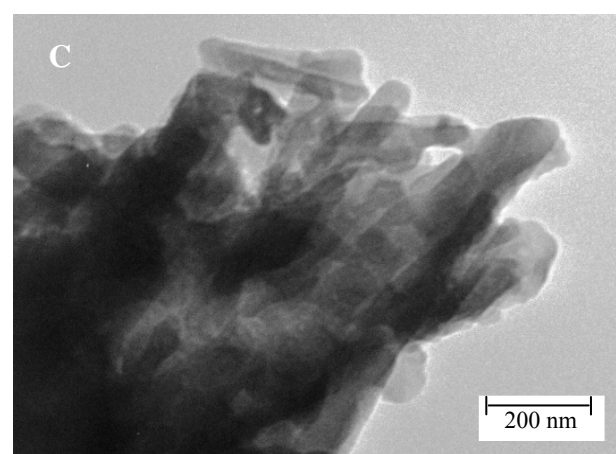
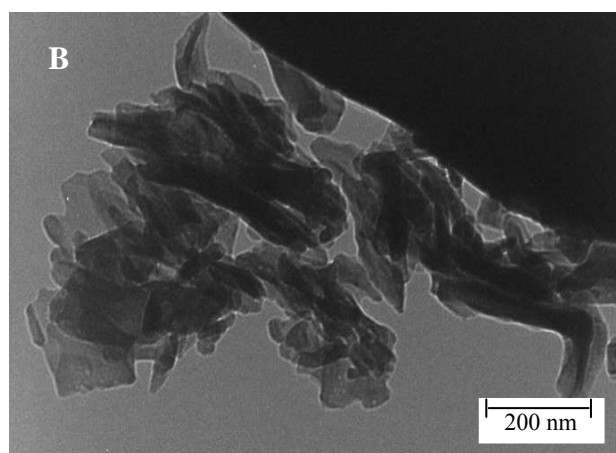
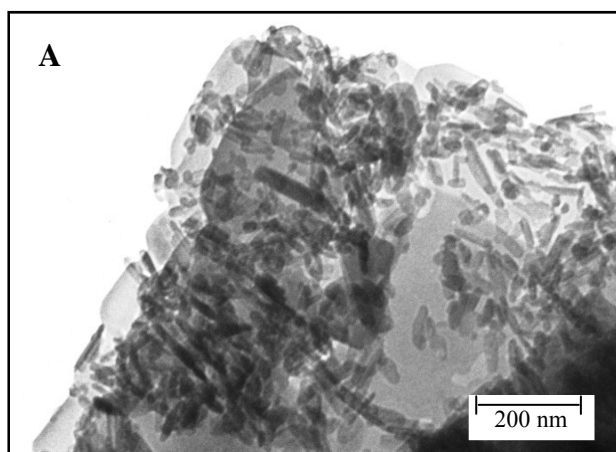


Figure 3.20 TEM images of 2.5 wt% V_2O_5 supported on strontium (a), magnesium (b) and barium (c) hydroxyapatites

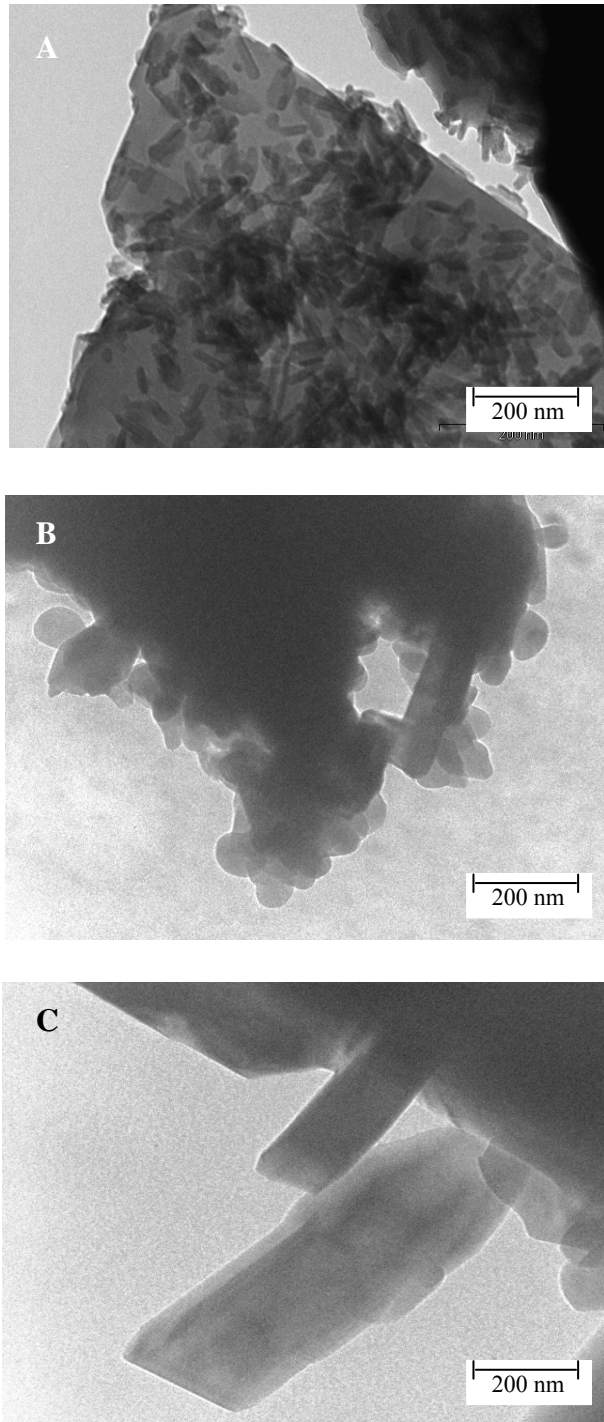


Figure 3.21 TEM images of 10 wt% V₂O₅ supported on strontium (a), magnesium (b) and barium (c) hydroxyapatites

Fig. 3.18 and Fig. 3.19 show the scanning electron micrographs of the 2.5 and 10 wt% V₂O₅ supported on hydroxyapatites. Agglomeration of the particles is more evident in 10 wt% V₂O₅

compared to the 2.5 wt% V₂O₅, and is probably due to the increase in the vanadium loading [48]. Irregular plate-like shapes are also observed for catalysts with higher loadings. The M/P and M/V ratios obtained from EDX agrees with data from ICP elemental analysis. SEM-EDX micrographs showed that vanadium is uniformly distributed on the surface of the hydroxyapatites. From TEM images, (Figs. 3.20 and 3.21), all the catalysts display crystalline rod-like particles with a particle size ranging from 200-260 nm.

3.3.2 Catalytic activity

All the catalysts were tested in a temperature range of 350-550 °C, GHSV of 4000 h⁻¹ and varying *n*-octane to oxygen molar ratios. Blank reactions were conducted under the same reaction conditions in order to obtain the effect of the catalysts on the reaction. The conversion of *n*-octane in a blank reaction is in the range of 2.5-7.1 %. Figures 3.22 and 3.23 shows the effect of temperature on the *n*-octane conversion at an *n*-octane to oxygen molar ratio of 1:2. All the catalysts showed an increase in the conversion with increase in temperature. 10 wt % V₂O₅ supported on hydroxyapatites showed high conversion relative to 2.5 wt % V₂O₅ supported on hydroxyapatite catalysts.

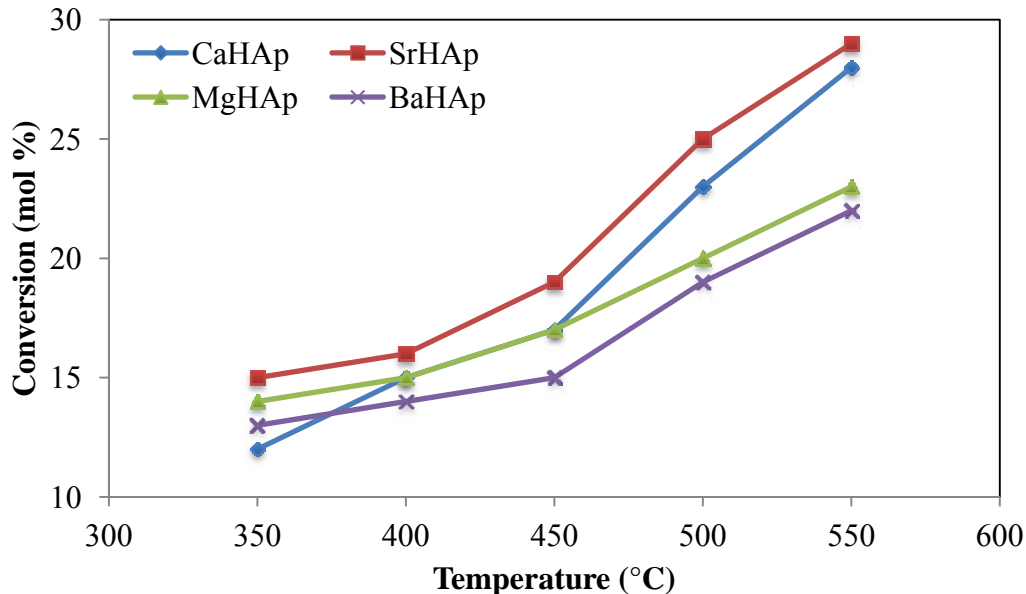


Figure 3.22 Effect of temperature on the conversion of *n*-octane over 2.5 V₂O₅ wt% supported on hydroxyapatites at *n*-octane to oxygen molar ratio of 1:1 (GHSV = 4000 h⁻¹)

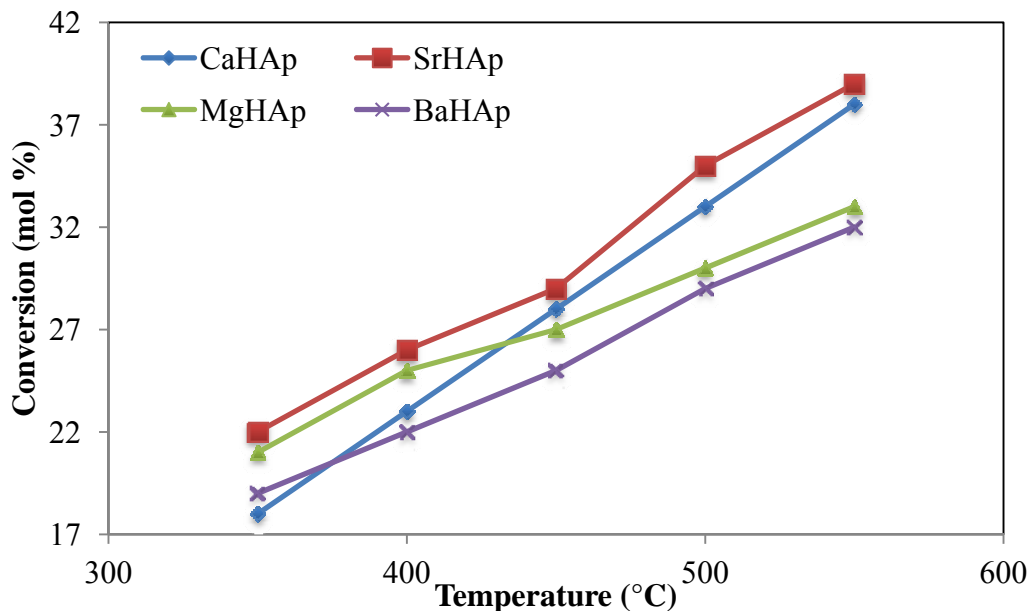


Figure 3.23 Effect of temperature on the conversion of *n*-octane over 10 V₂O₅ wt% supported on hydroxyapatites at *n*-octane to oxygen molar ratio of 1:1 (GHSV = 4000 h⁻¹)

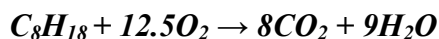
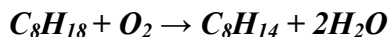
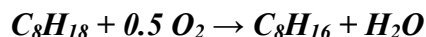
The activity of the vanadium containing catalysts is usually affected by the reducibility of the oxygen species present in the catalyst, with higher catalytic activity achieved on catalysts with greater reducibility of the oxygen species [49, 50]. This is observed for the catalytic activity of the 10 wt % V₂O₅ loaded on hydroxyapatite catalysts and the order of catalytic activity (e.g. at a 450 °C and an *n*-octane to oxygen molar ratio of 1:2) is as follows:

$$\text{Sr-HAp (31\%)} > \text{Mg-HAp (26\%)} > \text{Ba-HAp (23\%)} > \text{Ca-HAp (19\%)}$$

The activity of the catalysts can also be explained by the differences in the nature of the active (acidic and basic) sites [51]. The order of the catalytic activity for 10 wt % V₂O₅ supported on hydroxyapatites is in correlation with the number of acidic sites present on the surface of the catalysts (Table 3). A range of octenes, aromatics, cracked products and carbon oxides (CO_x) were present in the product stream. Octenes were the major products for all the catalysts. Cracked products included mainly butane, propane and ethane, whereas oxygenates included C₈ compounds such as octanal, octanol, 2-octanone and 2-octanol together with lower oxygenates, which included acetone, acetic acid, butanol and propanol.

3.3.2.1 Influence of *n*-octane to oxygen molar ratios

The selectivity pattern of products was dependent on the *n*-octane to oxygen molar ratios and the oxygen requirements to several products are shown by the equations below.



In the absence of oxygen, i.e. the feed consisting of *n*-octane in nitrogen only octenes show the highest selectivity, whereas at the *n*-octane to oxygen ratio of 1:2, selectivity to octenes was relatively low and CO_x showed the highest selectivity. For mild oxidative environments, i.e. *n*-octane to oxygen molar ratios of 1:0.5 and 1:1, high selectivities to octenes and low selectivity towards CO_x were achieved.

3.3.2.2 Unsupported hydroxyapatites

Hydroxyapatites alone i.e. unsupported hydroxyapatites showed very low conversion relative to the vanadium supported hydroxyapatites. Unsupported Sr-HAp showed the highest conversion of 13% among the other unsupported hydroxyapatites. The lowest conversion of 8% was shown by unsupported Ca-HAp. In the product profile of unsupported hydroxyapatites, CO_x is the major product. The oxidative environment didn't show much affect on the selectivities of the products when unsupported hydroxyapatites were used as catalysts.

3.3.2.3 2.5 wt% V₂O₅ supported on hydroxyapatites

Dehydrogenation (in the absence of oxygen)

In dehydrogenation studies, at a temperature of 450 °C all the catalyst showed a life time of 8 hours. After 8 hours, due to coking on the surface of the catalyst, the catalyst lost its activity and the conversion of *n*-octane decreased. In the absence of oxygen all the catalysts showed less than 1% selectivity towards CO_x. The moles of CO_x formed are in agreement with the moles of oxygen present in the catalyst which supports the Mars-Van-Krevelen's ODH mechanism. Table

3.4 shows the selectivity of octenes from the dehydrogenation of *n*-octane using 2.5 wt% supported on hydroxyapatite catalysts. Trans-3-octene and trans-2-octene are the major products among all the octenes formed in the dehydrogenation of *n*-octane (Table 3.4). Selectivity towards the trans isomer is higher than to the cis isomer, which can be attributed to the relative thermodynamic stability of trans isomer [52].

All the catalysts exhibited lowest selectivity towards 4-octene among all the octene isomers, indicating that the *n*-octane activation at C4 is unfavorable compared to C2 and C3. The rate-determining step in alkane activation is the homolytic rupture of the C–H bond to form the surface alkyl species, which is then followed by a fast elimination of a second hydrogen from a neighbouring carbon to form the olefinic bond [53, 54].

Table 3.4 Selectivity of products in dehydrogenation of *n*-octane with 2.5 wt% V₂O₅ supported on hydroxyapatites at an iso-conversion of 24% (Temperature = 450 °C)

Octene	Calcium	Strontium	Magnesium	Barium
1-octene	18.7	13.5	20.5	19.6
trans-2-octene	18.0	19.3	20.3	18.4
cis-2-octene	14.1	11.9	10.6	11.6
trans-3-octene	22.6	23.5	22.5	18.4
cis-3-octene	6.5	8.5	7.9	6.5
trans-4-octene	10.5	9.6	10.7	9.6
cis-4-octene	0.81	0.58	0.35	0.59
1,7- octadiene	8.3	5.7	7.1	7.8
CO _x	0.52	0.83	0.93	0.95

However, the low selectivity to 4-octene suggests that, apart from the thermodynamic properties, factors such as steric effects and the number of active centers also influence the selectivity. In the activation of *n*-octane, the steric effects are likely to play a vital role as the accessibility to the active sites by such a large molecule is likely to become a limiting factor and thereby have a significant impact on the catalytic behavior [53]. Considering the alkane dehydrogenation mechanism and by inspecting the relative abundance of octene isomers, it is likely that *n*-octane activation has occurred predominantly at C2 and C3 and to a far lesser extent at C4.

Oxidative dehydrogenation

Figs. 3.24, 3.25 and 3.26 shows the product selectivity of the 2.5 wt% V₂O₅ supported on hydroxyapatites at an iso-conversion of 27 % and temperature of 450 °C with varying *n*-octane to oxygen molar ratios. In all catalysts, oxidative dehydrogenation is the main reaction resulting in octenes as the major products, with 3-octene the dominant isomer. The 2.5VSr-HAp showed highest selectivity towards octenes, especially trans-3-octene. This could be attributed to Lewis acidity (Fig. 3.16) of the Sr-HAp support which favours the formation of octenes. The Lewis acidity of the 2.5VCa-HAp is low relative to 2.5VSr-HAp, as a result 2.5VCa-HAp shows a lower selectivity towards octenes compared to 2.5VSr-HAp (Fig 3.24 and 3.26). At an *n*-octane to oxygen molar ratio of 1:0.5, all the vanadium supported on hydroxyapatite catalysts showed high selectivity towards octenes. When the *n*-octane to oxygen molar ratios were increased, selectivity towards octenes decreased for the 2.5VMg-HAp and 2.5VBa-HAp. This could be attributed to the Brønsted acidity (Fig. 3.16) of 2.5VMg-HAp and 2.5VBa-HAp which favours the adsorption of octane and the desorption of acidic products, thereby resulting in further oxidation to carbon oxides and water. Brønsted acidity favours the adsorption of octane and enhances the desorption of acidic products, thereby enhancing further oxidation to carbon oxides and water [55].

3-Octene is almost always the dominant isomer at all *n*-octane to oxygen molar ratios, whereas 4-octene showed the lowest selectivity (Figs. 3.27, 3.28 and 3.29), although there is no difference in the energies of the C-H bond at C2, C3 and C4 in the alkane chain [26, 53, 54]. The same selectivity pattern is also observed in the blank reactions. The position of activation is not affected by either the metal present in the hydroxyapatite or the *n*-octane to oxygen molar ratios.

The mechanism involved is likely similar to the dehydrogenation mechanism explained in the previous section [53].

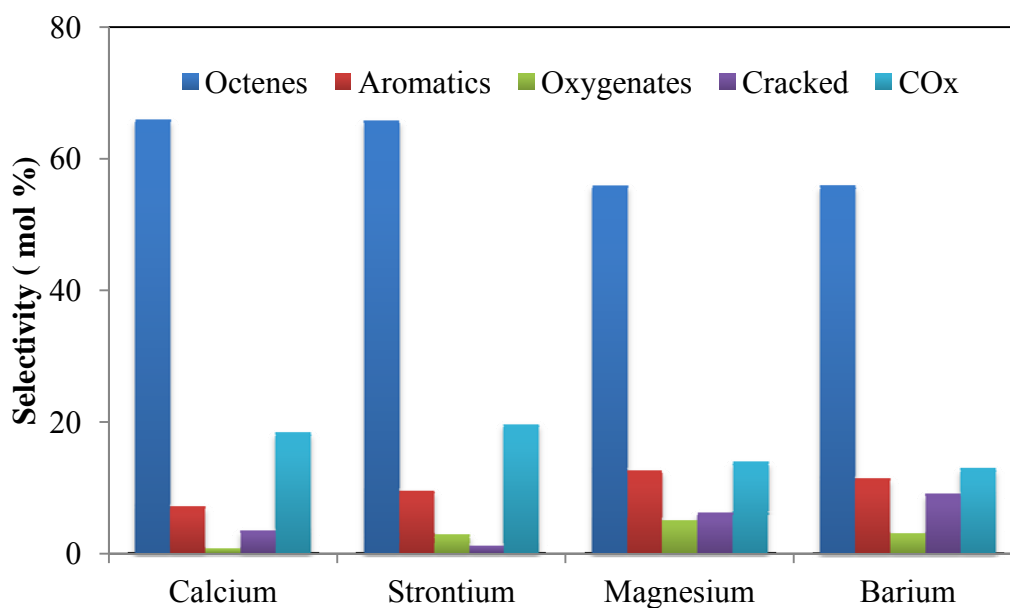


Figure 3.24 Product selectivity over 2.5 wt% V_2O_5 supported on hydroxyapatites at iso-conversion (27%), temperature = 450 °C and *n*-octane to oxygen molar ratio of 1: 0.5

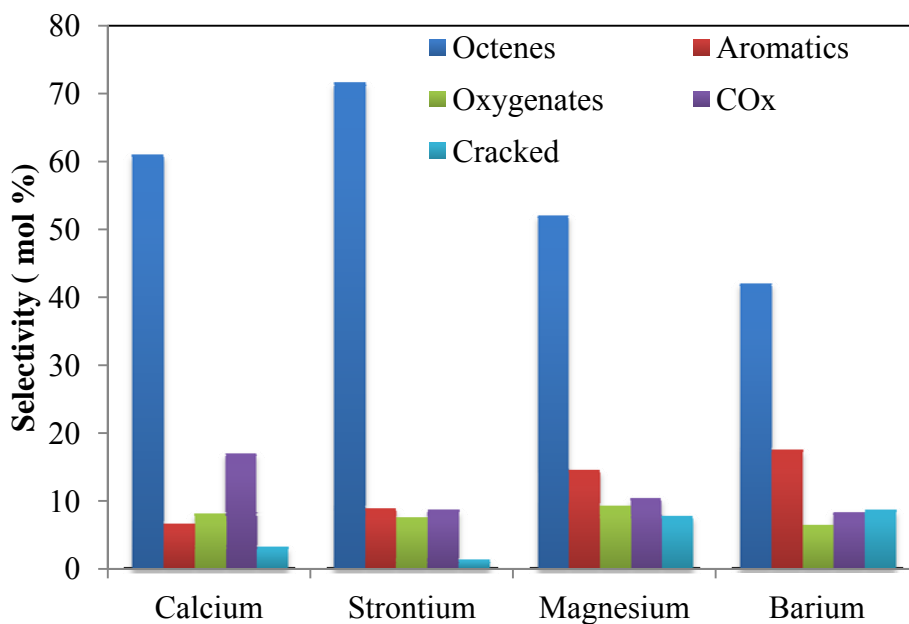


Figure 3.25 Product selectivity over 2.5 wt% V_2O_5 supported on hydroxyapatites at iso-conversion (27%), temperature = 450 °C and *n*-octane to oxygen molar ratio of 1: 1

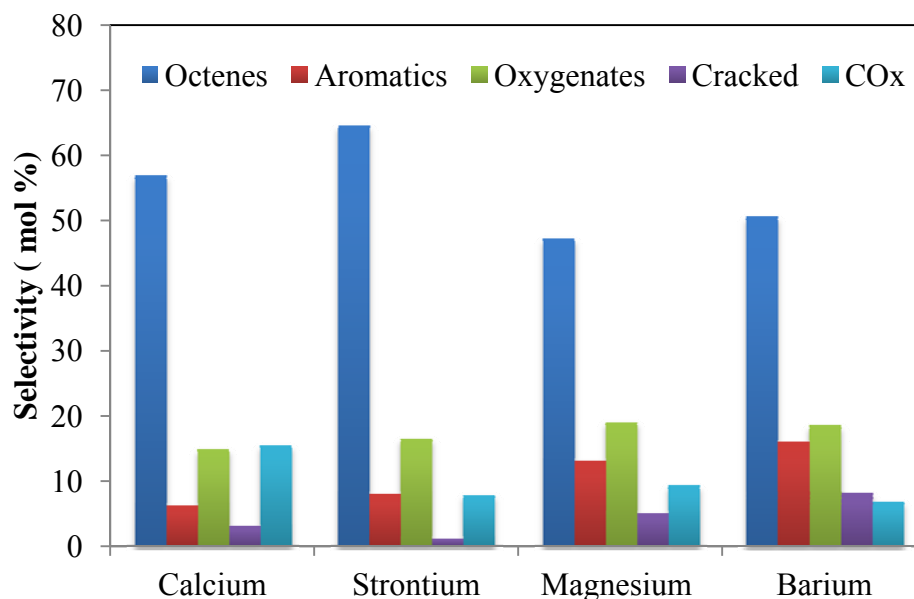


Figure 3.26 Product selectivity over 2.5 wt% V_2O_5 supported on hydroxyapatites at iso-conversion (27%), temperature = 450 °C and *n*-octane to oxygen molar ratio of 1:2

At all *n*-octane to oxygen molar ratios, 2.5VMg-HAp showed highest selectivity towards oxygenates and lowest selectivity towards octenes due to the V_2O_5 phase (Fig. 3.12) and Brønsted acidity (Table 3.3). Further, the lower selectivity towards olefins is attributed to the incorporation of the magnesium oxide into the vanadium oxide affecting the formation of V_2O_5 with V=O bonds, where V^{5+} are in octahedral co-ordination [33]. The V=O double bonds result in incorporation of oxygen in the intermediate reaction products, thus leading to the formation of oxygenate compounds [14, 56]. 2.5VBa-HAp showed highest selectivity towards the C_8 aromatics compared to carbon oxides, indicating that aromatic formation provides an energetically favourable pathway, thus lowering CO_x formation [54]. This is due to the Lewis acidity and Brønsted acidity of 2.5VBa-HAp (Table 3.3). The Brønsted acidity of the 2.5V Ba-HAp, which is lower than the acidity of 2.5VMg-HAp, favours the formation of aromatic products (Figs. 3.30, 3.31 and 3.32).

The similar acidity shown by 2.5VCa-HAp and 2.5V Sr-HAp results in significant selectivity towards aromatics only at an *n*-octane to oxygen molar ratio of 1:0.5, but this decreases slightly for the *n*-octane to oxygen molar ratio of 1:1 and 1:2 due to the secondary combustion of the ODH products [54]. 2.5VBa-HAp also showed relatively high selectivity towards cracked

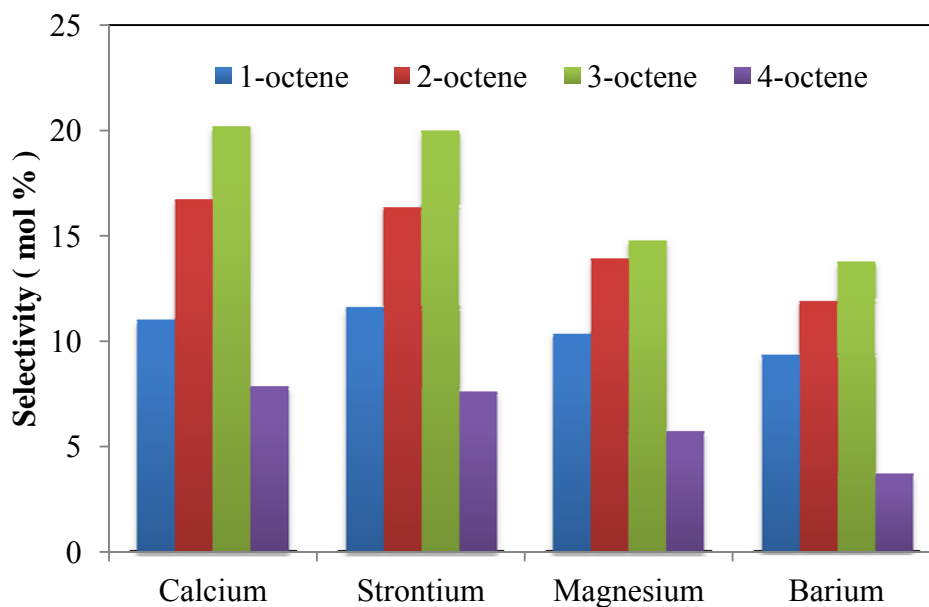


Figure 3.27 Selectivity of octenes over 2.5 wt% V₂O₅ supported on hydroxyapatites at iso-conversion (27%), temperature = 450 °C and *n*-octane to oxygen molar ratio of 1:0.5

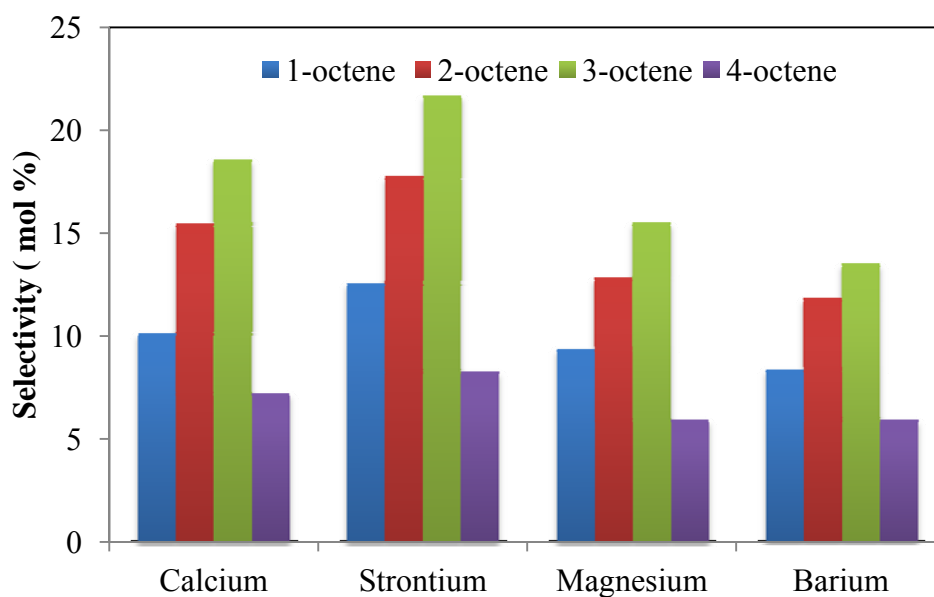


Figure 3.28 Selectivity of octenes over 2.5 wt% V₂O₅ supported on hydroxyapatites at iso-conversion (27%), temperature = 450 °C and *n*-octane to oxygen molar ratio of 1:1

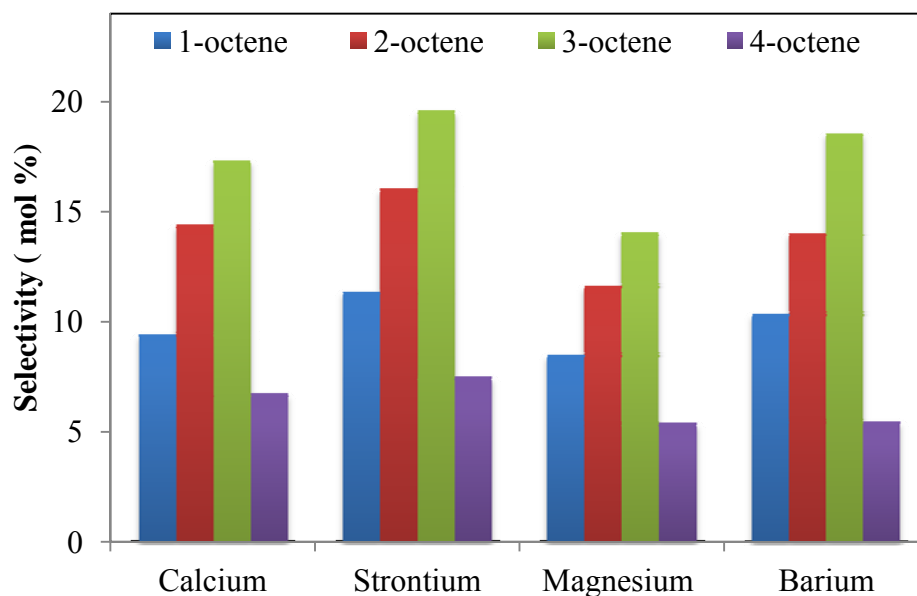


Figure 3.29 Selectivity of octenes over 2.5 wt% V_2O_5 supported on hydroxyapatites at iso-conversion (27%), temperature = 450 °C and *n*-octane to oxygen molar ratio of 1:2

products (Fig. 9) and they are favoured by high temperature rather than specific *n*-octane to oxygen molar ratios [57]. The amount of cracked products is, however, small and indicates that the oxidative reaction pathway shows similar trends as the VMgO catalysts [54]. 2.5VCa-HAP showed high selectivity towards CO_x and low selectivity towards aromatics at all *n*-octane to oxygen molar ratios (Figs. 3.24, 3.25 and 3.26), probably due to the secondary combustion of the aromatics which increases the formation of CO_x .

In the activation of *n*-octane, the cyclization to form a six-membered ring, and eventually the corresponding aromatics, could either take place through C_1 to C_6 or C_2 to C_7 bonding to give ethylbenzene (or styrene) and *o*-xylene respectively [58]. Figure 12(a) shows the percentage of 1,6- cyclization over 2.5 wt% V_2O_5 supported on hydroxyapatites. The 1,6-cyclization mode is favored for the formation of aromatics when the *n*-octane to oxygen molar ratio is 1:0.5 for all 2.5 wt% supported on hydroxyapatite catalysts and for 2.5VCa-HAP and 2.5VSr-HAP at all *n*-octane to oxygen molar ratios, this can be attributed to the selectivity to 1-octene which undergoes 1,6-cyclization in the formation of aromatics (Fig. 3.33). This is probably due to the Lewis acidity of 2.5VCa-HAP and 2.5VSr-HAP (Table 3.3). 2.5VCa-HAP and 2.5VSr-HAP

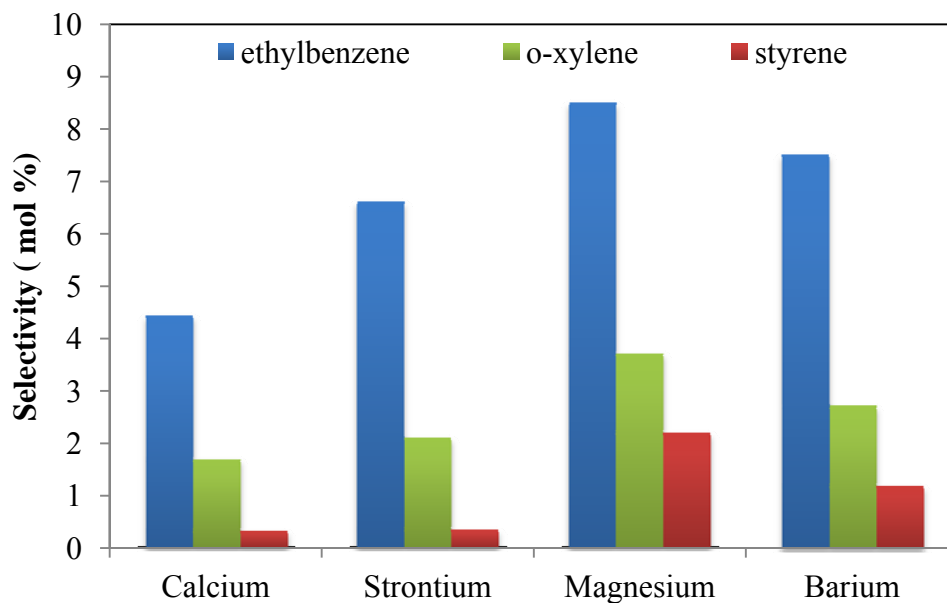


Figure 3.30 Selectivity of aromatics over 2.5 wt% V₂O₅ supported on hydroxyapatites at iso-conversion (27%), temperature = 450 °C and *n*-octane to oxygen molar ratio of 1:0.5

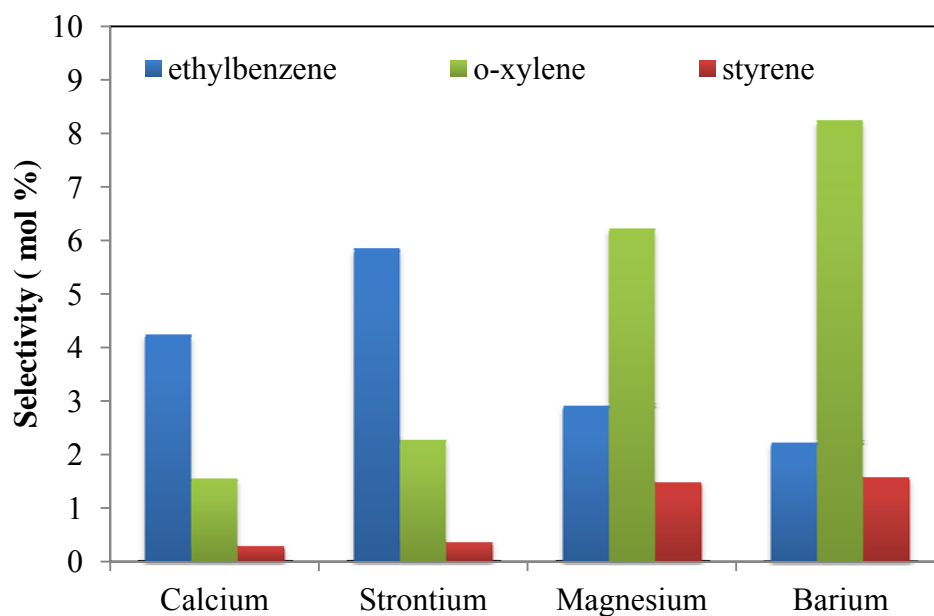


Figure 3.31 Selectivity of aromatics over 2.5 wt% V₂O₅ supported on hydroxyapatites at iso-conversion (27%), temperature = 450 °C and *n*-octane to oxygen molar ratio of 1:1

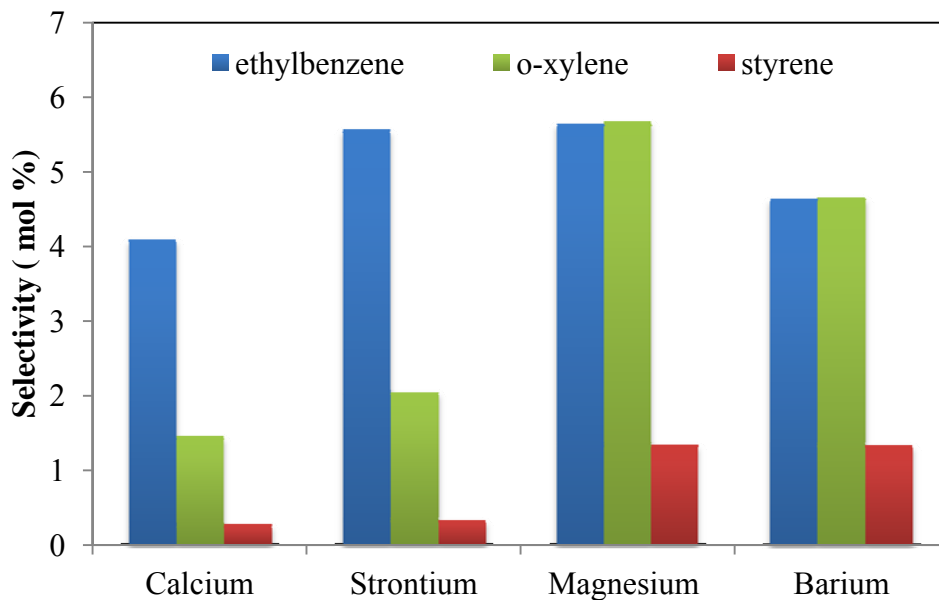


Figure 3.32 Selectivity of aromatics over 2.5 wt% V₂O₅ supported on hydroxyapatites at iso-conversion (27%), temperature = 450 °C and *n*-octane to oxygen molar ratio of 1:2

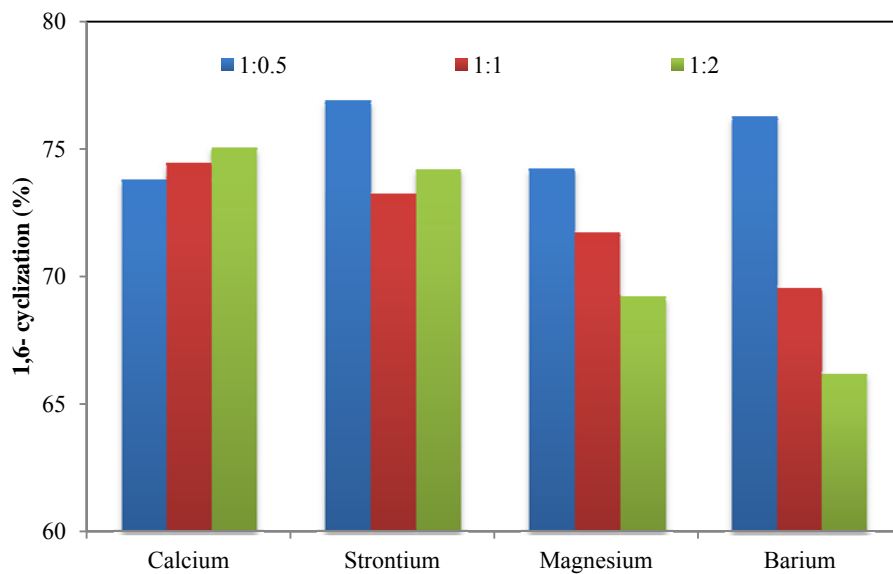


Figure 3.33 1,6-cyclisation of aromatics over 2.5 wt% V₂O₅ supported on hydroxyapatites at iso-conversion (27%), temperature = 450 °C with varying *n*-octane to oxygen molar ratios

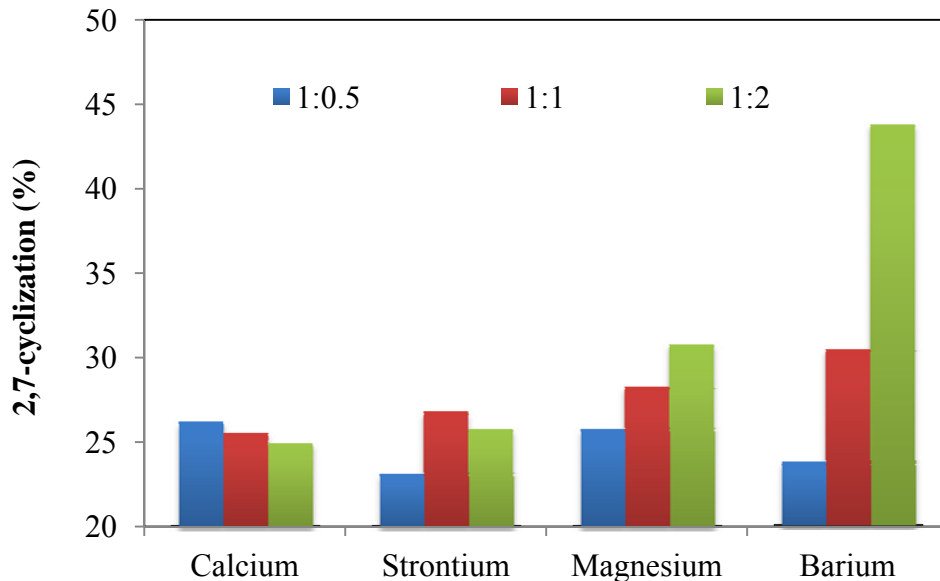


Figure 3.34 2,7-cyclisation of aromatics over 2.5 wt% V_2O_5 supported on hydroxyapatites at iso-conversion (27%), temperature = 450 °C with varying *n*-octane to oxygen molar ratios

showed more selectivity towards this 1,6-cyclization mode probably due to the number of Lewis acidic sites and moderate strength acidic sites. Figure 13(a) shows the percentage of 2,7-cyclization over 2.5 wt% V_2O_5 supported on hydroxyapatites. The 2,7-cyclization mode is favoured in the formation of aromatics at an *n*-octane to oxygen ratio of 1:2 for all 2.5 wt % V_2O_5 supported on hydroxyapatite catalysts. This can be attributed to the high selectivity of 2-octenes and 3-octenes which likely undergo 2,7-cyclization in the formation of aromatics (Fig. 3.34).

3.3.2.4 10 wt% V_2O_5 supported on Hydroxyapatites

Figures 3.35, 3.36 and 3.37 shows the product selectivity at a conversion of 27% and temperature fixed at 450 °C with varying *n*-octane to oxygen molar ratios. Over all catalysts, octenes again are the major product, i.e. dehydrogenation is the dominant reaction. The selectivity to octenes decreased with an increase in oxygen concentration due to the availability of more oxygen which enhances combustion of *n*-octane. Among all the catalysts, 10VSr-HAp showed highest selectivity towards 1-octene and aromatics at all *n*-octane to oxygen molar ratios, with 3-octene as the major product and 4-octene the minor product (Figs. 3.38, 3.39 and 3.40). This could be attributed to the Lewis acidic nature of the 10VSr-HAp catalyst (Table 3.3).

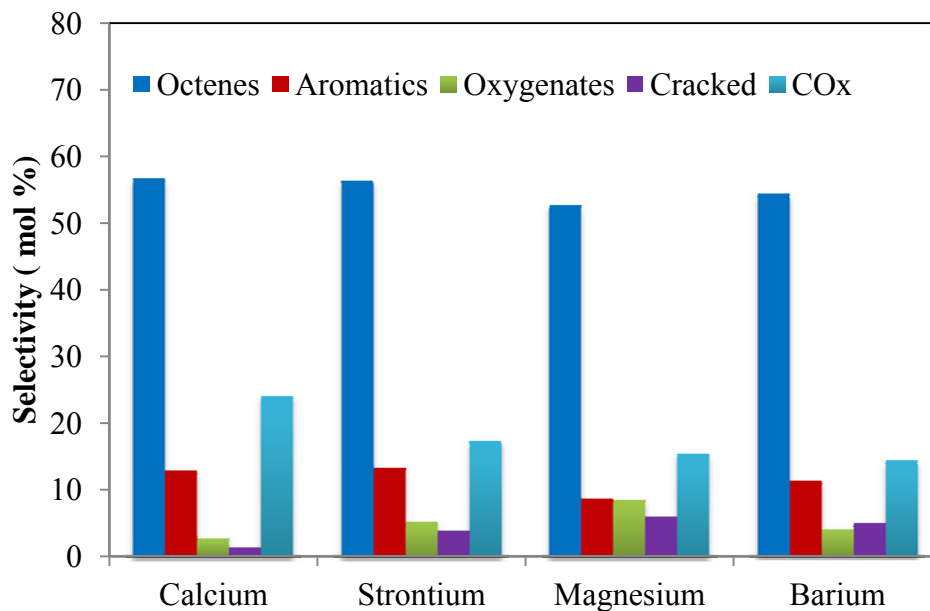


Figure 3.35 Product selectivity over 10 wt% V_2O_5 supported on hydroxyapatites at iso-conversion (27%), temperature = 450 °C and *n*-octane to oxygen molar ratio of 1: 0.5

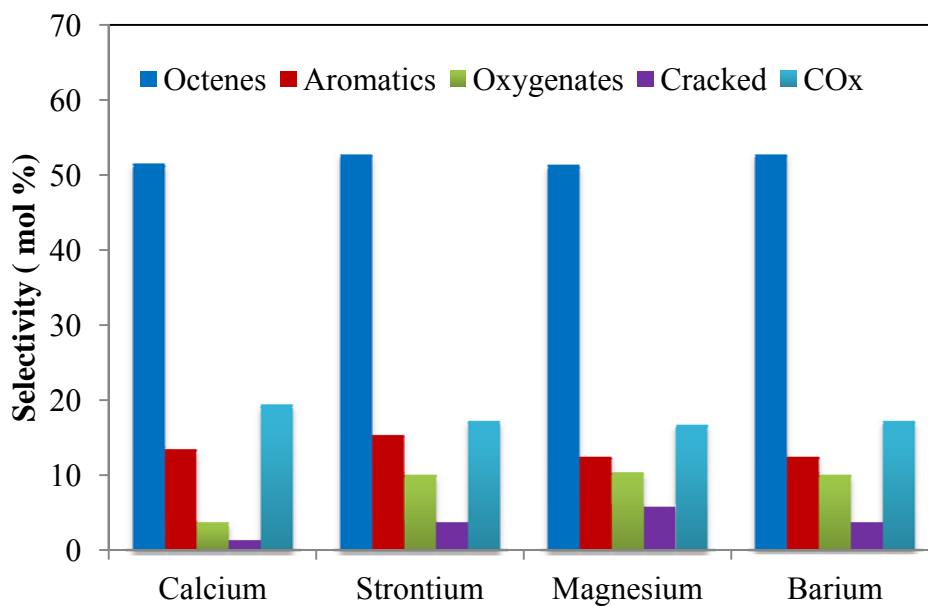


Figure 3.36 Product selectivity over 10 wt% V_2O_5 supported on hydroxyapatites at iso-conversion (27%), temperature = 450 °C and *n*-octane to oxygen molar ratio of 1:1

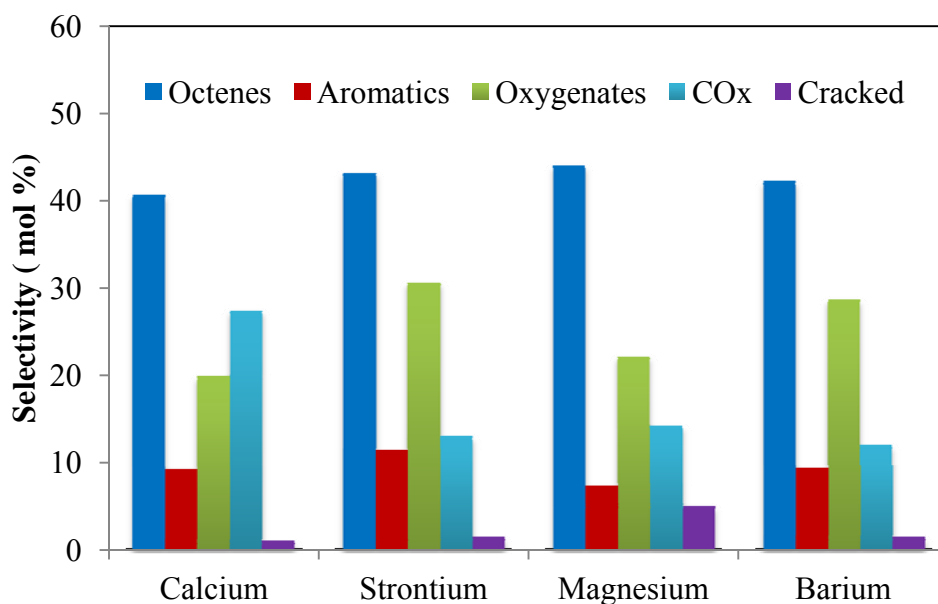


Figure 3.37 Product selectivity over 10 wt% V_2O_5 supported on hydroxyapatites at iso-conversion (27%), temperature = 450 °C and *n*-octane to oxygen molar ratio of 1:2

10VMg-HAp also showed the same trend in the formation of octenes and aromatics due to its Lewis acidic nature. A similar type of activity was previously reported by Sugiyama and co-workers [25, 59] for lower alkanes like propane and ethane. Selectivity towards aromatics for the 10 wt% V_2O_5 supported on hydroxyapatite catalysts (Figs. 3.41, 3.42 and 3.43) is due to the presence of the pyrovanadate phase together with vanadium pentoxide on the surface of the hydroxyapatite, which was confirmed by XRD (Fig. 3.13), Raman spectroscopy (Fig. 3.1) and IR spectroscopy. The presence of the isolated VO_4 tetrahedral species enhances the selectivity towards olefins [45], which are also the precursors for aromatics [53]. The selectivity of oxygenates depend on the *n*-octane to oxygen molar ratios, i.e. as the oxygen molar ratio increases, selectivity towards oxygenates also increases. Among the oxygenate products, the selectivity towards C_1 - C_7 oxygenates was higher than C_8 oxygenates at *n*-octane to oxygen molar ratios of 1:0.5 and 1:1.

Under oxygen rich environments, C_8 oxygenates dominate and 2-octanol is the major product. 10VMg-HAp showed highest selectivity towards the oxygenates at *n*-octane to oxygen molar ratios of 1:0.5 and 1:1, whereas 10VSr-HAp showed highest selectivity towards oxygenates at an

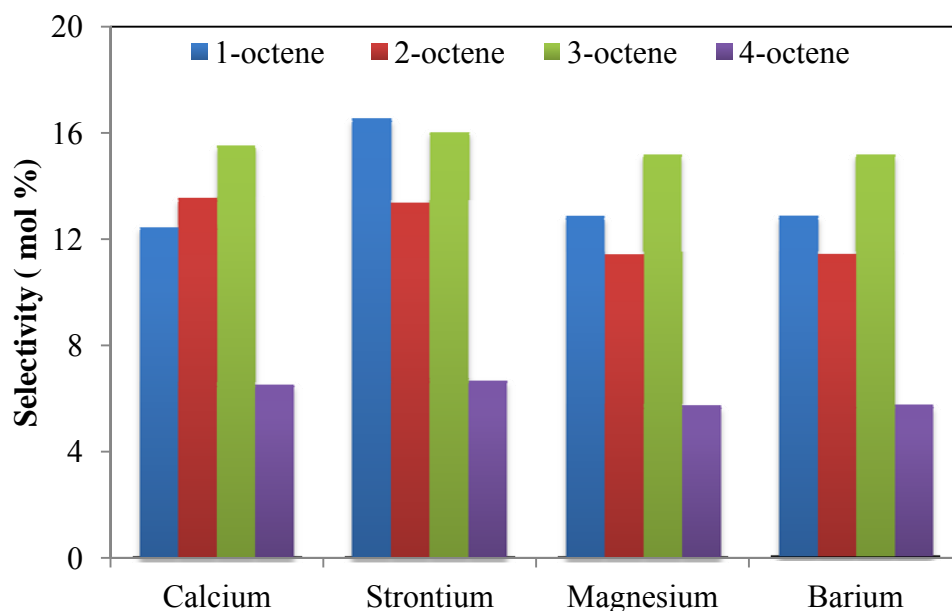


Figure 3.38 Selectivity of octenes over 10 wt% V₂O₅ supported on hydroxyapatites at iso-conversion (27%), temperature = 450 °C and *n*-octane to oxygen molar ratio of 1:0.5

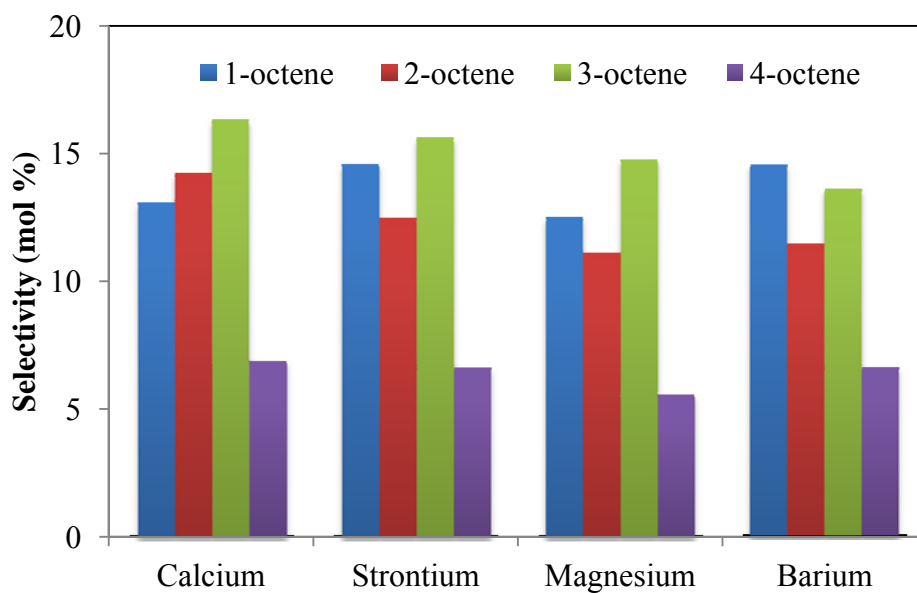


Figure 3.39 Selectivity of octenes over 10 wt% V₂O₅ supported on hydroxyapatites at iso-conversion (27%), temperature = 450 °C and *n*-octane to oxygen molar ratio of 1:1

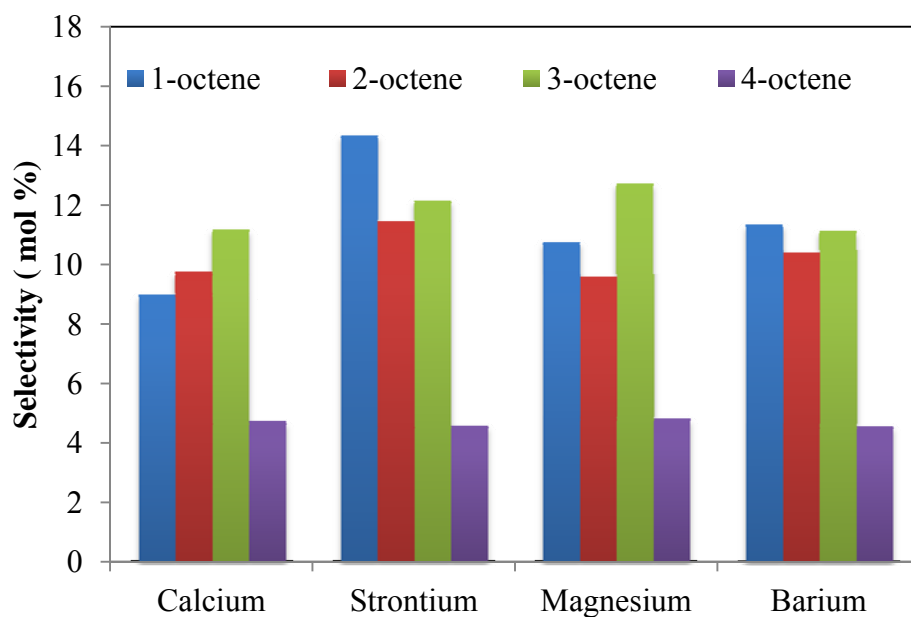


Figure 3.40 Selectivity of octenes over 10 wt% V_2O_5 supported on hydroxyapatites at iso-conversion (27%), temperature = 450 °C and *n*-octane to oxygen molar ratio of 1:2

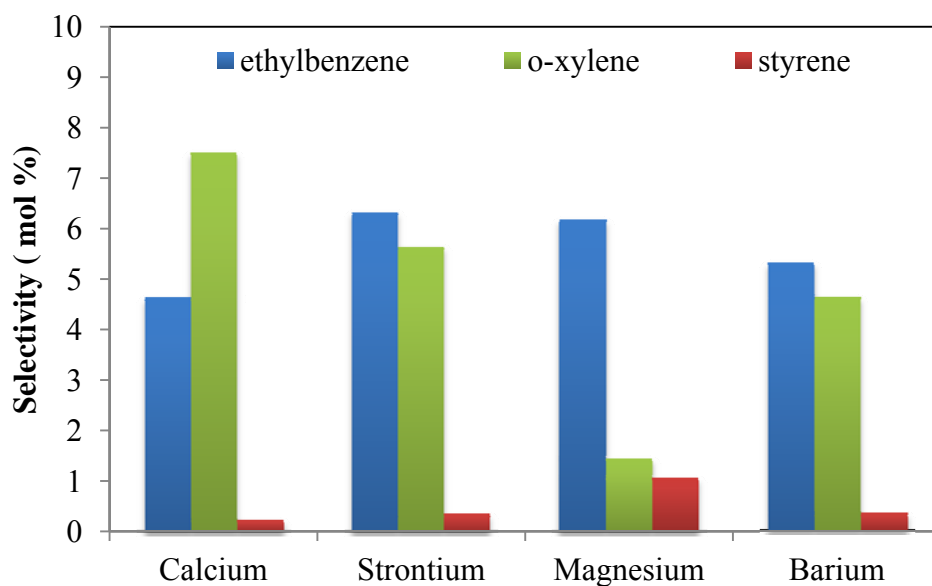


Figure 3.41 Selectivity of aromatics over 10 wt% V_2O_5 supported on hydroxyapatites at iso-conversion (27%), temperature = 450 °C and *n*-octane to oxygen molar ratio of 1:0.5

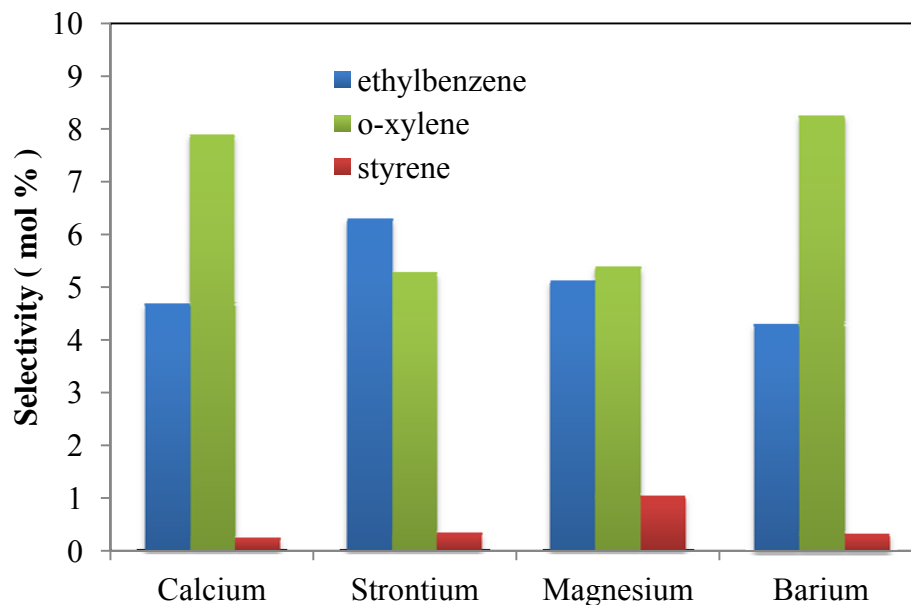


Figure 3.42 Selectivity of aromatics over 10 wt% V_2O_5 supported on hydroxyapatites at iso-conversion (27%), temperature = 450 °C and *n*-octane to oxygen molar ratio of 1:1

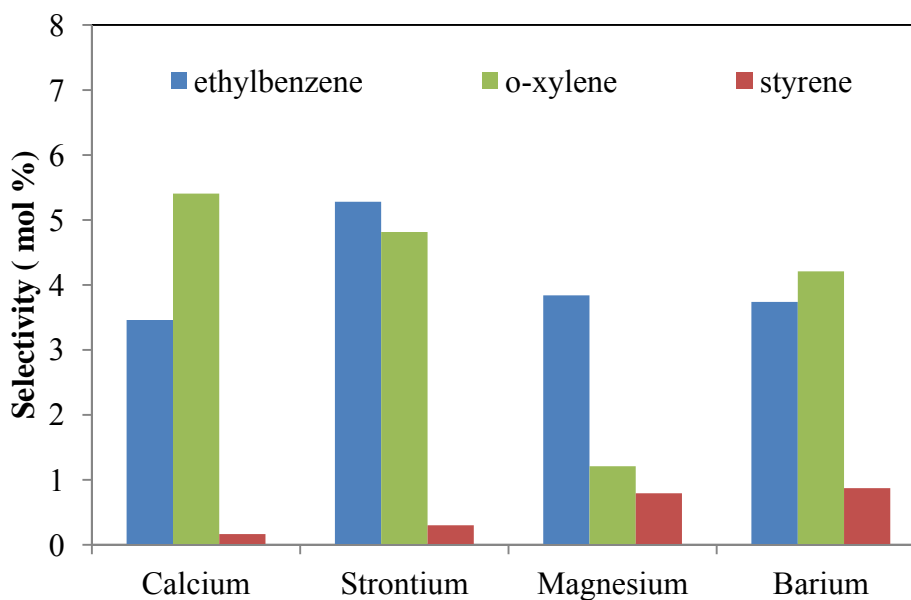


Figure 3.43 Selectivity of aromatics over 10 wt% V_2O_5 supported on hydroxyapatites at iso-conversion (27%), temperature = 450 °C and *n*-octane to oxygen molar ratio of 1:2

n-octane to oxygen molar ratio of 1:2 (Fig. 9). This could be explained by the Brønsted acidity of the 10VSr-HAp, catalyst which enhances the oxidation of octenes to oxygenates under oxygen

rich environments [54]. 10VBa-HAp showed a similar selectivity as 10VSr-HAp but showed low selectivity towards CO_x and cracked products relative to the other hydroxyapatites, due to the small number of Lewis and Brønsted acidic sites. 10VCa-HAp showed significant acidity relative to 10VSr-HAp, which is reflected in the selectivity towards aromatics (Table 3.3).

The selectivity towards cracked products was dependent on the temperature rather the *n*-octane to oxygen molar ratios (Figs. 3.35, 3.36 and 3.37). The primary cracked products are C2, C4 and C5 alkenes for all molar ratios. 10VMg-HAp showed high selectivity towards cracked products due to the Brønsted acidity of the 10VMg-HAp catalyst which favours the formation of oxygenate compounds, followed by the cracking of the products which are further oxidized to carbon oxides and water. This results in a decrease in the selectivity of oxygenate compounds at an *n*-octane to oxygen molar ratio of 1:2, where 10VMg-HAp showed low selectivity towards aromatics and high selectivity towards CO_x relative to 10VSr-HAp and 10VBa-HAp, which have the lowest number of Brønsted acidic sites in comparison to 10VMg-HAp (Figs. 3.35, 3.36 and 3.37).

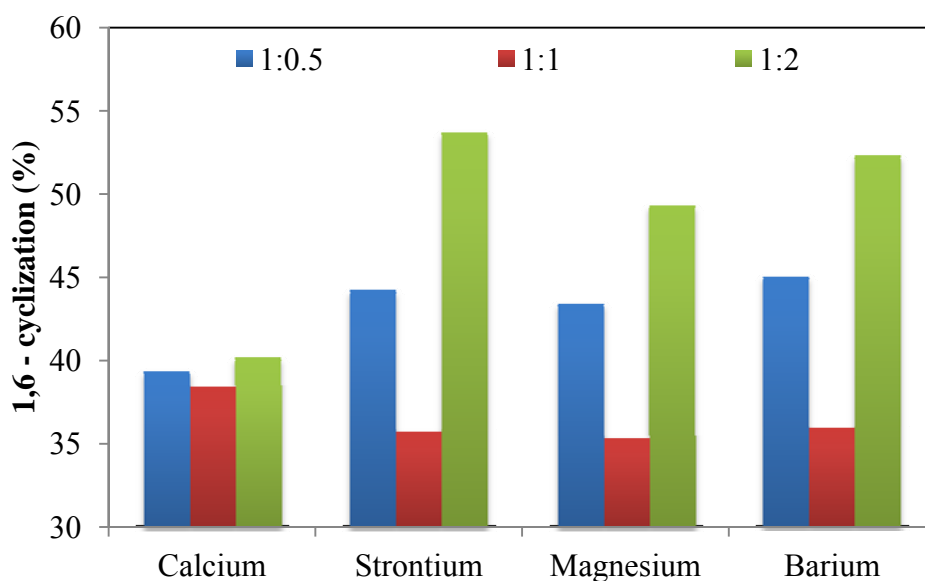


Figure 3.44 1,6-cyclisation of aromatics over 10 wt% V_2O_5 supported on hydroxyapatites at iso-conversion (27%), temperature = 450 °C with varying *n*-octane to oxygen molar ratios

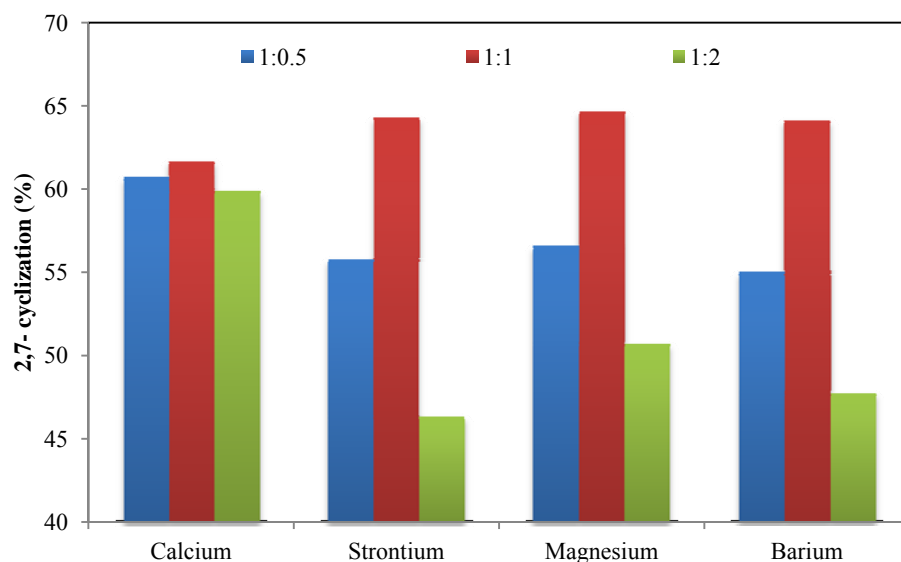


Figure 3.45 2,7-cyclisation of aromatics over 10 wt% V_2O_5 supported on hydroxyapatites at iso- conversion (27%), temperature = 450 °C with varying *n*-octane to oxygen molar ratios

Figure 3.44 shows the percentage of products formed via the 1,6-cyclization mode in 10 wt % V_2O_5 supported on hydroxyapatite catalysts. The 1,6-cyclization mode is favored for the formation of aromatics for all 10 wt% V_2O_5 supported on hydroxyapatite catalysts at an *n*-octane to oxygen molar ratio of 1:2, which can be again attributed to the selectivity to 1-octene which undergoes 1,6-cyclization in the formation of aromatics (Fig. 3.44). This is probably due to the Lewis acidity of 10 wt% V_2O_5 supported on hydroxyapatite catalysts (Table 3.3). Figure 3.45 shows the percentage of products formed via the 2,7-cyclization mode in the 10 wt% V_2O_5 supported on hydroxyapatite catalysts. The 2,7-cyclization is preferred for 10 wt% V_2O_5 loaded hydroxyapatites at *n*-octane to oxygen molar ratio of 1:1, this can be attributed to the high selectivity of 2-octenes and 3-octenes which likely undergo 2,7-cyclization in the formation of aromatics (Fig. 3.45).

3.4 Conclusion

All the characterization techniques showed that vanadium is supported on the hydroxyapatites and that it is uniformly dispersed. At 2.5 wt% loadings, vanadium exists as vanadium pentoxide, but for 10 wt% loadings vanadium is in the vanadium pentoxide and pyrovanadate phases, which is confirmed by XRD and supported by IR and Raman spectroscopy

data. Nitrogen adsorption isotherms showed that all the catalysts are mesoporous materials. The TPR profiles showed that reducibility and the temperature of reduction is affected by the vanadium loading on the hydroxyapatites. TPD showed that acidity of the catalysts depends on both the metal present in the hydroxyapatite and vanadium loading.

In oxidative dehydrogenation experiments, the selectivity towards products depends on the *n*-octane to oxygen molar ratios and on the phase composition of vanadium on the hydroxyapatites. Among all the catalysts, vanadium oxide supported on Sr-HAp showed best activity. The trend of the catalytic activity is in agreement with the acidic strength and reducibility of the catalyst. For an *n*-octane to oxygen molar ratio of 1:0.5 all the catalysts showed highest selectivity towards octenes, whereas molar ratios of 1:1 and 1:2 showed higher selectivity towards aromatics and oxygenates, although octenes are still dominant products. All the catalyst showed moderate to high selectivity towards carbon oxides, since all catalysts have Brønsted acidity which favours the further oxidation of ODH products to carbon oxides. 2.5VCa-HAp and 10VCa-HAp showed highest selectivity towards octenes and CO_x, 2.5VSr-HAp, 10VSr-HAp, 2.5VBa-HAp and 10VBa-HAp showed highest selectivity towards aromatics. 2.5VMg-HAp and 10VMg-HAp showed selectivity towards aromatics and oxygenates. The 1,6-cyclization mode towards aromatics is favoured for 2.5VMg-HAp and 2.5VBa-HAp, while 2,7- cyclization is favoured when 10 wt% V₂O₅ is supported on 10VCa-HAp and 10VSr-HAp. The cyclization mode is related to the dominant octene isomer formed over the respective catalysts.

Acknowledgements

We would like to thank the NRF and THRIP for support. Thanks are also extended to the Electron Microscopy Unit at the University of Kwazulu-Natal (Westville).

References

- [1] C.J. Pereira, *Science* 285 (1999) 670-671.
- [2] D. Sanfilippo, *CATTECH* 4 (2000) 56-73.
- [3] V. Cortés Corberán, *Top. Catal.* 52 (2009) 962-969.
- [4] M.M. Bhasin, J.H. McCain, B.V. Vora, T. Imai, P.R. Pujadó, *Appl. Catal. A.* 221 (2001) 397-419.
- [5] M.M. Bettahar, G. Costentin, L. Savary, J.C. Lavalley, *Appl. Catal. A.* 145 (1996) 1-48.

- [6] S.F. Håkonsen, A. Holmen, Handbook of Heterogeneous Catalysis, Wiley-VCH Verlag GmbH & Co. KGaA, 2008.
- [7] B. Solsona, M.I. Vázquez, F. Ivars, A. Dejoz, P. Concepción, J.M. López Nieto, J. Catal. 252 (2007) 271-280.
- [8] H.H. Kung, M.C. Kung, Appl. Catal. A. 157 (1997) 105-116.
- [9] G.C. Bond, Appl. Catal. A. 157 (1997) 91-103.
- [10] T. Blasco, J.M.L. Nieto, Appl. Catal. A. 157 (1997) 117-142.
- [11] A.O. Chapman, G.R. Akien, N.J. Arrowsmith, P. Licence, M. Poliakoff, Green Chem. 12 (2010) 310-315.
- [12] H.B. Friedrich, A.S. Mahomed, Appl. Catal., A. 347 (2008) 11-22.
- [13] E.A. Mamedov, V. Cortés Corberán, Appl. Catal. A. 127 (1995) 1-40.
- [14] H.H. Kung, in: H.P. D.D. Eley, O.H. Werner (Eds.), Adv. Catal., Academic Press, 1994, pp. 1-38.
- [15] M. Cozzolino, R. Tesser, M. Di Serio, P. D'Onofrio, E. Santacesaria, Catal. Today. 128 (2007) 191-200.
- [16] N. Cheikhi, M. Kacimi, M. Rouimi, M. Ziyad, L.F. Liotta, G. Pantaleo, G. Deganello, J. Catal. 232 (2005) 257-267.
- [17] K. Elkabouss, M. Kacimi, M. Ziyad, S. Ammar, F. Bozon-Verduraz, J. Catal. 226 (2004) 16-24.
- [18] A. Yasukawa, E. Ueda, K. Kandori, T. Ishikawa, J. Colloid Interface Sci. 288 (2005) 468-474.
- [19] M. Khachani, M. Kacimi, A. Ensuque, J.-Y. Piquemal, C. Connan, F. Bozon-Verduraz, M. Ziyad, Appl. Catal. A. 388 (2010) 113-123.
- [20] A. Yasukawa, S. Ouchi, K. Kandori, T. Ishikawa, J. Mater. Chem. 6 (1996) 1401-1405.
- [21] S. Sugiyama, T. Minami, H. Hayashi, M. Tanaka, N. Shigemoto, J.B. Moffat, J. Chem. Soc., Faraday Trans. 92 (1996) 293-299.
- [22] S. Sugiyama, T. Minami, T. Higaki, H. Hayashi, J.B. Moffat, Ind. Eng. Chem. Res. 36 (1997) 328-334.
- [23] S. Sugiyama, Y. Fujii, K. Abe, H. Hayashi, J.B. Moffat, Energy Fuels. 13 (1999) 637-640.
- [24] S. Sugiyama, T. Shono, D. Makino, T. Moriga, H. Hayashi, J. Catal. 214 (2003) 8-14.

- [25] S. Sugiyama, T. Osaka, Y. Hirata, K.-I. Sotowa, *Appl. Catal. A*. 312 (2006) 52-58.
- [26] V.D.B.C. Dasireddy, S. Singh, H.B. Friedrich, *Appl. Catal. A* (2012) 10.1016/j.apcata.2012.01.034
- [27] T. Ishikawa, H. Saito, K. Kandori, *J. Chem. Soc., Faraday Trans.* 88 (1992) 2937-2942.
- [28] Y. Matsumura, S. Sugiyama, H. Hayashi, N. Shigemota, K. Saitoh, J.B. Moffat, *J. Mol. Catal.* 92 (1994) 81-94.
- [29] H.-W. Kim, L.-H. Li, Y.-H. Koh, J.C. Knowles, H.-E. Kim, *J. Am. Ceram. Soc.* 87 (2004) 1939-1944.
- [30] P. Parhi, A. Ramanan, A.R. Ray, *Mater. Lett.* 60 (2006) 218-221.
- [31] K.V.R. Chary, G. Kishan, T. Bhaskar, C. Sivaraj, *J. Phys. Chem. B*. 102 (1998) 6792-6798.
- [32] D. Siew Hew Sam, V. Soenen, J.C. Volta, *J. Catal.* 123 (1990) 417-435.
- [33] L. Balderas-Tapia, I. Hernández-Pérez, P. Schacht, I.R. Córdova, G.G. Aguilar-Ríos, *Catal. Today*. 107-108 (2005) 371-376.
- [34] M.D. O'Donnell, Y. Fredholm, A. de Rouffignac, R.G. Hill, *Acta Biomaterialia*. 4 (2008) 1455-1464.
- [35] C.R. Dias, M.F. Portela, G.C. Bond, *J. Catal.* 157 (1995) 344-352.
- [36] S. Sugiyama, T. Osaka, Y. Ueno, K.-I. Sotowa, *J. Jpn. Pet. Inst.* 51 (2008) 50-57.
- [37] Y. Kamiya, E. Nishikawa, A. Satsuma, M. Yoshimune, T. Okuhara, *Microporous Mesoporous Mater.* 54 (2002) 277-283.
- [38] K. Bhattacharyya, S. Varma, A.K. Tripathi, S.R. Bharadwaj, A.K. Tyagi, *J. Phys. Chem. C*. 112 (2008) 19102-19112.
- [39] Y. Yang, S. Lim, C. Wang, D. Harding, G. Haller, *Microporous Mesoporous Mater.* 67 (2004) 245-257.
- [40] G.C. Bond, J.P. Zurita, S. Flamerz, P.J. Gellings, H. Bosch, J.G. Van Ommen, B.J. Kip, *Appl. Catal.* 22 (1986) 361-378.
- [41] C.R. Dias, M.F. Portela, G.C. Bond, *J. Catal.* 157 (1995) 353-358.
- [42] H. Bosch, B.J. Kip, J.G. van Ommen, P.J. Gellings, *J. Chem. Soc., Faraday Trans.* 1. 80 (1984) 2479-2488.
- [43] I.E. Wachs, B.M. Weckhuysen, *Appl. Catal. A*. 157 (1997) 67-90.

- [44] H.K. Matralis, C. Papadopoulou, C. Kordulis, A. Aguilar Elguezabal, V. Cortes Corberan, *Appl. Catal. A*. 126 (1995) 365-380.
- [45] L. Balderas-Tapia, J.A. Wang, I. Hernández-Pérez, G.G. Aguilar-Ríos, P. Schacht, *Mater. Lett.* 58 (2004) 3034-3039.
- [46] K.V.R. Chary, G. Kishan, C.P. Kumar, G.V. Sagar, *Appl. Catal. A*. 246 (2003) 335-350.
- [47] M.M. Khader, *J. Mol. Catal. A: Chem.* 104 (1995) 87-94.
- [48] J. Huuhtanen, M. Sanati, A. Andersson, S. Lars T. Andersson, *Appl. Catal. A*. 97 (1993) 197-221.
- [49] A. Corma, J.M.L. Nieto, N. Paredes, *J. Catal.* 144 (1993) 425-438.
- [50] Ozie S. Owen, Mayfair C. Kung, H.H. Kung, *Catal. Lett.* 12 (1992) 45-50.
- [51] N. Elazarifi, A. Ezzamarty, J. Leglise, L.-C.d. Ménorval, C. Moreau, *Appl. Catal. A*. 267 (2004) 235-240.
- [52] R.T. Morrison, R.N. Boyd, *Organic Chemistry, Sixth Ed.*, ed., Prentice Hall, New Jersey, 1992.
- [53] E.A. Elkhalfa, H.B. Friedrich, *Appl. Catal. A*. 373 (2010) 122-131.
- [54] E.A. Elkhalfa, H.B. Friedrich, *Catal. Lett.* 141 (2011) 554-564.
- [55] J.C. Vedrine, J.M.M. Millet, J.-C. Volta, *Catal. Today*. 32 (1996) 115-123.
- [56] S.T. Oyama, *J. Catal.* 128 (1991) 210-217.
- [57] G.J. Panuccio, K.A. Williams, L.D. Schmidt, *Chem. Eng. Sci.* 61 (2006) 4207-4219.
- [58] S. Sugiyama, T. Miyamoto, H. Hayashi, J.B. Moffat, *J. Mol. Catal. A: Chem.* 135 (1998) 199-208.
- [59] B.C. Shi, B.H. Davis, *J. Catal.* 157 (1995) 626-630.

CHAPTER 4

STUDIES TOWARDS A MECHANISTIC INSIGHT INTO THE ACTIVATION OF *n*-OCTANE USING VANADIUM SUPPORTED ON ALKALINE EARTH METAL HYDROXYAPATITES

Abstract

To gain insight into the mechanism for the formation of products in the activation of *n*-octane, the role of the octene isomers, i.e. 1-octene, 2-octene, 3-octene and 4-octene, together with 1,7-octadiene were investigated using 2.5 and 10 wt% V₂O₅ supported on calcium, strontium, magnesium and barium hydroxyapatites as catalysts. The fresh catalysts were characterized by DR-UV-Vis spectroscopy, XPS, *in situ* X-ray diffraction and oxygen chemisorption. The redox natures of the fresh catalysts are explained by TPR-TPO-TPR analysis and used catalysts were characterized by XRD, ICP-OES, BET, FTIR, SEM, TEM and TPD. Oxidative dehydrogenation reactions were carried out in a continuous flow fixed bed reactor by varying the hydrocarbon to oxygen molar ratios. The selectivity towards the desired products was dependent on the phase composition of the catalyst and on the hydrocarbon to oxygen molar ratios. All the octene isomers showed good selectivity towards aromatics. Oxygenates and carbon oxides (CO_x) were also formed. Highest selectivity towards aromatics was shown by the 2-octene and 3-octene isomers with both loadings at all hydrocarbons to oxygen molar ratios. However, as the oxygen molar ratios were increased, a decrease in the selectivity towards aromatics and an increase in selectivity towards CO_x was observed. The terminal octene and 1,7-octadiene preferred the 1,6-cyclization mode towards aromatics formation, whereas for 2-octene and 3-octene the 2,7 cyclization mode was followed. The oxidation-reduction pathway in this reaction resembles the Mars-van Krevelen mechanism. Initially, *n*-octane is reduced to octenes, followed by oxidation and oxidative dehydrogenation to aromatics and oxygenates. Combustion to give carbon oxides is a side reaction, at all stages, though at times, quite minor.

Keywords: hydroxyapatite, V₂O₅, 1-octene, 2-octene, 3-octene, 4-octene and 1,7-octadiene, oxidative dehydrogenation.

4.1 Introduction

The development of catalytic processes for the selective oxidation of alkanes has constituted a significant breakthrough for the production of chemicals and intermediates. Furthermore, the oxidation of alkanes in the presence of oxygen, which includes oxidation and oxidative dehydrogenation (ODH), are competitive petrochemical conversion processes [1, 2]. This includes the ODH of alkanes to alkenes and alkenes to dienes, oxidation of alkanes to oxygenates and cracked products and the complete oxidation to CO_x [2]. The selective oxidation of alkanes is a challenge due to the relative inertness of alkanes and the ease at which possible products or intermediates react. Since alkenes, aromatics and oxygenates are preferred products in the activation of alkanes, it is critical to control further reactions that lead to the formation of CO_x . Huff and Schmidt [3, 4] demonstrated in the heterogeneous ODH of alkanes on $\text{Pt}/\text{Al}_2\text{O}_3$ catalysts that the primary products produced were alkenes along with a minimal amount of carbon oxides and water. For alkenes which undergo substantial cleavage by auto-oxidation, primary products often accumulate and the oxidation soon becomes a co-oxidation process of primary products and alkenes. The gas phase oxidative cracking of higher hydrocarbons involves a series of steps and the formation of products is dependent on the temperature and hydrocarbon to oxygen molar ratios [5]. In the partial oxidation of a mixture of alkene isomers, Subramanian et al. [6] showed that the specific hydrocarbon to oxygen molar ratio for each alkene isomer is the important parameter for the conversion of these isomers. Under ideal conditions, catalytic partial oxidation of alkene isomers and mixtures is modeled by combining both heterogeneous and homogeneous chemistry.

The major steps in the mechanism for the gas phase reaction of alkanes with six or more carbons are the unimolecular decomposition of the alkane with H-atom abstraction, decomposition of four distinct alkyl radicals by C-C bond scission, isomerisation by internal H-atom abstraction to other alkyl radicals and reactions with molecular oxygen to produce hydroperoxyalkyl radicals leading to branching reactions [7]. The rate coefficients of these reactions are dependent on the type of hydrogen atom being abstracted and its environment [8]. This proposed gas phase mechanism consisted of 7193 irreversible reactions. Due to the complexity in chemistry and the species in transport, application of detailed mechanistic models has been restricted to hydrocarbons such as methane and ethane [3, 7, 9].

Studies involving the cyclization and aromatization of *n*-octane have been carried out non-oxidatively in the presence of hydrogen [10, 11]. However, there were limitations associated with this process, viz. catalyst deactivation caused by coke formation and the endothermic nature of the reaction. ODH offers a viable alternative for the production of olefins and aromatics [12] and more specifically, studies on the ODH of *n*-octane have been carried out [13-15] over vanadium oxide catalytic systems producing octenes, aromatics and oxygenates. Recently we reported on the ODH of *n*-octane over V₂O₅ supported hydroxyapatites with different V₂O₅ loadings [16]. In another study, we reported the influence of *n*-octane to oxygen molar ratios and the effect of the metal present in the hydroxyapatites on the selectivity of octenes and aromatics [17]. The objective of this investigation was to determine the effect of vanadium supported on hydroxyapatite catalysts and hydrocarbon to oxygen ratio on the pathways of the product formation from the activation of *n*-octane.

4.2 Experimental

4.2.1 Catalyst synthesis and characterization

All catalysts are synthesized via the method elaborated in our previous studies [16, 17]. In a typical method, the hydroxyapatites were prepared by co-precipitation of solutions of metal nitrate salts with a solution of ammonium hydrogen phosphate. Different weight percentages of vanadium pentoxide supported catalysts were prepared by treating the respective hydroxyapatite with ammonium metavanadate. The fresh and spent catalysts were characterized by the techniques described previously. The nature and the environment of vanadium was determined by using a Cary 400 DR-UV-Vis spectrophotometer and the dispersion of vanadium on the hydroxyapatite supports by oxygen chemisorption. Oxygen chemisorption was carried out using a Mircometics ASAP 2020 Chemisorption analyser. Before the measurements, catalysts samples (0.03-0.04 g) were reduced in flowing hydrogen (30 mL/min) for 3 h at 600 °C and then flushed at the same temperature for 30 min with helium (30 mL/min). Oxygen (30 mL/min) was passed through the sample for 3 h until saturation of the sample was attained. The oxygen uptake was quantified using a TCD detector. The reproducibility of data was ± 2 %. Vanadia dispersion, expressed as a ratio between the vanadium on the surface of the hydroxyapatite and oxygen uptake, was calculated assuming an O₂:V chemisorption stoichiometry of 2:1 [18]. For temperature programmed oxidation (TPO), 5% oxygen in argon was passed over the catalysts

under conditions similar to those of the temperature programmed reduction (TPR) studies described earlier [16]. XPS analysis was carried out using a Kratos Axis Ultra DLD spectrometer, with an achromatic Al K α source operated at 120 W. The base pressure in the analysis chamber was maintained at about 1×10^{-9} mbar. Pass energies of 160 eV and 40 eV were used for the acquisition of survey and detailed regional scans, respectively. Binding energies were calibrated against the C (1s) signal from adventitious carbon contamination, which was assumed to have a binding energy of 284.7 eV. *In situ* XRD was performed on the catalyst samples under reaction conditions, using a PANalytical X'Pert Pro instrument. Scans from 10 to 80° were carried out using a Cu K α radiation source. An Anton-Parr *in situ* cell (internal volume, 500 cm³) was fitted to the instrument to study phase changes in the catalyst samples under reaction conditions. The gaseous *n*-octane in oxygen at a molar ratio of 1:1.5 is introduced into the XRD cell at a GHSV of 3250 h⁻¹. XRD diffractograms were recorded at an interval of 50 °C up to 600 °C while heating. The sample was cooled at the same temperature conditions. Quantitative analysis of the phases present in the catalyst during the *in situ* XRD studies was done by using X'pert PAN analytical software. The crystallographic information files that were used to refine the phases present in the catalysts were obtained from literature [19-24].

4.2.2 Catalytic testing

Gas phase oxidation reactions were carried out in a continuous flow fixed bed reactor in down flow mode as described previously [16]. The catalytic tests were carried out at different hydrocarbon to oxygen molar ratios, viz.. 1:0.5, 1:1 and 1:2 at a GHSV of 4000 h⁻¹ and over a temperature range of 350-550°C. The catalytic testing was carried out with different octene isomers, namely 1-octene, 2-octene, 3-octene, 4-octene and 1,7-octadiene. The concentration of hydrocarbons in the gaseous mixture was maintained at 11.3 % (v/v) and the flow rate of oxygen was varied to obtain the respective molar ratios. Blank experiments were carried out under the same conditions and showed that non-catalytic contributions were negligible. Carbon balances ranged between 98-101 % and all data points were obtained in triplicate with a standard deviation of $\pm 2\%$.

4.3 Results and Discussion

4.3.1 Characterization of fresh catalysts

4.3.1.1 Diffuse reflectance UV-Vis Spectroscopy

Figure 4.1 shows DR-UV-Vis spectra of 2.5 wt% V_2O_5 supported on hydroxyapatite catalysts. All catalysts display a strong band around ~ 260 nm that can be attributed to an oxygen to a square-pyramidal vanadium (V^{5+}) charge-transfer transition [25]. A wide and strong absorption is observed in the range from 200 to 500 nm, which is composed of bands with many origins, such as $a_2(\pi)$, $b_1(\pi) \rightarrow b_2(xy)$ transitions owing to bridging oxygen in square-pyramidal coordination, $\pi \rightarrow \pi^*$ transitions and the charge transfer of the $V=O$ double bond from oxygen to vanadium [26]. Two main bands at ~ 280 and 390 nm are attributed to oxygen-to-pseudo-tetrahedral $V(V)$ and oxygen-to-pseudo-octahedral $V(V)$ charge transfer transitions, involving oxygen in bridging ($V-O-V$) and terminal ($V=O$) positions [27].

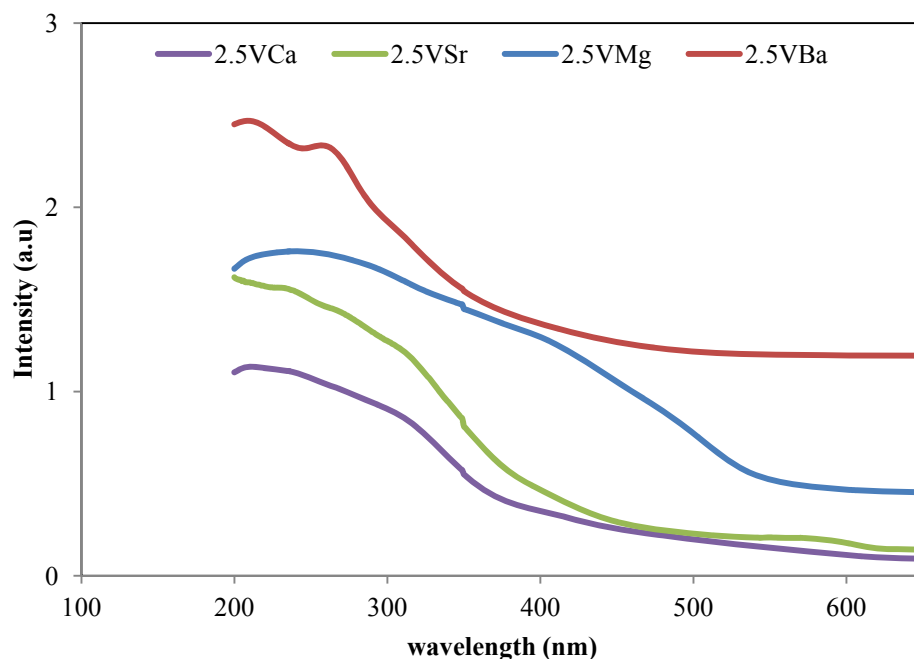


Figure 4.1 DR-UV-Vis spectrum of 2.5 wt% V_2O_5 supported on hydroxyapatites

Figure 4.2 shows the DR-UV-Vis spectra of 10 wt % V_2O_5 supported on hydroxyapatite catalysts. All these catalysts showed higher intensity spectra than the 2.5 wt % V_2O_5 supported on hydroxyapatites. This could be due to the presence of the pyrovanadate phase present in the catalysts [16]. In addition, the presence of two oxidation states, V^{5+} and V^{4+} , causes the increase

in intensity for the intervalence bands in the NIR region [27]. There is also a slight shift of the bands due to a greater distortion of pseudo-tetrahedral vanadium (V^{5+}) species in 10 wt% V_2O_5 supported on hydroxyapatite catalysts. Since V^{4+} ions have ionic radii larger than V^{5+} ions, the former would exhibit a larger bond length, thus a decrease in vibration frequency. As the hybrid materials contain V^{4+} and V^{5+} centers, the V-O-V vibrational absorptions shift towards lower frequency.

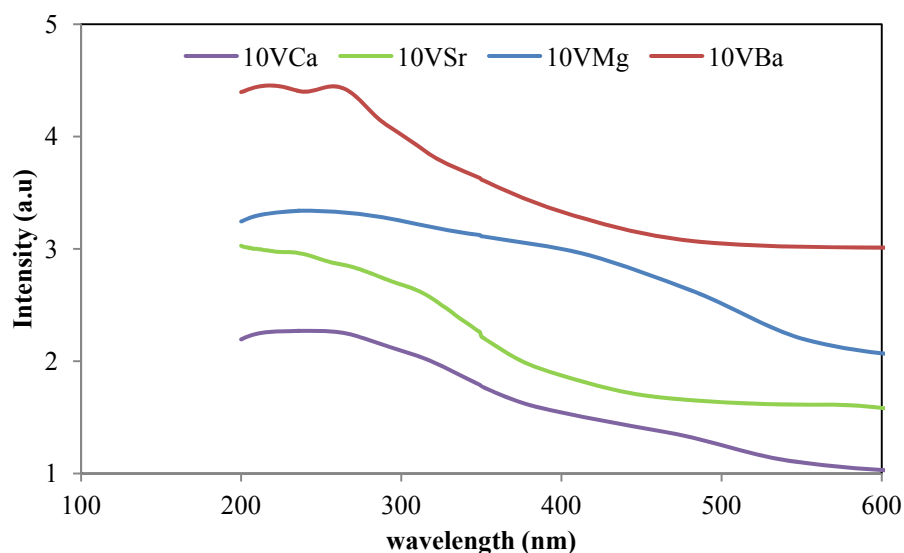


Figure 4.2 DR-UV-Vis spectrum of 10 wt% V_2O_5 supported on hydroxyapatites

4.3.1.2 Oxygen chemisorption

Table 4.1 Oxygen chemisorption data

Catalyst	Surface area (m^2/g)	Oxygen uptake (cm^3/g)	Dispersion of vanadium (%)
2.5VCa-HAp	49.2	3.5	19.3
2.5VSr-HAp	54.8	4.5	27.6
2.5VMg-HAp	52.1	4.1	24.3
2.5VBa-HAp	38.2	3.6	20.1
10VCa-HAp	12.7	8.1	79.2
10VSr-HAp	14.8	10.2	88.4
10VMg-HAp	13.5	9.5	84.1
10VBa-HAp	11.5	8.6	81.7

The oxygen chemisorption of the vanadium pentoxide supported on hydroxyapatite catalysts are shown in Table 4.1. The results showed that the oxygen chemisorption capacities of the catalyst increases with the vanadium loading present on the hydroxyapatites. As the vanadium loading increases, the dispersion of vanadium on the surface of the hydroxyapatites increases. The surface area results after the chemisorption are in agreement with the fresh catalyst surface areas (Chapter 2). This indicates that the vanadium is reoxidised to vanadium pentoxide after chemisorption [18]. It was also observed that the surface area of the catalysts decreases with vanadium loading on the hydroxyapatites (Chapter 2). This is probably due to the clogging of pores of the hydroxyapatite support with the vanadium molecules. The trend in the surface areas is supported by an increase in vanadium dispersion with an increase in vanadium loading on hydroxyapatite supports.

4.3.1.3 Temperature programmed oxidation

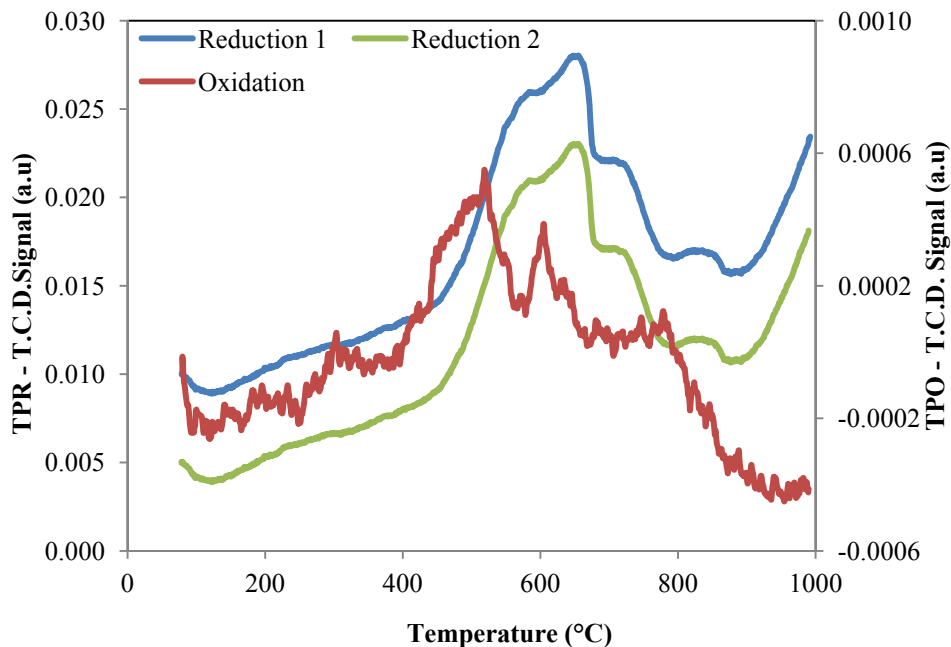


Figure 4.3 TPR-TPO-TPR profiles of 2.5VCa-HAp

The concentration of oxygen vacancies created by reduction experiments and the oxidation behavior of the catalysts were determined by using temperature programmed oxidation (TPO). Before TPO, the catalysts were pretreated in order to avoid structural changes as detailed below. For TPR, temperature ramping was stopped at 950 °C and the temperature maintained until the

hydrogen consumption reached the base line. There was no phase transition of the hydroxyapatites support during this treatment, which was corroborated by XRD [16].

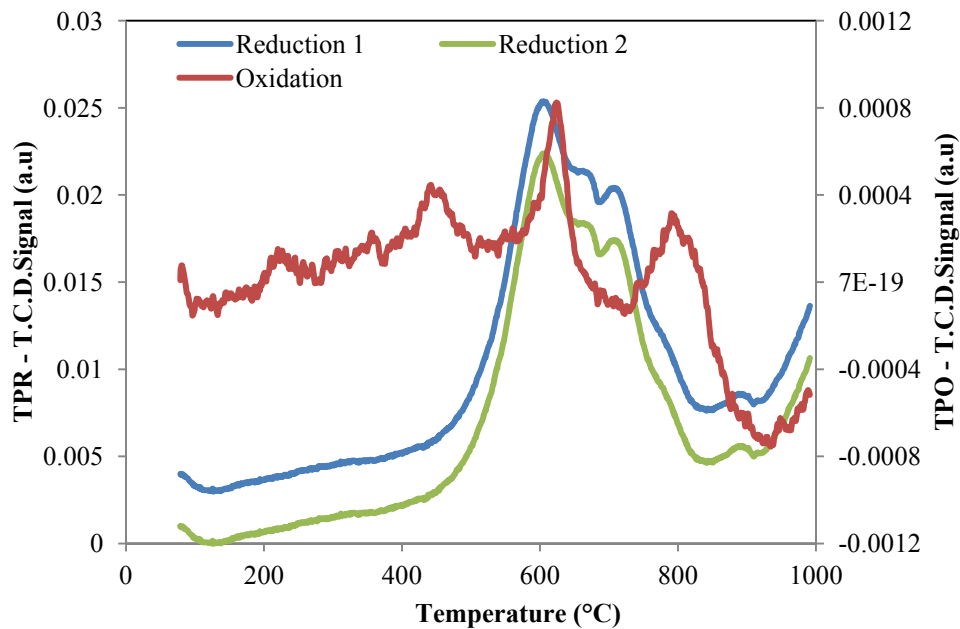


Figure 4.4 TPR-TPO-TPR profiles of 2.5VSr-HAp

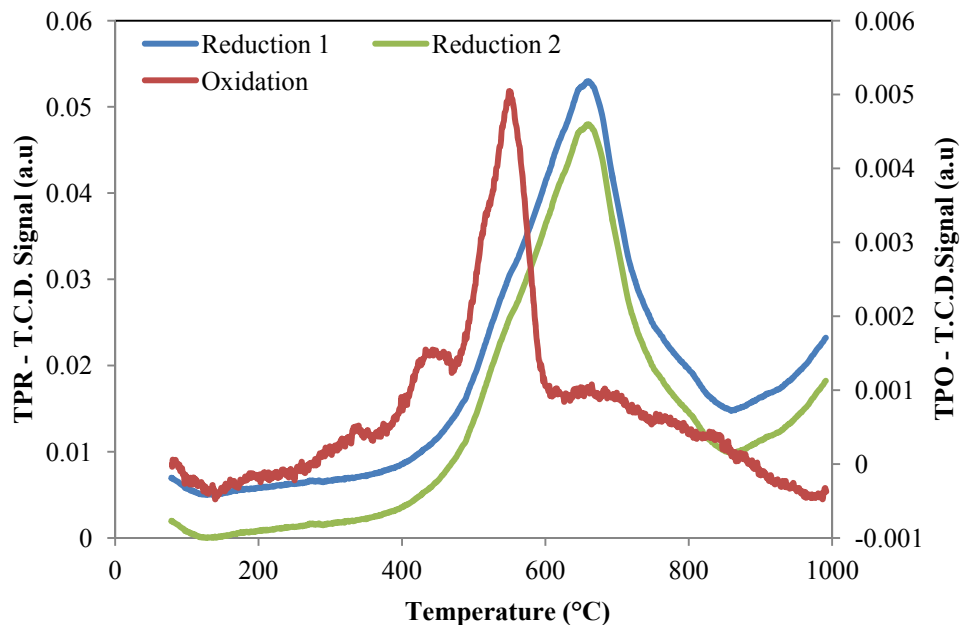


Figure 4.5 TPR-TPO-TPR profiles of 2.5VMg-HAp

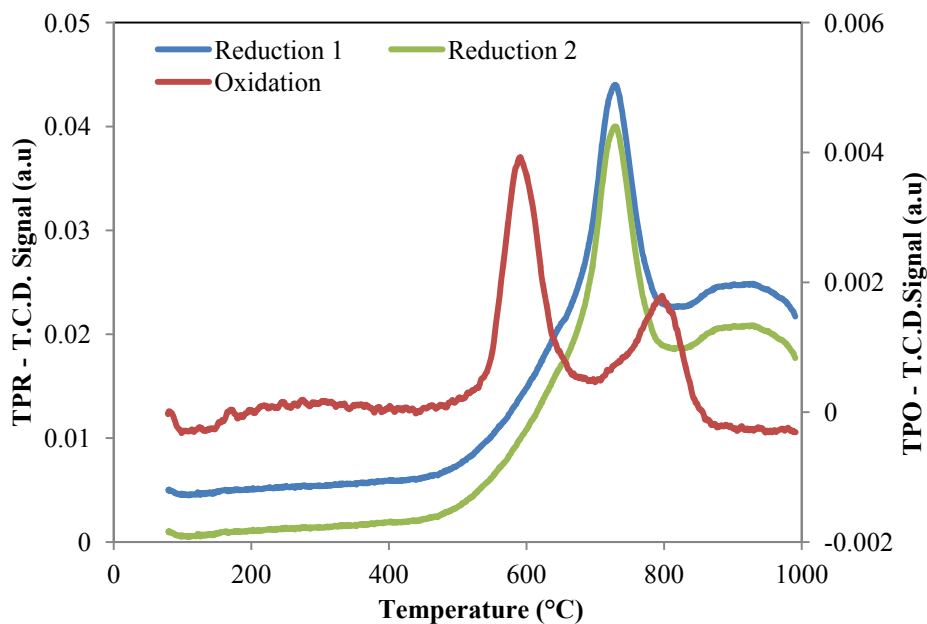
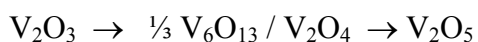


Figure 4.6 TPR-TPO-TPR profiles of 2.5VBa-HAp

Once the catalyst was cooled to room temperature in Ar, the TPO experiment was conducted. The TPO profiles are shown in Figures 4.3 - 4.10. The onset temperature for all TPO profiles is at 400 °C, hence the oxidation occurs at a lower temperature compared to reduction. The TPO profiles exhibits two separate peaks, which represent the two step oxidation process in the formation of V_2O_5 . The TPO profile resembles the envelope of the TPR profile viewed from higher to lower temperatures. This suggests that the transitions observed in the TPR experiments with V_2O_5 are reversed in TPO experiments [28]. Two steps can be distinguished according to the integrated oxygen consumption, the first peak at around 400-600 °C corresponds the transition of V_2O_3 to VO_2 , and the second sharp peak at around 600–800 °C represents the formation of V_2O_5 .



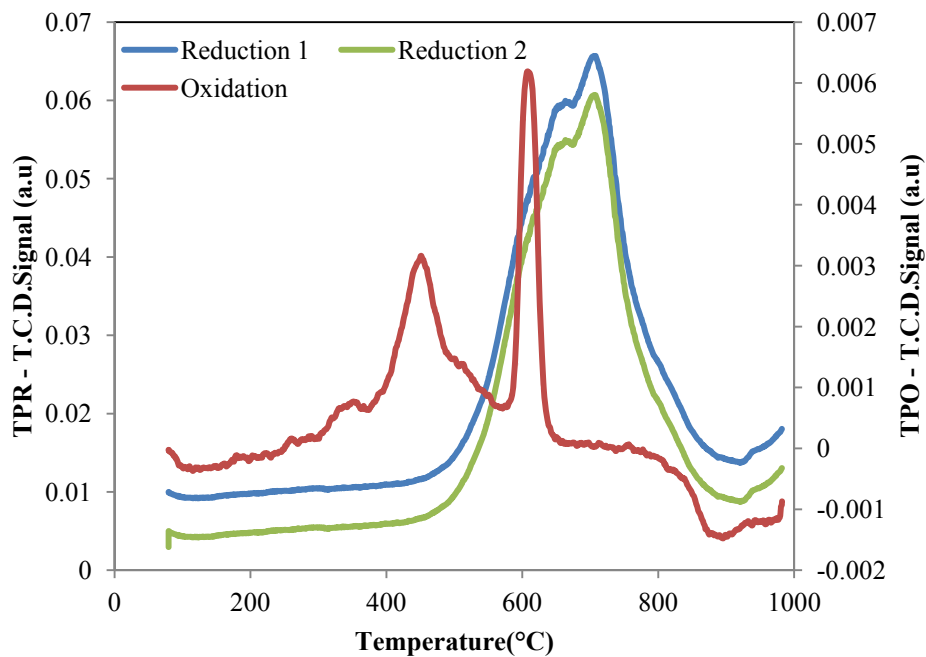


Figure 4.7 TPR-TPO-TPR profiles of 10VCa-HAp

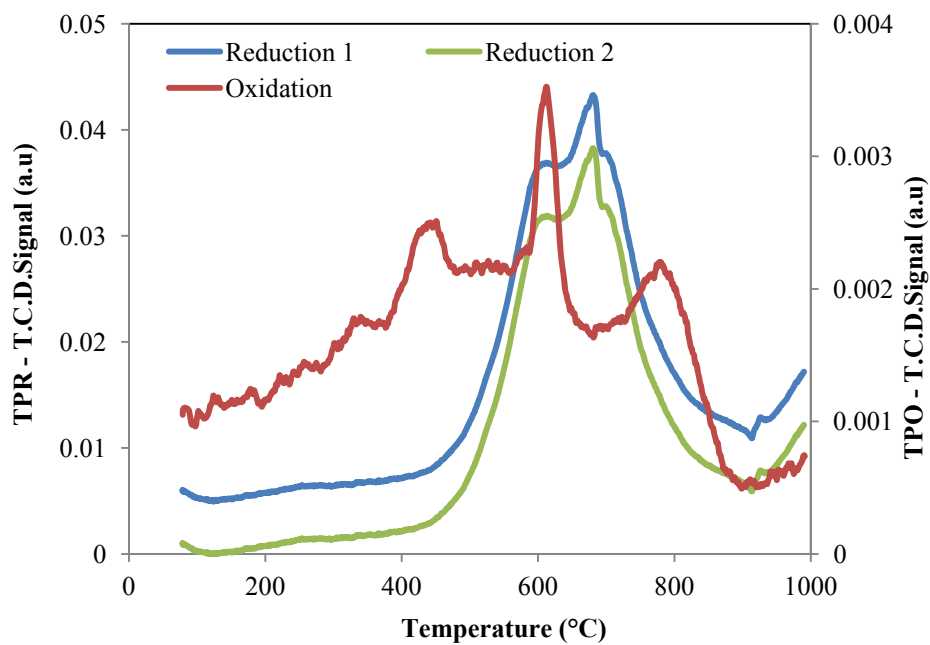


Figure 4.8 TPR-TPO-TPR profiles of 10VSr-HAp

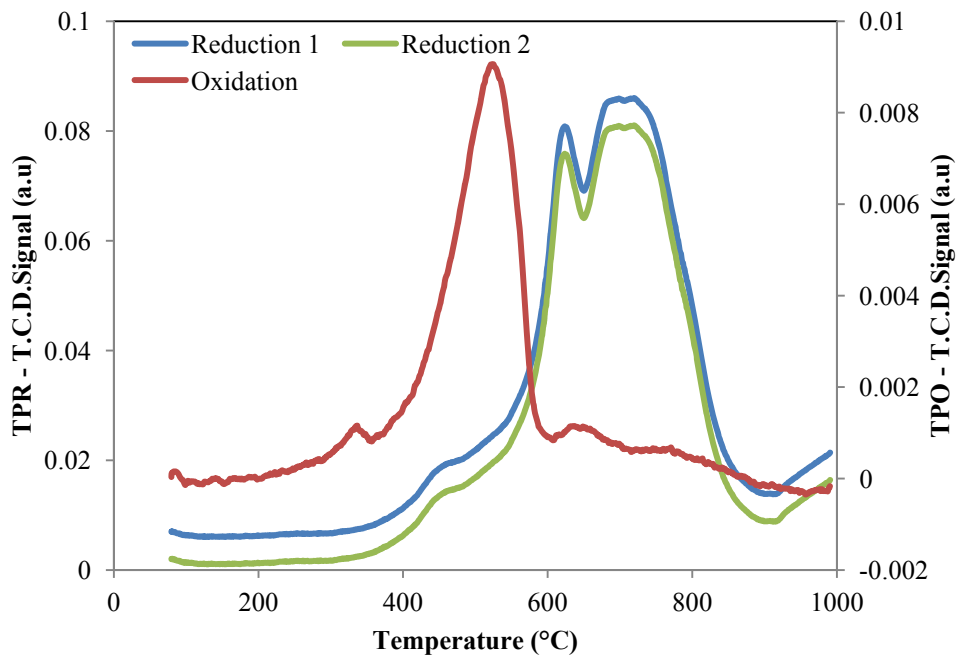


Figure 4.9 TPR-TPO-TPR profiles of 10VMg-HAp

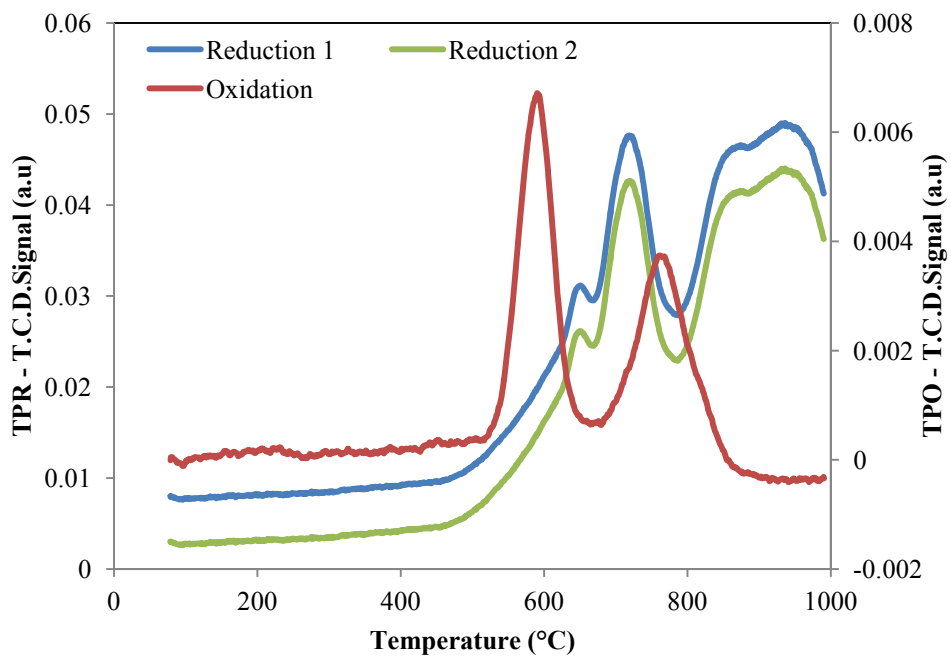


Figure 4.10 TPR-TPO-TPR profiles of 10VBa-HAp

Table 4.2 TPO data of vanadium supported on hydroxyapatites

Catalyst	Peak Temperature (°C)	Mol. of oxygen consumed (cm ³ /g)	Average oxidation state of vanadium	Degree of Reduction (%)
2.5VCa-HAp	520	2.55	3.94	53.4
	605	1.85	4.61	27.0
	780	0.75	4.89	12.9
2.5VSr-HAp	240	0.58	3.21	9.3
	457	0.97	3.57	18.9
	267	1.88	4.26	37.3
	798	1.58	4.84	28.6
2.5VMg-HAp	439	1.24	3.46	21.4
	554	2.80	4.49	65.8
	704	0.84	4.80	7.4
2.5VBa-HAp	595	3.59	4.33	63.4
	805	1.33	4.83	32.4
10VCa-HAp	457	1.85	2.67	16.8
	613	2.85	4.72	26.4
10VSr-HAp	448	1.28	3.47	27.9
	614	2.47	4.37	52.7
	787	0.89	4.70	18.1
10VMg-HAp	343	0.54	3.19	14.9
	530	3.80	4.59	64.9
	624	0.44	4.76	14.1
10VBa-HAp	594	2.60	3.96	64.7
	777	2.04	4.71	31.8

The TPO profiles of the 2.5 wt% V₂O₅ on hydroxyapatites showed more peaks than those for the 10 wt% hydroxyapatites due to the strong interaction of the oxidised vanadium with the support. Compared to V₂O₅, supported vanadia catalysts are easier to reduce and oxidise. These results furthermore suggest that polymeric and crystalline vanadia species present with higher vanadium loadings are easier to oxidise, but more difficult to reduce, whereas highly dispersed vanadia present with lower vanadium loadings are easier to reduce, but more difficult to oxidise (Table 4.2). As the vanadium content increased, the peak at the lower temperature gradually grew in area, however, the peak at higher temperature progressively diminished. The shift of the peak temperatures for lower vanadium loadings increases indicating that the oxidation of the corresponding vanadium species becomes difficult in the samples with low vanadium content. This is in agreement with the results obtained by Majunke and Baerns [29] who observed a higher degree of reduction for lower vanadium loadings when the same reduction treatment was used. The peak shapes, along with the oxygen consumption and the corresponding oxidation states of the oxidized vanadium, indicate that vanadium was predominantly oxidised to V⁴⁺ and further oxidation to V⁵⁺ occurred (Table 4.2). The XRD investigations of the oxidised catalysts showed that vanadium is oxidized to V₂O₃ (V³⁺) and further oxidized to V₂O₅ (V⁵⁺). The d-spacings correlate with JCPDS File No. 26-278 for V₂O₃ and with JCPDS File No. 9-387 for V₂O₅ respectively [21].

4.3.1.4 Temperature programmed reduction after oxidation

The second reduction profile correlates with the first reduction profile of the catalysts, indicating that vanadium is in the V₂O₅ phase after oxidation (Figs. 4.3- 4.10). A shoulder and a peak appear in the 600 °C and 700 °C range. According to Bond et al. [30] and Dias et al. [31], the first peak can be attributed to VO_x monolayer species which are more reducible than pure V₂O₅. The shoulder detected is probably associated with small crystallites of V₂O₅. Also temperatures corresponding to the TPR peaks show an increase with V₂O₅ content. This increase of V₂O₅ content leads to higher heterogeneity of the vanadium reduction centres which causes an increase in the temperature of reduction [16]. It is also generally accepted that monomeric vanadates and polyvanadates chains are formed at low vanadium loading [32, 33]. When the concentration increases, polyvanadate chains condense to form a surface vanadium monolayer and finally crystalline V₂O₅ appears for concentrations above the monolayer capacity.

Table 4.3 TPR-TPO-TPR data of vanadium supported on hydroxyapatites

Catalyst	Peak Temperature (°C)	Mol. of hydrogen consumed (cm ³ /g)	Average oxidation state of vanadium	Degree of Reduction (%)
2.5VCa-HAp	588	2.11	4.61	19.3
	662	4.25	3.84	38.9
	725	1.22	3.62	11.5
	847	1.85	3.27	17.2
2.5VSr-HAp	614	4.97	4.08	45.6
	676	1.95	3.72	27.8
	718	1.85	3.39	16.9
2.5VMg-HAp	553	1.24	4.77	11.3
	668	5.05	3.85	56.2
	753	2.14	3.45	19.6
2.5VBa-HAp	615	1.59	4.70	14.5
	735	4.93	3.80	55.1
	899	2.39	3.37	21.9
10VCa-HAp	660	5.11	4.06	46.7
	710	4.25	3.28	38.9
10VSr-HAp	597	5.37	4.01	49.3
	685	2.49	3.47	27.4
	725	1.05	3.28	9.6
10VMg-HAp	553	1.14	4.79	10.4
	668	5.35	3.82	49.5
	753	2.74	3.32	25.1
10VBa-HAp	660	2.49	4.54	22.8
	725	4.93	3.64	46.2
	875	1.89	3.29	19.9

The peak shapes along with the hydrogen consumption and the corresponding oxidation states of the reduced vanadium indicate that vanadium was predominantly reduced to V⁴⁺ and that some further reduction to V³⁺ occurred (Table 4.3). The XRD investigations on the reduced catalysts

shows that vanadium is reduced to VO_4 (V^{4+}) and V_2O_3 (V^{3+}) phases. The d-spacings correlate with the JCPDS File No. 25-1003 for VO_4 and JCPDS File No. 26-278 for V_2O_3 respectively.

For the lower vanadium loadings the first peak between 630-660 °C is probably due to reduction of the vanadium in slightly different environments as indicated by the hydrogen consumption and average oxidation state. The second peak, between 700-770 °C, is presumably for a further reduction step of vanadium from V^{5+} to the V^{4+} state. For the 10 wt % loadings, there are small shoulders present indicating that the vanadium exists in two phases, most likely, including the pyrovanadate phase which is more reducible than V_2O_5 . The reduction peak for pyrovanadate is shown between 750-775 °C. Compared to the V_2O_5 , the reduction of the oxygen in distorted VO_4 units is relatively easy [34]. As the vanadium content increased, the peak at the lower temperature gradually increased; whereas, the peak at a higher temperature decreased progressively (Table 4.3). The shoulder at around 820-840 °C shows the reduction to V^{3+} . The shifts of the peak temperatures from the lower vanadium loadings indicate that the reduction of the corresponding oxygen species becomes difficult in the samples with high vanadium content [35].

4.3.1.5 X-ray photon spectroscopy (XPS)

Figures 4.11 and 4.12 show the XPS spectra of V_2O_5 supported on hydroxyapatite catalysts. The characteristic peak for the V^{5+} state was observed at 517.3 eV which agrees with literature [36, 37], $\text{V}2\text{p}3/2$ binding energy and $\text{V}2\text{p}3/2$ - $\text{V}2\text{p}1/2$ splitting values are in correlation with the NIST Database [38]. The spectra for the V^{5+} oxide showed the $\text{V}2\text{p}3/2$ splitting peak at 517 eV and $\text{V}2\text{p}1/2$ splitting at 524.3 eV for all the catalysts, showing that vanadium is in the V_2O_5 phase on the surface of the hydroxyapatite. The $\text{V}2\text{p}1/2$ - $\text{V}2\text{p}3/2$ splitting occurred in between 7.32-7.31 eV. The reference peak for the $\text{O}1\text{s}$ splitting was shown at 531.2 eV for all the catalysts [38]. Since the energy splitting value between the V^{5+} and V^{4+} oxidation states is 1 eV, these oxidation states are distinguished by deconvoluting the XPS spectra. The characteristic peak for V^{4+} oxidation state is observed at 516.9 eV for 10 wt % V_2O_5 supported on hydroxyapatite catalysts, indicating the presence of the pyrovanadate phase along with the vanadium pentoxide phase.

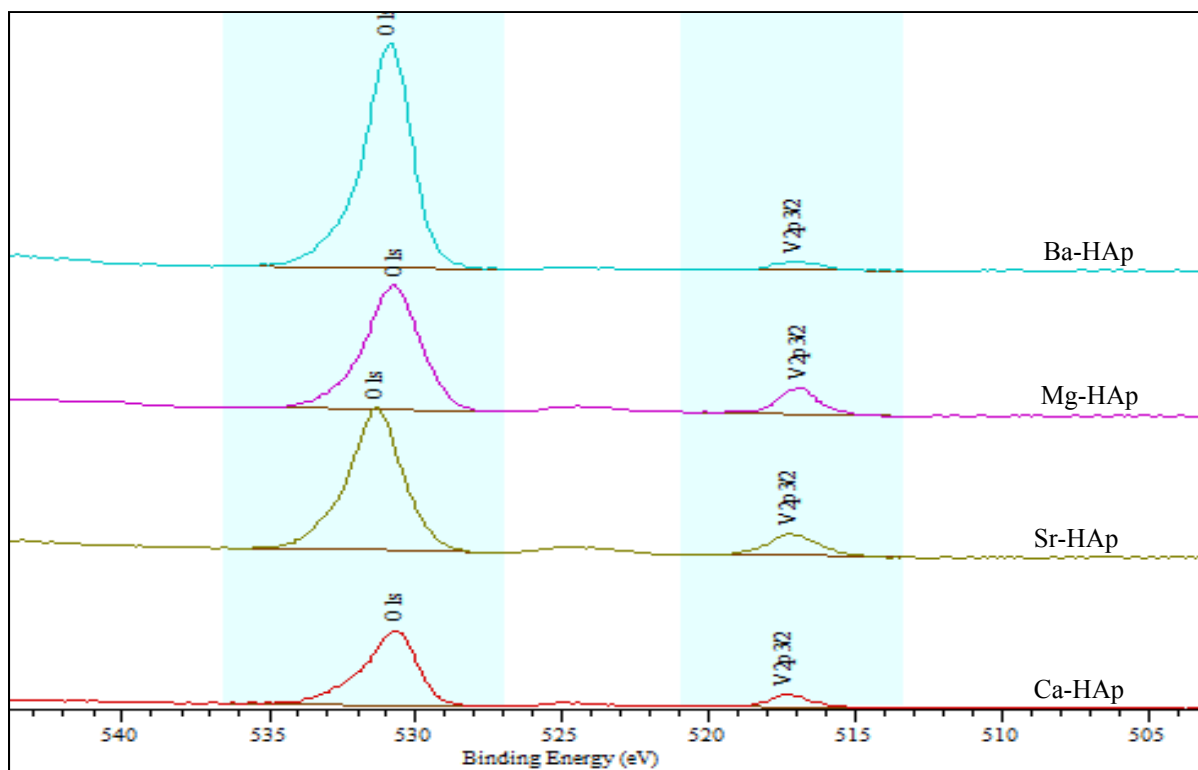


Figure 4.11 XPS spectra of 2.5 wt % V_2O_5 supported on hydroxyapatites

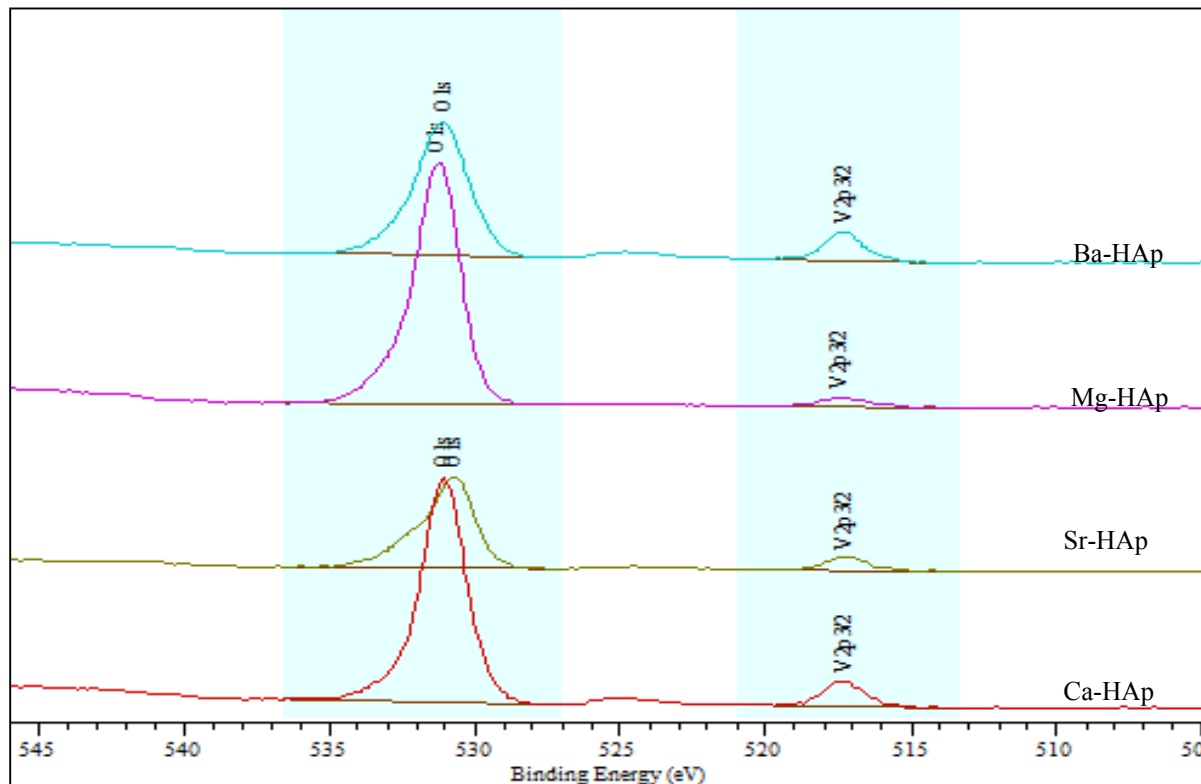


Figure 4.12 XPS spectra of 10 wt % V_2O_5 supported on hydroxyapatites

The deconvolution was performed in the catalyst samples after TPR and TPO to monitor the relative ratio of V^{5+} , V^{4+} and V^{3+} .

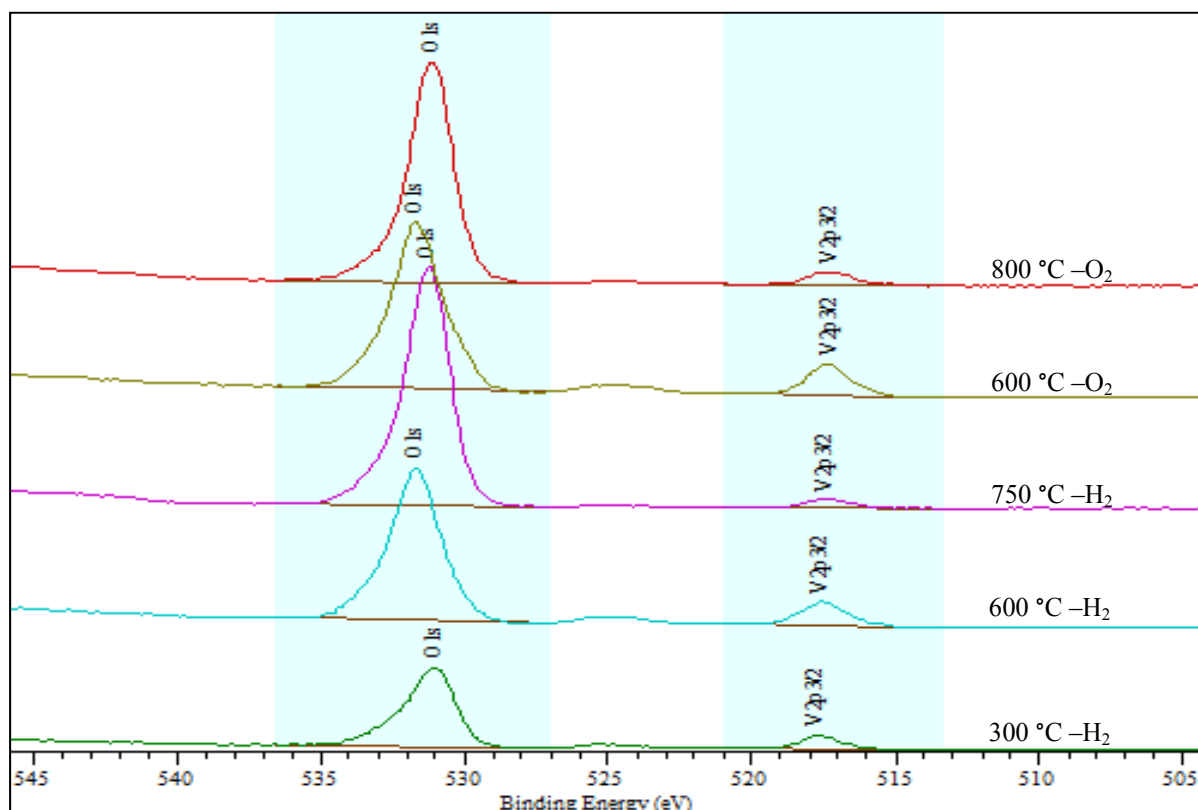


Figure 4.13 XPS spectra of 2.5 wt % V_2O_5 supported on calcium hydroxyapatite catalyst samples under reduction and oxygen environments

Figure 4.13 shows the XPS spectra of 2.5 wt% V_2O_5 supported on calcium hydroxyapatite catalyst under reduction and oxidation environments. Under hydrogen, at 300 °C the characteristic peak for V^{5+} is observed at 517.3 eV. $V_{2p3/2}$ binding energy and $V_{2p3/2}$ - $V_{2p1/2}$ splitting values are in correlations with the NIST Database. The reference peak for the O1s splitting was shown at 531.2 eV at all temperatures. At 600 °C, the characteristic peak for the V^{4+} oxidation state is observed at 516.9 eV showing the reduction of V^{5+} to V^{4+} . V^{4+} is further reduced to V^{3+} , shown by the peak at 515.4 eV for a temperature of 750 °C. During oxidation, V^{3+} is oxidized to V^{4+} at 600 °C and further oxidized to V^{5+} at 800 °C. In the redox environment, at all temperatures, the V^{5+} oxidation state is present as a major phase, as shown by the peak at 517.3 eV. At each temperature, vanadium is in a mixed oxidation state which is also evidenced

by TPR and XRD investigations [16]. It can be concluded that the V_2O_5 phase is a reversible phase, which can be reduced to the V^{3+} oxidation state and can be reoxidised to the V^{5+} oxidation state.

4.3.2 Catalytic Results

1-Octene

Selectivity of oxygenates is high at 1-octene to oxygen molar ratios of 1:0.5 and 1:1. At the 1:0.5 molar ratio the CO_x selectivity increases for the 2.5 wt% catalysts in the order $Ca < Sr < Mg < Ba$. The increase in the CO_x selectivity results in a decrease in the aromatics selectivity, i.e. CO_x is formed during the secondary combustion of aromatics (Figs. 4.14, 4.15 and 4.16). Low selectivity of cracked products is shown at a hydrocarbon to oxygen ratio of 1:0.5 relative to the ratios of 1:1 and 1:2. For the oxidative reaction of *n*-octane, and generally for long chain alkanes, it was proposed that the cracked products are formed via steam and dry homogenous cracking that was enhanced by formation of water and carbon dioxide in a preceding oxidation step on the catalyst surface [39, 40].

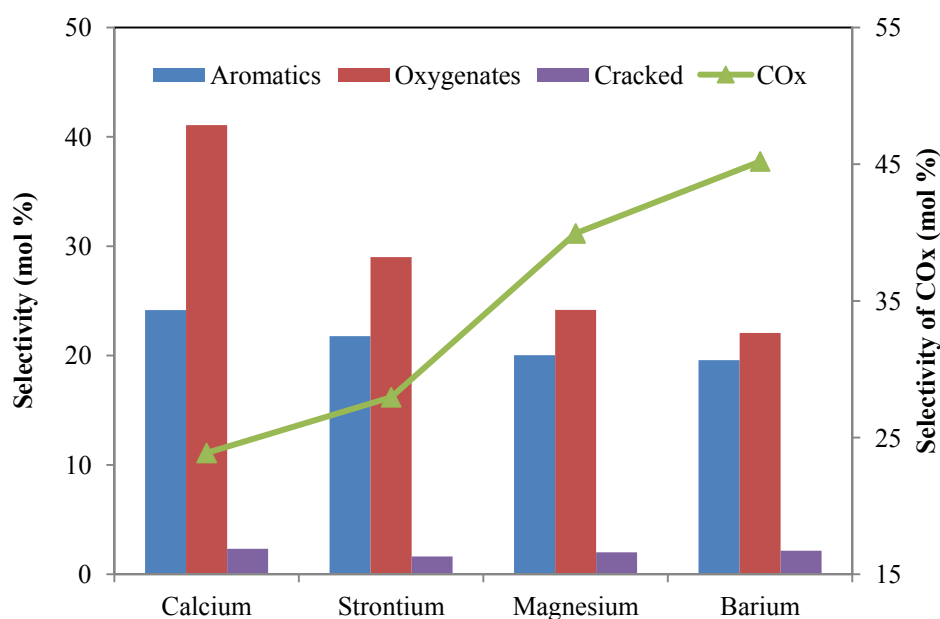


Figure 4.14 Selectivity of products in the ODH of 1-octene with 2.5 V_2O_5 wt% supported on hydroxyapatites at iso-conversion (27%), temperature = 450 °C and 1-octene to oxygen molar ratio of 1:0.5

For the 1-octene to oxygen molar ratio of 1:1, oxygenates are dominant in the product profile when 2.5VMg-HAp is used as the catalyst. This is due to the strongly acidic magnesium

hydroxyapatite in the presence of V_2O_5 containing V=O bonds, where V^{5+} in octahedral coordination results in the incorporation of oxygen in the intermediate reaction products, leading to formation of oxygenate compounds [35].

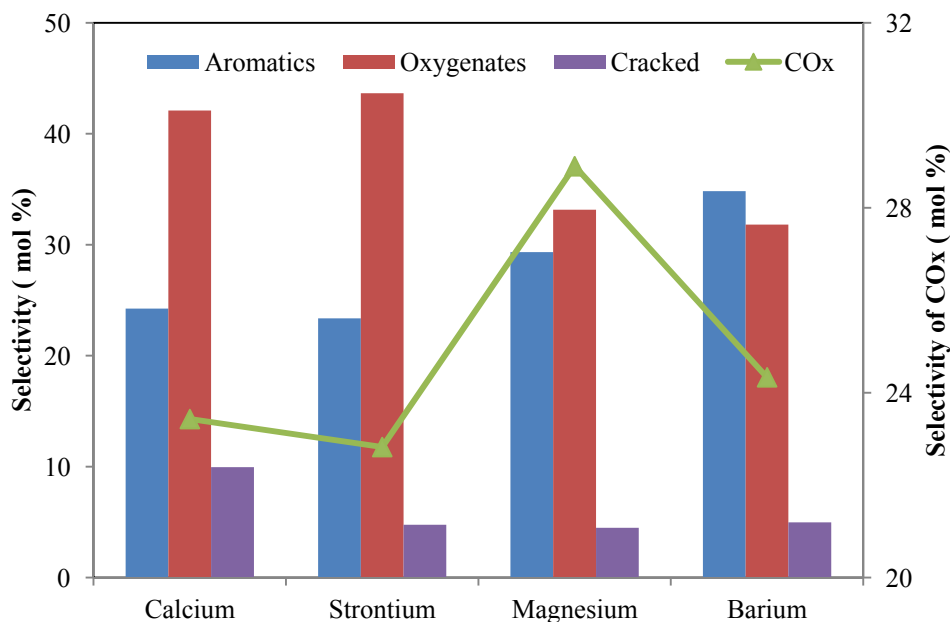


Figure 4.15 Selectivity of products in the ODH of 1-octene with 2.5 V_2O_5 wt% supported on hydroxyapatites at iso-conversion (27%), temperature = 450 °C and 1-octene to oxygen molar ratio of 1:1

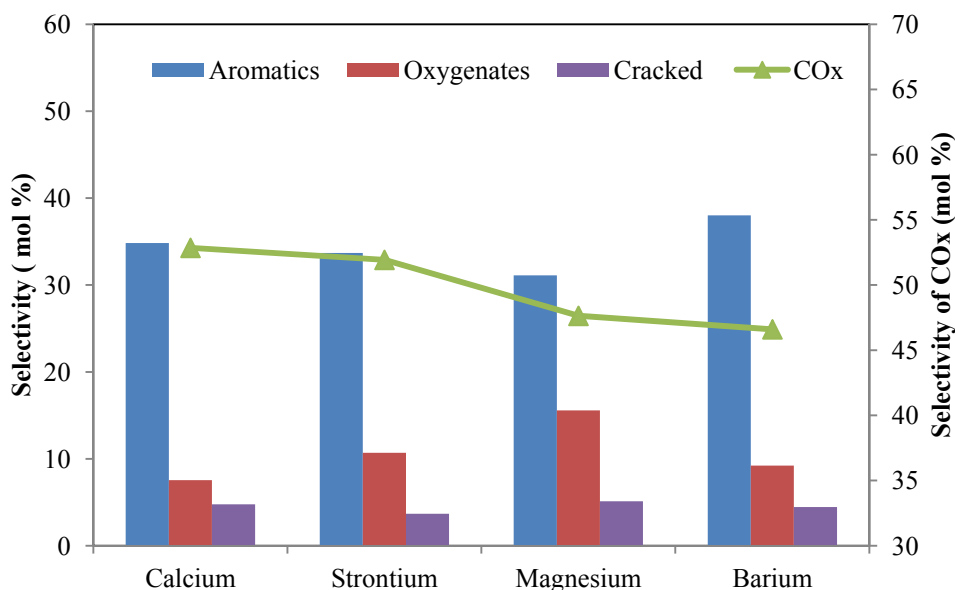


Figure 4.16 Selectivity of products in the ODH of 1-octene with 2.5 V_2O_5 wt % supported on hydroxyapatites at iso-conversion (27%), temperature = 450 °C and 1-octene to oxygen molar ratio of 1:2

At the 1-octene to oxygen ratio of 1:2, 2.5VBa-HAp showed highest selectivity towards aromatics. This is probably due to the specific acidity of 2.5VBa-HAp, which enhances the ODH on the surface of the catalyst in a highly oxidising environment. At a 1-octene to oxygen molar ratio of 1:0.5 it showed low selectivity towards both aromatics and oxygenates (Figs. 4.14, 4.15 and 4.16). In the oxygen rich environment, the abstraction of lattice oxygen of the 2.5VBa-HAp, followed by the incorporation of the gaseous oxygen into the vacancy formed with the abstraction, should principally contribute to the selectivity of aromatics and oxygenates [41].

Selectivity to CO_x dominates over the selectivity to aromatics at all 1-octene to oxygen molar ratios (Figs. 4.17, 4.18 and 4.19), when 10 wt % V_2O_5 supported hydroxyapatites are used. Selectivity of aromatics decreases with the increase in the oxygen concentration, which can be attributed to the secondary combustion of the formed ODH products i.e. the combustion of the precursor octenes and the formed aromatics [15]. 10VBa-HAp showed high selectivity towards oxygenates among all hydroxyapatites supports relative to cracked products. This could be attributed to the typical Lewis acidic nature of the 10VBa-HAp which favours the oxidation of 1-octene to oxygenates (Figs. 4.17, 4.18 and 4.19).

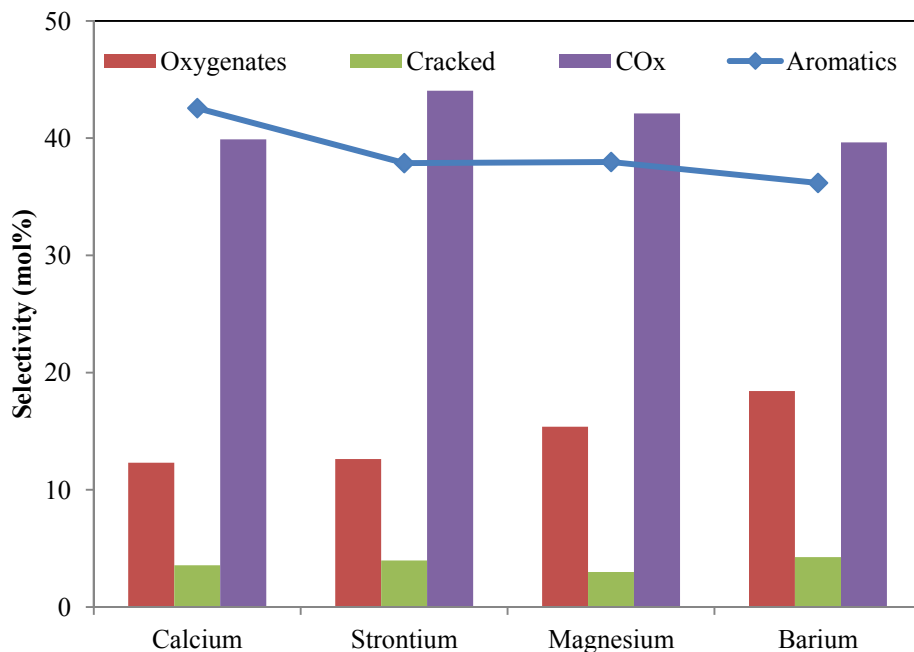


Figure 4.17 Selectivity of products in the ODH of 1-octene with 10 wt% V_2O_5 supported on hydroxyapatites at iso-conversion (27%), temperature = 450 °C and 1-octene to oxygen molar ratio of 1:0.5

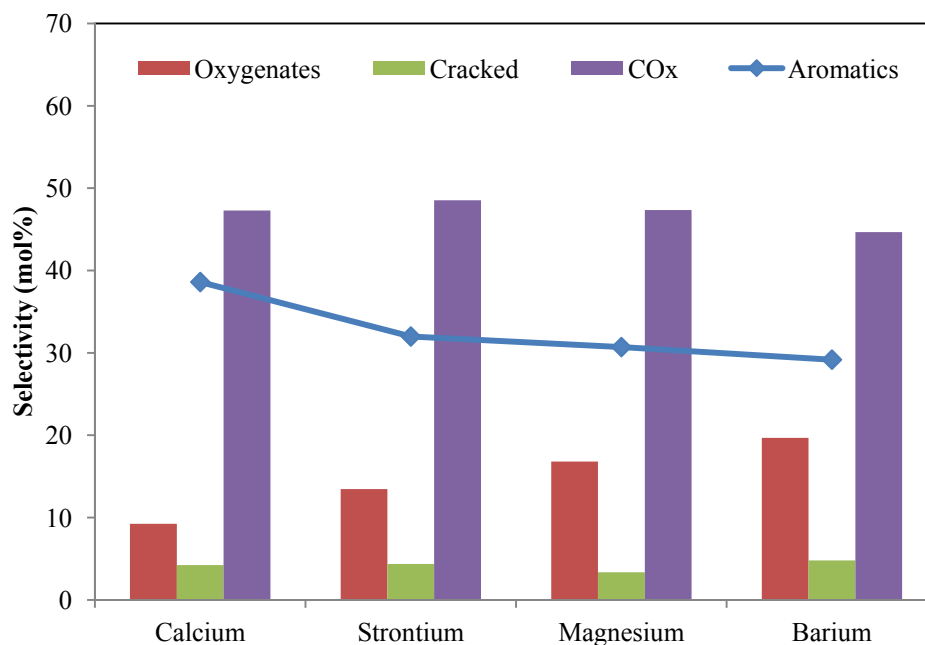


Figure 4.18 Selectivity of products in the ODH of 1-octene with 10 wt% V₂O₅ supported on hydroxyapatites at iso-conversion (27%), temperature = 450 °C and 1-octene to oxygen molar ratio of 1:1

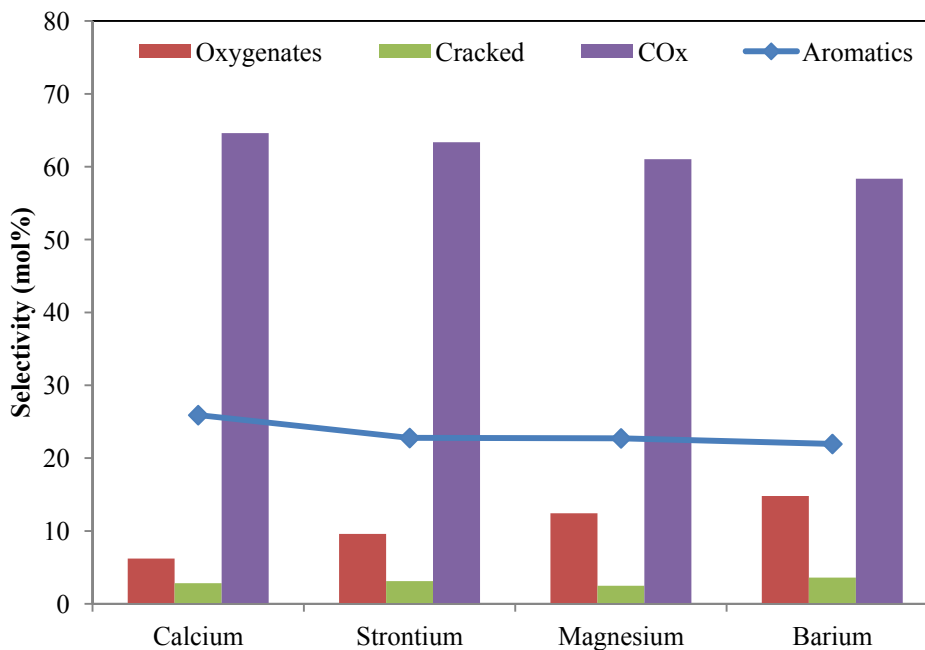


Figure 4.19 Selectivity of products in the ODH of 1-octene with 10 wt% V₂O₅ supported on hydroxyapatites at iso-conversion (27%), temperature = 450 °C and 1-octene to oxygen molar ratio of 1:2

2-Octene

2.5VSr-HAp showed highest selectivity towards the cracked products at all 2-octene to oxygen molar ratios. From these results it is evident that cracking over 2.5VSr-HAp decreases the selectivity of CO_x relative to 2.5VCa-HAp and 2.5VBa-HAp (Figs. 4.20, 4.21 and 4.22). Selectivity to aromatics is high at low oxygen ratios and decreases with the increase in oxygen ratio. This is due to the secondary combustion of ODH products under oxygen rich environments [14, 15]. The highest selectivity towards aromatics is shown by 2.5VMg-HAp, which was also evident by the VMgO systems in the oxidative dehydrogenation of *n*-octane [14].

Selectivity towards CO_x is high at 2-octene to oxygen molar ratios of 1:2 relative to other oxygen molar ratios (Figs. 4.20, 4.21 and 4.22). For all 2-octene to oxygen molar ratios the 2.5VBa-HAp showed highest selectivity towards CO_x due to its specific acidity which favours the deep oxidation of the ODH products. In the oxygen rich environment, the abstraction of lattice oxygen by the vanadium oxide on the barium hydroxyapatites, followed by the incorporation of the gaseous oxygen into the vacancy formed with the abstraction, should principally contribute to the selectivity of aromatics and oxygenates, which is followed by the secondary combustion to CO_x [15].

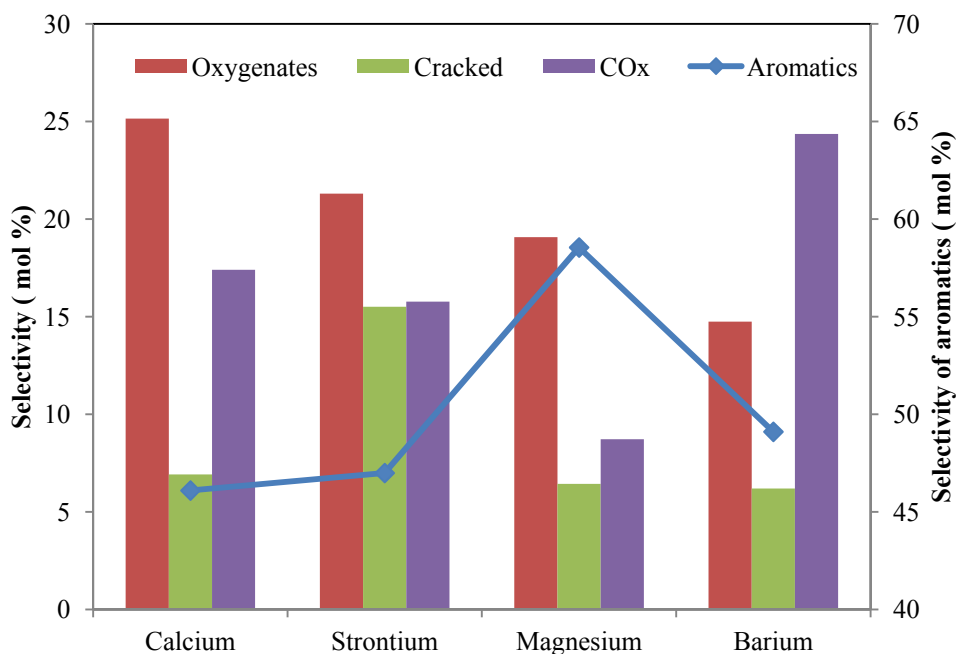


Figure 4.20 Selectivity of products in the ODH of 2-octene with 2.5 wt% V₂O₅ supported on hydroxyapatites at iso-conversion (27%), temperature = 450 °C and 2-octene to oxygen molar ratio of 1:0.5

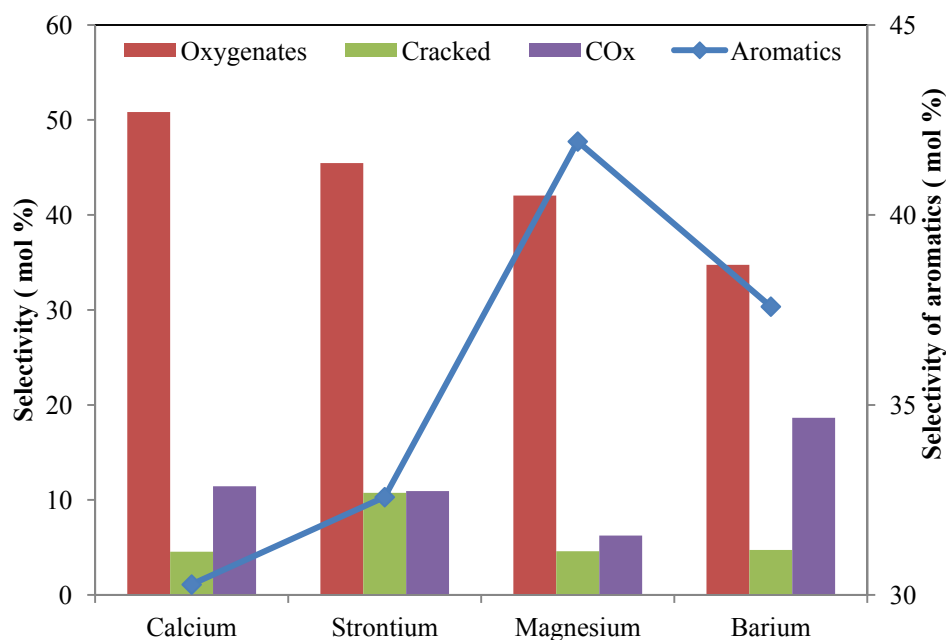


Figure 4.21 Selectivity of products in the ODH of 2-octene with 2.5 wt% V_2O_5 supported on hydroxyapatites at iso-conversion (27%), temperature = 450 °C and 2-octene to oxygen molar ratio of 1:1

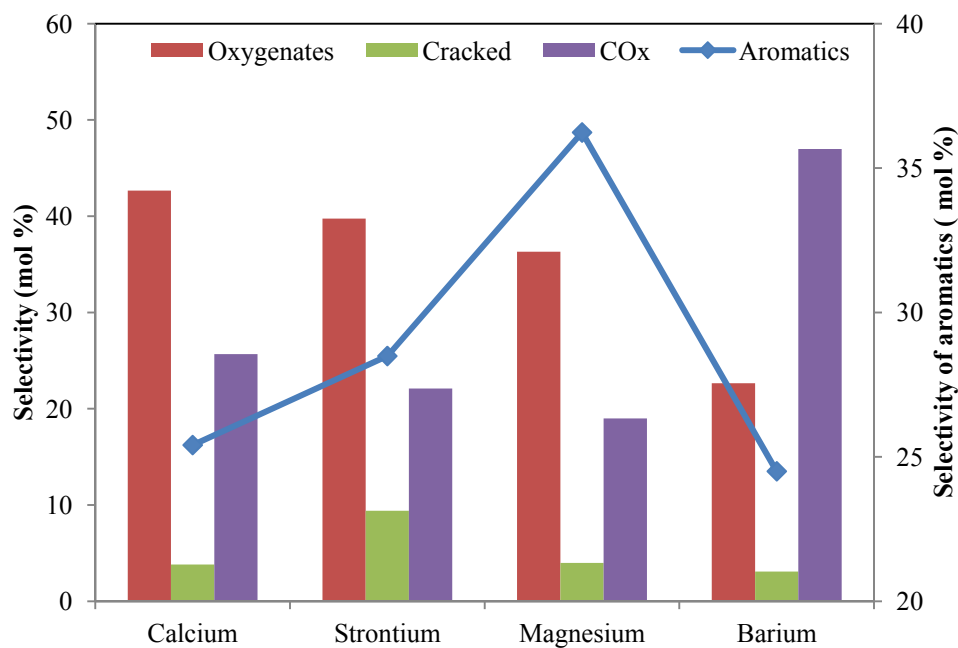


Figure 4.22 Selectivity of products in the ODH of 2-octene with 2.5 wt% V_2O_5 supported on hydroxyapatites at iso-conversion (27%), temperature = 450 °C and 2-octene to oxygen molar ratio of 1:2

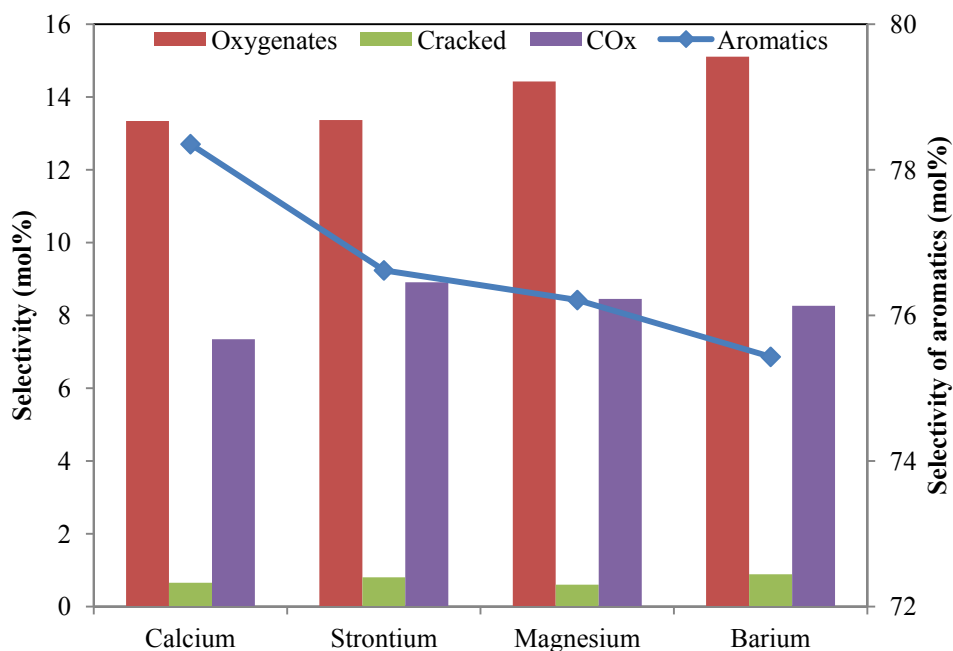


Figure 4.23 Selectivity of products in the ODH of 2-octene with 10 wt% V_2O_5 supported on hydroxyapatites at iso-conversion (27%), temperature = 450 °C and 2-octene to oxygen molar ratio of 1:0.5

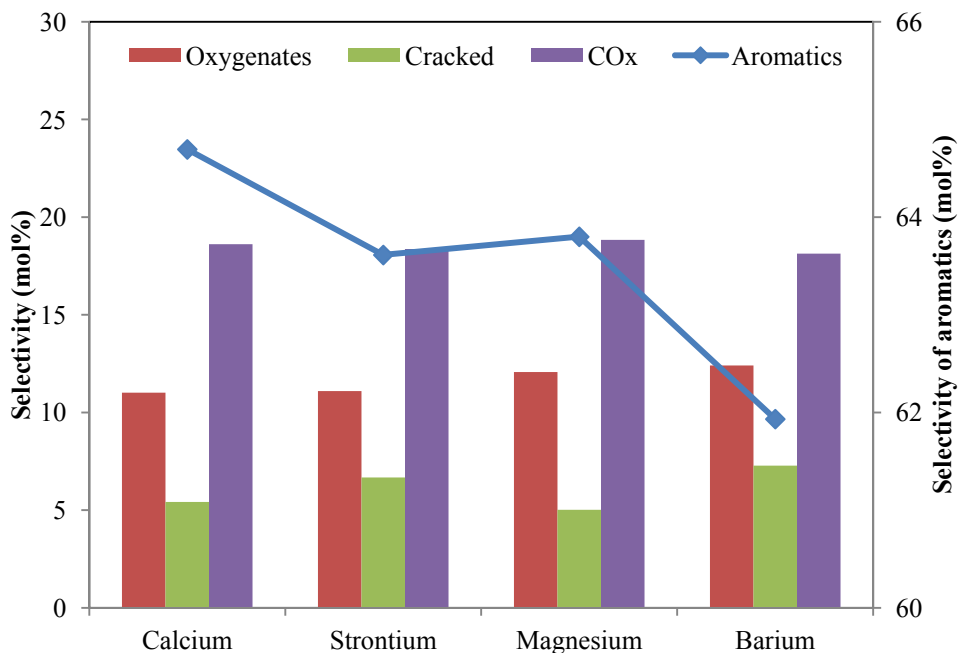


Figure 4.24 Selectivity of products in the ODH of 2-octene with 10 wt% V_2O_5 supported on hydroxyapatites at iso-conversion (27%), temperature = 450 °C and 2-octene to oxygen molar ratio of 1:1

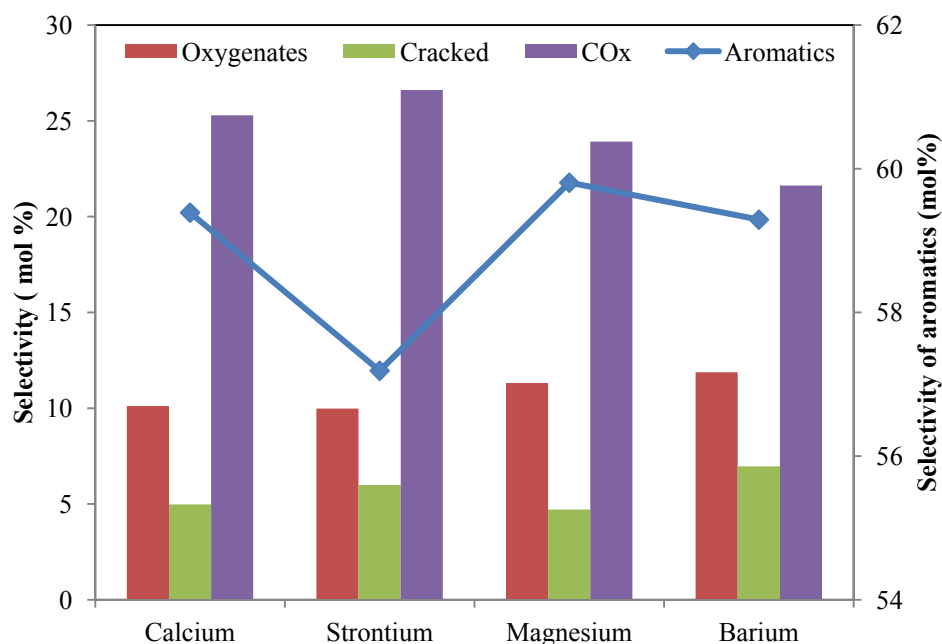


Figure 4.25 Selectivity of products in the ODH of 2-octene with 10 wt% V₂O₅ supported on hydroxyapatites at iso-conversion (27%), temperature = 450 °C and 2-octene to oxygen molar ratio of 1:2

2-octene showed highest selectivity towards aromatics at all 2-octene to oxygen molar ratios over the 10wt% vanadium supported hydroxyapatites (Figs. 4.23, 4.24 and 4.25). Selectivity of oxygenates dominates over the selectivity of CO_x at a 2-octene to oxygen molar ratio of 1:0.5. Under oxygen rich environments, like 1:1 and 1:2, the selectivity of CO_x dominates over oxygenates, due to the increase in combustion of the products. 10VBa-HAp showed high selectivity towards oxygenates at a 2-octene to oxygen molar ratio of 1:0.5 and 10VSr-HAp showed high selectivity towards CO_x at a 2-octene to oxygen molar ratio of 1:2 when 10 wt % V₂O₅ supported hydroxyapatites are used. Cracked products selectivity also increases with decrease in the 2-octene to oxygen molar ratio. The effect of selectivity on cracked products is likely due to temperature (thermal cracking), rather than the 2-octene to oxygen molar ratio, as no noticeable change in the selectivity of cracked products at 2-octene to oxygen molar ratios of 1:1 and 1:2 is seen (Figs. 4.23, 4.24 and 4.25).

3-Octene

Oxygenates showed a decrease in selectivity from 2.5VCa-HAp, 2.5VSr-HAp, 2.5VMg-HAp to 2.5VBa-HAp respectively (Figs. 4.26, 4.27 and 4.28). 2.5VMg-HAp showed highest selectivity

towards CO_x at all 3-octene to oxygen molar ratios due to the presence of vanadium in the +5 oxidation state which favors the CO_x formation. This is due to the strong acidity of the magnesium hydroxyapatite support where the $\text{V}=\text{O}$ bonds in V_2O_5 causes the incorporation of oxygen in the intermediate reaction products [34].

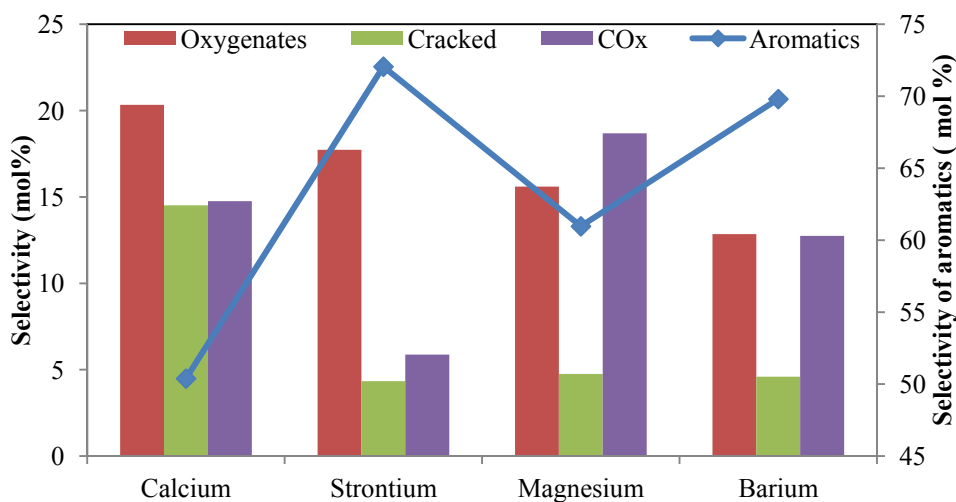


Figure 4.26 Selectivity of products in the ODH of 3-octene with 2.5 wt% V_2O_5 supported on hydroxyapatites at iso-conversion (27%), temperature = 450 °C and 3-octene to oxygen molar ratio of 1:0.5

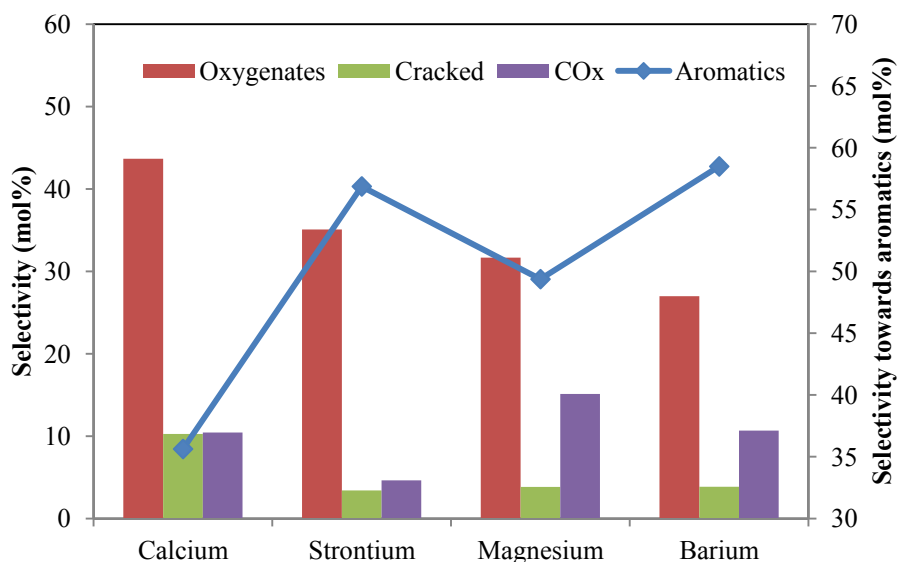


Figure 4.27 Selectivity of products in the ODH of 3-octene with 2.5 wt% V_2O_5 supported on hydroxyapatites at iso-conversion (27%), temperature = 450 °C and 3-octene to oxygen molar ratio of 1:1

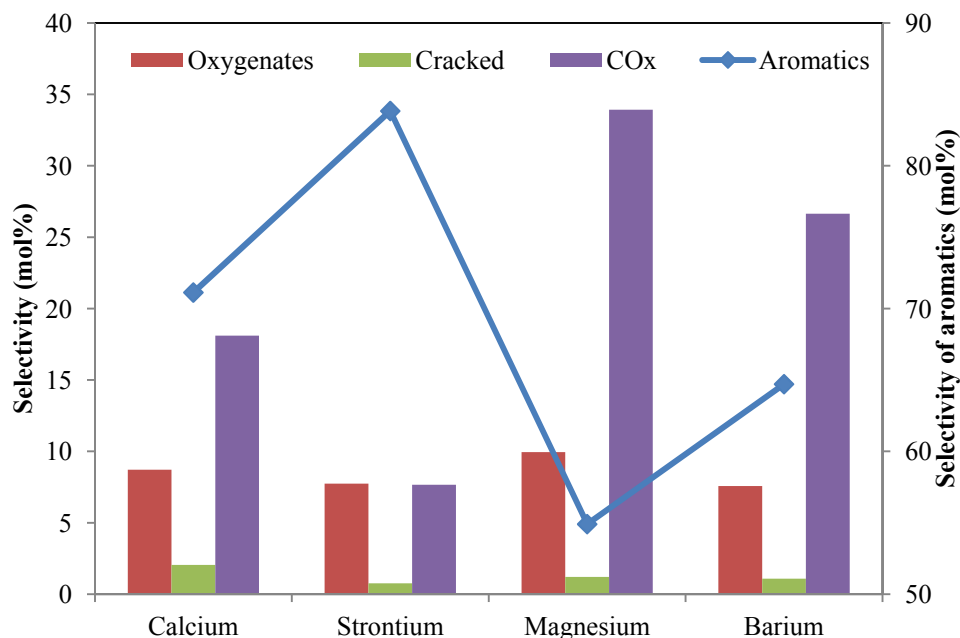


Figure 4.28 Selectivity of products in the ODH of 3-octene with 2.5 wt% V_2O_5 supported on hydroxyapatites at iso- conversion (27%), temperature = 450 °C and 3-octene to oxygen molar ratio of 1:2

All catalysts showed low selectivity towards cracking products and high selectivity towards aromatics when 3-octene was fed, indicating that cracking is not favoured when activation of *n*-octane is done at the 3rd carbon (Figs. 4.26, 4.27 and 4.28). Oxygenates showed highest selectivity under mild oxygen environments, at 3-octene to oxygen molar ratios of 1:0.5 and 1:1. As the oxygen molar ratio relative to 3-octene increased the selectivity of oxygenates decreased. This could be attributed to the secondary combustion of the oxygenates to CO_x under oxygen rich environments.

Aromatics are the dominant products at all 3-octene to oxygen molar ratios when 10 wt% V_2O_5 supported hydroxyapatites are used as catalysts. 10VBa-HAp showed low selectivity towards cracked products and oxygenates relative to the other hydroxyapatites at all 3-octene to oxygen molar ratios (Figs. 4.29, 4.30 and 4.31) as it showed highest selectivity towards aromatics. 10VCa-HAp and 10VSr-HAp showed higher selectivity towards oxygenates and cracked products compared to other catalysts. At 3-octene to oxygen molar ratio of 1:0.5 and 1:1 oxygenates have high selectivity relative to cracked products, but at a 3-octene to oxygen molar ratio of 1:2 cracked products showed high selectivity relative to oxygenates.

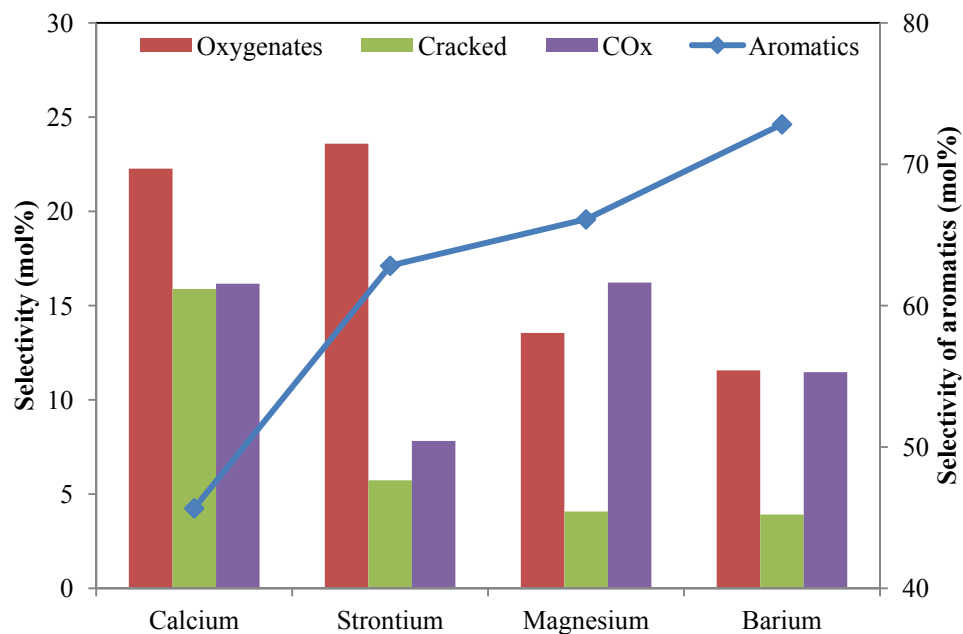


Figure 4.29 Selectivity of products in the ODH of 3-octene with 10 wt% V_2O_5 supported on hydroxyapatites at iso-conversion (27%), temperature = 450 °C and 3-octene to oxygen molar ratio of 1:0.5

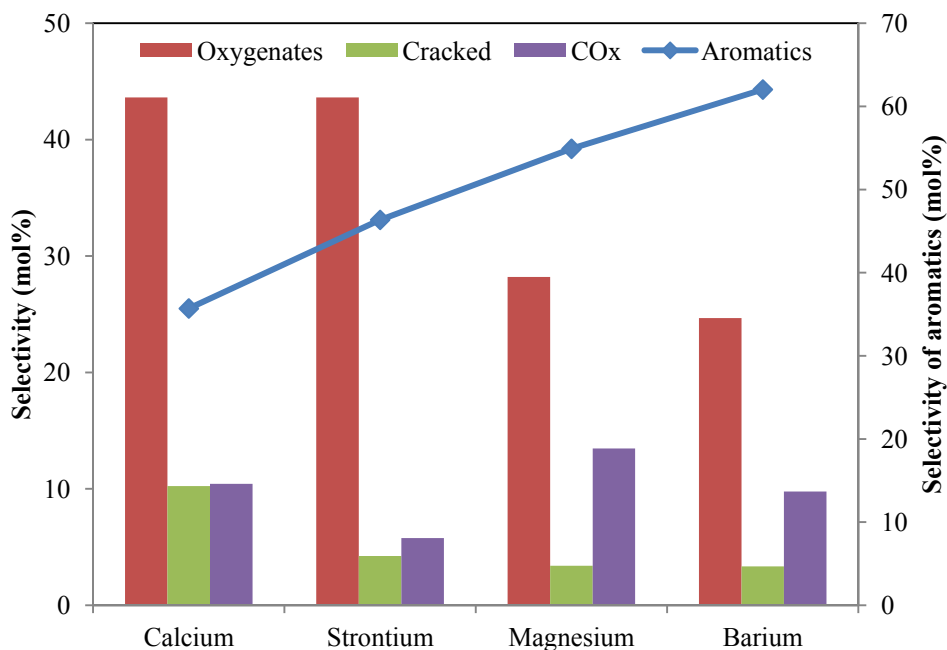


Figure 4.30 Selectivity of products in the ODH of 3-octene with 10 wt% V_2O_5 supported on hydroxyapatites at iso-conversion (27%), temperature = 450 °C and 3-octene to oxygen molar ratio of 1:1

However, the selectivity trend of cracked products for all 3-octene to oxygen molar ratio is very similar, showing that the selectivity of cracked products is affected by temperature, rather than the 3-octene to oxygen molar ratios (Figs. 4.29, 4.30 and 4.31).

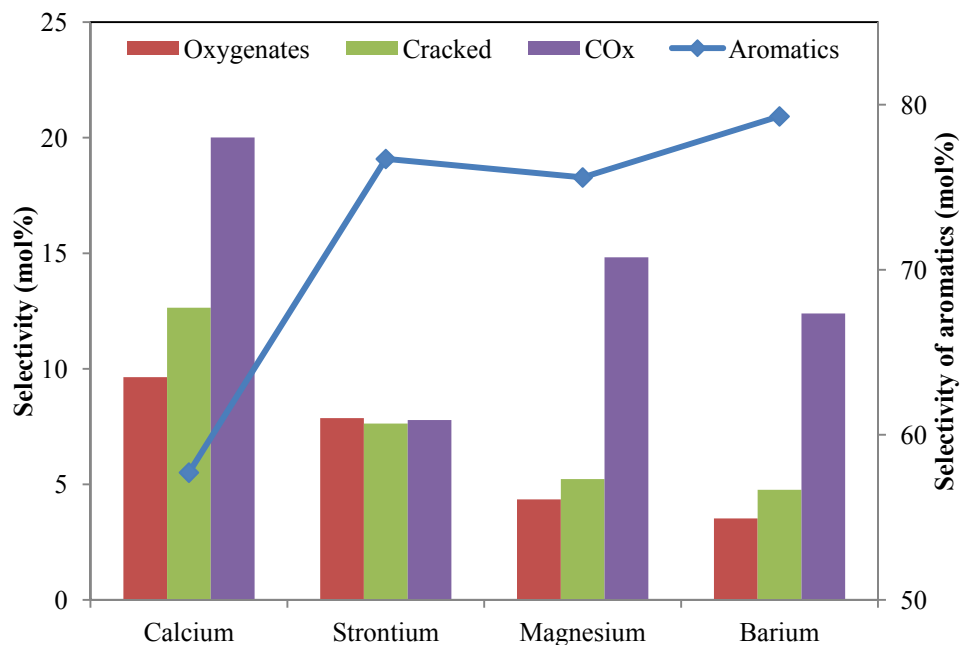


Figure 4.31 Selectivity of products in the ODH of 3-octene with 10 wt% V₂O₅ supported on hydroxyapatites at iso-conversion (27%), temperature = 450 °C and 3-octene to oxygen molar ratio of 1:2

10VMg-HAp and 10VCa-HAp showed high selectivity towards CO_x at 3-octene to oxygen molar ratios of 1:0.5 and 1:1, but at a 3-octene to oxygen molar ratio of 1:2, 10VCa-HAp showed higher selectivity towards CO_x relative to 10VMg-HAp (Figs. 4.29, 4.30 and 4.31). This could be attributed to the combustion of ODH products to CO_x, which results in the low selectivity in aromatics for 10VCa-HAp relative to other hydroxyapatites [16].

4-Octene

Highest selectivity to oxygenates is shown by 2.5VSr-HAp when 4-octene is fed and the highest aromatic selectivity is shown by 2.5VMg-HAp (Figs. 4.32, 4.33 and 4.34). The selectivity pattern is similar to that of 2-octene i.e. 2.5VMg-HAp showed highest selectivity towards aromatics at all 4-octene to oxygen molar ratios and the lowest selectivity towards aromatics is

shown by 2.5VSr-HAp. 2.5VSr-HAp showed highest selectivity towards oxygenates at all 4-octene to oxygen molar ratios (Figs. 4.32, 4.33 and 4.34).

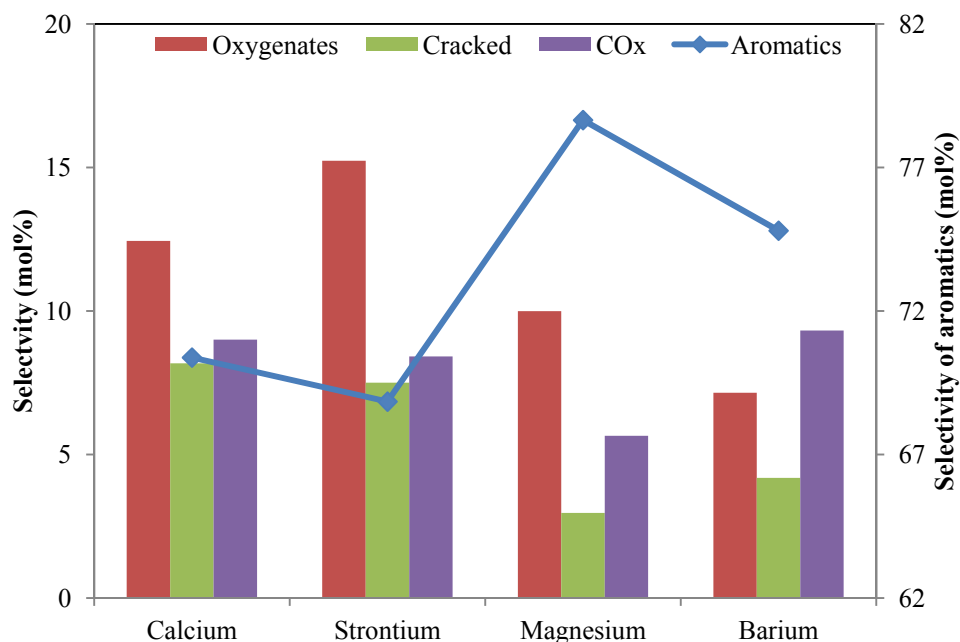


Figure 4.32 Selectivity of products in the ODH of 4-octene with 2.5 wt% V_2O_5 supported on hydroxyapatites at iso-conversion (27%), temperature = 450 °C and 4-octene to oxygen molar ratio of 1:0.5

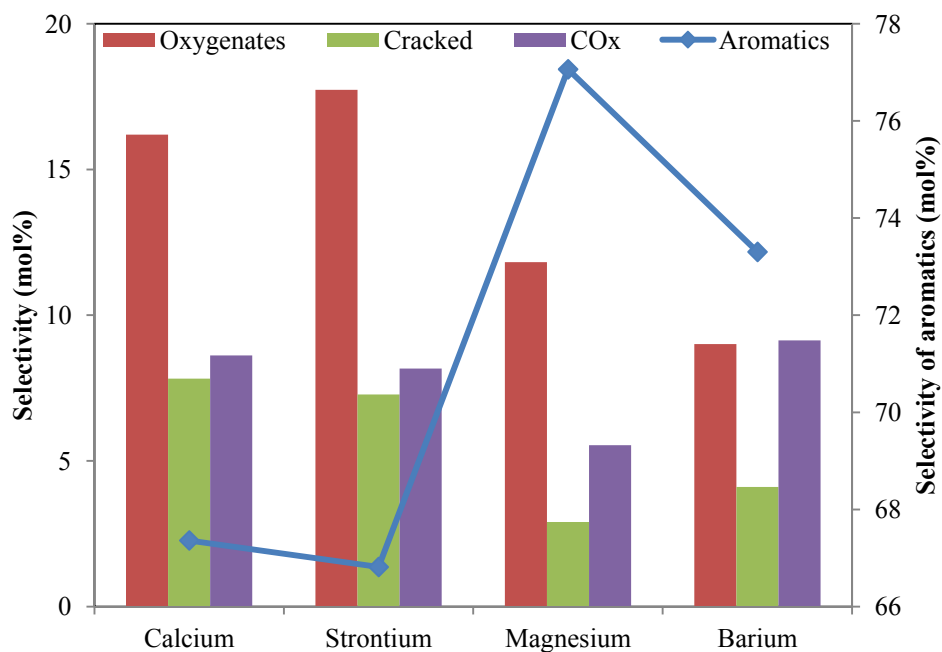


Figure 4.33 Selectivity of products in the ODH of 4-octene with 2.5 wt% V_2O_5 supported on hydroxyapatites at iso-conversion (27%), temperature = 450 °C and 4-octene to oxygen molar ratio of 1:1

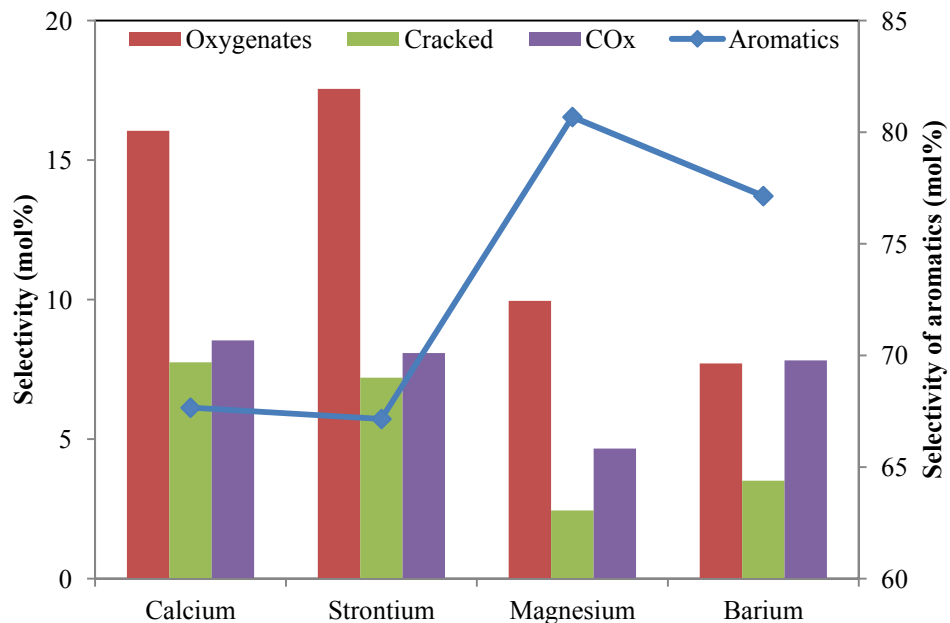


Figure 4.34 Selectivity of products in the ODH of 4-octene with 2.5 wt% V_2O_5 supported on hydroxyapatites at iso- conversion (27%), temperature = 450 °C and 4-octene to oxygen molar ratio of 1:2

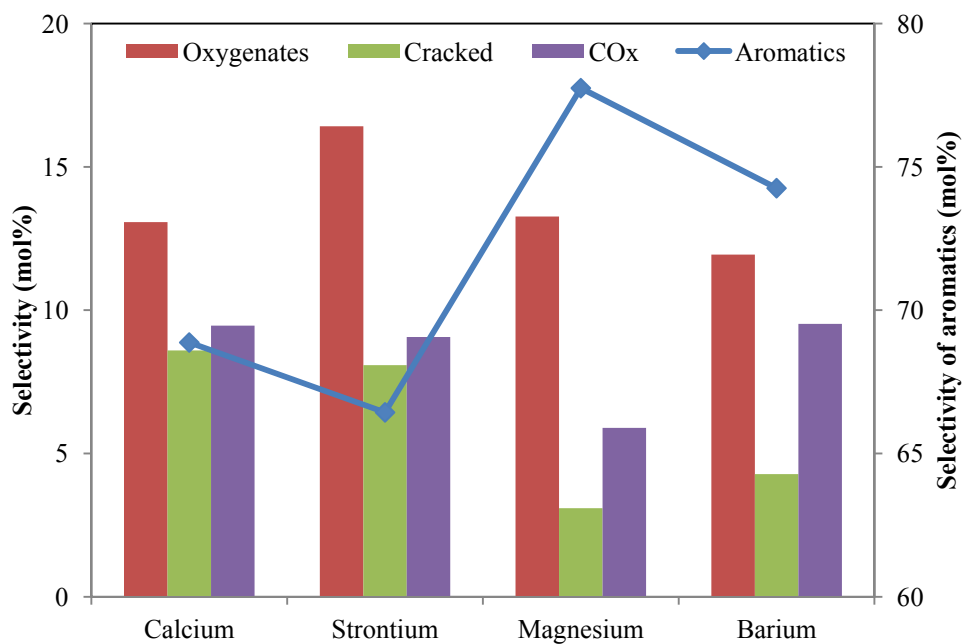


Figure 4.35 Selectivity of products in the ODH of 4-octene with 10 wt% V_2O_5 supported on hydroxyapatites at iso- conversion (27%), temperature = 450 °C and 4-octene to oxygen molar ratio of 1:0.5

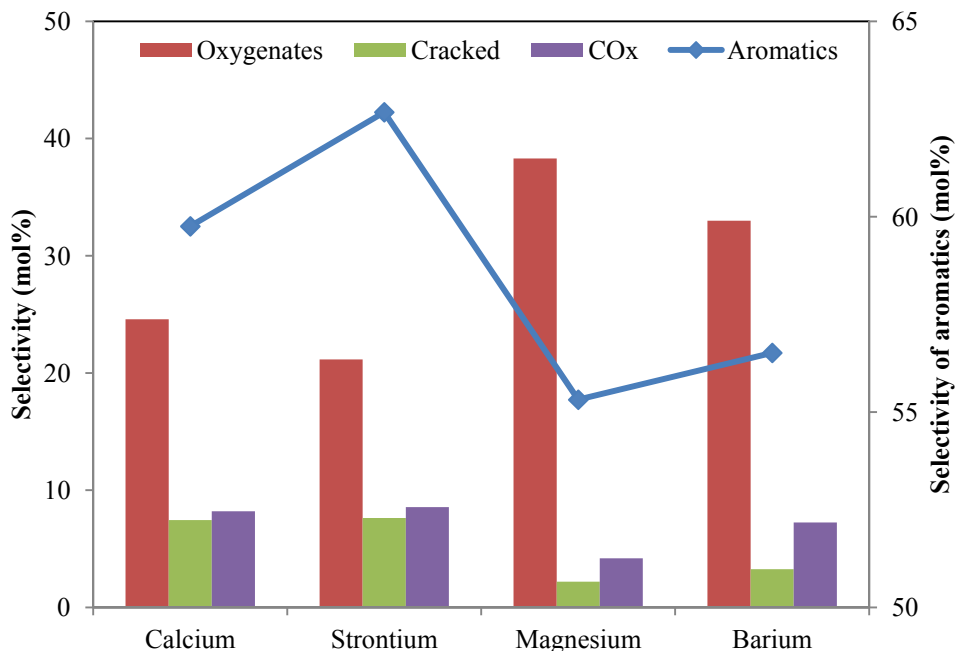


Figure 4.36 Selectivity of products in the ODH of 4-octene with 10 wt% V_2O_5 supported on hydroxyapatites at iso-conversion (27%), temperature = 450 °C and 4-octene to oxygen molar ratio of 1:1

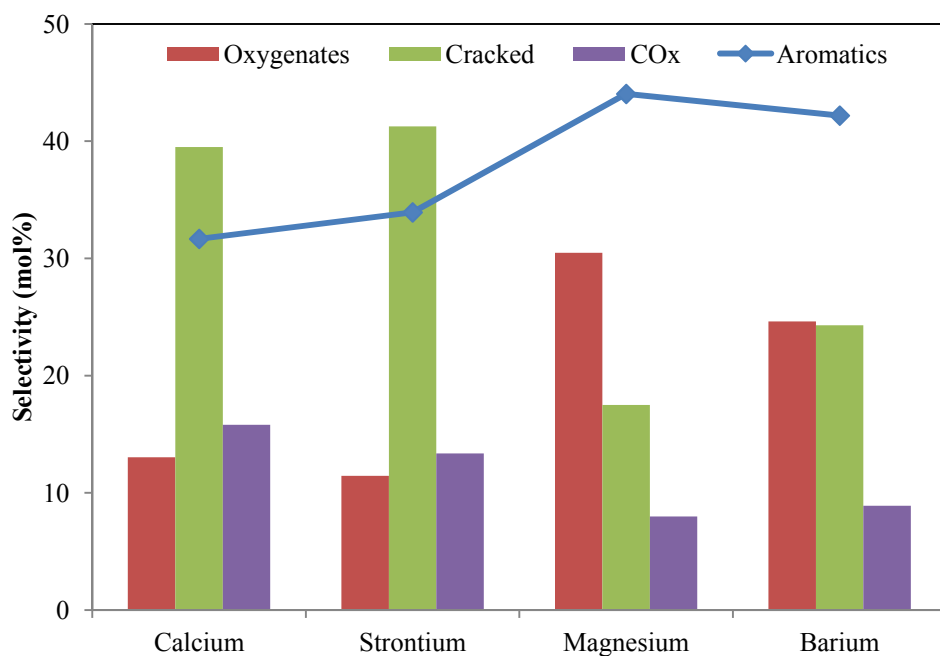


Figure 4.37 Selectivity of products in the ODH of 4-octene with 10 wt% V_2O_5 supported on hydroxyapatites at iso-conversion (27%), temperature = 450 °C and 4-octene to oxygen molar ratio of 1:2

For CO_x , 2.5VCa-HAp showed highest selectivity which is favoured by the combustion of ODH products [16, 17].

Aromatics are the dominant products at all 4-octene to oxygen molar ratios when 10 wt% V_2O_5 supported hydroxyapatites used as catalysts, but the selectivity decreases with increase in the strength of the oxidative environment (Figs. 4.35, 4.36 and 4.37). 10VMg-HAp showed high selectivity towards aromatics at 4-octene to oxygen molar ratio of 1:0.5 and 1:2, and it showed high selectivity towards oxygenates at 4-octene to oxygen molar ratios of 1:1 and 1:2. This could be attributed to the Brønsted acidity of 10VMg-HAp which favours the retention of the initial ODH products formed on the catalyst under oxygen rich environments and subsequent oxygenates and aromatics formation (Figs. 4.35, 4.36 and 4.37).

1,7-Octadiene

2.5VCa-HAp showed high selectivity towards aromatics at all 1,7-octadiene to oxygen molar ratios investigated (Figs. 4.38, 4.39 and 4.40). 2.5VBa-HAp showed a preference for aromatic formation, while 2.5VCa-HAp showed high selectivity towards oxygenates at 1:0.5 and 1:1. 1, 7-octadiene to oxygen molar ratios, but for an 1,7-octadiene to oxygen molar ratio of 1:2 it showed lowest selectivity towards oxygenates and highest selectivity towards CO_x . This could be attributed to the combustion of oxygenates to CO_x (Figs. 4.38, 4.39 and 4.40).

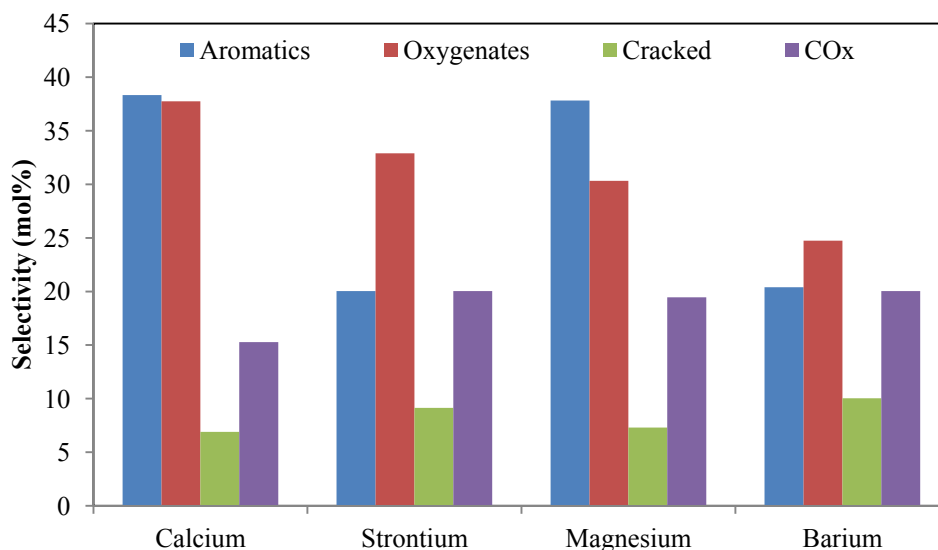


Figure 4.38 Selectivity of products in the ODH of 1,7-octadiene with 2.5 wt% V_2O_5 supported on hydroxyapatites at iso- conversion (27%), temperature = 450 °C and 1,7-octadiene to oxygen molar ratio of 1:0.5

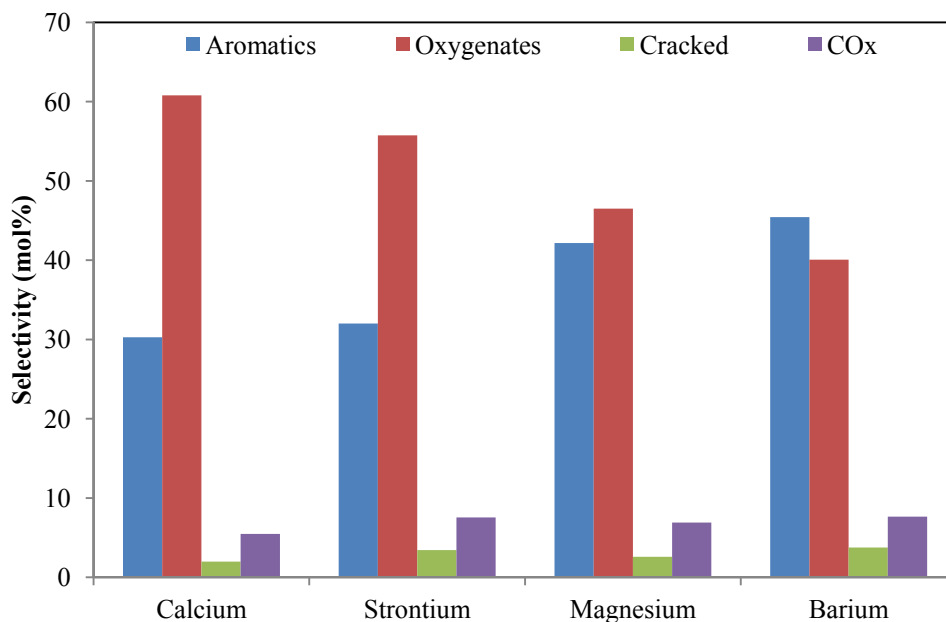


Figure 4.39 Selectivity of products in the ODH of 1,7-octadiene with 2.5 wt% V₂O₅ supported on hydroxyapatites at iso- conversion (27%), temperature = 450 °C and 1,7-octadiene to oxygen molar ratio of 1:1

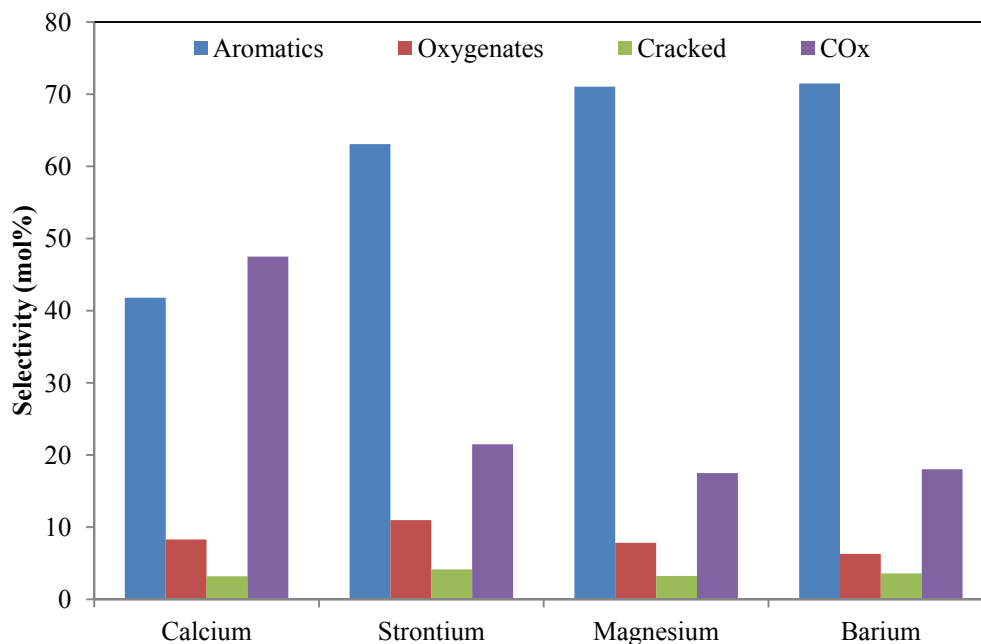


Figure 4.40 Selectivity of products in the ODH of 1,7-octadiene with 2.5 wt% V₂O₅ supported on hydroxyapatites at iso- conversion (27%), temperature = 450 °C and 1,7-octadiene to oxygen molar ratio of 1:2

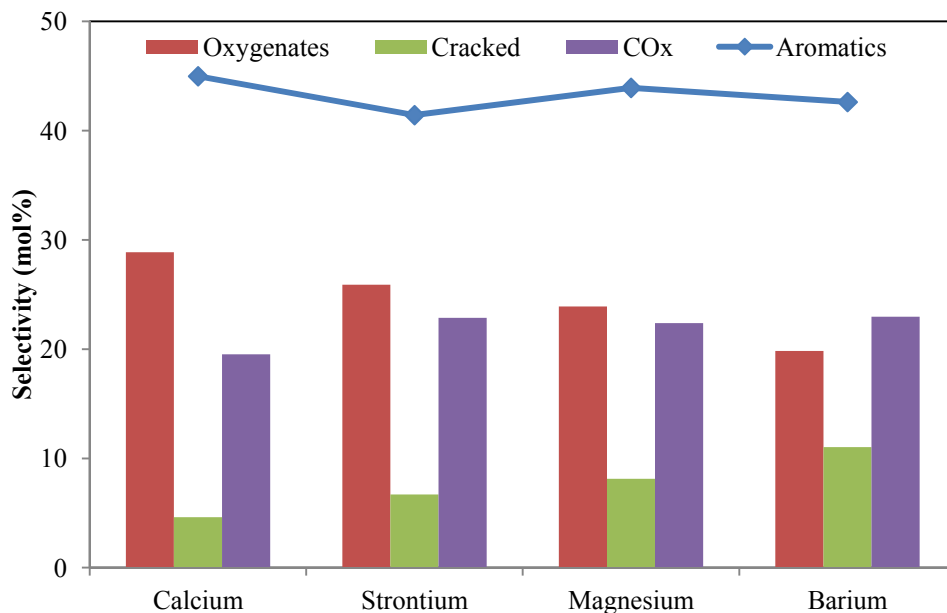


Figure 4.41 Selectivity of products in the ODH of 1,7-octadiene with 10 wt% V_2O_5 supported on hydroxyapatites at iso- conversion (27%), temperature = 450 °C and 1,7-octadiene to oxygen molar ratio of 1:0.5

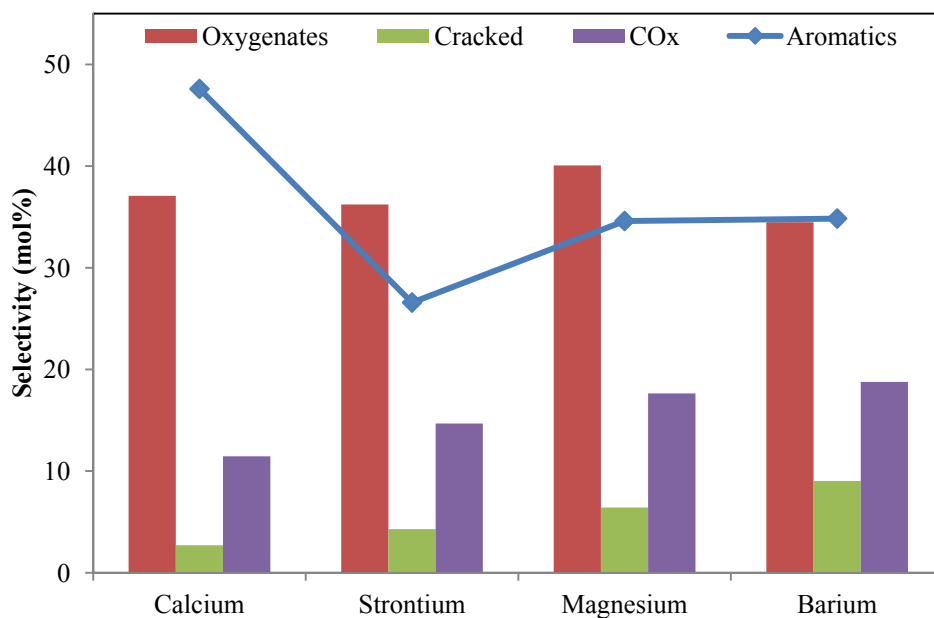


Figure 4.42 Selectivity of products in the ODH of 1,7-octadiene with 10 wt% V_2O_5 supported on hydroxyapatites at iso- conversion (27%), temperature = 450 °C and 1,7-octadiene to oxygen molar ratio of 1:1

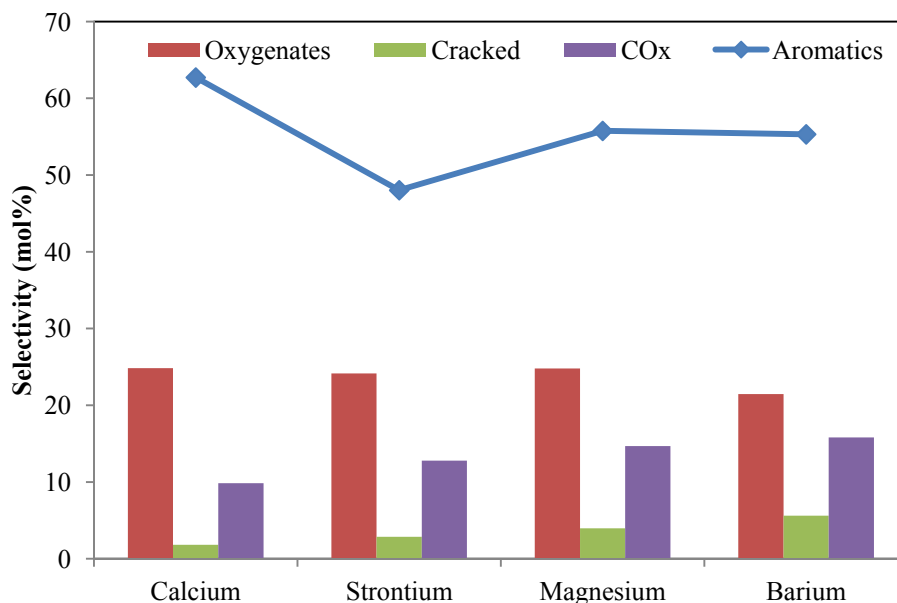


Figure 4.43 Selectivity of products in the ODH of 1,7-octadiene with 10 wt% V₂O₅ supported on hydroxyapatites at iso-conversion (27%), temperature = 450 °C and 1,7-octadiene to oxygen molar ratio of 1:2

Aromatics dominated when 1,7-octadiene was used as feed. But as the 1,7-octadiene to oxygen molar ratio changes from 1:0.5 to 1:1, the selectivity to the aromatics decreased, but when the ratio is changed from 1:1 to 1:2 the selectivity of aromatics increased (Figs. 4.41, 4.42 and 4.43). The low values of aromatics under mild oxygen environments may be attributed to the fact that the aromatics lie far to the right in the conceivable ODH reaction series (Chapter 3, Section 3.2.2.1). The selectivity of CO_x decreases with increase in the oxygen concentration. The selectivity of oxygenates follows the inverse trend to selectivity of aromatics suggesting competitive pathways (Figs. 4.41, 4.42 and 4.43). 10VCa-HAp showed highest selectivity towards the aromatic products, whereas 10VMg-HAp showed highest selectivity towards oxygenates due to the presence of V⁵⁺ on the strongly acidic Mg-HAp [14, 16].

4.3.3 Modes of cyclization

The formation of the aromatics either takes place via C1 to C6 or C2 to C7 bonding. The former is believed to lead to the formation of ethyl benzene or styrene, while the latter results in *o*-xylene formation. 1-octene and 1,7-octadiene favour the formation of aromatics through 1,6 cyclization and 1-octene showed that more than 85 % of cyclization follows the 1,6-cyclization route. A noticeable feature is that 1-octene is preferentially consumed during the

formation of aromatics, showing that 1,6- ring closure leads to cyclization and eventually gives ethylbenzene or styrene. 1-octene is an isomer that can provide 6 sequential sp^3 carbon atoms for this type of cyclization; the sp^3 carbon, unlike the doubly bonded carbon atom (sp^2 carbon), possesses free rotation along the bond axis, and hence the flexibility needed for the ring formation.

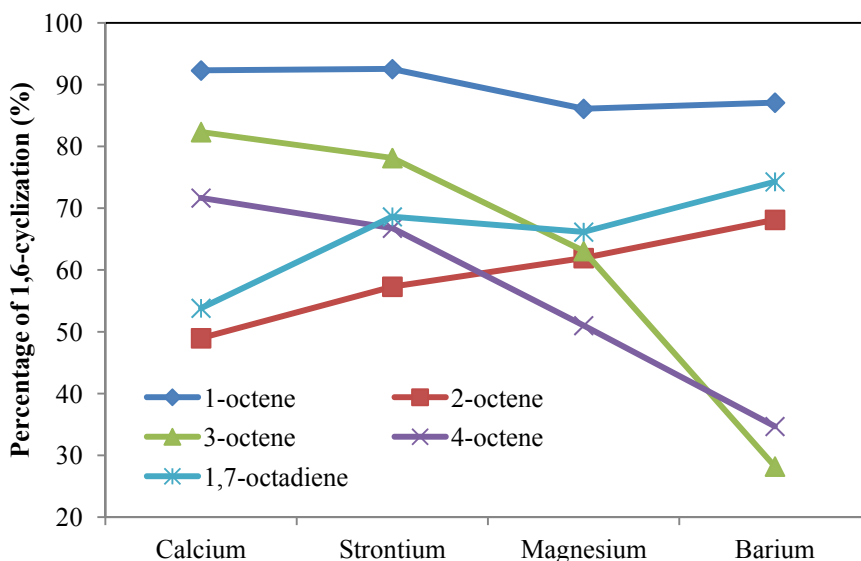


Figure 4.44 Percentage of 1,6 cyclization in the formation of aromatics at a hydrocarbon to oxygen ratio of 1:2 with 2.5 wt% V_2O_5 supported hydroxyapatites at iso-conversion (27%), temperature = 450 °C

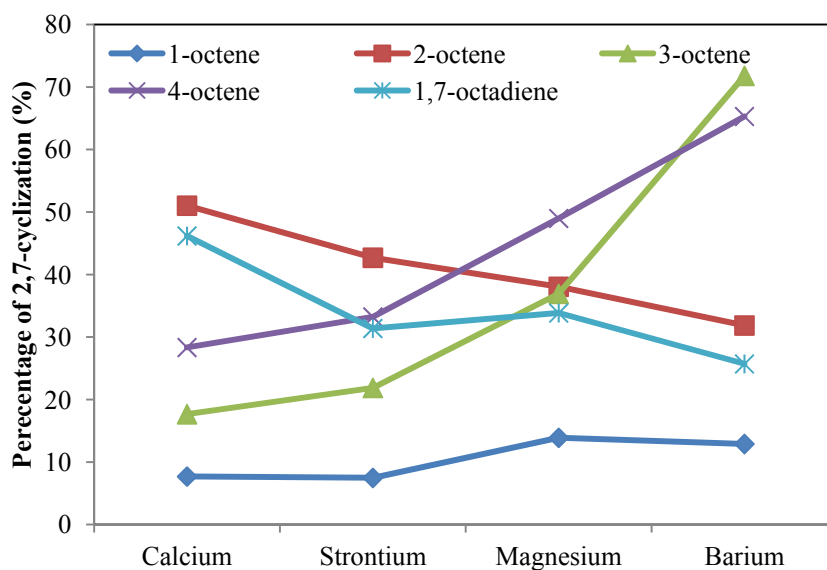


Figure 4.45 Percentage of 2,7 cyclization in the formation of aromatics at a hydrocarbon to oxygen ratio of 1:2 with 2.5 wt% V_2O_5 supported hydroxyapatites at iso-conversion (27%), temperature = 450 °C

In support of the proposal, 2-octenes, 3-octenes and 4-octenes do not favour the 1,6-cyclization mode because of lack of the flexibility, as the “inflexible” sp^2 carbons in these isomers would be involved regardless of the direction of 1,6-ring closure.

Among all the hydroxyapatites, 2.5VCa-HAp showed highest tendency towards 1,6-cyclization for 3-octene and 4-octene isomers (Figs. 4.45 - 4.47). Due to the isomerization of 3-octene and 4-octene during the reaction, 2,7-cyclization is favoured by the 2.5VBa-HAp catalyst [6,7]. 2-Octene favours 2,7-cyclization with 2.5VCa-HAp and 1,6-cyclization with 2.5VBa-HAp (Figs. 4.43 and 4.44) whereas 1-octene and 1,7-octadiene prefer the 1,6-cyclization route when 10 wt % V_2O_5 on hydroxyapatites is used. 2.5VMg-HAp and 2.5VBa-HAp showed more than 75 % of 1,6-cyclization in the formation of aromatics with these two feeds. However, 2.5VBa-HAp showed more than 60% of 1,6-cyclization with 4-octene due to its weak acidity which favours the isomerization of octenes [6,7]. 3-Octene is the only isomer which showed less than 10 % of 1, 6-cyclization in the formation of aromatics throughout all the hydroxyapatite supported vanadium catalysts (Figs. 4.44 and 4.46). 2-Octene, 3-octene and 4-octene prefer 2,7-cyclization in the formation of aromatics when 10 wt % V_2O_5 on hydroxyapatites are used. It has been evidenced from our previous studies that 2,7-cyclization is more favoured with an increase in the vanadium content for 3-octene and 4-octene isomers [15, 16] .

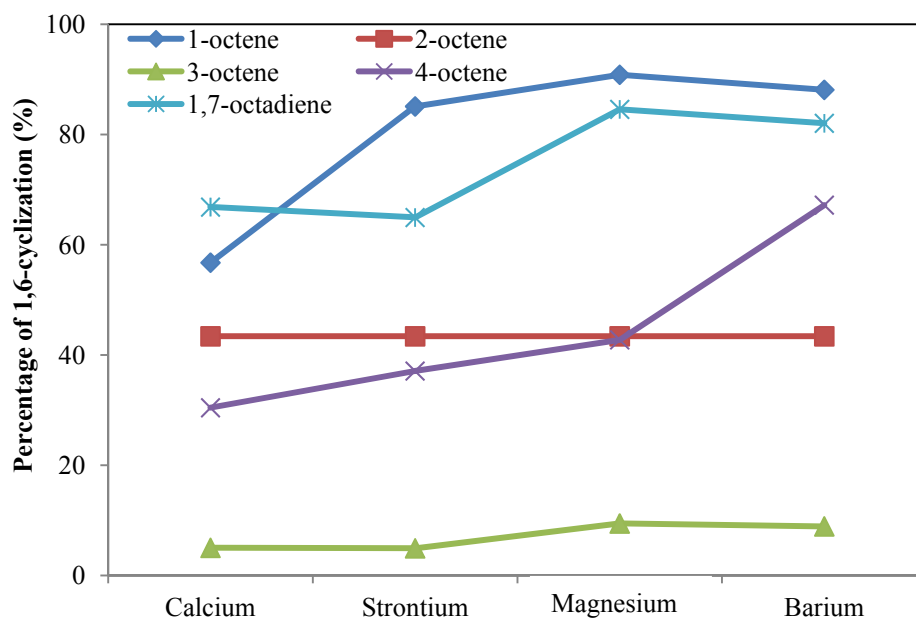


Figure 4.46 Percentage of 1,6 cyclization in the formation of aromatics at an hydrocarbon to oxygen ratio of 1:2 with 10 wt% V_2O_5 supported hydroxyapatites at iso-conversion (27%), temperature = 450 °C

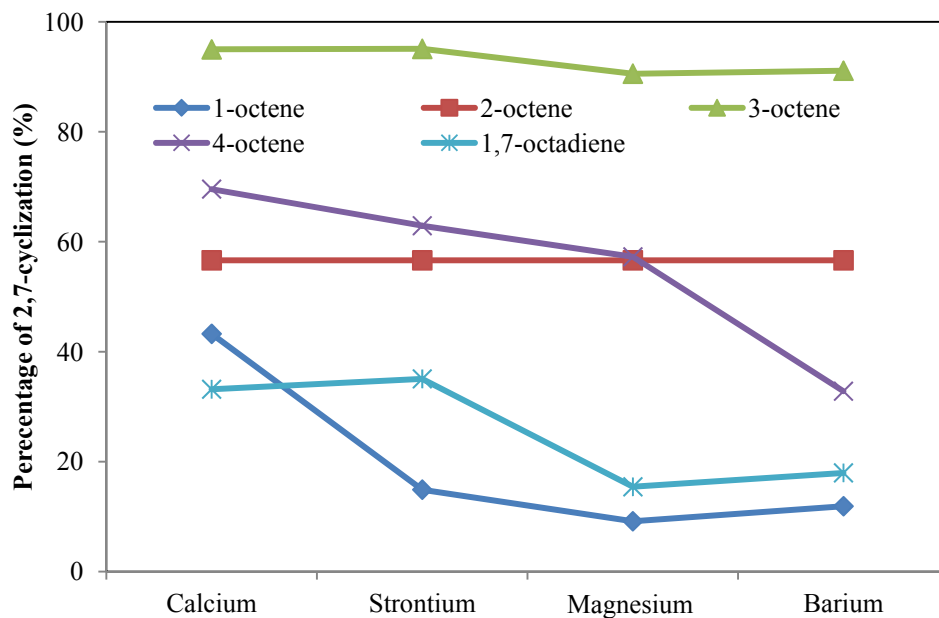


Figure 4.47 Percentage of 2,7 cyclization in the formation of aromatics at an hydrocarbon to oxygen ratio of 1:2 with 10 wt% V_2O_5 supported hydroxyapatites at iso-conversion (27%), temperature = 450 °C

4.3.4 Proposed mechanism for the reaction

The oxidation and oxidative dehydrogenation reactions of alkanes and alkenes are known to follow a Mars-van Krevelen mechanism [42]. The mechanism of the oxidation and oxidative dehydrogenation [28] over vanadium supported hydroxyapatite catalysts may involve a reversible V^{4+}/V^{3+} to V^{5+} redox cycle as illustrated in Figs. 4.48 and 4.49. The catalyst was reduced to an average valance of vanadium of around 3+ (V_2O_3), as listed in Table 4.2. Rietveld refinement investigations from *in situ* XRD (Fig.4.48) investigations and the XPS studies under redox environments showed the partial existence of V^{4+} ions also.

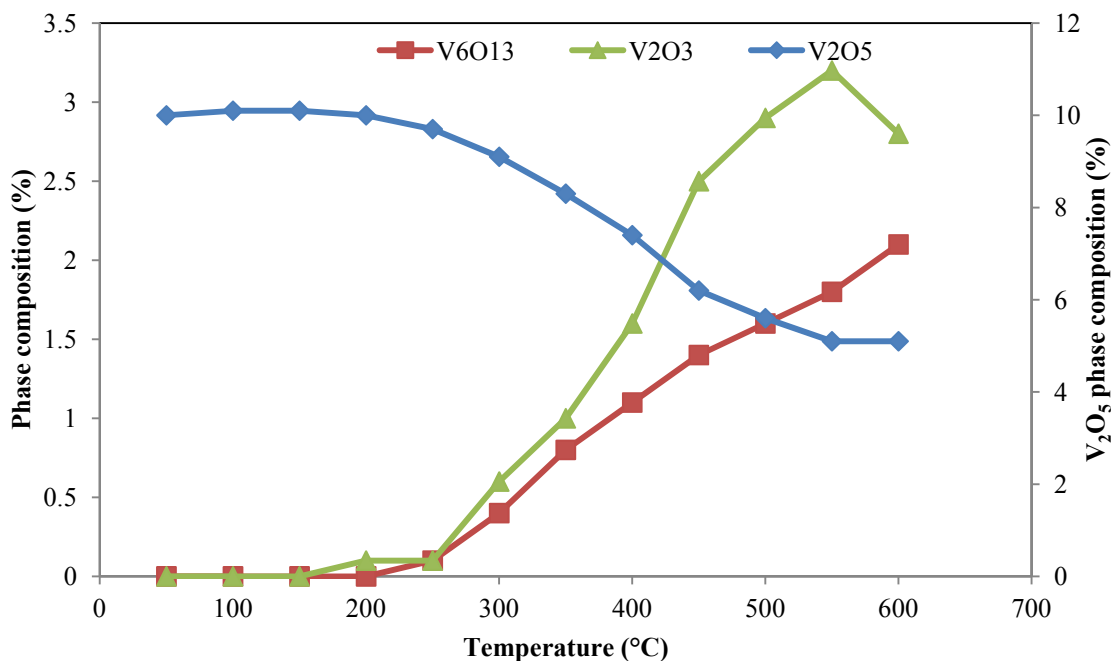


Figure 4.48 Transformation of V_2O_5 phase in 2.5V-HAp during the catalytic testing reaction with *n*-octane (heating cycle)

At lower temperatures, V_2O_5 (V^{5+}) is reduced to V_2O_4 (V^{4+}) as evidenced in TPR, with increase in temperature V_2O_4 (V^{4+}) is reduced to V_2O_3 (V^{3+}). The onset temperature for the transformation of V_2O_5 is 250 °C. As this experiment was conducted in a redox environment, V_2O_3 (V^{3+}) was oxidized to V_2O_5 (V^{5+}) via the path way explained in section 4.3.1.3. Thus vanadium pentoxide is the major phase at every temperature because it is reduced to V^{3+} by octane, and it is oxidised to the V^{5+} form by the oxygen present in the feed. With an increase in the reduction, the average oxidation state of vanadium decreased, and the amount of V^{3+} increased. Therefore, deep reduction of V^{5+} to V^{3+} occurred when no gas phase oxygen was present in the reaction mixture. The paths of reduction and reoxidation are reversible, and thus the redox cycle between V^{3+} and V^{5+} will result in the highest oxygen capacity of the vanadium supported hydroxyapatite catalysts. The phase transformation of V_2O_5 in the cooling cycle (Fig. 4.49) is similar as the phase transformation of V_2O_5 in the heating cycle, indicating that phase transformation of V_2O_5 is a reversible reaction, which is also evidenced by TPR-TPO-TPR results.

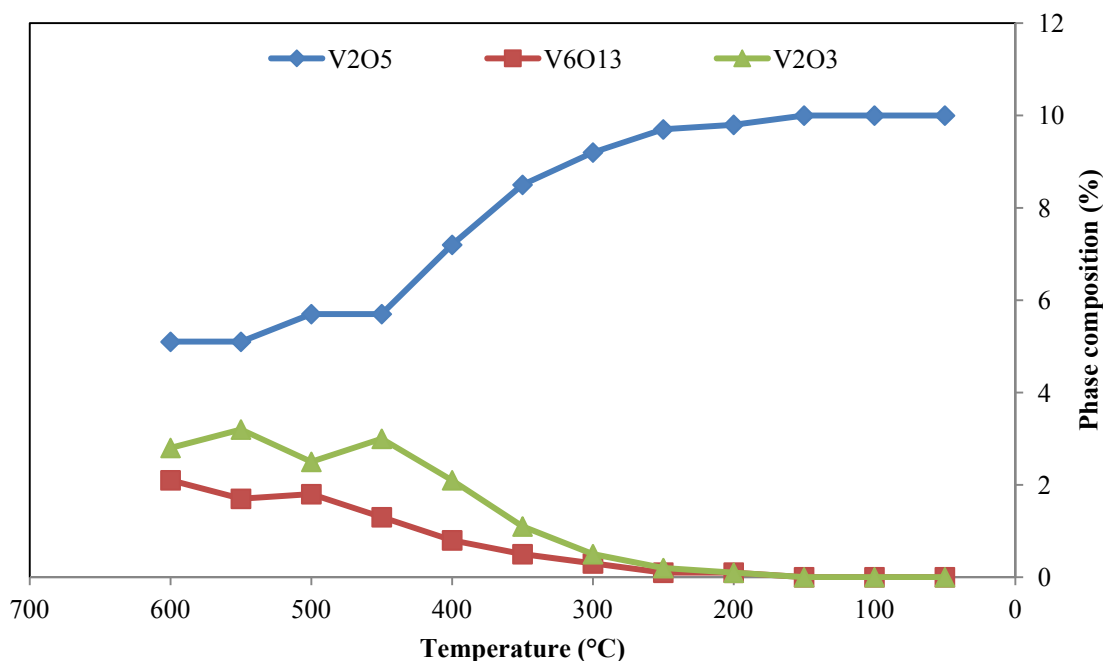


Figure 4.49 Transformation of V_2O_5 phase in 2.5V-HAp during the catalytic testing reaction with *n*-octane (cooling cycle)

The oxidation of V_2O_3 occurs at comparable rates to the reduction of V_2O_5 and the overall oxidation rate should increase with the extent of reduction, instead of decreasing as is evident by the Rietveld analysis of the *in situ* XRD diffractograms (Fig. 4.48- 4.49). This clearly suggests that the reduced vanadium species, i.e. V^{3+} and V^{4+} , are oxidised with equal facility and that both oxidation of V^{3+} to V^{4+} and V^{5+} is much slower than V^{4+} to V^{5+} (Fig. 4.13). A strong detrimental effect of V^{3+} on the oxidation ability of the reduced catalysts suggests that V^{3+} species were formed and accumulated in the outer surface layer of the hydroxyapatite catalysts and this is entirely consistent with the negligible oxygen diffusion from the bulk to the surface in the catalyst in reduction studies. Catalytic results showed that when the catalysts were used under steady state reaction conditions with an *n*-octane to oxygen molar ratio of 1:2, they exhibited stable catalytic performance with good *n*-octane conversion and product selectivity. These phenomena may suggest that at steady state reaction conditions, deep reduction of vanadium V^{3+} is avoided due to the oxidation by the gas phase oxygen (Fig. 4.50). The surface redox cycle takes place between V^{5+} and V^{4+} , i.e. the surface V^{5+} is first reduced with octane to V^{4+} , then V^{4+} is quickly oxidized to V^{5+} with lattice oxygen and adsorbed oxygen or directly from the gas phase [43]. From the catalytic results, we can conclude that the reduction of *n*-octane to octenes includes a reduction of V^{5+} to V^{4+} , and which occurs at lower temperatures. Thus the selectivity

of octenes is higher at lower temperatures and it decreases with increase in temperature. As evidenced by the phase transformation of V_2O_5 under octane, V^{4+} further reduced to V^{3+} or V^{5+} is reduced to V^{3+} to form aromatics from octenes. As lattice oxygen is inserted into the molecule, the reaction can occur in the absence of gas phase O_2 . The desorption of oxidation products creates oxygen vacancies which are replenished from gas-phase O_2 in a subsequent step. In this present study monomeric vanadyl species cannot be desorbed. Thus the capability of oxygen insertion is associated with the presence of crystalline and polymeric vanadium species. On other hand, the oxygen present in the feed reoxidises the V^{4+} / V^{3+} to V^{5+} and during this reoxidation, carbon oxides will form (Fig. 4.50).

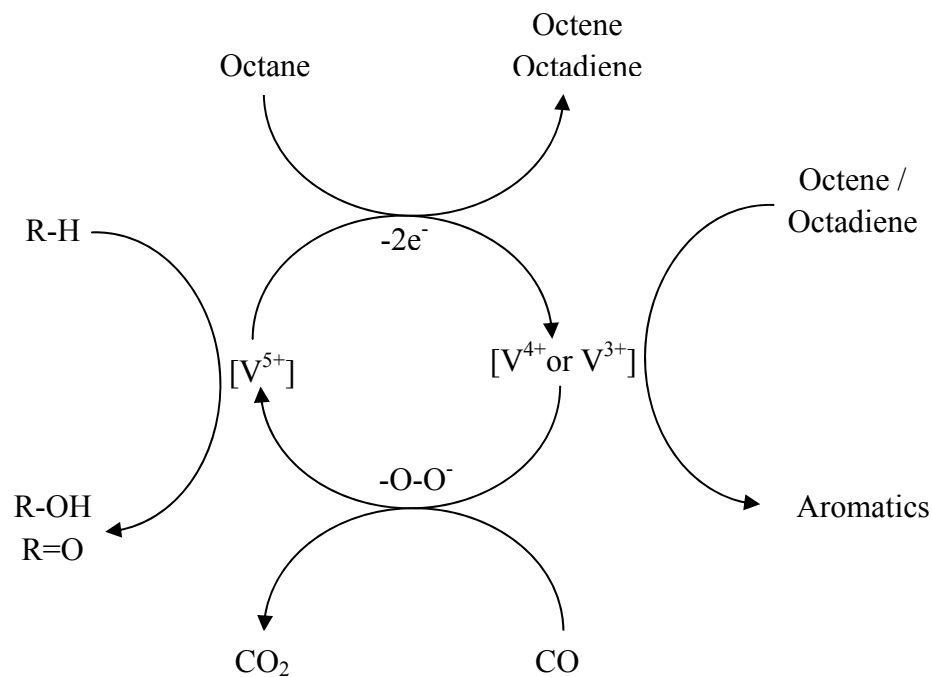


Figure 4.50 Oxidation – Reduction pathway in vanadium supported hydroxyapatites

4.4 Characterization of the used catalysts

All the used catalysts from all reactions showed similar characterization results. There is no difference in the XRD pattern and there is no drastic change in the acidic sites and in the morphology of the used catalysts from all reactions.

4.4.1 Infrared spectroscopy

The stretching mode vibrations of P-O were found in between 900-1200 cm^{-1} for the phosphate groups (Appendix, Fig. A10, Fig. A12). The bands at 350 and 250 cm^{-1} are due to the vibrations of the bond between metal and the phosphate [44, 45]. The peak in between 1150-1250 cm^{-1} gives evidence that V_2O_5 is in the form of a single layer on the hydroxyapatites [35]. The terminal V=O stretching is observed in between 1020-1120 cm^{-1} . The bands in the region of 920-950 cm^{-1} are likely due to V=O group stretching and a band in between 750-800 cm^{-1} indicated the O-V-O mode and the presence of monomeric vandylys [35]. The characteristic peaks of V_2O_5 are observed around 1060, 1020, 920, 710 and 490 cm^{-1} . The peak at around 630-670 cm^{-1} is characteristic of asymmetric stretching of the V-O-V group in the pyrovanadate phase [46].

4.4.2 Raman spectroscopy

In the Raman spectra the bond bending vibrations of the V-O ions are observed at around 470-510 cm^{-1} (Appendix, Fig. A13, Fig. A14). The peaks at around 880 and 970 cm^{-1} represent V-O stretching vibrations in the spectra. The peak at 465-495 cm^{-1} is related to the V-O-V bending vibration. The peaks at around 470-485 cm^{-1} show the presence of V_2O_5 phase on the hydroxyapatite [47, 48]. The vibration mode of the hydroxyl group is observed at around 1050 cm^{-1} . In the Raman spectra of stoichiometric hydroxyapatite this peak is observed in the region of 900-1130 cm^{-1} . The peaks for PO_4^{3-} of the hydroxyapatites are observed at around 390, 690 and 1140 cm^{-1} .

4.4.3 BET surface area analysis

The texture of the used catalysts was found to depend on the V_2O_5 composition and the higher loading resulted in a drastic decrease in the surface area as well as pore volume (Table 4.4). This could be attributed to the blocking of pores with coke which is formed in the reaction, making it inaccessible to the nitrogen molecules. The decrease in the surface area of the used

Table 4.4 BET surface area, pore volume, pore size, pore width, crystallite size, crystallinity and elemental analysis of used V₂O₅ supported hydroxyapatites

Catalyst	M/P ¹	M/V ¹	M/P ²	M/V ²	Surface Area (m ² /g)	Pore Volume (cm ³ /g)	Average Pore Size(Å)	Average Pore Width(Å)	Crystallite Size ³ (nm)	Crystallinity ⁴ (%)
2.5VCa- HAp	1.64	0.032	1.64	0.031	51.2	0.175	1423	352	3.11	0.21
2.5VSr- HAp	1.65	0.033	1.64	0.033	48.5	0.095	1035	484	3.08	0.16
2.5VMg- HAp	1.63	0.030	1.64	0.032	47.1	0.093	352	593	3.21	0.25
2.5VBa- HAp	1.63	0.030	1.63	0.030	33.9	0.029	192	629	3.10	0.31
10VCa-HAp	1.64	0.131	1.64	0.131	11.2	0.110	195	592	5.01	0.54
10VSr- HAp	1.65	0.133	1.63	0.135	9.3	0.042	151	640	5.05	0.69
10VMg- HAp	1.63	0.130	1.64	0.133	19.7	0.061	331	894	5.63	0.68
10VBa-HAp	1.63	0.130	1.64	0.133	8.54	0.0174	132	963	5.98	0.76

¹ICP-OES, ²EDX, ³Calculated by Scherer's equation and ⁴X_c = 1 - (V_{112/300} / I₃₀₀), where X_c is degree of crystallinity V_{112/300} is the intensity of the shoulder between (112) and (300) diffraction peaks and I₃₀₀ is the intensity of the (300) peak [49]

catalysts is also related with the activity of the catalysts. The catalysts which showed good activity in the catalytic reactions showed a greater decrease in their surface area relative to the other catalysts. The used catalysts also showed the Type –IV isotherm (IUPAC) lying in the p/p^0 range of 0.6-0.85 demonstrating the catalysts do not lose their mesoporous character [50]. The isotherms and the pore size distributions remained substantially the same over the range of vanadium concentration and it is very similar to those of the fresh catalysts, which means that the catalytic reaction didn't clog the pore structure of the catalyst [51].

4.4.4 XRD-Diffractograms

In the powder diffraction patterns for the used catalysts taken at room temperature, the d-spacing's are correlated with the respective JCPDS File No's 9-390, 33-138, 36-0272, 13-0404 for calcium, strontium, magnesium, and barium hydroxyapatites (Fig. 4.51).

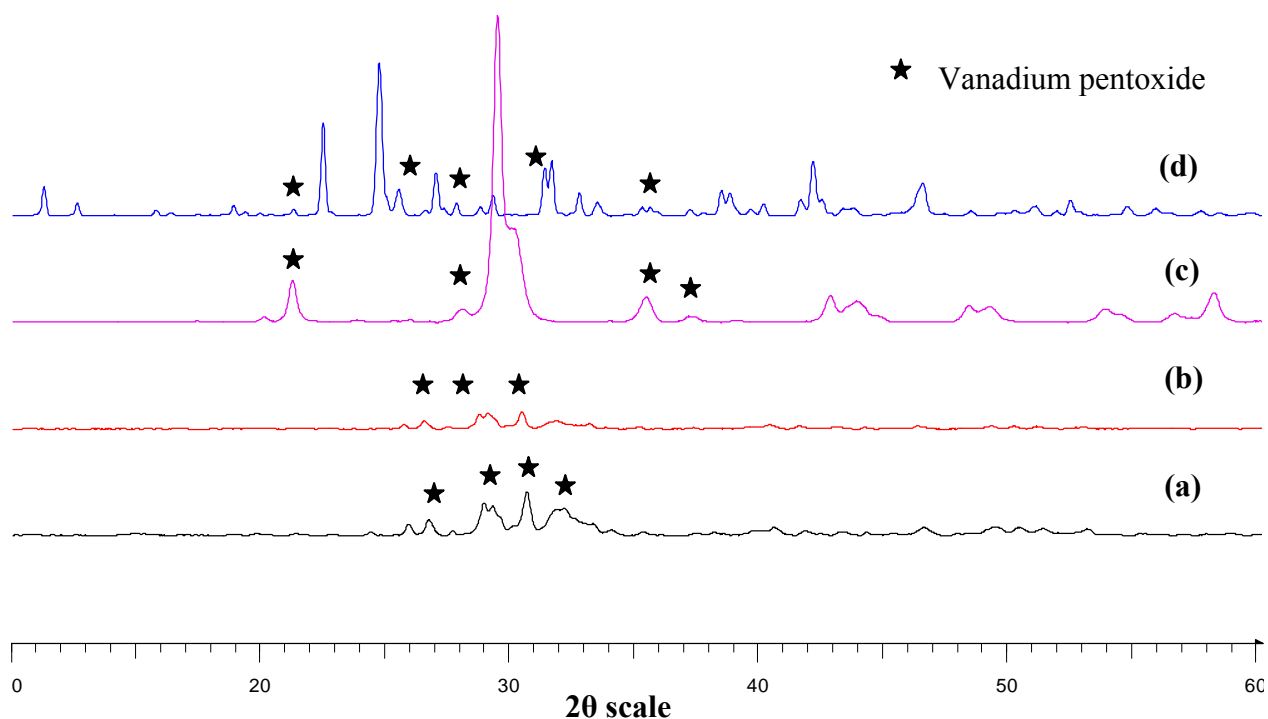


Figure 4.51 XRD diffractograms of used 2.5 wt% V_2O_5 supported calcium (a) strontium (b), magnesium (c) and barium (d) supported hydroxyapatites

The presence of V_2O_5 is also evident with the d-spacing referenced in JCPDS File No. 9-387. The pyrovanadate phase which is observed in the fresh catalyst is also present in the used

catalysts. It is identified by correlating the d-spacing's with the JCPDS file no 25-1103 (Fig. 4.52). There is no other phase observed in the used catalysts. However, there is a noticeable change in the crystallite sizes and crystallinity of the catalysts (Table 4.4). The magnitude of change in the crystallite sizes and crystallinity values correlated with the catalytic activity; the greatest change was induced by the catalyst which showed the highest catalytic activity and the smallest by the catalyst that showed lowest catalytic activity. This implies that these changes are likely to be due to the reduction-oxidation cycle that accompanied the catalytic activity.

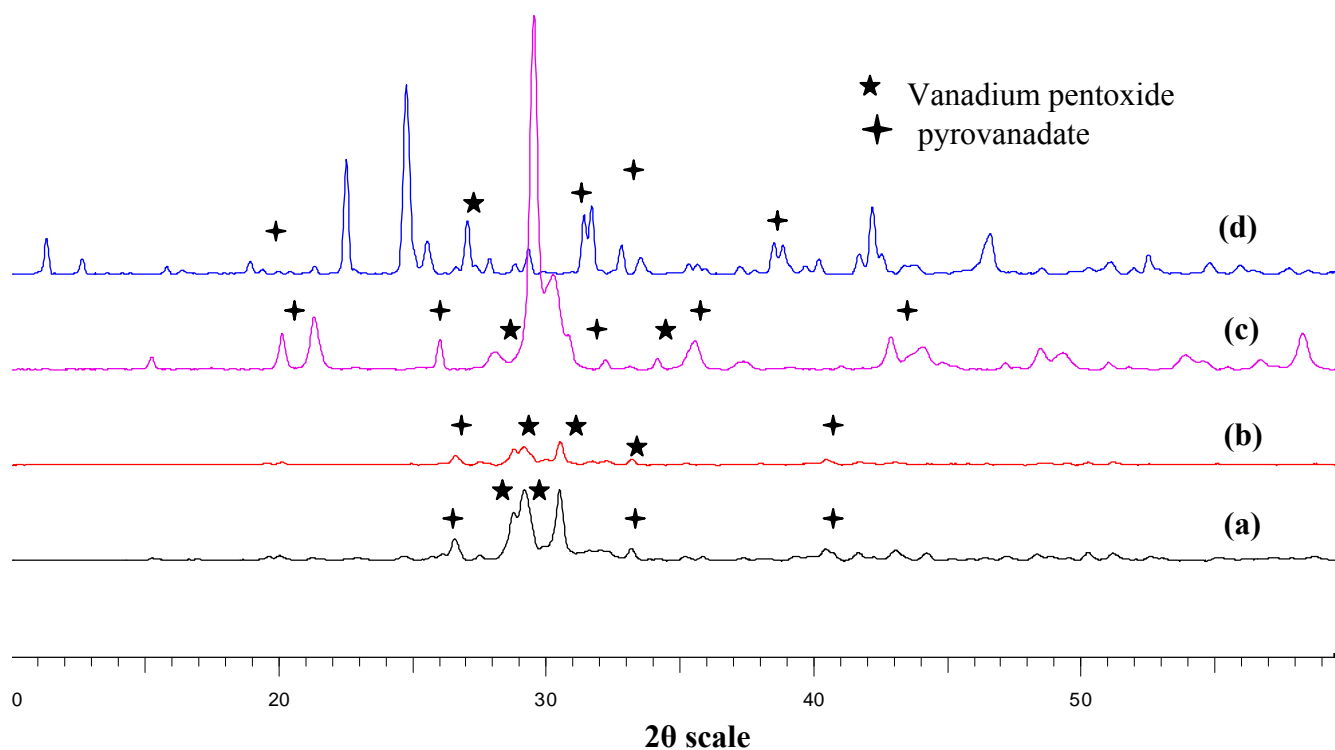


Figure 4.52 XRD diffractograms of used 10 wt% V_2O_5 supported calcium (a) strontium (b), magnesium (c) and barium (d) supported on hydroxyapatites

4.4.5 Temperature programmed desorption

Temperature programmed desorption profiles showed a wide range distribution of acidic sites on the surface of the used catalysts, and relative to the fresh catalysts the acidity is lower for the used catalyst (Fig. 4.53 and Fig. 4.54). This is probably due to the blocking of acidic sites with the carbon layer which was formed during the reaction. But the acidity trend for the used catalysts is the same as for the fresh catalyst. The magnitude of decrease in the number of acidic sites also related to the activity of the catalysts (Fig. 4.53 and Fig. 4.54). The catalyst which

showed good activity and gave a high selectivity towards CO_x showed a lower number of acidic sites relative to the other catalysts (after reaction).

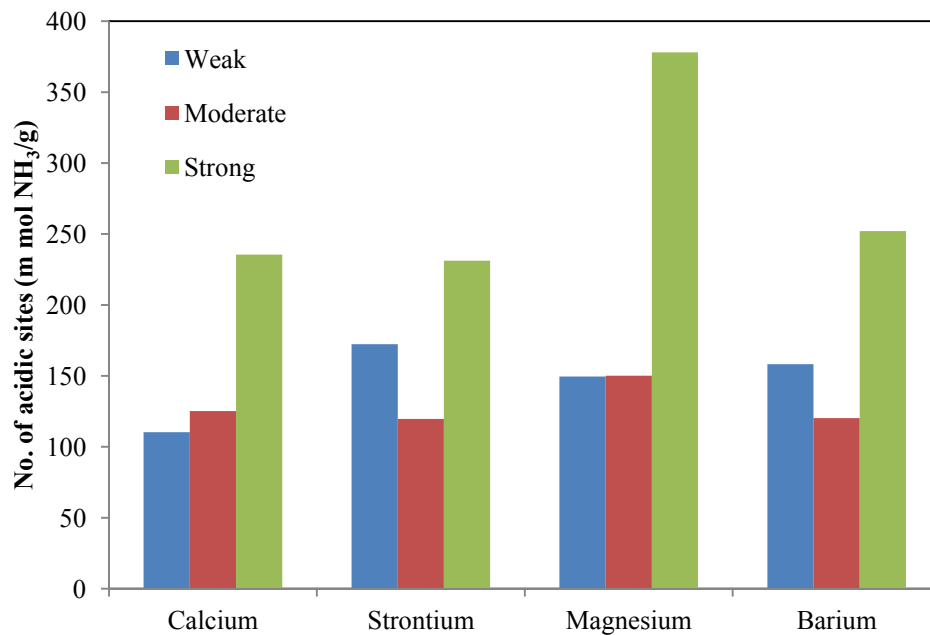


Figure 4.53 Distribution of acidic sites on 2.5 wt% V_2O_5 on hydroxyapatite catalysts used at a hydrocarbon of oxygen ratio of 1:2.

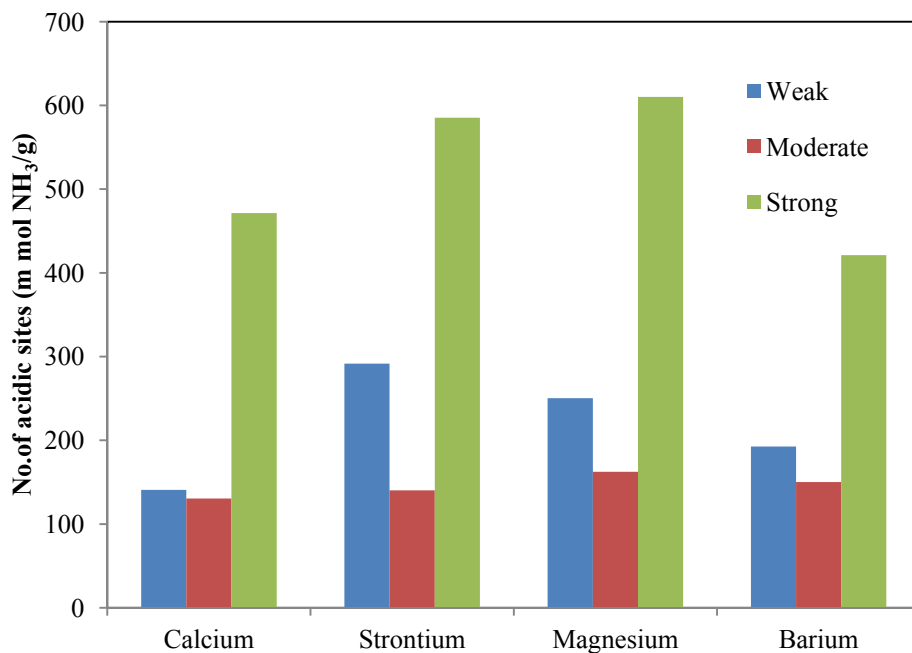


Figure 4.54 Distribution of acidic sites on 10 wt% V_2O_5 supported on hydroxyapatite catalysts used at a hydrocarbon of oxygen ratio of 1:2.

4.4.6 SEM and TEM

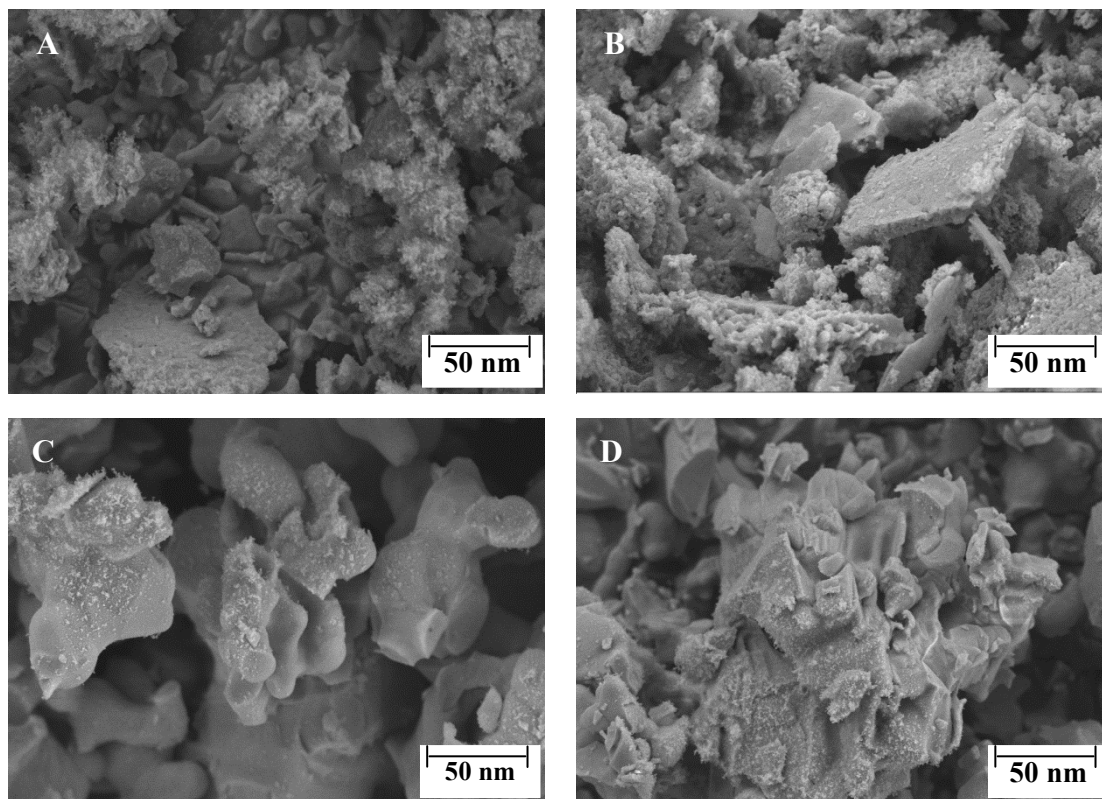


Figure 4.55 SEM images of 10wt % V_2O_5 supported on calcium (a), strontium (b), magnesium (c) and barium (d) hydroxyapatite catalysts used at a hydrocarbon to oxygen ratio of 1:2.

The SEM images showed the surface morphology of the used catalysts and showed similarity with those of the fresh catalysts. There was no drastic change in the surface morphology of the used catalysts (Fig. 4.55). The decrease in the porosity and the decrease in the crystallinity of the catalysts are evidenced in the SEM images. After the reaction, the 2.5 wt% V_2O_5 on the hydroxyapatite catalysts retained their polycrystalline natures, and the 10 wt% V_2O_5 on hydroxyapatite catalysts showed only a small decrease in their crystalline nature. SEM-EDX results for the Ca/P and Ca/V ratios are in agreement with the ICP-OES results. These results showed that there is no leaching of the metals during the reaction. TEM images also confirm the decrease in the crystallinity of the catalysts. There is a significant change in the particle size of the used catalysts when compared to the fresh catalysts. Particle sizes varied from 240-260 nm, similar to the particle size of the fresh catalysts (Fig. 4.56).

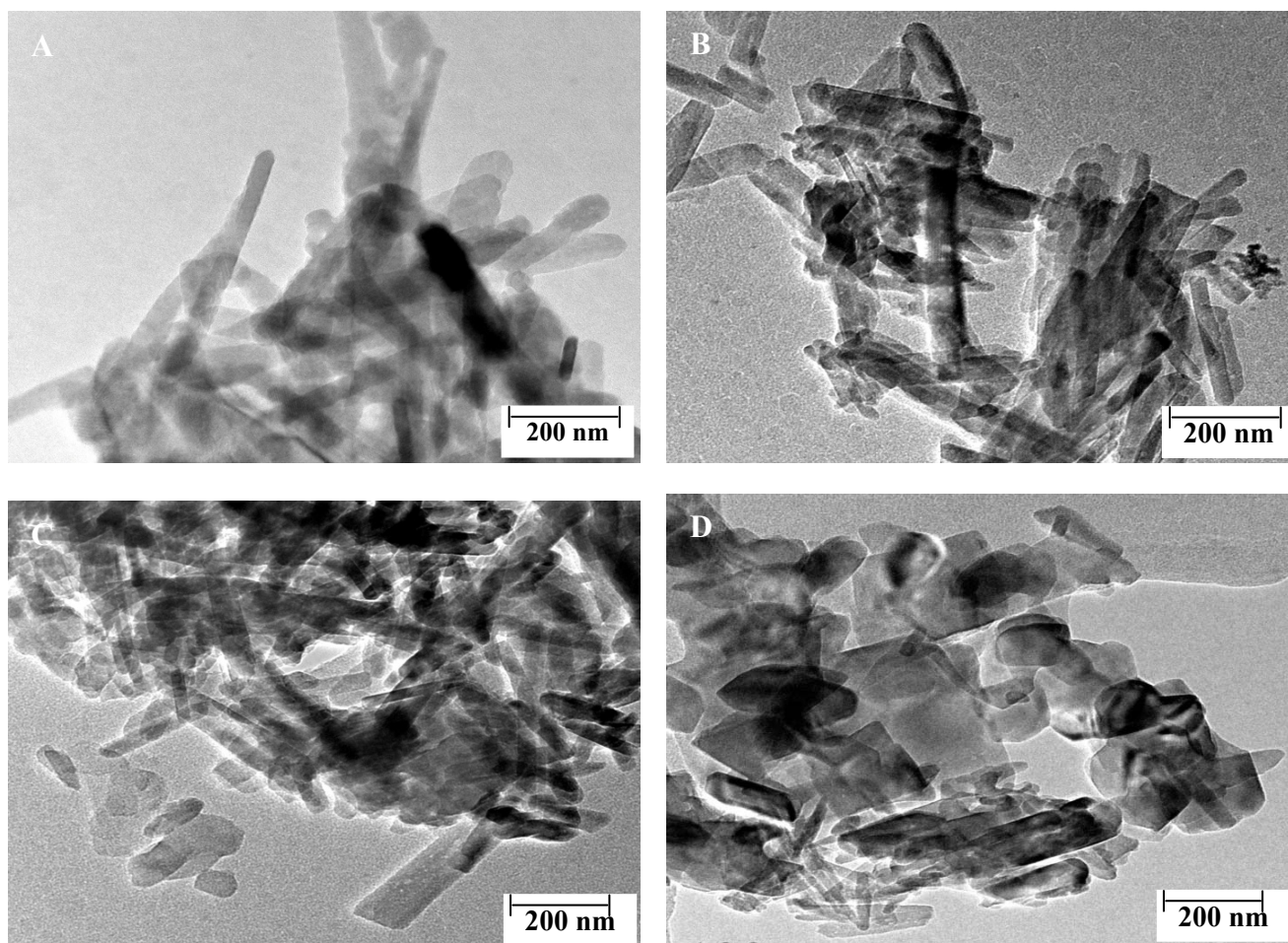


Figure 4.56 TEM images of 10 wt% V₂O₅ supported on calcium (a), strontium (b), magnesium (c) and barium (d) hydroxyapatite catalysts used at a hydrocarbon to oxygen ratio of 1:2.

4.5 Conclusion

TPO profiles of the catalytic materials showed that vanadium will be reoxidised to V₂O₅ after reduction but the average oxidation state after the reoxidation is +4.5. The TPR-TPO-TPR experiment showed that reduction 1 and reduction 2 are similar in reduction pathway of V₂O₅. Chemisorption studies showed that vanadium is well dispersed on the surface of the hydroxyapatite and vanadium is in the +5 oxidation state as shown by XPS analysis. XPS analysis on the reduced and reoxidised catalysts showed that vanadium is reduced to the +3 oxidation state and reoxidised to the +5 oxidation state.

Highest selectivity towards aromatics is shown by the 2-octene and 3-octene isomers with both 2.5 wt % V₂O₅ and 10 wt % V₂O₅ on hydroxyapatites at all hydrocarbon to oxygen molar ratios. There was a marked decrease in the selectivity of aromatics and increase in the selectivity of CO_x as the oxygen partial pressure increased. 10VCa-HAp showed significant selectivity towards aromatics at all hydrocarbon to oxygen molar ratios, with 1-octene, 2-octene and 1,7-octadiene. 2.5VMg-HAp and 10VMg-HAp showed high selectivity towards oxygenates with all octene isomers and a significant selectivity towards aromatics with 3-octene. High selectivity towards the cracked products was shown by 10 VCa-HAp and on 10VSr-HAp with 3-octene at a hydrocarbon to oxygen ratio of 1:2.

1-octene and 1,7-octadiene prefer to form aromatics via the 1,6-cyclization mode and 2-octene and 3-octene prefer to form aromatics via the 2,7 cyclization mode. Rietveld analysis on the *in situ* XRD diffractograms showed that the oxidation-reduction path way in this reaction follows the Mars-van Krevelen mechanism. *n*-Octane was first oxidatively dehydrogenated to octenes (as shown in Chapter 3, Section 3.3.2.3), and the oxidative dehydrogenation further takes place forming aromatics and oxygenates, followed by combustion to CO₂. No phase changes were observed in the used catalysts. However, some textural changes were induced by the catalytic testing which was observed by SEM and TEM.

Acknowledgements

We would like to thank Dr. Marco Conte, Cardiff Catalysis Institute for his assistance in the *in situ* XRD studies. We would like to thank the NRF and THRIP for support. Thanks are also extended to the Electron Microscopy Unit at the University of KwaZulu-Natal (Westville).

References

- [1] G. Centi, Catal. Lett. 22 (1993) 53-66.
- [2] C. Batiot, B.K. Hodnett, Appl. Catal. A 137 (1996) 179-191.
- [3] M.C. Huff, L.D. Schmidt, AIChE J. 42 (1996) 3484-3497.
- [4] M. Huff, L.D. Schmidt, J. Catal. 155 (1995) 82-94.
- [5] H. Zhu, X. Liu, Q. Ge, W. Li, H. Xu, Fuel Process. Technol. 87 (2006) 649-657.
- [6] R. Subramanian, G.J. Panuccio, J.J. Krummenacher, I.C. Lee, L.D. Schmidt, Chem. Eng. Sci. 59 (2004) 5501-5507.

- [7] M. Hartmann, L. Maier, H.D. Minh, O. Deutschmann, *Combust. Flame* 157 (2010) 1771-1782.
- [8] H.J. Curran, P. Gaffuri, W.J. Pitz, C.K. Westbrook, *Combust. Flame* 129 (2002) 253-280.
- [9] R. Quiceno, J. Pérez-Ramírez, J. Warnatz, O. Deutschmann, *Appl. Catal. A* 303 (2006) 166-176.
- [10] A. Trunschke, D.L. Hoang, J. Radnik, K.W. Brzezinka, A. Brückner, H. Lieske, *Appl. Catal. A* 208 (2001) 381-392.
- [11] A. Széchenyi, F. Solymosi, *Appl. Catal. A* 306 (2006) 149-158.
- [12] M.M. Bhasin, J.H. McCain, B.V. Vora, T. Imai, P.R. Pujadó, *Appl. Catal. A* 221 (2001) 397-419.
- [13] H.B. Friedrich, A.S. Mahomed, *Appl. Catal. A* 347 (2008) 11-22.
- [14] E.A. Elkhalfa, H.B. Friedrich, *Appl. Catal. A* 373 (2010) 122-131.
- [15] E.A. Elkhalfa, H.B. Friedrich, *Catal. Lett.* 141 (2011) 554-564.
- [16] V.D.B.C. Dasireddy, S. Singh, H.B. Friedrich, *Appl. Catal. A* 421–422 (2012) 58-69.
- [17] V.D.B.C. Dasireddy, S. Singh, H.B. Friedrich, *Appl. Catal. A* (2012) (Submitted to *Applied Catalysis A: General*).
- [18] S.T. Oyama, G.T. Went, K.B. Lewis, A.T. Bell, G.A. Somorjai, *J. Phys. Chem.* 93 (1989) 6786-6790.
- [19] J. Galy, G. Miehe, *Solid State Sci.* 1 (1999) 433-448.
- [20] N.Y. Mostafa, P.W. Brown, *J. Phys. Chem. Solids.* 68 (2007) 431-437.
- [21] V. Petkov, P.N. Trikalitis, E.S. Bozin, S.J.L. Billinge, T. Vogt, M.G. Kanatzidis, *J. Am. Chem. Soc.* 124 (2002) 10157-10162.
- [22] J. Höwing, T. Gustafsson, J.O. Thomas, *Acta Crystallogr. Sect. B: Struct Sci.* 59 (2003) 747-752.
- [23] W.R. Robinson, *Acta Crystallogr. Sect. B: Struct Sci.* 31 (1975) 1153-1160.
- [24] H. Horiuchi, M. Tokonami, N. Morimoto, K. Nagasawa, *Acta Crystallogr. Sect. B: Struct Sci.* 28 (1972) 1404-1410.
- [25] C.-W. Kwon, A. Vadivel Murugan, G. Campet, J. Portier, B.B. Kale, K. Vijaymohanan, J.-H. Choy, *Electrochem. Commun.* 4 (2002) 384-387.
- [26] Y.J. Liu, J.L. Schindler, D.C. DeGroot, C.R. Kannewurf, W. Hirpo, M.G. Kanatzidis, *Chem. Mater.* 8 (1996) 525-534.

- [27] R. Baran, Y. Millot, T. Onfroy, F. Averseng, J.-M. Krafft, S. Dzwigaj, *Microporous Mesoporous Mater.* 161 (2012) 179-186.
- [28] S. Besselmann, C. Freitag, O. Hinrichsen, M. Muhler, *Phys. Chem. Chem. Phys.* 3 (2001) 4633-4638.
- [29] F. Majunke, M. Baerns, *Catal. Today* 20 (1994) 53-59.
- [30] G.C. Bond, J.P. Zurita, S. Flamerz, P.J. Gellings, H. Bosch, J.G. Van Ommen, B.J. Kip, *Appl. Catal.*, 22 (1986) 361-378.
- [31] C.R. Dias, M.F. Portela, G.C. Bond, *J. Catal.* 157 (1995) 353-358.
- [32] H. Bosch, B.J. Kip, J.G. van Ommen, P.J. Gellings, *J. Chem. Soc. Faraday Trans. 1* 80 (1984) 2479-2488.
- [33] I.E. Wachs, B.M. Weckhuysen, *Appl. Catal. A* 157 (1997) 67-90.
- [34] L. Balderas-Tapia, J.A. Wang, I. Hernández-Pérez, G.G. Aguilar-Ríos, P. Schacht, *Mater. Lett.* 58 (2004) 3034-3039.
- [35] L. Balderas-Tapia, I. Hernández-Pérez, P. Schacht, I.R. Córdova, G.G. Aguilar-Ríos, *Catal. Today* 107-108 (2005) 371-376.
- [36] N.H. Batis, H. Batis, A. Ghorbel, J.C. Vedrine, J.C. Volta, *J. Catal.* 128 (1991) 248-263.
- [37] M.E. Harlin, V.M. Niemi, A.O.I. Krause, *J. Catal.* 195 (2000) 67-78.
- [38] M.C. Biesinger, B.P. Payne, A.P. Grosvenor, L.W.M. Lau, A.R. Gerson, R.S.C. Smart, *Appl. Surf. Sci.* 257 (2011) 2717-2730.
- [39] A. Dejoz, J.M. López Nieto, F. Márquez, M.I. Vázquez, *Appl. Catal. A* 180 (1999) 83-94.
- [40] T. Blasco, J. M. López Nieto, A. Dejoz, M.I. Vazquez, *J. Catal.* 157 (1995) 271-282.
- [41] S. Sugiyama, T. Osaka, Y. Ueno, K.-I. Sotowa, *J. Jpn. Pet. Inst.* 51 (2008) 50-57.
- [42] P. Mars, D.W. van Krevelen, *Chem. Eng. Sci.* 3, Supplement 1 (1954) 41-59.
- [43] D. Wang, H.H. Kung, M.A. Barteau, *Appl. Catal. A* 201 (2000) 203-213.
- [44] P. Parhi, A. Ramanan, A.R. Ray, *Mater. Lett.* 60 (2006) 218-221.
- [45] K.V.R. Chary, G. Kishan, T. Bhaskar, C. Sivaraj, *J. Phys. Chem. B* 102 (1998) 6792-6798.
- [46] D. Siew Hew Sam, V. Soenen, J.C. Volta, *J. Catal.* 123 (1990) 417-435.
- [47] M.D. O'Donnell, Y. Fredholm, A. de Rouffignac, R.G. Hill, *Acta Biomaterialia.* 4 (2008) 1455-1464.

- [48] C.R. Dias, M.F. Portela, G.C. Bond, *J. Catal.* 157 (1995) 344-352.
- [49] H.-W. Kim, L.-H. Li, Y.-H. Koh, J.C. Knowles, H.-E. Kim, *J. Am. Ceram. Soc.* 87 (2004) 1939-1944.
- [50] Y. Kamiya, E. Nishikawa, A. Satsuma, M. Yoshimune, T. Okuhara, *Microporous Mesoporous Mater.* 54 (2002) 277-283.
- [51] Y. Yang, S. Lim, C. Wang, D. Harding, G. Haller, *Microporous Mesoporous Mater.* 67 (2004) 245-257.

CHAPTER 5

SUMMARY AND CONCLUSION

Alkenes are important raw materials in a wide range of applications in the petrochemical industry due to their low cost and ability to be functionalized easily. For over sixty years and until recently, most of the commercial production of alkenes was through the dehydrogenation of alkanes in the absence of oxygen. These reactions are endothermic and operate at temperatures ranging from 450 to 550 °C, but low conversions due to limitations associated with the thermodynamic equilibrium are obtained. Also, alkene selectivity is low and carbon deposition on the active sites of the catalyst is favoured. The introduction of oxygen renders the reaction exothermic, eliminates most limitations imposed by thermodynamics and reduces carbon deposits on the catalyst. As a result, oxidative dehydrogenation (ODH) of alkanes is now preferred and plays a growing role in the petrochemical industry. Also, ODH of alkanes over redox catalysts has some advantages with respect to steam cracking or catalytic dehydrogenation, viz. the reaction is exothermic, a catalyst regeneration step is not required since catalyst regeneration occurs in situ by the oxygen feed and relatively low reaction temperatures (350–500 °C) are required.

Currently, considerable interest is devoted to studying the ODH of alkanes on supported vanadia catalysts and these catalysts show high activity in various partial oxidation and oxidative dehydrogenation reactions of hydrocarbons and it is generally accepted that supported vanadates are active catalysts for oxidative dehydrogenation. Optimum surface vanadium dispersion is one of the contributing factors in obtaining very active and selective catalysts operating under mild temperature and pressure conditions, achieving high conversions and selectivities, preventing coke formation and at the same time improving the lifetime of the catalyst. Hydroxyapatite (HAp) as support offers high stability and various substitutions are allowed by the apatite structure. Transition metal cations, which have potential as catalytic active centres, can be readily accommodated into the apatite framework based on the large cation exchange ability of HAp. The OH group within the phosphate frame-work leads to the formation of active oxygen species which are essential for ODH reactions.

All the characterization techniques showed that vanadium pentoxide is supported on hydroxyapatite and is well dispersed. For the 10 and 15 wt% loadings, vanadium exhibits two types of phases, the vanadium pentoxide and pyrovanadate phase, confirmed by XRD diffractograms and supported by IR. TPR profiles showed that as the vanadium concentration increases, reduction occurs at higher temperatures. TPD showed that total acidity of the catalysts increases as the vanadium loading increases. TPO profiles showed that vanadium will be oxidised to V_2O_5 after reduction, but the average oxidation state after oxidation is +4.5. TPR-TPO-TPR experiments showed that the first and second reductions follow similar pathways. XPS analysis showed that vanadium is in the +5 oxidation state on the surface of the hydroxyapatites. XPS analysis on the reduced catalyst indicated that vanadium existed in the +3 oxidation state. Further analysis on this catalyst after oxidation showed a +5 oxidation state. From diffractograms obtained by *in situ* XRD under octane at lower temperatures, V_2O_5 (V^{5+}) is reduced to V_2O_4 (V^{4+}) as evidenced in TPR. With an increase in temperature, V_2O_4 (V^{4+}) is further reduced to V_2O_3 (V^{3+}). The onset temperature for the transformation of V_2O_5 is 250 °C. As this experiment was conducted in a redox environment, the resulting V_2O_3 (V^{3+}) phase was oxidized to V_2O_5 (V^{5+}).

Oxidative dehydrogenation reactions carried out in a continuous flow fixed bed reactor indicated that selectivity towards desired products was dependent on the vanadium concentration and the phase composition of the catalyst. Good selectivity towards octenes was achieved using the 2.5 wt% V_2O_5 on Ca-HAp loaded catalyst. There was a marked decrease in octene selectivity and a significant increase in the formation of C8 aromatics when higher loadings of vanadium were used. For a conversion of 24% at 450 °C, the 15 wt% V_2O_5 on Ca-HAp showed a selectivity of 72% towards octenes. A maximum selectivity of 10 % for C8 aromatics was obtained using the 15 wt% V_2O_5 on Ca-HAp catalyst at a conversion of 36 % at 550 °C.

The oxidative dehydrogenation experiments over vanadium pentoxide supported on alkaline earth metal hydroxyapatites showed that vanadium pentoxide, which is the dominant phase in the lower loadings, gave high selectivity towards octenes and low selectivity towards aromatics. All the catalysts showed moderate to high selectivity towards carbon oxides, since vanadium pentoxide also favours the formation of oxygenates. The selectivity of the products was dependent on the *n*-octane to oxygen molar ratios and the phase of vanadium present on

hydroxyapatites. *n*-Octane to oxygen molar ratios of 1:0.5 showed highest selectivity towards octenes whereas molar ratios of 1:1 and 1:2 showed highest selectivity towards aromatics and oxygenates. Ca-HAp showed selectivity towards octenes and CO_x, Sr-HAp and Ba-HAp showed selectivity towards aromatics, whereas Mg-HAp showed selectivity towards aromatics and oxygenates. Good selectivity towards octenes was achieved using the 2.5 wt% V₂O₅ loaded hydroxyapatite catalysts. There was a marked decrease in octene selectivity and a significant increase in the formation of C8 aromatics when the 10 wt % loaded catalyst was used. Overall, for the activation of *n*-octane, 3-octene in the octenes, *o*-xylene in the aromatics and 2-octanone in the oxygenates were the major products. At iso-conversion of 27% at 450 °C, the 2.5VSr-HAp showed a selectivity of 71% towards octenes at an *n*-octane to oxygen molar ratio of 1:1, whereas the lowest selectivity of 40 % towards octenes was showed by 2.5VCa-HAp, at an *n*-octane to oxygen molar ratio of 1:2. The highest selectivity towards C8 aromatics was obtained by the 10VSr-HAp of 17 %. A maximum selectivity of 31% and 30% towards oxygenates was obtained when 10VSr-HAp and 10VBa-HAp were used as catalysts respectively, at an *n*-octane to oxygen molar ratio of 1:2.

In the reaction pathway studies using *n*-octene, all the isomers showed good selectivity towards aromatics. Oxygenates and carbon oxides (CO_x) were also formed. Highest selectivity towards aromatics was shown by the 2-octene and 3-octene isomers, with both loadings of V₂O₅ at all hydrocarbon to oxygen molar ratios. However, as the hydrocarbons to oxygen molar ratios were decreased, an increase in the selectivity towards aromatics and an increase in selectivity towards CO_x was observed. The terminal octene and 1,7-octadiene preferred the 1,6-cyclization mode, whereas 2-octene and 3-octene followed the 2,7 cyclization mode during the formation of aromatic compounds. Highest selectivity towards aromatics is shown by 2-octene and 3-octene isomers with both 2.5 wt% V₂O₅ and 10 wt% V₂O₅ on hydroxyapatites at all hydrocarbon to oxygen molar ratios. There was a marked increase in the selectivity of aromatics and increase in the selectivity of CO_x as the hydrocarbon to oxygen molar ratio decreased. 10VCa-HAp showed significant selectivity towards aromatics at all hydrocarbon to oxygen molar ratios with 1-octene, 2-octene and 1,7-octadiene. 2.5VMg-HAp showed high selectivity towards oxygenates with all the octene isomers and a significant selectivity towards aromatics with 3-octene. High selectivity towards the cracked products is shown by 10VCa-HAp and 10VSr-HAp with 3-octene at a ratio

of 1:2. Here, 1-octene and 1,7-octadiene prefer to form aromatics in the 1,6-cyclization mode and 2-octene and 3-octene prefer to form aromatics via the 2,7 cyclization mode. The oxidation-reduction path way in this reaction follows the Mars-van Krevelen mechanism. *n*-Octane was initially oxidatively dehydrogenated to octenes followed by oxidative dehydrogenation forming aromatics and oxygenates. No phase changes were observed in the used catalysts. However, some textural changes were induced by the catalytic testing which was observed by SEM and TEM.

APPENDIX

A1. Schematic representation of Reactor

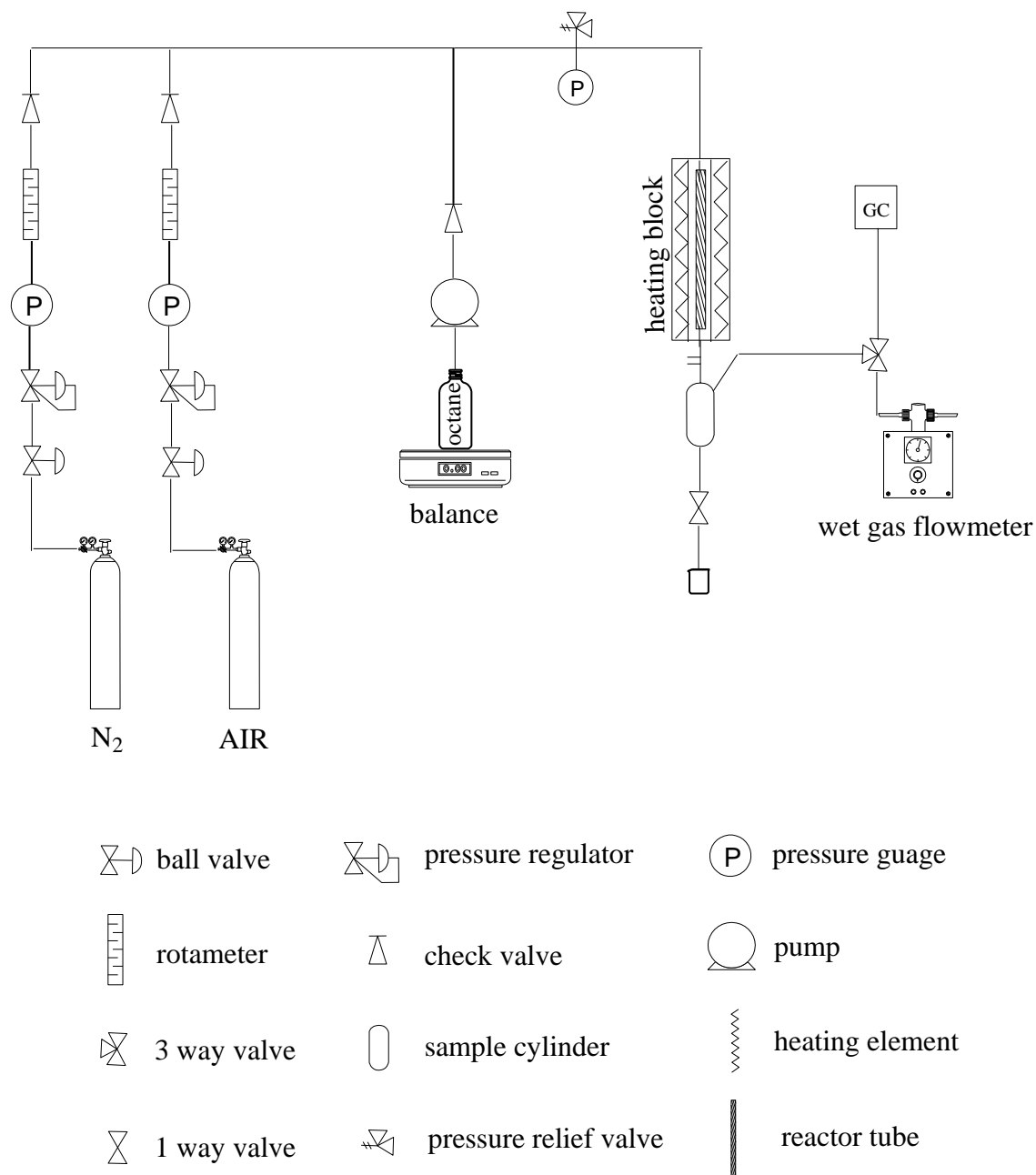


Figure A1. Reactor design used for experimental work

A2. GC-Method used for analyzing organic (gaseous and liquid) samples

Channel Parameters:

Run Time: 30.00 min

Sampling Rate: 3.1250 pts/s

Carrier Parameters:

Carrier A Control: He (300 Kpa)

Column A length: 50.00 m

Vacuum Compensation: Off

Diameter: 530 μ m

Split Ratio: 150:1

Initial Set point: 2.0 ml/min

Valve Configuration and Setting:

Valve 1: SPLIT On

Valve 2: NONE

Valve 3: NONE

Detector Parameters:

	Detector A
Detector	FID
Range	1
Time Constant	200
Autozero	ON
Polarity	-

Detector A Gas Flows

Air: 450.0 ml/min

Hydrogen: 45.0 ml/min

Heated Zones:

Injector A: CAP

Setpoint: 220 °C

Detector A: 250 °C

Oven Program:

Cryogenics: Off

Total Run Time: 30.0 min

Initial Temp: 40°C

Max. Temp: 300 °C

Initial Hold: 15.0 min

Equilibration Time: 0.2 min

Ramp 1: 20.0 °C/min to 100 °C, hold for 5.0 min

Ramp 2: 20.0 °C/min to 200 °C, hold for 2.0 min

Processing Parameters:

Bunch Factor: 2 points

Noise threshold: 50 µV

Area Threshold: 100.0 µV

Peak Separation Criteria:

Width Ratio: 0.2

A3. GC-Method used for analyzing carbon oxides

Channel Parameters:

Run Time: 7.0 min

Sampling Rate: 6.25 pts/s

Carrier Parameters:

Carrier B Control: He (300 KPa)

Column B length: 30.00 m

Vacuum Compensation: Off

Diameter: 530 μm

Split Flow: 500.0 ml/min

Initial Set point: 6.0 ml/min

Valve Configuration and Setting:

Valve 1: SPLIT On

Valve 2: NONE

Valve 3: NONE

Detector Parameters:

	Detector B
Detector	TCD
Range	3
Time Constant	200
Autozero	ON
Polarity	-
Detector B Gas Flows	Helium: 30.0 ml/min

Heated Zones:

Injector B: CAP

Set point: 220 °C

Detector B: 250 °C

Oven Program:

Cryogenics: Off

Total Run Time: 7.0 min

Initial temp: 40 °C

Max. Temp: 250 °c

Initial Hold: 2.50 min

Equilibration Temp: 0.5 min

Ramp 1: 20.0 °C/min to 80 °C, hold for 2.5 min

Processing Parameters:

Bunch Factor: 2 points

Noise threshold: 1 μV

Area Threshold: 100.0 μV

Peak Separation Criteria:

Width Ratio: 0.2

Valley-to-peak Ratio: 0.01

Table A1 Standards used for calibration

Chemical	Supplier	Purity (%)
<i>n</i> -Octane	Merck	99
1-Octene	Aldrich	98
<i>trans</i> -2-Octene	Fluka	98
<i>cis</i> -2-Octene	AlfaAesar	98
<i>trans</i> -3-Octene	Aldrich	98
<i>trans</i> -4-Octene	Fluka	98
<i>cis</i> -4-Octene	AlfaAesar	97
1,7-Octadiene	Fluka	97
Ethylbenzene	AlfaAesar	99
<i>o</i> -Xylene	AlfaAesar	99
Styrene	Aldrich	99
Ethylcyclohexane	Fluka	99
<i>n</i> -heptane	Fluka	99.8
1-heptene	Aldrich	97
<i>n</i> -hexane	ACROS	99.5
1-hexene	ACROS	97
<i>n</i> -Nonane	Fluka	99
Cyclooctane	Fluka	99
<i>cis</i> -Cyclooctene	Aldrich	95
<i>cis,cis</i> -1,5-Cyclooctadiene	Fluka	98
Propylcyclopentane	Fluka	98
2,4-Dimethylhexane	Fluka	99
2-ethyl-1-hexanol	Fluka	98
1-Octanol	AlfaAesar	99
Octanal	Aldrich	99
2-Octanone	Fluka	97
3-Octanone	Fluka	97

Table A2 Gaseous standards used for calibration

Mixture	Component	Percentage (%)
Mixture 1	Ethane	3.0
	Ethene	6.0
	<i>n</i> -Butane	9.2
	Nitrogen	81.8
Mixture 2	Methane	2.0
	Propane	4.0
	Propene	6.0
	Nitrogen	88.0
Mixture 3	Carbon monoxide	5.0
	Carbon dioxide	15.0
	Nitrogen	80.0

A4. GC analysis

All products that were obtained from the reaction were quantified using Gas Chromatography (GC). To this end, a Perkin Elmer Clarus 400 instrument was used and was equipped with a Thermal Conductivity Detector (TCD) for the sequential analysis of carbon oxides using a Carboxen 106 PLOT column and a Flame Ionization Detector (FID) for all other organic products using a 50m PONA column, respectively. All the products are verified by analysis analyzing using Perkin Elmer Clarus 500 GC-MS instrument.

A5. FID Sampling

Gaseous organic products were analysed on the FID by injecting a 0.2 ml gas sample withdrawn at the specific analysis time. The GC chromatogram for a gaseous sample is shown in Figure A2. The compounds are identified by the retention times where the retention times are given in the Table A4. These compounds are verified by GC-MS analysis with a NIST library search (Figures A5 and A8).

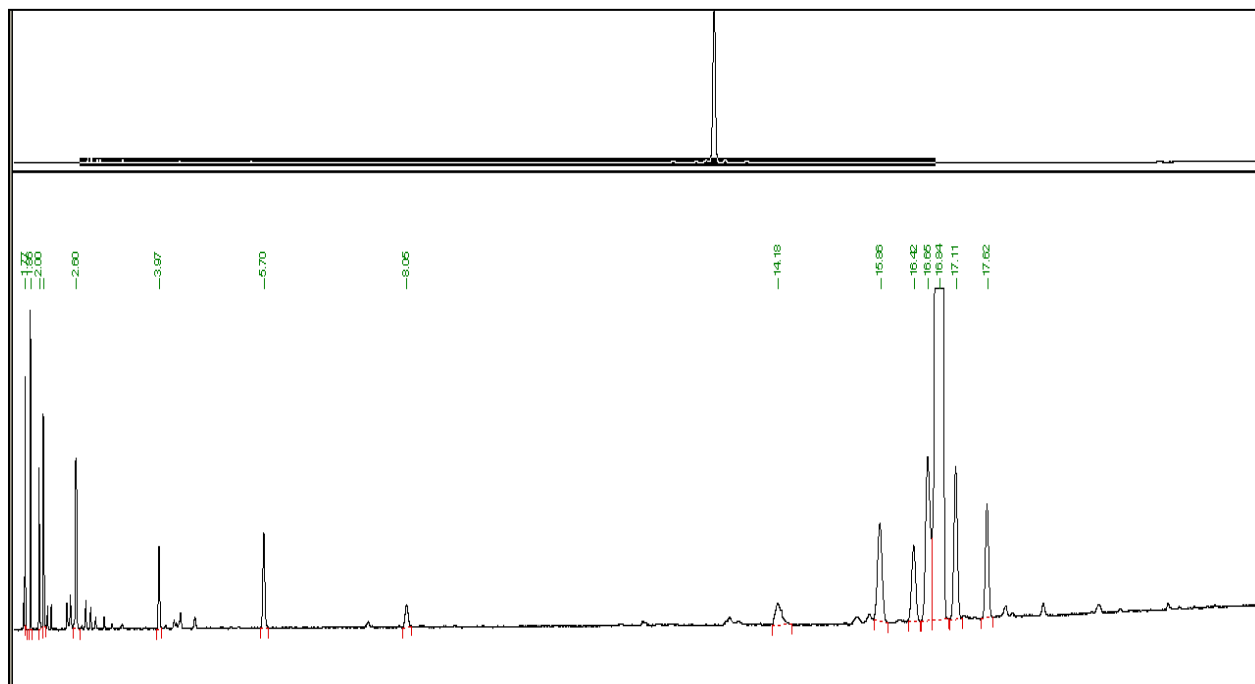


Figure A2. GC-FID chromatogram for a gaseous sample

Liquid organic products that condensed in the sample cylinder were drained *via* the needle valve and accurately weighed. In some cases, two distinct layers were observed i.e. an organic layer and an aqueous layer. These were then carefully separated and re-weighed to obtain their

individual contributions to the total mass of liquid products. The GC method to analyse these layers is explained below. Chromatograms were then obtained for each of the layers separated. GC- chromatograms for an organic layer and an aqueous layer was shown in Figure A3 and Figure A6. The GC-MS analysis of these layers and the library match was shown in Figures A4, A5, A7 and A8.

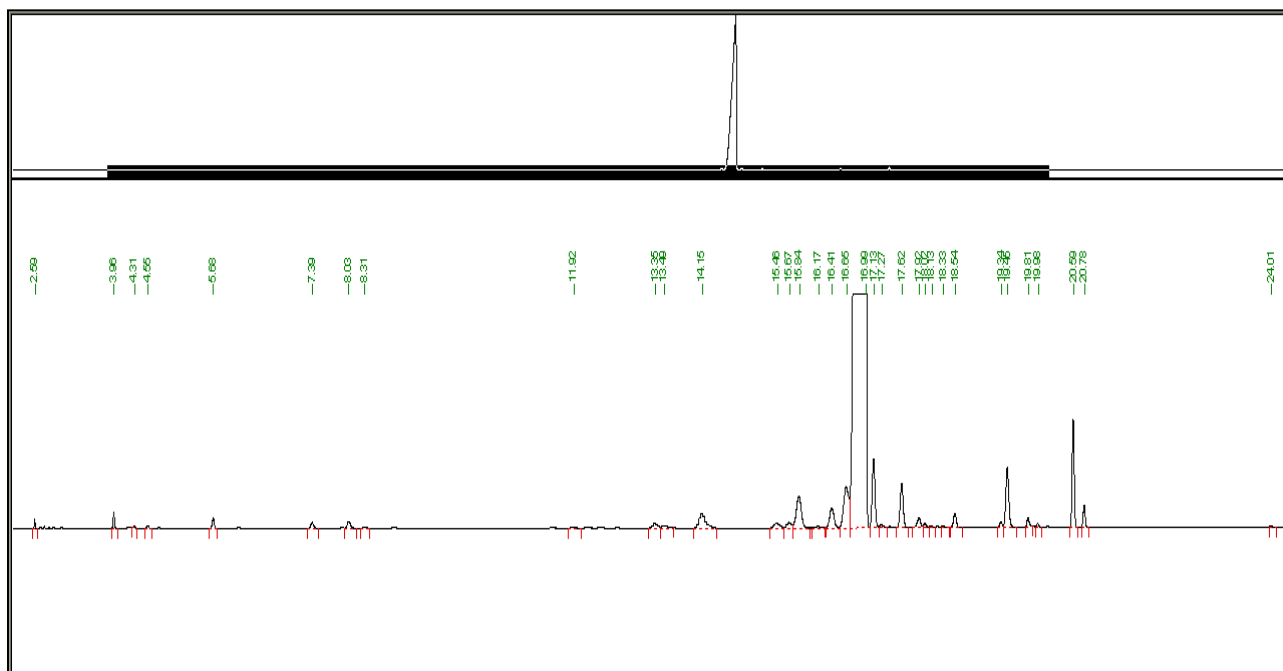


Figure A3. GC-FID chromatogram for a organic layer

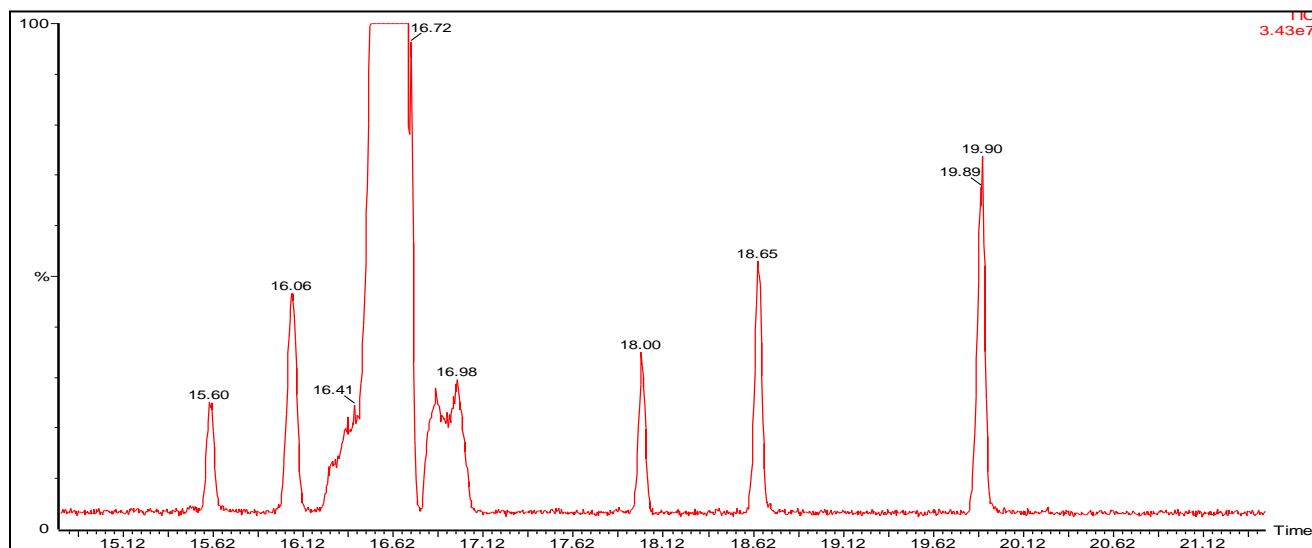


Figure A4. GC-MS chromatogram for a organic layer

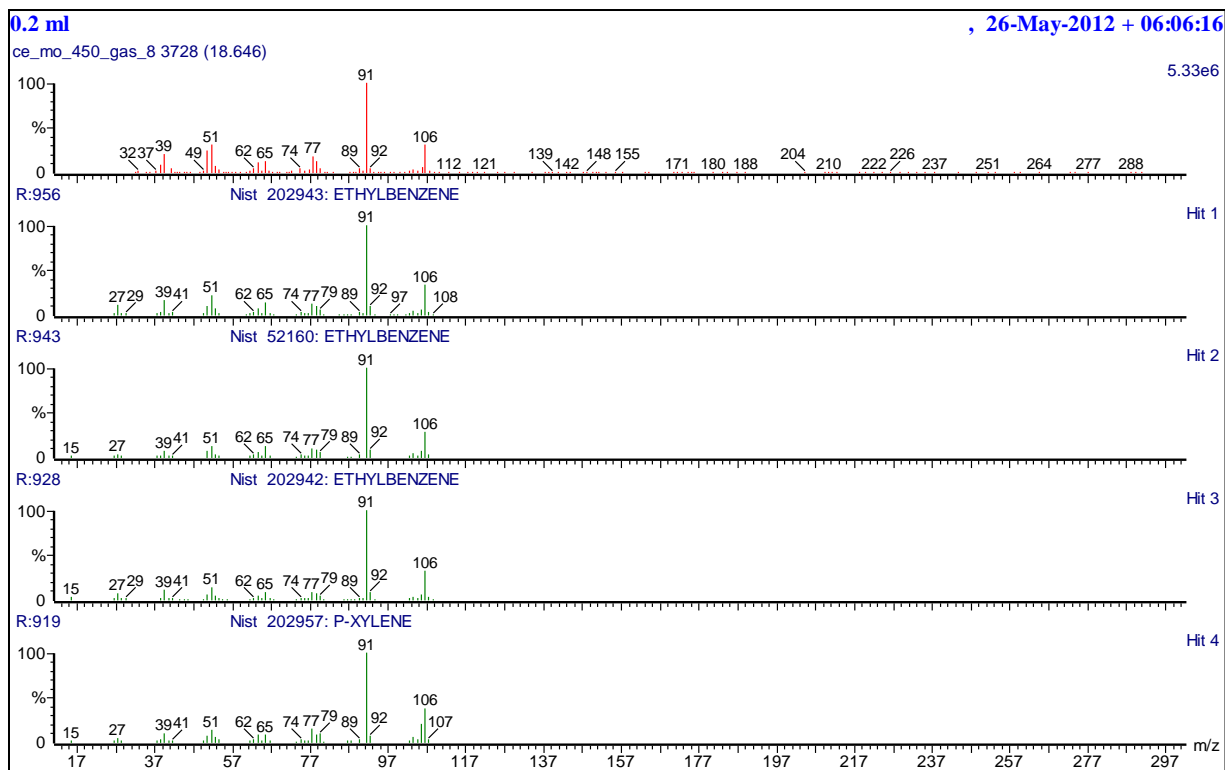


Figure A5. GC-MS NIST library search match for ethyl benzene (R. T = 18.46 min)

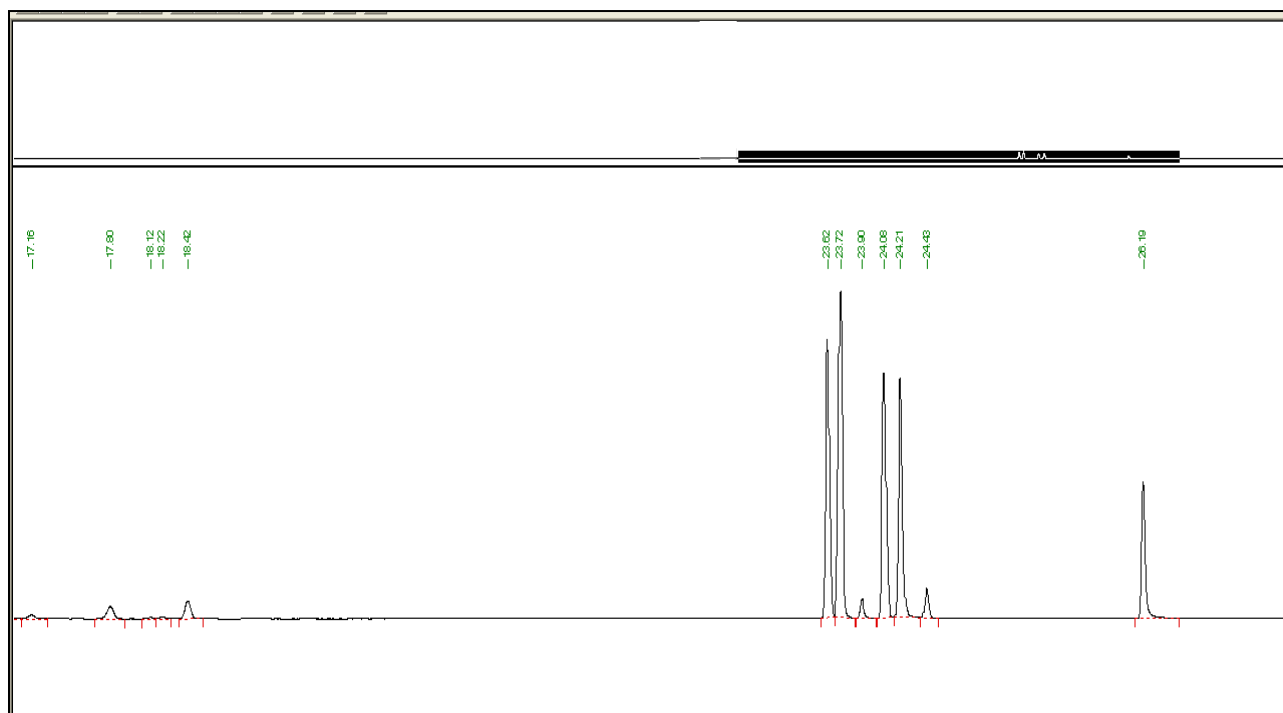


Figure A6. GC-FID chromatogram for a aqueous layer

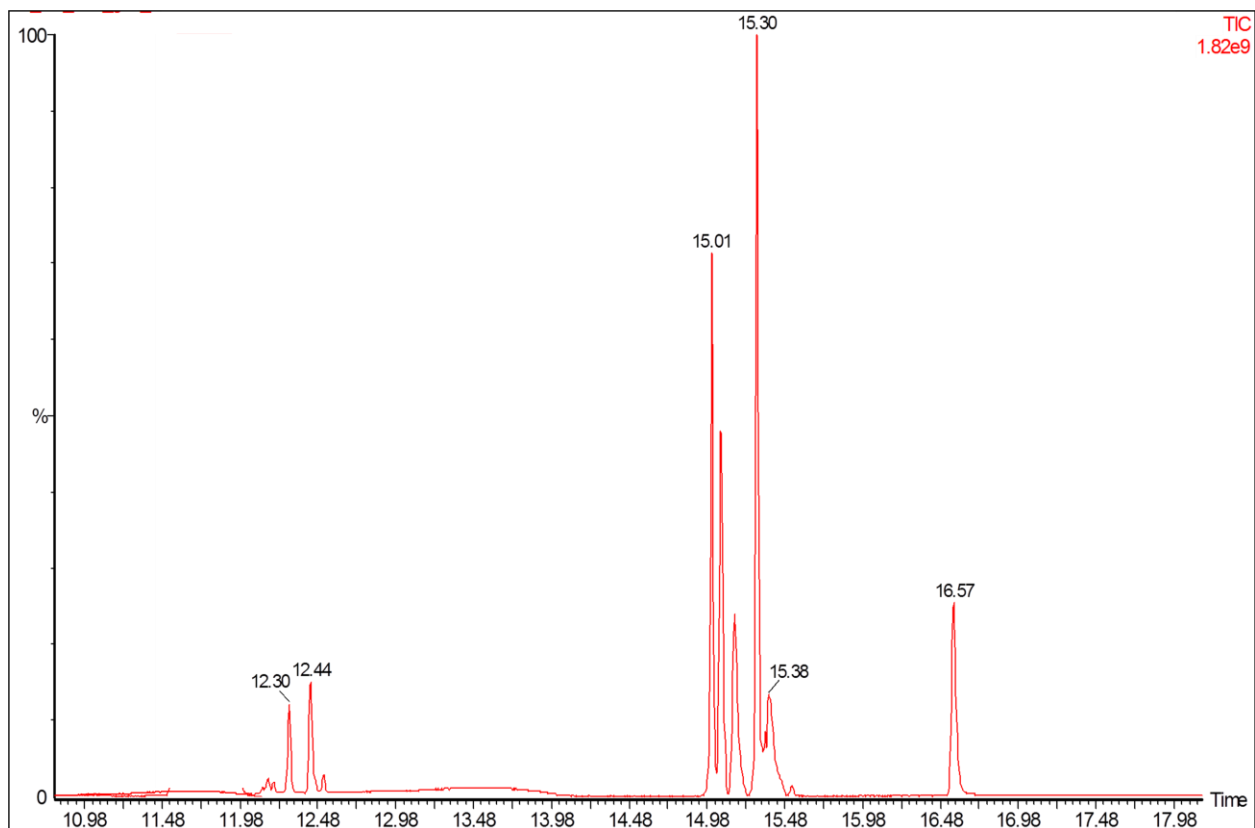


Figure A7. GC-MS chromatogram for aqueous layer

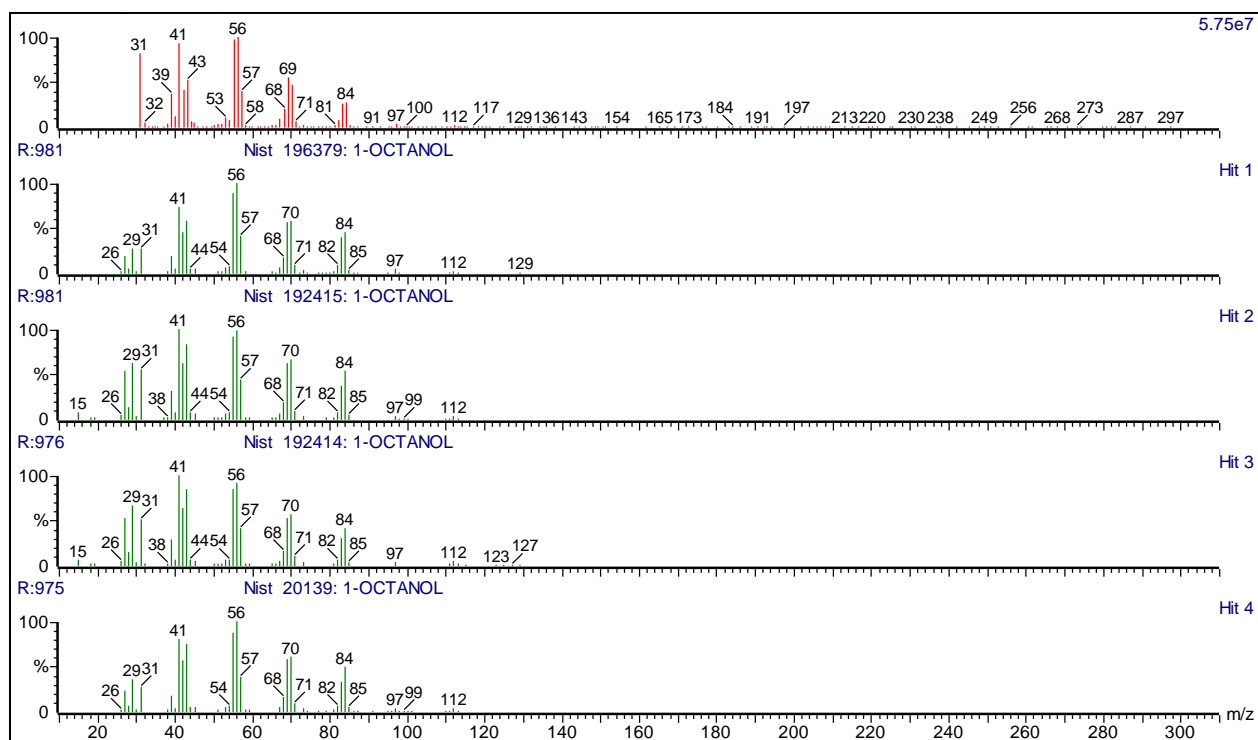


Figure A8. GC-MS NIST library search match for 1-octanol (R. T = 16.57 min)

A6. TCD sampling

Both carbon monoxide and carbon dioxide were produced during the various reactions. These were analysed by withdrawing a 100 μl gas sample using a 500 μl gas tight syringe supplied by Scientific Glass Engineering Pty. Ltd. (SGE).

In order to quantify the data obtained from the chromatograms during one analysis to usable data, such as yield and conversion, parameters including run time, mass of feed used, mass of products collected and gas flow rates were recorded. In addition, the water content of the individual layers in the liquid products was determined by Karl Fischer Analysis using a Metrohm 870 KF Titrino Plus instrument. The values obtained were used to correct the mass of the organic and aqueous layers as shown in the example below.

A7. KF calculation

Mass of organic layer = 59.5160 g

Average water content as determined by KF = 1.26 %

Actual Mass of organics in the organic layer = 59.5160

A8. Calculation of response factors (RF):

Assign *n*-octane a RF of 1 and calculate all other Response Factors relative to this:

Mass of *n*-octane in standard solution = 0.0073 g

Mass of trans-2-octene in standard solution = 0.00715g

Injection volume = 0.1 μl

Peak area of *n*-octane = 46684.56

Peak area of trans-2-octene = 51712.54

$$\text{Response factor of trans-2-octene} = \frac{\text{peak area of trans-2-octene} \times \text{mass of } n\text{-octane}}{\text{mass of trans-2-octene} \times \text{peak area of } n\text{-octane}}$$

Table A3 Relative response factor of trans-2-octene

Injection volume (μl)	Amount of trans-2-octene	Peak area of trans-2-octene	Amount of n-octane injected	Peak area of n-octane	Relative response factor (RF)
0.1	0.00071	51712.4	0.000703	46684.56	0.91
0.2	0.00153	113505.4	0.001406	94551.7	0.90
0.3	0.00224	158300.4	0.002109	135843.9	0.91
0.4	0.00286	229127.5	0.002812	205057.4	0.91
0.5	0.00317	247929.5	0.003515	249743.4	0.90

Average response factor of trans-2-octene = 0.91

Table A4 Retention times, Response factors and gradient of the calibration graph of compounds

Component	R. T. (min)	R.F	Equation (y=..)
methane	1.545	0.91	3.77E+14
ethane/ethene	1.566	0.92	5.11E+14
propane / propene	1.647	0.94	1.08E+14
methanol	1.76	0.93	1.78E+14
butane	1.851	0.92	1.19E+14
ethanol	2.006	0.53	3.53E+14
acetone	2.171	0.52	4.57E+14
2-propanol	2.248	0.51	4.37E+14
1-pentene	2.432	0.93	1.01E+14
2-methyl-2-propanol	2.477	0.72	8.13E+14
pentane	2.37	0.76	8.81E+14
butanone	3.258	0.69	6.82E+14
1-hexene	3.52	0.95	1.36E+14
hexane	3.692	0.93	1.32E+14

Component	R. T. (min)	R.F	Equation (y=..)
methylcyclopentane	4.311	0.92	1.24E+14
heptane	6.98	0.91	1.63E+14
2,4-dimethylhexane	8.97	0.94	1.79E+14
toluene	10.47	1.12	1.57E+14
4-methylheptane	11.72	1.14	1.83E+14
1,7-octadiene	12.52	0.90	1.85E+14
1-octene	13.8	0.98	1.90E+14
3-octene	14.9	0.98	1.75E+14
trans-4-octene	14.53	0.97	1.83E+14
octane	15.26	0.95	1.82E+14
trans-2-octene	15.59	0.94	1.79E+14
1,3-octadiene	16.523	0.92	1.54E+14
ethylcyclohexane	16.92	0.90	1.87E+14
propylcyclopentane	16.931	0.95	1.75E+14
ethylbenzene	17.58	1.13	1.93E+14
styrene	18.34	1.17	1.75E+14
xylene	18.49	1.15	1.92E+14
cis-cyclooctene	18.829	1.20	1.78E+14
cyclooctane	19.16	1.16	1.90E+14
cis.cis-1,5-cyclooctadiene	19.52	1.12	1.84E+14
4-octanone	20.839	0.73	1.32E+14
3-octanone	21.28	0.91	1.87E+14
2-octanone	21.394	0.84	1.80E+14
3-octanol	21.83	0.76	1.51E+14
octanal	21.84	0.71	1.40E+14
2-octanol	21.992	0.78	1.46E+14
octene oxide	22.244	0.85	1.61E+14
benzyl alcohol	22.765	0.89	1.28E+14
1-octanol	24.446	0.85	1.86E+14
octanoic acid	26.396	0.61	1.23E+14

A9. Determination of moles of trans-2-octene from a liquid organic sample

Mass of the organic layer = 3.2056 g

Percentage peak area of trans-2-octene = 0.81

Calculated Response Factor = 0.91

Corrected area = Percentage peak area x Response factor = $0.81 \times 0.91 = 0.7371$

Normalised area (%) = $\frac{\text{corrected area}}{\text{sum of corrected areas of all products in sample}} \times 100$

$$= 0.7325$$

Mass component out (g) = $\frac{\text{normalised area}}{100} \times \text{mass of organic layer}$

$$= \frac{(0.7325 \times 3.2056)}{100} = 0.0235 \text{ g}$$

Moles component out (mol) = $\frac{\text{mass of component out}}{\text{molar mass of component}}$

$$= \frac{0.0235}{112.21} = 2.095 \times 10^{-4} \text{ mol}$$

Moles of carbon in component = moles component \times carbon number

$$= 0.0017 \text{ mol of carbon}$$

A10. Determination of moles of butane from a gaseous organic sample

Actual peak area of butane = 2059.96

Butane calibration = 1.15×10^{12}

Moles in 0.1 ml injected = (actual peak area) / (butane calibration)

$$= 1.8 \times 10^{-9}$$

Volume of gas out = 12325 ml

Moles of butane in out gas = $(1.8 \times 10^{-9} \times 12325) / 0.1 \text{ ml}$

$$= 2.22 \times 10^{-4} \text{ mol}$$

$$\begin{aligned}\text{Moles carbon of butane out} &= 2.22 \times 10^{-04} \times 4 \\ &= 8.88 \times 10^{-04} \text{ mol}\end{aligned}$$

A11. Determination of moles of CO from gaseous sample

$$\text{Actual peak area of CO} = 725.32$$

$$\text{CO mole calibration} = 2.75 \times 10^{11}$$

$$\begin{aligned}\text{Moles of CO in injection volume} &= (922.34) / (2.75 \times 10^{11}) \\ &= 3.35 \times 10^{-09}\end{aligned}$$

$$\text{Volume of gas out} = 12325 \text{ ml}$$

$$\begin{aligned}\text{Moles of CO out (mol)} &= (3.35 \times 10^{-09} \times 12325) / 0.1 \text{ mol} \\ &= 0.00413 \text{ mol}\end{aligned}$$

$$\text{Moles of carbon out} = 0.00413 \times 1 = 0.00413 \text{ moles}$$

A12. Analysis of Temperature programmed Reduction, Oxidation and Desorption

Calculation of average oxidation state of vanadium in TPR

$$\text{Degree of reducibility (\%)} = \frac{\text{moles of hydrogen consumed}}{\text{moles of vanadium in the sample}} \times 100$$

$$\text{Average oxidation state of vanadium} = 5 - \frac{(\text{moles of hydrogen consumed} \times 2)}{\text{moles of vanadium in the sample}}$$

Calculation of average oxidation state of vanadium in TPO

$$\text{Degree of reduction (\%)} = \frac{\text{moles of oxygen consumed}}{\text{moles of vanadium in the sample}} \times 100$$

$$\text{Average oxidation state of vanadium} = 3 + \frac{(\text{moles of oxygen consumed} \times 2)}{\text{moles of vanadium in the sample}}$$

Calculation of number of acidic sites from TPD

$$\text{No. of acidic sites (acidity)} = \frac{\text{moles of ammonia consumed}}{\text{mass of the catalyst}}$$

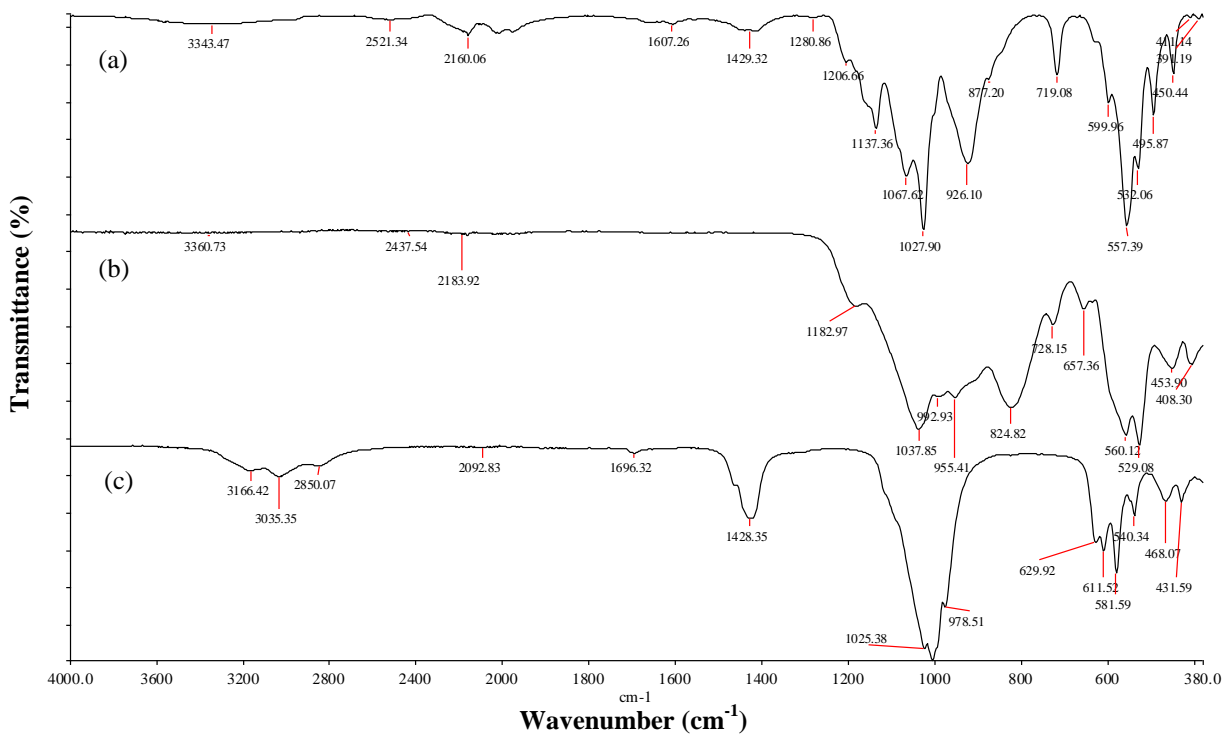


Figure A9. Infrared spectra of 2.5 wt% V_2O_5 supported on strontium (a), magnesium (b) and barium (c) hydroxyapatites

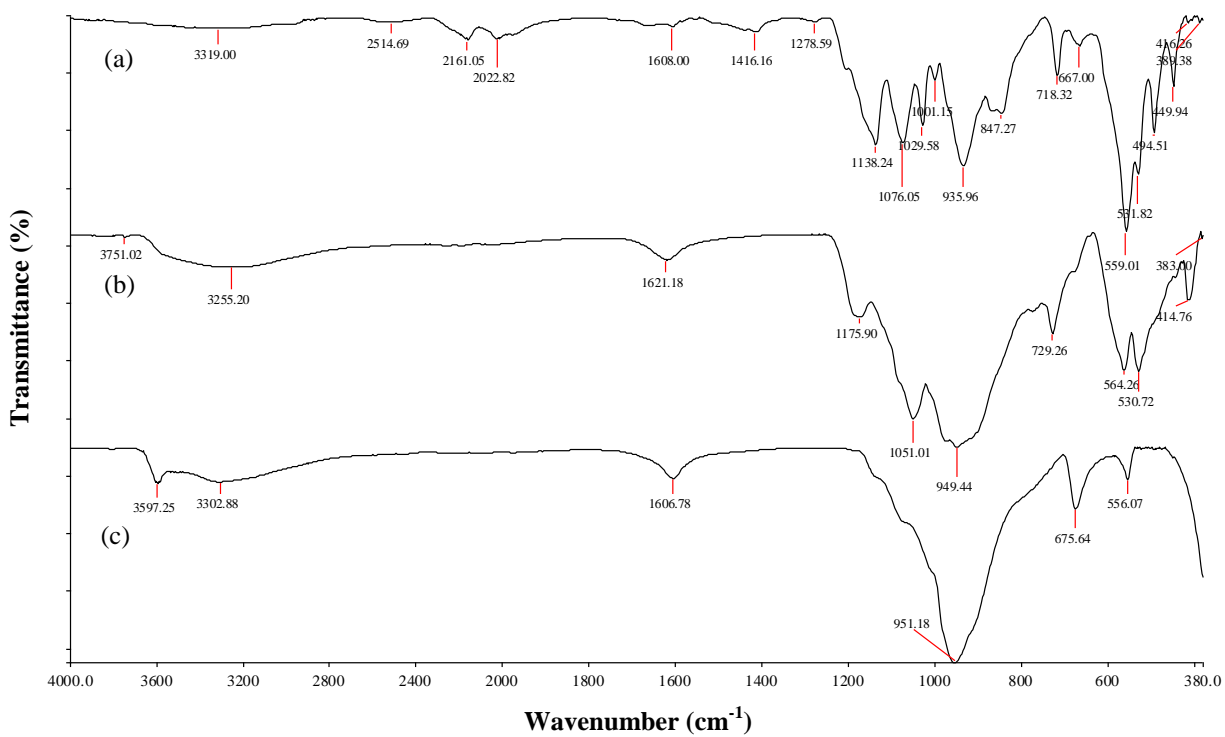


Figure A10. Infrared spectra of 10 wt% V_2O_5 supported on strontium (a), magnesium (b) and barium (c) hydroxyapatites

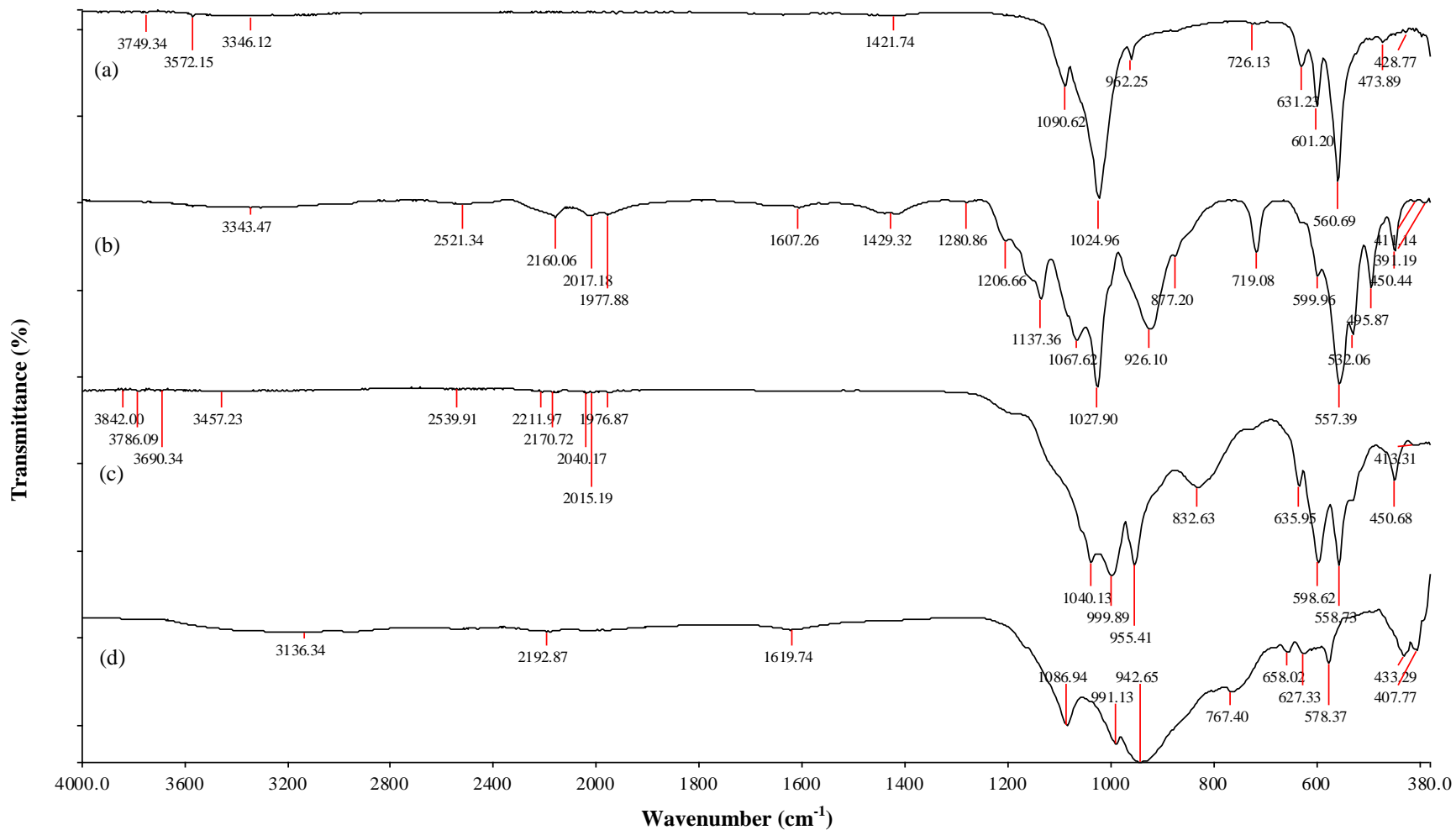


Figure A11. Infrared spectra of 2.5 wt% V₂O₅ supported on calcium (a), strontium (b), magnesium (c) and barium (d) hydroxyapatites used at a hydrocarbon to oxygen ratio of 1:2

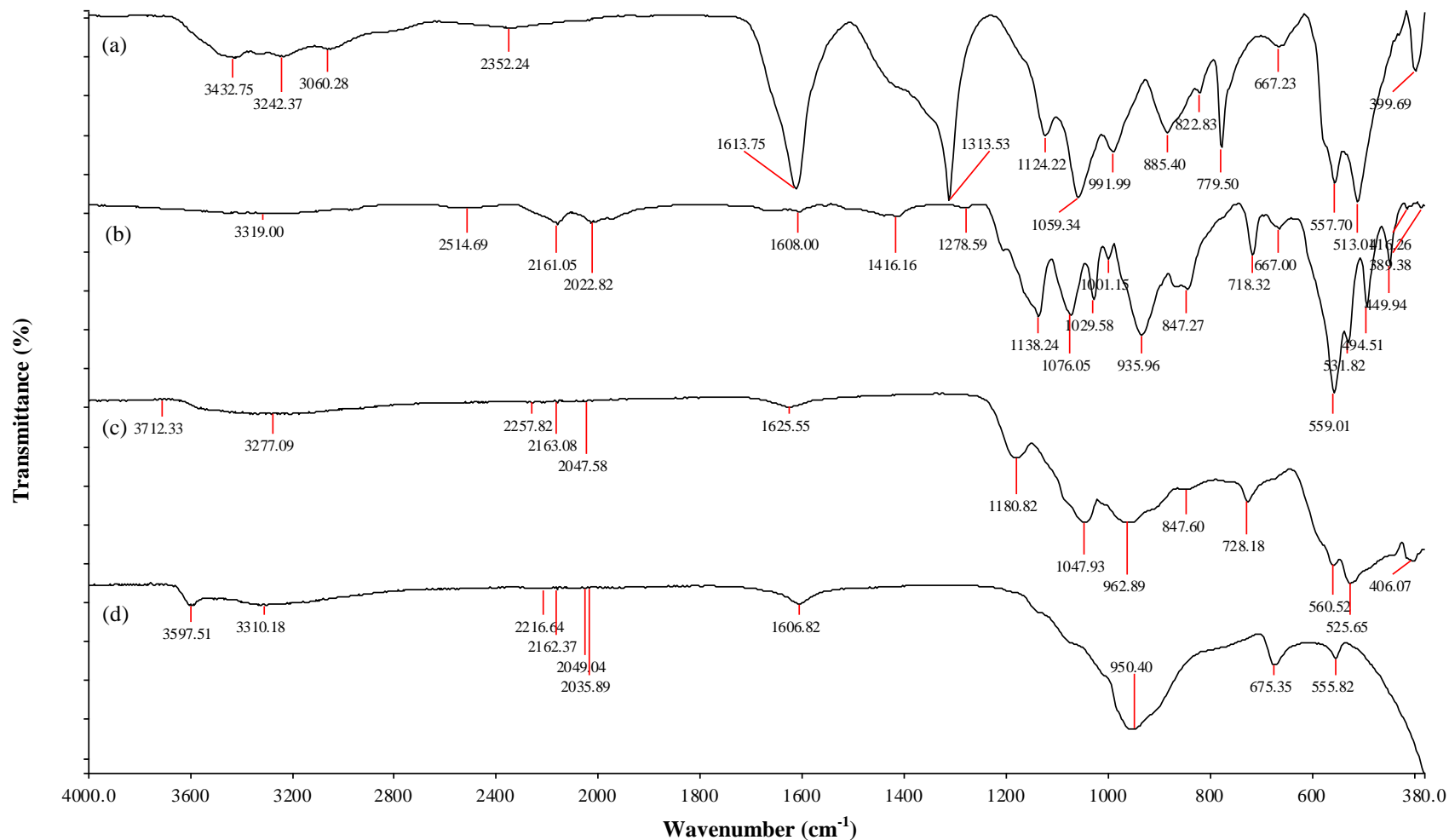


Figure A12. Infrared spectra of 10 wt% V₂O₅ supported on calcium (a), strontium (b), magnesium (c) and barium (d) hydroxyapatites used at a hydrocarbon to oxygen ratio of 1:2

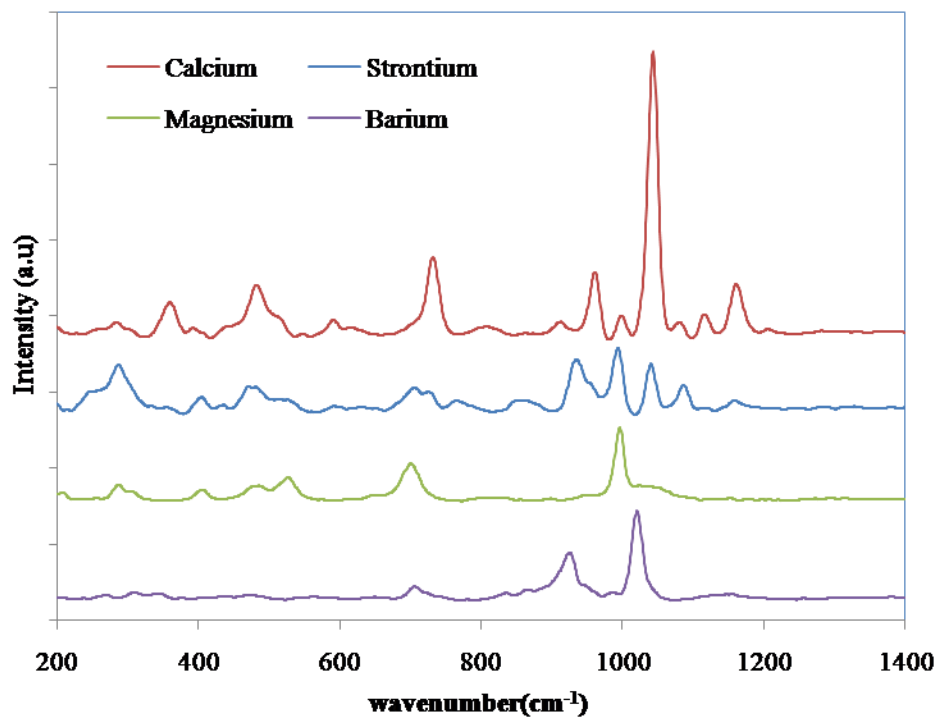


Figure A13. Raman spectra of 2.5 wt% V_2O_5 supported on hydroxyapatites used at a hydrocarbon to oxygen ratio of 1:2

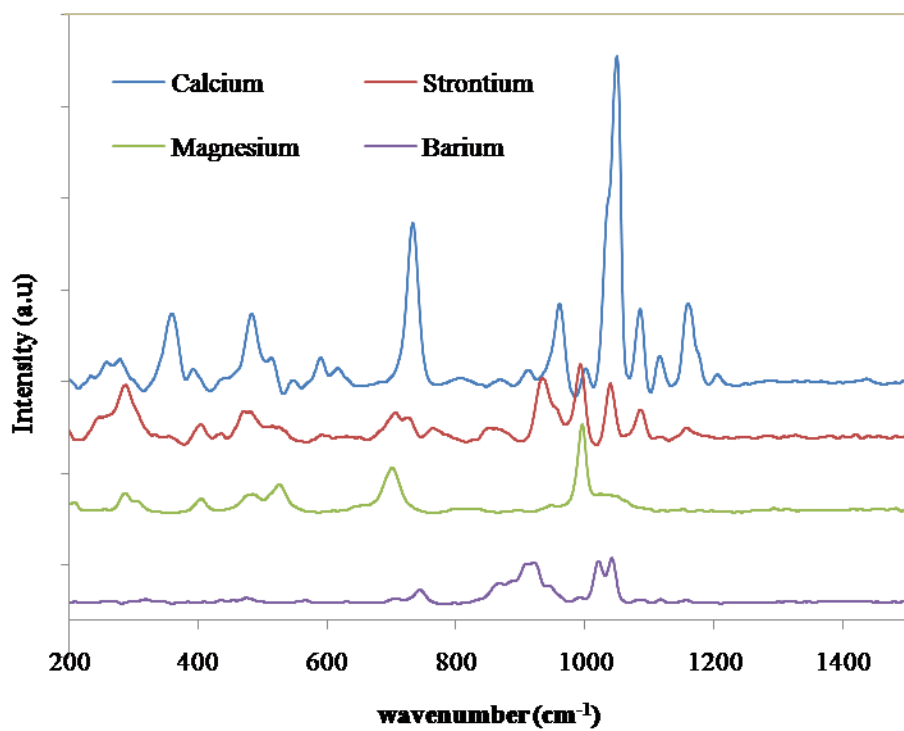


Figure A14. Raman spectra of 10 wt% V_2O_5 supported on hydroxyapatites used at a hydrocarbon to oxygen ratio of 1:2